ENVIRONMENTAL APPLICATIONS

OF

ESI FT-ICR MASS SPECTROMETRY:

OXIDIZED PEPTIDES AND METAL SULFIDE CLUSTERS

by

Jeffrey M. Spraggins

A dissertation submitted to the Faculty of the University of Delaware in partial fulfillment of the requirements for the degree of Doctor of Philosophy in Analytical Chemistry

Fall 2009

ENVIRONMENTAL APPLICATIONS

OF

ESI FT-ICR MASS SPECTROMETRY:

OXIDIZED PEPTIDES AND METAL SULFIDE CLUSTERS

by

Jeffrey M. Spraggins

Approved: _____
Klaus Theopold, Ph.D.
Chair of the Department of Chemistry and Biochemistry

Approved: _____
George H. Watson, Ph.D.
Dean of the College of Arts and Sciences

Approved: _____
Debra Hess Norris, M.S.
Vice Provost for Graduate and Professional Education

I certify that I have read this dissertation and that in my opinion it meets the academic and professional standard required by the University as a dissertation for the degree of Doctor of Philosophy.

Signed: _____

Douglas Ridge, Ph.D.
Professor in charge of dissertation

I certify that I have read this dissertation and that in my opinion it meets the academic and professional standard required by the University as a dissertation for the degree of Doctor of Philosophy.

Signed: _____

Murray Johnston, Ph.D.
Member of dissertation committee

I certify that I have read this dissertation and that in my opinion it meets the academic and professional standard required by the University as a dissertation for the degree of Doctor of Philosophy.

Signed: _____

Sharon Neal, Ph.D.
Member of dissertation committee

I certify that I have read this dissertation and that in my opinion it meets the academic and professional standard required by the University as a dissertation for the degree of Doctor of Philosophy.

Signed: _____

Barbara Larsen, Ph.D.
Member of dissertation committee

ACKNOWLEDGMENTS

I would like to start by thanking my advisor Dr. Ridge. I have been fortunate enough to have an adviser, who not only elevated my knowledge in the field of chemistry, but also enriched other aspects of my life by being a colleague, mentor, and friend. I cannot thank you enough, Dr. Ridge, for your guidance and support.

Also, thank you to my committee for all of your time and effort in making this possible. You questions and insight have helped sharpened my focus and kept me on track throughout this process.

Developing my skills as an educator has been a priority throughout my graduate studies and I would like to thank everyone that supported me and helped develop my understanding of what it means to be an effective educator. Thank you to all the GK-12 fellows and advisors. Working with you over the last two years has been a wonderful experience that I will never forget. Thank you to Gabriele Bauer and the HETC program. Also, I would like to thank all the professors I have worked with that have provided such great examples of effective teaching.

There are a number of people without whom my research would not have been possible. I would like to thank Julie Lloyd, Murray Johnston, and Julia Laskin for their help with the oxidized peptide project. In particular, I appreciate all of Julia's time and energy during my time at Pacific Northwest National Laboratory. I would like to thank our collaborators in the College of Marine Studies, Kate Mullaugh and George Luther who we worked closely with over the past few years. Thank you John Dykins for always being there to help with the instruments. Thank you to Pat McMahon and Jim Cleaver for dealing with all my computer issues. And also, I

would like to thank my wife's cousin, Thomas Goth. The JavaScript program you wrote saved me countless hours of data crunching.

Thank you to all the graduate students that I have worked so closely with during my time at UD. Scott Robinson who helped me get started in the Ridge group. All the members of the Johnston and Riordan groups who were always willing to lend a helping hand. But most importantly, thank you Kaitlin. Thank you for your help with the instruments, thank you for your insight, but mostly I am thankful for our friendship.

I need to thank all of my friends and family for their love and support. Especially my parents Jeff and Tia, my brother Justin and sister Crystal. You have always been there for me, ready to offer encouragement when I needed it. The strength of our family has always helped me properly keep things in perspective.

And finally, to my wife, Adrienne, Thank You. You have helped me through every step of this process. You have been my motivational force to get this done. I dedicate this to you.

TABLE OF CONTENTS

Appendices

LIST OF TABLES

LIST OF FIGURES

ABSTRACT

The research described in the following dissertation focuses on the use of ESI FT-ICR mass spectrometry for the analysis of complex environmental systems. The projects we have chosen are multidisciplinary by design including the fields of analytical, physical, inorganic, environmental and biochemistry. To begin with, the unique fragmentation pathways resulting from oxidative stress to angiotensin II are characterized using surfaced induced dissociation, RRKM modeling and molecular dynamics calculations. The final chapters focus on the study of metal sulfide nucleation in aqueous environments using thiol capping agents to interrupt particle growth and gas phase ion-molecule reactions of metal salt clusters with hydrogen sulfide.

The gas phase fragmentation reactions of singly charged angiotensin II (AngII, $DR^{+}VYIHPF$) and the ozonolysis products AngII+O ($DR^{+}VY^{*}IHPF$), AngII+3O ($DR^{+}VYIH^{*}PF$), and AngII+4O ($DR^{+}VY^{*}IH^{*}PF$) were studied using SID FT-ICR mass spectrometry, RRKM modeling, and molecular dynamics. Oxidation of Tyr (AngII+O) leads to a low-energy charge-remote selective fragmentation channel resulting in the b_4 fragment ion. Modification of His (AngII+3O and AngII+4O) leads to a series of new selective dissociation channels. For AngII+3O and AngII+4O, the formation of $[MH+3O]^{+}$-45 and $[MH+3O]^{+}$-71 are driven by charge-remote processes

while it is suggested that b_5 and $[MH+3O]^+$-88 fragments are a result of charge-directed reactions. Energy-resolved SID experiments and RRKM modeling provide threshold energies and activation entropies for the lowest energy fragmentation channel for each of the parent ions. Fragmentation of the ozonolysis products was found to be controlled by entropic effects. Mechanisms are proposed for each of the new dissociation pathways based on the energies and entropies of activation and parent ion conformations sampled using molecular dynamics.

Developed through collaboration with the College of Marine Studies, our focus shifted to the study of metal sulfide clusters. The initial experiments include the observation of metal salt cluster growth in solution using ESI mass spectrometry. Relative intensities of the observed clusters ($[Cd_x(NO_3)_{2x+1}]$-, x = 1-5) shift to larger clusters following dilution of aqueous solutions with methanol. The time-dependent variance in the relative signal intensity is evidence of salt nucleation in water-methanol binary solvent systems suggesting larger clusters may persist in low dielectric constant solutions as found in supercritical aquatic systems.

With the methodology in place to effectively elecrospray cadmium salt clusters, observing metal sulfide cluster formation became the primary focus. The first approach was to use capping agents to interrupt particle growth at various stages of nucleation. Sulfidic metal clusters were observed for reactions of cadmium nitrate with hydrogen sulfide using 2-mercaptopyridine as a molecular capping agent. While

NO_3 ligands were substituted by sulfate for larger clusters ($[Cd_x(NO_3)_{2x+1}]$-, x = 2-5), no reaction products were observed for the single cadmium nitrate complex.

Finally, gas phase ion-molecule reactions between metal salt clusters and hydrogen sulfide were used to understand metal sulfide cluster formation. A simplified sequential pseudo first-order kinetic model was used to describe reactions. Anionic clusters were shown to react with low reaction efficiencies (k_x/k_c < 5%) with the exception of $[Cd_4(CH_3COO)_9]^-$ which displayed enhanced reactivity following formation of the $[Cd_4S(CH_3COO)_7]^-$ intermediate. No reaction products were observed for any anionic cadmium chloride cluster. Large cationic cadmium acetate clusters ($[Cd_x(CH_3COO)_{2x-1}]^+$, x = 2-4) were shown to react fast initially with greatly reduced efficiencies as the reaction proceeds. All other metal salt solutions ($Cd(NO_3)_2$, $CdCl_2$ and $ZnCl_2$) generate solvated single metal complexes which react with H_2S to form bisulfide species. While an increase in the number of solvent molecules causes a decrease in reaction efficiencies, solvent molecules persist throughout the reaction suggesting they play no role in the mechanism of metal sulfide formation. Additionally, counter ions were shown to affect reaction rates with $NO_3^- > OH^- > Cl^-$ in terms of reaction efficiency.

Chapter 1

OVERVIEW

The research described herein focuses on the utilization of ESI FT-ICR mass spectrometry for the analysis of complex environmental systems. It is a chronological account of my studies in the Department of Chemistry and Biochemistry at the University of Delaware. I begin with the study of the effects oxidation has on fragmentation patterns of peptides. The aim of this project was to elucidate the mechanisms for the new selective fragments resulting from peptide ozonolysis. I then transition to my work with environmentally significant metal sulfide clusters. The project was a collaborative effort to characterize metal sulfide nucleation mechanisms using a combination of solution based capping experiments and gas phase ion-molecule reactions. These research projects take advantage of the powerful capabilities of FT-ICR mass spectrometry and apply them to unique environmentally significant questions. Here I outline the work presented in this dissertation.

Applications of FT-ICR mass spectrometry is the comprehensive theme of my work, therefore, a discussion of the fundamentals of the technique is essential. In Chapter 2 I begin with a description of ion motion in a uniform magnetic field and how the trapped ions are manipulated throughout the experiment. An explanation of the advantages of FT-ICR are also provided. The mechanism of electrospray ionization is outlined followed by descriptions of the instruments used for this work.

The elucidation of fragmentation patterns for oxidized peptides is covered in Chapter 3. The unique low-energy unimolecular dissociation mechanisms for peptide ozonolysis reaction products are characterized using a combination of experimental and computational chemistry. Following a discussion on significance and background, the selective fragmentation channels for each of the peptide oxidation products is described. Energy-resolved SID data is then used for onset energy analysis and RRKM modeling. Finally, molecular dynamics experiments were done to understand the conformational restrictions of the proposed fragmentation mechanisms.

Chapter 4 marks the beginning of a series of chapters covering my work with environmentally significant metal sulfide clusters. The importance of metal sulfide species is established followed by essential definitions of complexes, clusters and particles. Our work using ESI FT-ICR mass spectrometry is also placed in the larger framework of the overall collaborative project with Dr. George Luther's group in the College of Marine Studies at the University of Delaware.

In Chapter 5 I demonstrate the ability of ESI mass spectrometry monitor metal salt nucleation in low dielectric constant binary water-methanol solutions. Time-dependent sampling is used to monitor signal variance following dilution of aqueous salt solutions with methanol. This work is placed in an environmental context and is the foundation for later studies of metal salt cluster reactions with hydrogen sulfide.

ESI FT-ICR mass spectrometry analysis of thiol capped metal sulfide clusters is described in Chapter 6. I demonstrate the ability of ESI mass spectrometry to detect sulfidic metal clusters following reaction with hydrogen sulfide using

2-mercaptopyridine as a molecular capping agent. Additionally, the connectivity between solution phase chemistry and the gas phase ion-molecule reactions between metal salt clusters and hydrogen sulfide is established.

Chapter 7 presents results from the gas phase ion-molecule reactions of metal salt clusters and hydrogen sulfide. Reaction efficiencies are determined for a number of cationic and anionic systems using a simplified pseudo first-order kinetic model. The first of their kind, these experiments provide unique perspective on the characterization of metal sulfide nucleation mechanisms. Comparisons are made based on metal ion, ligating species, and number of solvent molecules. This technique provides important kinetic data on the formation of metal sulfide clusters.

Finally, I end with an overview of my work and thoughts on how this research fits into larger applications in Chapter 8. The Appendices of this dissertation include experimental details such as example spectra and Mathematica results. Additionally, included is a problem-based learning activity I developed during my time as a member of the Graduate Teaching Fellows Program in K-12 Education (GK-12) at the University of Delaware (See Appendix A). Designed for high school physical science classes, students learn about hydrothermal vents while being introduced to topics such as the difference between physical and chemical properties, chemical bonding and energy transfer in environmental systems. The problem is published through the Problem-Based Learning Clearinghouse which can be found at www.udel.edu/pblc. I felt it was appropriate to include with this work, not only based on content, but also because of the priority I placed on developing my skills as an educator during my time at the University of Delaware.

Chapter 2

METHODS

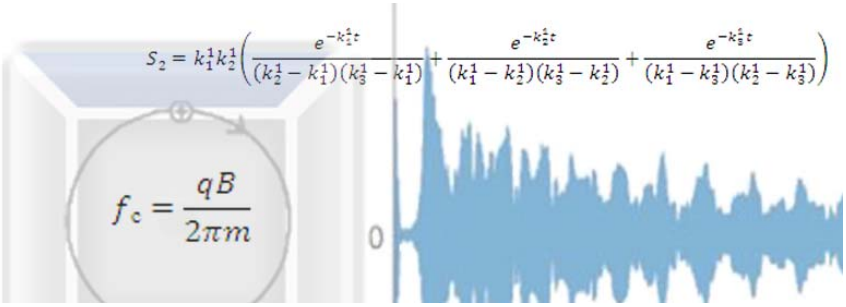

2.1 FT-ICR Mass Spectrometry

The entirety of the work reported herein utilizes Fourier transform ion cyclotron resonance mass spectrometry (FT-ICR MS or FT-MS) for the analysis of environmentally relevant systems. FT-ICR mass spectrometry has a rich history stemming from experiments done by Lawrence in 1930 in which the theory of ion cyclotron resonance was developed to understand fundamental properties of the atom [1]. In the late 1970's, with the application of Fourier transform techniques to ICR, the method gained popularity with increased mass resolution and mass range [2,3]. Modern FT-ICR instruments provide superior resolving power (>500,000) and mass accuracy (<1 ppm) in comparison to other mass analyzers resulting in increased popularity and a variety of new applications as highlighted in a number of recent reviews [4-12]. In addition to ultra-high performance, FT-ICR mass spectrometers have the unique ability to act as a gas phase 'beaker' by being able trap ions for long periods of time. It is precisely the nondestructive trapping nature of the technique in

combination with ultra-high performance that makes it ideal for studying unimolecular dissociation reactions of charged peptides and gas phase ion-molecule reactions of metal sulfide clusters.

At the most basic level, all FT-ICR mass spectrometers consist of a magnet and an ICR analyzer cell. There have been a number of reviews written on the fundamentals of the instrument [13-15]. Modern instruments, for the most part, use a superconducting magnet to provide a stable magnetic field that is spatially uniform throughout the ICR cell. Superconducting magnets used for FT-ICR mass spectrometry are solenoid magnets with wider bores in comparison to those used for NMR spectroscopy. Although instruments can be found with a wide range of magnetic field strengths, most instruments made today incorporate 7, 9.4 or 12 tesla (9.4 tesla = 400 MHz for NMR) superconducting magnets.

Placed within the magnetic field is the ICR analyzer cell. Generally speaking, the ICR cell consists of 6 plates configured in a cube or cylinder: two trapping plates, two excitation plates and two detection plates (See Figure 2.1). As ions are brought into the ICR cell along the z-axis (parallel to the direction of the magnetic field) they are confined spatially within the x-y plane by the magnetic field and are trapped along the z-axis using the two 'trapping' plates (grey) that are perpendicular to the magnetic field. Initially, the front trapping plate is set to ground potential while the back trapping plate is at a raised potential allowing the ions to enter the cell. The ions are then trapped by raising the potential on the front trapping plate. Once trapped, ions can be held for a specified time period before excitation and detection as described below.

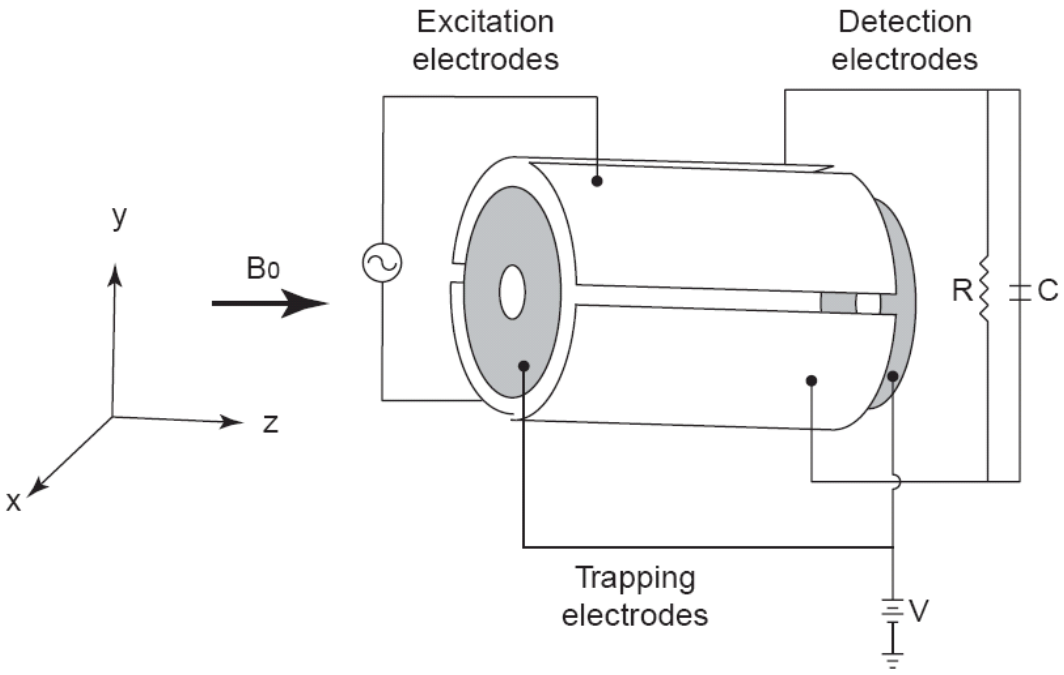

Figure 2.1. A cylindrical ICR cell. Colored grey are the trapping plates which confine the ions along the z-axis. The excitation and detection plates are aligned parallel to the direction of the magnetic field. (Reproduced from [9])

2.1.1 Ion Cyclotron Motion

At the foundation of FT-ICR MS is the cyclotron motion of ions moving in a unidirectional magnetic field. As shown in Figure 2.2, an ion in a spatially uniform magnetic field will move in a circular orbit in the plane perpendicular to the direction of the magnetic field. The Lorentz force (F_L, Hz), which is perpendicular to both the direction of the magnetic field and the direction of the velocity of the ion, causes the ion to travel in this circular orbit [14]. Referred to as the cyclotron frequency (f_c), this periodic orbit is dependent on the strength of the magnetic field (B), charge (q) and the mass of the ion (m) as seen in Equation 2.1 [14].

$$f_c = \frac{qB}{2\pi m} \qquad 2.1$$

This equation can be simplified to a more useful form

$$f_c = \frac{1.535611\times10^7 B}{m/z} \qquad 2.2$$

in which *z* represents the number of charges, *B* is the field in Tesla and *m* is the mass of the ion in Dalton [13]. The cyclotron frequency of an ion is independent of kinetic energy. In modern FT-ICR MS systems, the superconducting magnet provides a stable and constant magnetic field allowing the mass-to-charge ratio of an ion (*m/z*) to be determined with great precision and high resolution. In other mass spectrometers resolution and accuracy depend on mechanical precision and the stability of electrical power supplies. The stability of the magnet is a key reason for the high performance of FT-ICR in comparison to other mass spectrometry detectors.

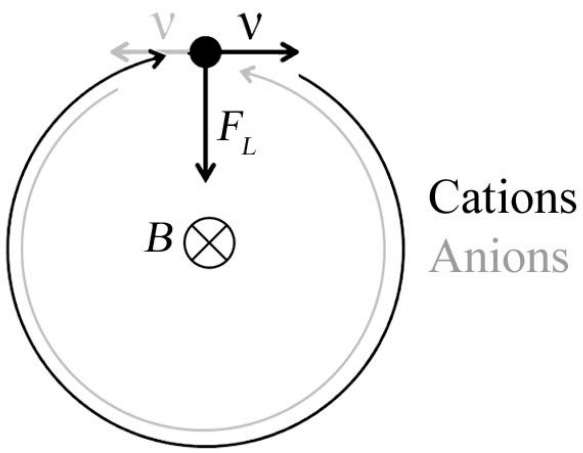

Figure 2.2. Cyclotron motion of an ion moving perpendicular to the direction a magnetic field (B). The Lorentz force (F_L) is an inward-directed force produced by the magnetic field which drives the circular orbit of charged species. Direction of orbiting ions is dependent on charge. (Adapted from [16])

2.1.2 Kinetic Energy and Cyclotron Radii

Kinetic energy does, however, determine the orbital radius of the cyclotron motion. If cyclotron frequency is converted to angular frequency ($\omega_c = 2\pi f_c$), then by definition (Equation 2.3) there is a direct relationship between the ion velocity perpendicular to the direction of the magnetic field in meters/second (v_{xy}) and cyclotron radius in meters (r) [13,14].

$$\omega_c = \frac{v_{xy}}{r} = \frac{qB}{m} \qquad 2.3$$

This equation can also be simplified

$$r = \frac{1.036427\times10^{-8}(m/z)v_{xy}}{B} \qquad 2.4$$

in terms of mass-to-charge ratio (*m/z*) and magnetic field (*B*) [13]. Ions that are trapped with thermal kinetic energies will typically have cyclotron radii in the micrometer range [14]. This can be demonstrated by looking at a straightforward example. The average x-y translational energy of an ion at equilibrium with the temperature of its environment is given by

$$\frac{m\langle v_{xy}^2\rangle}{2} \approx kT \qquad 2.5$$

where *k* is the Boltzmann constant and *T* is temperature in Kelvin. Solving for v_{xy} and substituting into Equation 2.4 results in the following relationship.

$$r = \frac{1.336510\times10^{-6}}{zB}\sqrt{mT} \qquad 2.6$$

Using this equation, it can be calculated that at room temperature a singularly charged ion with a mass of 1000 u in a 7 tesla magnetic field will have a cyclotron radius of 104 μm.

This relationship between kinetic energy and cyclotron radius is taken advantage of during quench, excitation, and fragmentation events (Figure 2.3). If a sinusoidal (rf) voltage is applied to the excitation plates (See Figure 2.1) at the same frequency as the cyclotron frequency of the trapped ions, energy will be absorbed by the ions driving them outward as their velocities increase. In a quench event, typically

done immediately before the analyte ions are trapped in the ICR cell, the rf voltage is applied for a long enough time period or with a great enough amplitude to cause the ions to spiral outward until they collide with the cell plates where they are neutralized and pumped away by the vacuum system (Figure 2.3).

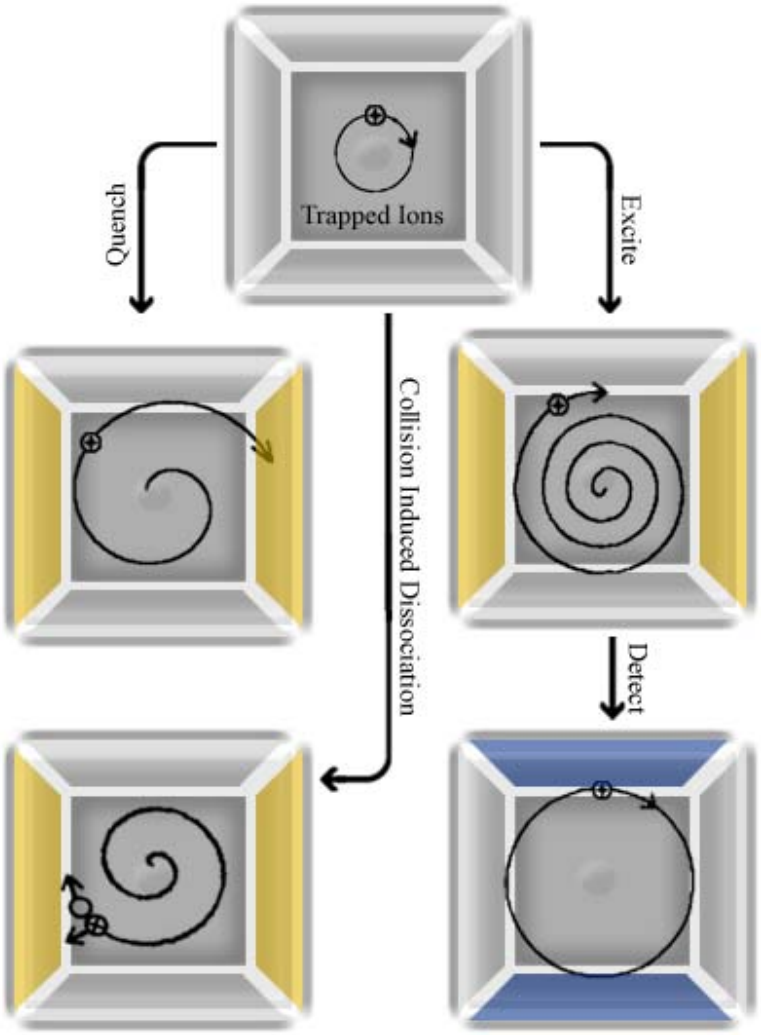

Figure 2.3. Trapped ions can be excited to higher kinetic energies and larger radii by applying rf voltages to the excitation plates (yellow) at the same frequencies as the cyclotron frequency of the trapped ions. This process can be used for quench events, fragmentation experiments or as part of an excitation/detection sequence. Detection plates (blue) monitor the image current of coherently orbiting excited ions.

Excitation is also used to efficiently detect trapped ions in an ICR cell. The initial radii of trapped ions, as discussed previously, are too small to efficiently detect. Ions must first be excited to larger radii to bring them into phase and to move them closer to the detection plates (See Figure 2.1). Similar to a quench event, a rf voltage is applied to the excitation plates which drive the ions to larger radii. For detection, however, the excitation time length and amplitude are set so that trapped ions are not expelled from the trap (Figure 2.3). In addition to simply moving the ions closer to the detection plates, this process also forces ions of like mass-to-charge ratios into cohesive ion packets. When ions are trapped in the ICR cell the angular position of trapped ions is randomly distributed in the plane perpendicular to the magnetic field. Detecting ions in this state would result in an image current with effectively no intensity being that every ion would have a 'partner ion' exactly 180° out of phase. The excitation process alleviates this problem by forcing the ions into phase as coherent ion packets. As an ion packet passes by one of the detection plates they draw electrons towards that plate (assuming trapped cations). As the ions approach the second detection plate, electrons are then drawn to it through the connecting circuit. This sinusoidal current, referred to as the image current [17], is amplified and digitized into a time domain signal or transient (image current vs. time). Using a Fourier transform, the time domain signal is then converted into a frequency domain spectrum (intensity vs. frequency) which can be converted into a mass spectrum (intensity vs. m/z) using a simple calibration quadratic formula [18]. This process is highlighted in Figure 2.4.

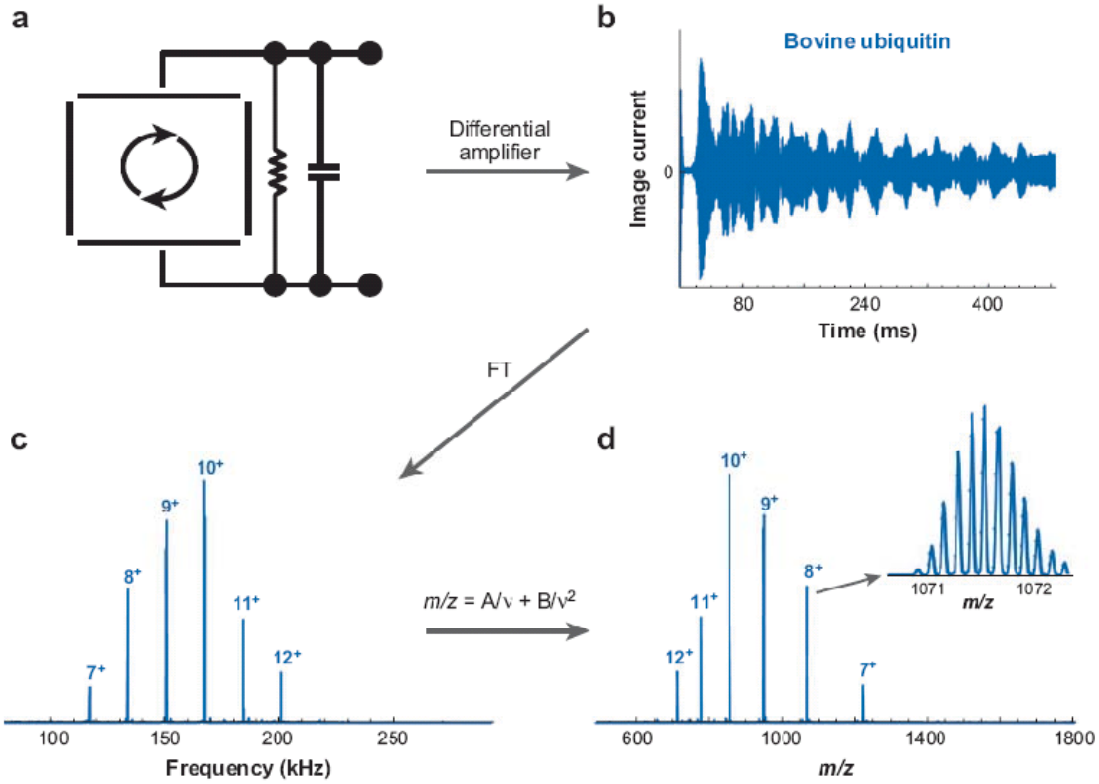

Figure 2.4. Once excited, (a) ions generate an image current along the circuit connecting the detection plates. This signal is amplified resulting in the (b) transient signal which, following a Fourier Transform, a (c) frequency domain spectrum is generated. A quadratic calibration equation is used to convert to a (d) mass spectrum. (Reproduce from [18])

The ability to selectively increase an ion's kinetic energy is also useful when performing fragmentation experiments (Figure 2.3). After trapping the ions in the ICR cell, selection of the precursor ion can be done by selectively ejecting all ions with *m/z* values lower and higher than the ion of interest. Basically, the cyclotron frequency of the ion of interest is left out of the rf voltages applied to the excitation plates. Once isolated, the precursor ion can be excited to higher kinetic energies great enough to induce fragmentation upon collision with a pulsed neutral gas such as

argon. The kinetic energy (*K.E.*) of the excited ions can be calculated by rearranging Equation 2.3 in terms of translational velocity, v_{xy}.

$$K.E. = \frac{mv_{xy}^2}{2} = \frac{q^2B^2r^2}{2m} \qquad 2.7$$

This can be simplified to the following form [13].

$$K.E. = \frac{4.824265\times10^7 z^2B^2r^2}{m} \qquad 2.8$$

where z is the unit charge, B is the magnetic field (Tesla), r is the cyclotron radius (meters) and m is the mass of the ion (Daltons) [13]. After dissociation, the resulting fragment ions are collisionally cooled and fall back to the center of the ICR cell where, after the neutral gas is pumped away, they can be excited and detected.

2.1.3 High Performance MS

The fundamentals of how FT-ICR mass spectrometry is performed leads to a unique set of advantages over other mass analyzers. A major advantage is the ability to trap ions for long time periods and then detect all the ions at once. To detect ions with different masses simultaneously all ions must first be excited using a broadband excitation event. Typically this is done using a rapid frequency sweep (rf chirp) where a frequency generator applies a series of r.f voltages to the excitation plates over the desired frequencies. The adaptation of traditional ICR experiments to include Fourier

Transform data processing [2,3], which enabled multichannel detection, allows the whole spectrum to be taken in the time it would take a non-FT system to record a single point. Additionally, the range of ion cyclotron frequencies (kHz-MHz) are very easy for modern electronics to process [14]. These advantages have led FT-ICR mass spectrometry to the forefront of ultra-high resolution mass spectrometry.

Performance specifications of an instrumental technique can be approached from many standpoints including dynamic range, resolution, resolving power and mass accuracy. Dynamic range is the range in which ion signal is linear with analyte concentration. Traditionally, resolution for FT-ICR mass spectrometry is defined as the full width of a spectral peak at half-maximum of the peak height ($\Delta m_{50\%}$) and resolving power refers to $m/\Delta m_{50\%}$. With a dynamic range of 10^2-10^5 [19], FT-ICR MS can produce results with mass resolution in the 10^6 range, resolving power routinely greater than 500,000 and mass accuracy often better than 1 ppm. Simply taking into consideration the cyclotron frequency of the analyte ion and acquisition time in seconds ($T_{acq'n}$)

$$\frac{m}{\Delta m_{50\%}} = \frac{f_c T_{acq'n}}{2} \qquad 2.9$$

an estimation of the resolving power can be made. More accurate theoretical values for resolution and resolving power, however, can be calculated using the following equations for low pressure detection, where the ICR time-domain signal persists throughout the acquisition period [13].

$$\Delta m_{50\%} = \frac{7.859\times10^{-8}m^2}{zBT_{acq'n}} \qquad 2.10$$

$$\frac{m}{\Delta m_{50\%}} = \frac{1.274\times10^{7}zBT_{acq'n}}{m} \qquad 2.11$$

Again, m is the mass of the ion in Daltons, z is the unit charge on the ion, B is the magnetic field strength in Tesla, and $T_{acq'n}$ is the acquisition time in seconds. On the other hand, experiments in which collisional damping reduces the ICR signal to essentially zero are defined as high pressure experiments. For this case, theoretical values for resolution and resolving power can be determined using Equations 2.12 and 2.13 [13].

$$\Delta m_{50\%} = \frac{3.590\times10^{-8}m^2}{zBk_{damp}} \qquad 2.12$$

$$\frac{m}{\Delta m_{50\%}} = \frac{2.785\times10^{7}zBk_{damp}}{m} \qquad 2.13$$

In these equations k_{damp} represents the collisional damping constant as defined by Equation 2.14 where $m_{neutral}$ and m_{ion} are the masses of the neutral and ion (Da) respectively [13].

$$\frac{1}{k_{damp}} = \frac{m_{neutral}}{m_{ion}+m_{neutral}} v_{collision} \qquad 2.14$$

The number of ion-molecule collisions per second ($v_{collision}$) can be determined using collision capture theory [20]. If ion-molecule collisions resulted in reaction, then number of ion-molecule collisions per second would be the same as a pseudo first-order rate constant for a collision rate limited reaction. If the pressure in the ICR cell is known, then $v_{collision}$ can be determined from the theoretical bimolecular rate constant. Further explanation can be found in Section 2.1.4.

2.1.4 Gas Phase Ion-Molecule Reactions

The FT-ICR mass spectrometer also has the unique advantage of being a nondestructive ion trap capable of storing ions for hundreds of seconds. The ICR cell can be equated to a gas phase 'beaker' that can monitor reactions between stored ions and neutral gas phase reactants in real time. Gas phase ion-molecule reactions can be used to understand complex solution processes [21]. In addition to being able to isolate single reactant ions prior to reaction, gas phase reactions in a FT-ICR mass spectrometer can be controlled so that reaction intermediates resulting from elementary steps towards a final reaction product are often observed. Furthermore, since the reactions are monitored in real time, kinetic information can be extracted. The Ridge group has long been at the forefront in the field of gas phase ion-molecule reactions [22-39] and the current contribution applies this insightful approach to the field of environmental chemistry in the study of metal sulfide cluster formation.

Kinetic studies of gas phase ion-molecule reactions using FT-ICR mass spectrometry are done by exposing trapped ions to a neutral reactant gas held at constant pressure for various reaction times in the ICR cell. The concentration of the neutral gas, in this case H_2S, is far greater than that of the trapped ions making [H_2S] effectively constant over the duration of the experiment justifying a pseudo first-order approximation. The bimolecular rate constant (k_x^2) and [H_2S] can then be written as a pseudo first-order rate constant (k_x^1).

$$rate = k_x^2[\text{Cluster}][H_2S] = k_x^1[\text{Cluster}] \quad 2.15$$

$$k_x^1 = k_x^2[H_2S] \quad 2.16$$

The reaction can then be kinetically described completely in terms of concentration for the cadmium cluster reactant ion. To experimentally determine k_x^1 the plot of the relative intensity vs. time for the reactant can be fit using nonlinear regression to the appropriate integrated rate equation. Generating integrated rate equations for complex reaction schemes can prove troublesome, therefore, for simplicity and to maintain consistency ionic cadmium clusters were grouped into 'families' of clusters based on the number of sulfur atoms added (S_x) upon reaction with H_2S(g). This treatment allows for a simplistic approach

$$S_0 = 1e^{-k_1^1 t} \quad 2.17$$

$$S_1 = \frac{k_1^1}{k_2^1 - k_1^1}\left(e^{-k_1^1 t} - e^{-k_1^1 t}\right) \quad 2.18$$

$$S_2 = k_1^1 k_2^1 \left(\frac{e^{-k_1^1 t}}{(k_2^1 - k_1^1)(k_3^1 - k_1^1)} + \frac{e^{-k_2^1 t}}{(k_1^1 - k_2^1)(k_3^1 - k_2^1)} + \frac{e^{-k_3^1 t}}{(k_1^1 - k_3^1)(k_2^1 - k_3^1)} \right) \quad 2.19$$

$$S_x = k_1^1 \ldots k_{x-1}^1 \left(\frac{e^{-k_1^1 t}}{(k_2^1 - k_1^1)(k_3^1 - k_1^1)\ldots(k_x^1 - k_1^1)} + \frac{e^{-k_2^1 t}}{(k_1^1 - k_2^1)(k_3^1 - k_2^1)\ldots(k_x^1 - k_2^1)} + \right.$$
$$\left. \ldots \frac{e^{-k_x^1 t}}{(k_1^1 - k_x^1)(k_2^1 - k_x^1)\ldots(k_{x-1}^1 - k_x^1)} \right) \quad 2.20$$

using only sequential integrated rate equations (See Equations 2.17-2.20) to describe the process of cadmium sulfide formation. It should be noted that because only one isotope was monitored for each cluster and isotopic distributions can vary greatly with the addition of multiple sulfur atoms, relative intensities were normalized using an isotopic adjustment factor (I_{iso}).

$$I_{iso} = \frac{\sum \text{Theoretical Abd. for all Isotopes}}{\text{Abd.of the Monitored Isotope}} \quad 2.21$$

Collision capture theory can be used to determine the H_2S reactant gas pressure, as described by Ridge [20], by calculating the theoretical bimolecular rate constant ($k^2_{coll'n}$) of a collision rate limited pseudo-first order process.

$$[H_2S] = \frac{k_x^1}{k^2_{coll'n}} \quad 2.22$$

The fastest observed pseudo first-order reaction (k_1^1 = 2.85 s^{-1}) between a cadmium cluster and hydrogen sulfide

Scheme 2.1

$$[Cd(NO_3)(CH_3OH)]^+ + H_2S(g) \xrightarrow[4\times10^{-9}\text{torr}]{} [Cd(SH)(CH_3OH)]^+ + HNO_3$$

$$k_1^1 = 2.85 \pm 0.27 s^{-1}$$

was assumed to be collision rate limited. The bimolecular collision rate can be calculated using the relationship

$$\frac{k^2_{coll'n}}{k_L} = 0.9754 + \frac{(\tau/\sqrt{2}+0.509)^2}{10.526} \qquad 0 < \tau < 2\sqrt{2} \qquad 2.23$$

where τ, a dimensionless parameter, can be defined by

$$\tau = 85.11\mu_D' \left(\frac{1}{\alpha' T}\right)^{1/2} \qquad 2.24$$

using the dipole moment (H_2S: μ_D' = 0.97 D) and volume polarizability (H_2S: α'=3.67 Å^3). The Langevin rate constant (k_L), which is directly proportional to the number of charges on the ion (Z), can be calculated

$$k_L = 2.342Z \left(\frac{\alpha'}{\mu'}\right)^{1/2} 10^{-9} \text{ cm}^3\text{molecule}^{-1}\text{s}^{-1} \qquad 2.25$$

using the volume polarizability of H_2S and the reduced mass (μ') of the ion and neutral. In this case, for the reaction between H_2S and $[Cd(NO_3)(CH_3OH)]^+$ (μ'= 29.193 Da), the collision rate limited bimolecular rate constant is found to be 1.22x10^{-9} cm^{3}molecule^{-1}s^{-1}. Furthermore, the theoretical hydrogen sulfide pressure in the ICR cell is calculated to be 6.62x10^{-8} torr using Equation 2.15. It should be noted that this exercise substantiates our initial assumption that the fastest pseudo first-order

process for observed cadmium clusters (Scheme 2.1) is collision rate limited. Although the UHV instrument pressure reading is 4.0×10^{-9} torr for this reaction, it is know that the gauge is inaccurate by slightly more than an order of magnitude when the instrument is in the magnetic field. Therefore, The calculated H_2S pressure of 6.62×10^{-8} torr and the assumption that the reaction of $[Cd(NO_3)(CH_3OH)]^+$ with H_2S is collision rate limited is reasonable.

For comparison between gas phase ion-molecule reactions, a more useful measure than pseudo first-order or bimolecular rate constants is reaction efficiency (k/k_c). The reaction efficiency for a given process can be defined as the probability of a single collision leading to reaction product(s). With the assumption that the reaction of $[Cd(NO_3)(CH_3OH)]^+$ with H_2S is 100% efficient (k/k_c =1.00), a simple equation can be written

$$\frac{k}{k_c} = \frac{k_x^1}{2.85\ \mathrm{s}^{-1}} \left(\frac{\mu'_x}{29.19\ \mathrm{Da}} \right)^{1/2} \left(\frac{4 \times 10^{-9}\mathrm{torr}}{P_x} \right) \qquad 2.26$$

to calculate efficiencies for reactions with H_2S using experimentally determined pseudo first-order rate constants (k_x^1) and taking into consideration differences in reduced mass (μ'_x) and H_2S pressure (P_x). It should be noted that because the highest experimental error was observed for the collision rate limited process ($2.85 \pm 0.27\ s^{-1}$) no calculated efficiency can have better than ~10% accuracy using Equation 2.19.

2.2 Electrospray Ionization

Ionization is essential for the manipulation and analysis of chemical species using mass spectrometry. The entirety of the work described herein was done using electrospray ionization in combination with FT-ICR mass spectrometry. Electrospray ionization (ESI), introduced in 1945 by Yamashita and Fenn [40,41], is referred to as a 'soft' ionization technique which is capable of transferring both covalently and non-covalently bound species to the gas phase without inducing dissociation upon ionization (Figure 2.5). Electrospray ionization is done by forcing a liquid, consisting of the analyte and solvent, through a conducting capillary. The potential applied to the capillary (~2-3 kV) causes charge separation in solution resulting in the formation of a "Taylor cone" at the tip of the capillary [42]. If the voltage is above a certain threshold, the Taylor cone will emit a jet of charged liquid droplets initiating the electrospray ionization process. Much work has been done to understand the mechanism for the transfer of ions from solution to the gas phase by this process [43-53]. It has been found that as the large highly-charged initial droplets begin to evaporate, the droplet is distorted as thin protrusions form. Secondary droplets are ejected from the tip of the protrusions in a similar process of that observed for Taylor cones. This sequence repeats itself until nanometer-sized droplets are formed at which time there is some debate as to the final steps of the mechanism by which gas phase ions are produced.

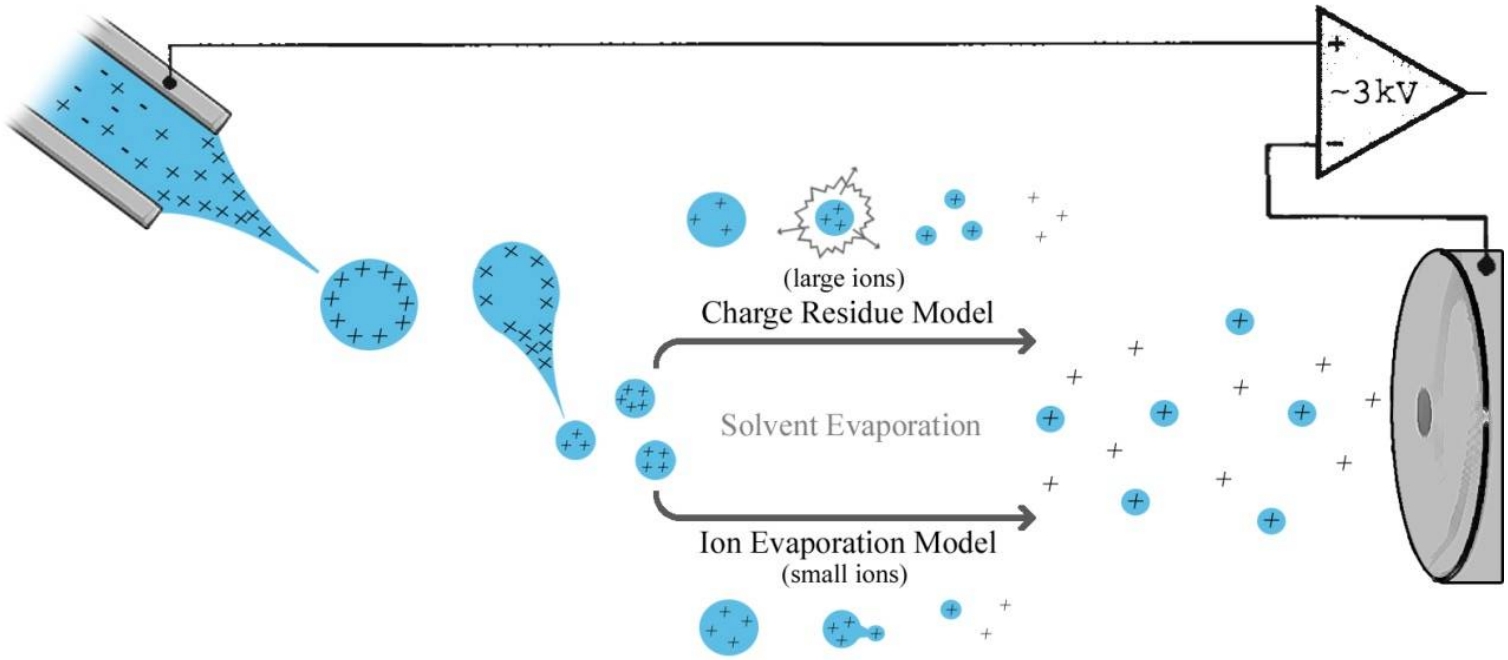

Figure 2.5. Proposed mechanisms for electrospray ionization. Charged droplets are formed by applying a high voltage to a capillary containing an that emit nanometer sized droplets. It is suggested that these smaller droplets produce free gas phase ions by way of either the charge residue model (large ions) or ion evaporation model (small ions).

The two competing theories for final transfer of ions to the gas phase is the charge residue model (CRM) and the ion evaporation model (IEM) [54]. The charged residue model, originally put forth by Dole [55], suggests that solvent evaporation causes instability in the secondary droplets resulting in "Coulombic explosions." Ultimately, this mechanism produces a droplet with a single analyte molecule and residual charge. Free gas phase ions are produced as the remaining solvent evaporates and the analyte retains the droplet's charge. On the other hand, Iribarne and Thomson have proposed the ion evaporation model [56,57]. They proposed that as droplets become smaller the surface fields become strong enough to overcome solvation forces and transfer anlyte ions from the droplet surface into the gas phase. Although there has been much debate over which mechanism is more accurate, recently there has been a certain level of compromise [43,58]. It is now believed that smaller ions may enter the gas phase via the ion evaporation model [58,59]while the inability of larger ions to desorb from the surface of droplets leads to the charge residue mechanism [60-62].

2.3 Instrumentation

2.3.1 PNNL 6T FT-ICR MS

The collaborative research project with Julia Laskin at Pacific Northwest National Laboratory involving fragmentation energetics of Angiotensin II was done using their specially fabricated 6 tesla FT-ICR mass spectrometer shown in Figure 2.6 [63]. The instrument has been specially designed to produce time- and energy-

resolved Surface Induced Dissociation (SID) spectra. Ions are produced using electrospray ionization (ESI emitter, 2.2 kV) at atmospheric pressure (Section 2.2) and enter through a heated stainless steel capillary (150 °C). Ions are efficiently transferred into the high vacuum region and focused into a beam using an electrodynamic ion funnel [64]. The ion beam then passes through a series of quadrupoles used for collisional focusing, mass selection and ion accumulation referred to as the Ion Source Region. Typical accumulation times range from 0.1-0.3 seconds, and accumulation is done at elevated pressure ($2x10^{-3}$ Torr) to allow internally excited ions to collisionally relax prior to entering the ICR cell. Ions are then extracted from the accumulation quadrupole and enter the ICR cell where they collide with the SID surface in MS/MS experiments. After collision, ions are captured by raising the trapping potentials (10-20 V). Ion collision energy is determined by the difference in potential between the accumulation quadrupole and the rear trapping plate of the ICR cell.

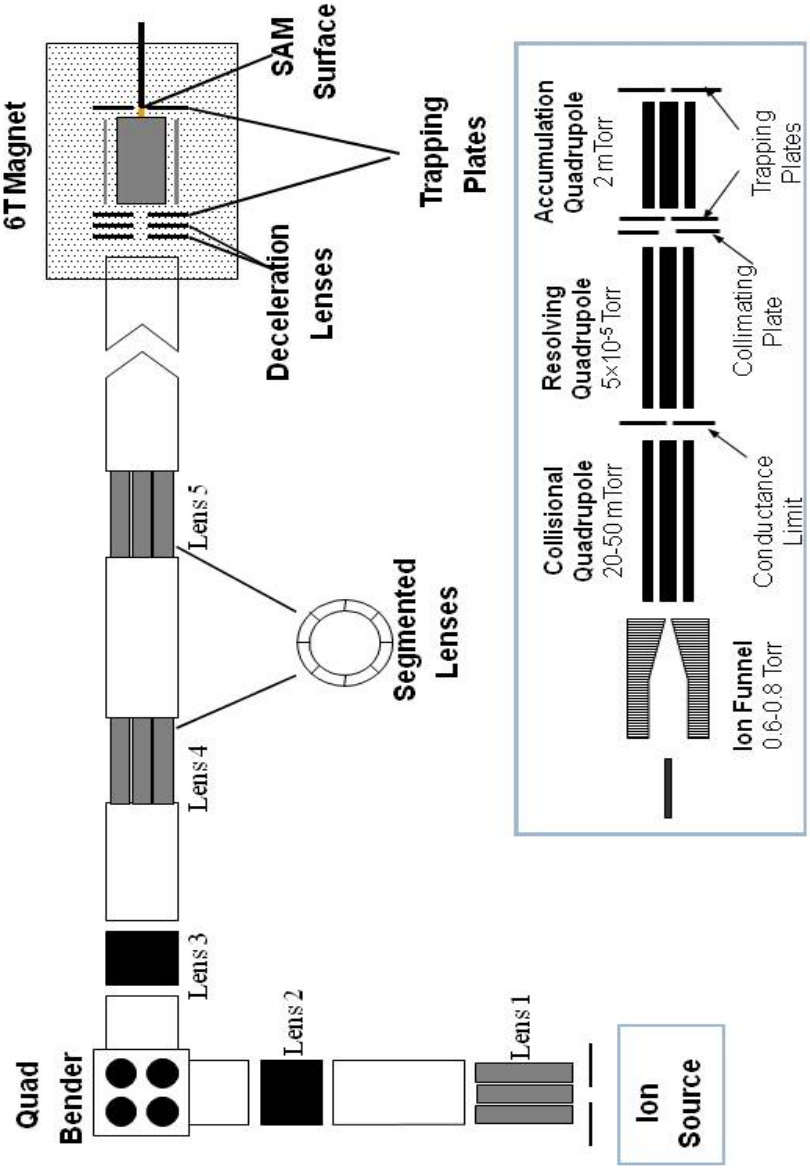

Figure 2.6. The 6 tesla home built FT-ICR mass spectrometer at Pacific Northwest National Laboratory. The instrument is equipped with a mass resolving and accumulation quadrupole in the Ion Source region. Energy-resolved SID experiments can be performed by adjusting the potential offset between the accumulation quadrupole and the SAM surface at the back of the ICR cell.

Surface Induced Dissociation in combination with FT-ICR mass spectrometry is particularly advantageous for a number of reasons. One of the more simplistic dissociation techniques, SID is performed by simply colliding ions with a

surface and observing the resulting fragments. In comparison to other collisional fragmentation techniques such as SORI-CID (See Section 2.3.2), large amounts of energy can be deposited into a molecule in a very short time. The distribution of internal energies of ions colliding with a surface is also much narrower than that of other techniques [65]. Additionally, sampling time is greatly reduced in SID because there is no introduction of a collision gas and subsequent removal of the gas prior to detection. SID experiments were done using a surface composed of a 2 μm film of carbon vapor deposited diamond on a titanium surface prepared by P1 Diamond Inc. In addition to varying the SID collision energy, time-resolved data can also be recorded by adjusting the delay time between collision with the surface and detection. The generated time- and energy-resolved parent ion survival curves can then be modeled using RRKM theory to gain insight into the energetics of the observed fragmentation channels. These calculations, done by Julia Laskin, will be described in more detail in Section 3.1.1.

2.3.2 Bruker 7T Apex Qe FT-ICR MS

All the work done involving cadmium clusters, both solution experiments and gas phase ion-molecule reactions, were done using a 7 tesla Bruker Apex Qe FT-ICR mass spectrometer, as seen in Figure 2.7 (Bruker Daltonics, Billerica, MA). The instrument can be simplified into four basic regions: the ions source, Qh interface, ion transfer optics and the detector. From introduction to detection, the ions pass through six pumping stages controlled by four turbo-molecular pumps (TP1-TP4) and two

mechanical roughing pumps. Under normal operating conditions, the ultra-high vacuum (UHV) region is maintained at a pressure of ~$5x10^{-10}$ Torr.

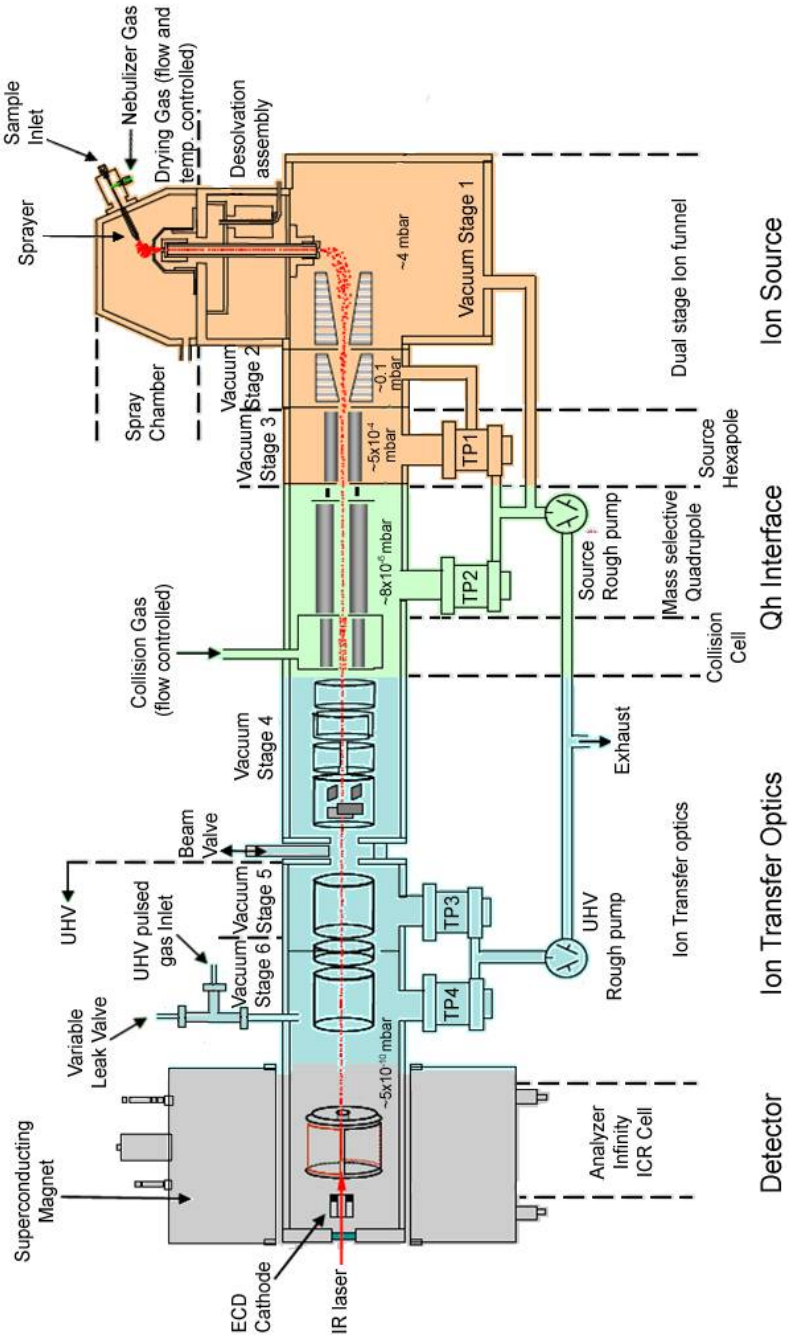

Figure 2.7. The 7 Tesla Bruker Apex Qe FT-ICR mass spectrometer at the University of Delaware. The instrument is equipped with a mass resolving quadrupole and accumulation hexapole (Collision Cell) in the Qh Interface. A modification has been made to introduce react gases through a Variable Leak Valve for ion-molecule reactions.

Ions produced by electrospray ionization (Section 2.2) at atmospheric pressure are directed through a glass capillary into Vacuum Stage 1 by a significant voltage differential (assuming cations: -3 kV). The ions are then directed orthogonally into the first ion funnel where they are focused into a defined ion beam using a combination of d.c. and rf voltages. The beam is decelerated and collisionally cooled as they pass through the second ion funnel into the Source Hexapole. Although this hexapole can be used to accumulate ions, in all experiments presented here it was used simply as a guide to pass the ion beam along from the Ion Source region to the Qh Interface.

The Qh Interface is a powerful aspect of the instrumental set-up allowing for mass selection, accumulation, fragmentation and ion-molecule reactions to occur before being trapped in the ICR cell. Ions first pass through the Mass Selective Quadrupole where, if necessary, a window of m/z values can be selected to continue into the Collision Cell where they can be accumulated for a specified time. The Collision Cell is typically at an elevated pressure of Argon (~$1x10^{-3}$ Torr) so that if the ions are brought into the cell gently (collision voltage: -2 to +1V) they are simply stored (0.1-1.5 sec) and collisionally cooled. The Collision Cell voltage differential can be adjusted (-2 to -10 V) to bring the ions into the cell more violently, fragmenting the ions via collision-induced dissociation with Argon. Additionally, argon can be exchanged for a reactant gas to carry out gas phase ion-molecule reactions in the Collision Cell. There is little kinetic control over the reaction using this technique because the pressure in the Collision Cell is orders of magnitude greater than that in the ICR cell and introduction flow rates have minimal control. After accumulation in

the Collision Cell, ions pass through a series of Transfer Ion Optics on their way to the ICR cell.

The ICR cell is a cylindrical ion trap which confines ions axially using two trapping electrodes (See Figure 2.1). Under normal conditions, once trapped, ions are simply excited and detected. The instrument has the capability to perform fragmentation experiments a number of ways within the ICR cell including Infrared Multiphoton Dissociation (IRMPD), Electron Capture Dissociation (ECD) and Sustained Off-Resonance Irradiation Collision Induced Dissociation (SORI-CID). For IRMPD an infrared laser is directed through the center of the ICR cell through a window on the back side of the vacuum chamber. If the trapped ions are able to absorb at the IR frequency of the laser, they will absorb multiple photons causing them to be excited to higher vibrational states until unimolecular dissociation occurs. If the trapped ions are multiply protonated species then ECD can be used as a fragmentation method. ECD is an electron-capture experiment where the trapped ions are bathed in low energy electrons. Protons on the trapped ions can take on a free electron to form highly reactive hydrogen radicals. The hydrogen radicals are then free to attack bonds resulting in fast, localized, dissociation. Finally, SORI-CID is a fragmentation technique in which off-resonance (500-2000 Hz) excitation is used in combination with a short (~0.25 sec), high pressure collision gas pulse (Argon Peak Pressure: ~$8x10^{-8}$ Torr) in the ICR cell. Both the amplitude of the off-resonance excitation voltage (SORI Power: ~0.2%) and the collision gas pulse length can be specified. Off-resonance excitation drives the radii of the cyclotron motion to expand and contract (i.e. oscillating ion kinetic energy) as the excitation rf voltages goes in and

out of phase with the cyclotron frequency. This process allows SORI-CID to induce fragmentation by slowly increasing the internal energy through multiple collisions.

For kinetic ion-molecule reaction experiments (See Section 2.1.4), ions can be stored for various time periods in the ICR cell at elevated pressures. Neutral reactant gases are introduced through a high precision Variable Leak Valve that has been added to the UHV Pulsed Valve Inlet. The reactant gas is introduced to the system through an external reservoir that is typically filled to a pressure of ~5 Torr. The pressure in the UHV region can then be raised to a constant reaction pressure, typically in the 10^{-9} Torr range, by slowly leaking the contents of the reservoir using the Variable Leak Valve. The instrument is operated as if performing a SORI-CID experiment except for that the SORI power is set to 0%. The SORI pulse length specifies the delay time that the ions are exposed to the neutral reactant gas prior to detection. Kinetic experiments can be done by varying this delay time.

2.4 References

1. Lawrence, E. O.; Edlefsen, N. E. On the Production of High Speed Protons. *Science.* **1930***, 72*, 376-377.

2. Comisarow, M. B.; Marshall, A. G. Frequency-Sweep Fourier Transform Ion Cyclotron Resonance Spectroscopy. *Chem. Phys. Lett.* **1974***, 26*, 489-490.

3. Comisarow, M. B.; Marshall, A. G. Fourier Transform Ion Cyclotron Resonance Spectroscopy. *Chem. Phys. Lett.* **1974***, 25*, 282-283.

4. Burgert, R.; Schnoeckel, H. Monitoring the Dissolution Process of Metals in the Gas Phase: Reactions of Nanoscale Al and Ga Metal Atom Clusters and their Relationship to Similar Metalloid Clusters. *Chem. Commun.* **2008**, 2075-2089.

5. Raczynska, E. D.; Gal, J.; Maria, P.; Zientara, K.; Szelag, M. Application of FT-ICR-MS for the Study of Proton-Transfer Reactions Involving Biomolecules. *Anal. Bioanal. Chem.* **2007***, 389*, 1365-1380.

6. Sleighter, R. L.; Hatcher, P. G. The Application of Electrospray Ionization Coupled to Ultrahigh Resolution Mass Spectrometry for the Molecular Characterization of Natural Organic Matter. *J. Mass Spectrom.* **2007***, 42*, 559-574.

7. Mopper, K.; Stubbins, A.; Ritchie, J. D.; Bialk, H. M.; Hatcher, P. G. Advanced Instrumental Approaches for Characterization of Marine Dissolved Organic Matter: Extraction Techniques, Mass Spectrometry, and Nuclear Magnetic Resonance Spectroscopy. *Chem. Rev.* **2007***, 107*, 419-442.

8. Rodgers, R. P.; Schaub, T. M.; Marshall, A. G. Petroleomics: MS Returns to its Roots. *Anal. Chem.* **2005***, 77*, 20A-27A.

9. Zhang, J.; McCombie, G.; Guenat, C.; Knochenmuss, R. FT-ICR Mass Spectrometry in the Drug Discovery Process. *Drug Discovery Today.* **2005***, 10*, 635-642.

10. Balaj, O. P.; Siu, C.; Balteanu, I.; Beyer, M. K.; Bondybey, V. E. Free Electrons, the Simplest Radicals of them all: Chemistry of Aqueous Electrons as Studied by Mass Spectrometry. *Int. J. Mass Spectrom.* **2004***, 238*, 65-74.

11. Weiss, K.; Schnoeckel, H. FT/ICR-Mass Spectrometry in Nanotechnology: The Investigation of Metalloid Clusters. *Anal. Bioanal. Chem.* **2003***, 377*, 1098-1101.

12. Pinto, D. M.; Boyd, R. K.; Volmer, D. A. Ultra-High Resolution for Mass Spectrometric Analysis of Complex and Low-Abundance Mixtures - the Emergence of FTICR-MS as an Essential Analytical Tool. *Anal. Bioanal. Chem.* **2002***, 373*, 378-389.

13. Marshall, A. G.; Hendrickson, C. L.; Jackson, G. S. Fourier Transform Ion Cyclotron Resonance Mass Spectrometry: A Primer. *Mass Spectrom. Rev.* **1998***, 17*, 1-35.

14. Amster, I. J. Fourier Transform Mass Spectrometry. *J. Mass Spectrom.* **1996***, 31*, 1325-1337.

15. Comisarow, M. B.; Marshall, A. G. The Early Development of Fourier Transform Ion Cyclotron Resonance (FT-ICR) Spectroscopy. *J. Mass Spectrom.* **1996***, 31*, 581-585.

16. Marshall, A. G.; Grosshans, P. B. Fourier Transform Ion Cyclotron Resonance Mass Spectrometry: The Teenage Years. *Anal. Chem.* **1991***, 63*, 215A-229A.

17. Comisarow, M. B. Signal Modeling for Ion Cyclotron Resonance. *J. Chem. Phys.* **1978***, 69*, 4097-4104.

18. Marshall, A. G. Accurate Mass Measurement: Taking Full Advantage of Nature's Isotopic Complexity. *Physica B (Amsterdam, Neth.).* **2004***, 346-347*, 503-508.

19. McLuckey, S. A. Instrumentation for Mass Spectrometry: 1997. *Adv. Mass Spectrom.* **1998***, 14*, Chapter 8/153-Chapter 8/196.

20. Ridge, D. Chapter 1. In *The Encyclopedia of Mass Spectrometry Volume 1: Theory and Ion Chemistry,* Armentrout, P., Ed.; Elsevier, 2003.

21. Fisher, K. J.; Dance, I. G.; Willett, G. D. Gas-Phase Inorganic Chemistry: How is it Relevant to Condensed-Phase Inorganic Chemistry?. *Rapid Commun. Mass Spectrom.* **1996***, 10*, 106-109.

22. Byrd, M.; Guttman, C. M.; Wallace, W. E.; Ridge, D. P. Gas-Phase Reactivity of Î·5-Cyclopentadienylcobalt Ion (CpCo+) Towards Saturated Hydrocarbons using Fourier-Transform Mass Spectrometry (FT-MS). *Abstracts of Papers, 223rd ACS National Meeting, Orlando, FL, United States, April 7-11, 2002.* **2002**, ANYL-079.

23. Luu, N. C.; Iyer, R. A.; Anders, M. W.; Ridge, D. P. Bioactivation Mechanisms of Haloalkene Cysteine S-Conjugates Modeled by Gas-Phase, Ion-Molecule Reactions. *Chem. Res. Toxicol.* **2000***, 13*, 610-615.

24. Luu, N. C.; Iyer, R. A.; Anders, M. W.; Ridge, D. P. Fourier-Transform Ion Cyclotron Resonance Mass Spectrometric Studies of Elimination Reactions of Anionic Bases with Metabolites of a Fluorinated Anesthetic Agent: Towards Modeling Bioactivation in the Gas Phase. *International Journal of Mass Spectrometry.* **2000***, 195/196*, 203-213.

25. Chen, O.; Groh, S.; Liechty, A.; Ridge, D. P. Binding of Nitric Oxide to Iron(II) Porphyrins: Radiative Association, Blackbody Infrared Radiative Dissociation and Gas-Phase Association Equilibrium. *J. Am. Chem. Soc.* **1999***, 121*, 11910-11911.

26. Ekeberg, D.; Uggerud, E.; Lin, H.; Sohlberg, K.; Chen, H.; Ridge, D. P. Dehydrogenation of Ethane by CpM+ (M = Fe, Co, Ni) in the Gas Phase. an FT-ICR-MS Study. *Organometallics.* **1999***, 18*, 40-44.

27. Bjarnason, A.; Ridge, D. P. Gas-Phase Reactions of M+ and MO+ (M = Sc, Ti, V) with Toluene. *Organometallics.* **1998***, 17*, 1889-1893.

28. Arnold, F. P.,Jr.; Ridge, D. P.; Rheingold, A. L. Reaction of Diantimony Anion with Mononuclear Metal Carbonyls. First Observed Instance of an Antimony-Transition-Metal Triple Bond. *J. Am. Chem. Soc.* **1995***, 117*, 4427-4428.

29. Pan, Y. H.; Ridge, D. P. Gas-Phase Reactions of Chromium, Iron, and Nickel Carbonyls of Cr(CO)5-, Fe(CO)4-, and Ni(CO)3- with Organic Electrophiles. *J. Am. Chem. Soc.* **1992***, 114*, 2773-2780.

30. Chen, H. L.; Hagan, T. E.; Groh, S. E.; Ridge, D. P. Gas-Phase Reactions of Iron Porphyrins with Nitrogen Oxide (NO2): Oxygen Atom Transfer to Anionic and Cationic Iron Porphyrins. *J. Am. Chem. Soc.* **1991***, 113*, 9669-9670.

31. Pan, Y. H.; Sohlberg, K.; Ridge, D. P. Reactions of Cobalt Ions Co1-4+ and Co4(CO)n+ with Cyclohexane: C-H Activation as a Function of Cluster Size and Ligand Substitution. *J. Am. Chem. Soc.* **1991***, 113*, 2406-2411.

32. Barry, R.; Strobel, F.; Haas, M.; Ridge, D.; Munson, B. Ion Molecule Reactions in Diisopropyl Ether. *Int. J. Mass Spectrom. Ion Processes.* **1989***, 89*, 133-148.

33. Ridge, D. P.; Meckstroth, W. K. Reactions in Ionized Metal Carbonyls: Clustering and Oxidative Addition. *Gas Phase Inorg.Chem.* **1989**, 93-113.

34. Ridge, D. P. Reactions of Transition Metal Ions with Cycloalkanes and Metal Carbonyls. *NATO ASI Series, Series C: Mathematical and Physical Sciences.* **1987***, 193*, 165-175.

35. Meckstroth, W. K.; Freas, R. B.; Reents, W. D., Jr.; Ridge, D. P. Relationship between Structure and Reactivity for Metal Clusters Formed in Ion-Molecule Reactions in Decacarbonyldimanganese and Pentacarbonyl(Pentacarbonylmanganio)Rhenium. *Inorg. Chem.* **1985***, 24*, 3139-3146.

36. Meckstroth, W. K.; Ridge, D. P. Very Large Metal Carbonyl Clusters Formed by ion/molecule Reactions in Decacarbonyldirhenium. *International Journal of Mass Spectrometry and Ion Processes.* **1984***, 61*, 149-152.

37. Peake, D. A.; Gross, M. L.; Ridge, D. P. Mechanism of the Reaction of Gas-Phase Iron Ions with Neutral Olefins. *J. Am. Chem. Soc.* **1984***, 106*, 4307-4316.

38. Wronka, J.; Ridge, D. P. Double Metal to Metal Bonds in Metal Carbonyl Clusters Formed in the Gas-Phase Negative Ion Chemistry of Iron Pentacarbonyl. *J. Am. Chem. Soc.* **1984***, 106*, 67-71.

39. Allison, J.; Ridge, D. P. Reactions of Atomic Metal Ions with Alkyl Halides and Alcohols in the Gas Phase. *J. Am. Chem. Soc.* **1979***, 101*, 4998-5009.

40. Yamashita, M.; Fenn, J. B. Negative Ion Production with the Electrospray Ion Source. *J. Phys. Chem.* **1984***, 88*, 4671-4675.

41. Yamashita, M.; Fenn, J. B. Electrospray Ion Source. another Variation on the Free-Jet Theme. *J. Phys. Chem.* **1984***, 88*, 4451-4459.

42. Taylor, G. Disintegration of Water Drops in an Electric Field. *Proceedings of the Royal Society of London.Series A, Mathematical and Physical Sciences.* **1964***, 280*, 383-397.

43. Konermann, L. A Simple Model for the Disintegration of Highly Charged Solvent Droplets during Electrospray Ionization. *J. Am. Soc. Mass Spectrom.* **2009***, 20*, 496-506.

44. Nemes, P.; Marginean, I.; Vertes, A. Spraying Mode Effect on Droplet Formation and Ion Chemistry in Electrosprays. *Anal. Chem.* **2007***, 79*, 3105-3116.

45. Ichiki, K.; Consta, S. Disintegration Mechanisms of Charged Aqueous Nanodroplets Studied by Simulations and Analytical Models. *J. Phys. Chem. B.* **2006***, 110*, 19168-19175.

46. Marginean, I.; Znamenskiy, V.; Vertes, A. Charge Reduction in Electrosprays: Slender Nanojets as Intermediates. *J. Phys. Chem. B.* **2006***, 110*, 6397-6404.

47. Storozhev, V. B.; Nikolaev, E. N. Computer Simulations of the Fission Process of Charged Nanometre Droplets. *Philos. Mag.* **2004***, 84*, 157-171.

48. Duft, D.; Achtzehn, T.; Mueller, R.; Huber, B. A.; Leisner, T. Coulomb Fission. Rayleigh Jets from Levitated Microdroplets. *Nature.* **2003***, 421*, 128.

49. Cole, R. B. Some Tenets Pertaining to Electrospray Ionization Mass Spectrometry. *J Mass Spectrom.* **2000***, 35*, 763-772.

50. Constantopoulos, T. L.; Jackson, G. S.; Enke, C. G. Challenges in Achieving a Fundamental Model for ESI. *Anal. Chim. Acta.* **2000***, 406*, 37-52.

51. Fernandez de la Mora, J. Electrospray Ionization of Large Multiply Charged Species Proceeds Via Dole's Charged Residue Mechanism. *Anal. Chim. Acta.* **2000***, 406*, 93-104.

52. Kebarle, P. A Brief Overview of the Present Status of the Mechanisms Involved in Electrospray Mass Spectrometry. *J. Mass Spectrom.* **2000***, 35*, 804-817.

53. Kebarle, P.; Tang, L. From Ions in Solution to Ions in the Gas Phase - the Mechanism of Electrospray Mass Spectrometry. *Anal. Chem.* **1993***, 65*, 972A-986A.

54. Kebarle, P. A Brief Overview of the Present Status of the Mechanisms Involved in Electrospray Mass Spectrometry. *Journal of Mass Spectrometry.* **2000***, 35*, 804-817.

55. Dole, M.; Mack, L. L.; Hines, R. L.; Mobley, R. C.; Ferguson, L. D.; Alice, M. B. Molecular Beams of Macroions. *J. Chem. Phys.* **1968***, 49*, 2240-2249.

56. Thomson, B. A.; Iribarne, J. V. Field-Induced Ion Evaporation from Liquid Surfaces at Atmospheric Pressure. *J. Chem. Phys.* **1979***, 71*, 4451-4463.

57. Iribarne, J. V.; Thomson, B. A. On the Evaporation of Small Ions from Charged Droplets. *J. Chem. Phys.* **1976***, 64*, 2287-2294.

58. Kebarle, P.; Peschke, M. On the Mechanisms by which the Charged Droplets Produced by Electrospray Lead to Gas Phase Ions. *Anal. Chim. Acta.* **2000***, 406*, 11-35.

59. Konermann, L. A Minimalist Model for Exploring Conformational Effects on the Electrospray Charge State Distribution of Proteins. *J. Phys. Chem. B.* **2007***, 111*, 6534-6543.

60. Felitsyn, N.; Peschke, M.; Kebarle, P. Origin and Number of Charges Observed on Multiply-Protonated Native Proteins Produced by ESI. *Int. J. Mass Spectrom.* **2002***, 219*, 39-62.

61. Iavarone, A. T.; Williams, E. R. Mechanism of Charging and Supercharging Molecules in Electrospray Ionization. *J. Am. Chem. Soc.* **2003***, 125*, 2319-2327.

62. Kaltashov, I. A.; Mohimen, A. Estimates of Protein Surface Areas in Solution by Electrospray Ionization Mass Spectrometry. *Anal. Chem.* **2005***, 77*, 5370-5379.

63. Laskin, J.; Denisov, E. V.; Shukla, A. K.; Barlow, S. E.; Futrell, J. H. Surface-Induced Dissociation in a Fourier Transform Ion Cyclotron Resonance Mass Spectrometer: Instrument Design and Evaluation. *Anal. Chem.* **2002***, 74*, 3255-3261.

64. Shaffer, S. A.; Tang, K.; Anderson, G. A.; Prior, D. C.; Udseth, H. R.; Smith, R. D. A Novel Ion Funnel for Focusing Ions at Elevated Pressure using Electrospray Ionization Mass Spectrometry. *Rapid Communications in Mass Spectrometry.* **1997***, 11*, 1813-1817.

65. Grill, V.; Shen, J.; Evans, C.; Cooks, R. G. Collisions of Ions with Surfaces at Chemically Relevant Energies: Instrumentation and Phenomena. *Rev. Sci. Instrum.* **2001***, 72*, 3149-3179.

Chapter 3

FRAGMENTATION PATTERNS OF OXIDIZED PEPTIDES ELUCIDATED BY SID, RRKM MODELING, AND MOLECULAR DYNAMICS

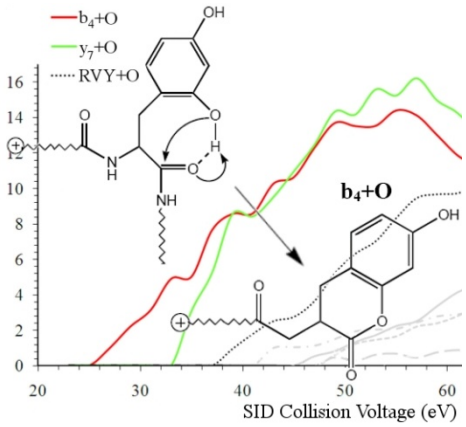

3.1 Introduction

The possibility of detrimental human health and environmental effects from ozone exposure [1-27] has prompted a number of studies of ozone oxidation of amino acids and peptides [28-32]. Prolonged human exposure to high ozone levels have shown to cause negative health effects including dry eye syndrome [19] and decreased respiratory function [18]. Environmentally, ozone can cause degenerative effects on animal lung function and plant health [12,13,25]. Spectroscopic studies have found Met, Trp, Tyr, Cys, His, and Phe to be the most vulnerable to oxidation after exposure to ozone in aqueous solution [29-32]. In addition, ESI MS/MS experiments of the ozone reaction products of single amino acids and small peptides

were done to determine the resulting product structures of the oxidized amino acid residues [28].

A recent study has addressed the rates of ozone oxidation and the mechanism of ozonolysis in aqueous solution for angiotensin II (DRVYIHPF) and the analogs DRVYIAPA and DRVAIHPA using mass spectrometry [33]. Although other minor oxidation products were observed, the primary reaction products following exposure to ozone were found to result in the addition of one oxygen atom to Tyr (AngII+O) and three oxygen atoms to His (AngII+3O). MS/MS spectra for the oxidation products exhibited some fragmentation processes that were distinct from the usual patterns observed in peptides with acidic amino acid side chains [34]. It was important to establish that the observed fragment ions were consistent with suggested structures of the oxidized peptides. The present examination of the energetics and dynamics of the collisional fragmentation of oxidized peptides is intended to provide a basis for relating postulated structures of the oxidized peptides to the observed MS/MS differences. Energetic and dynamic results of the kind reported here have not been previously available for oxidized peptides, so the results may facilitate studies of peptide oxidation by improving our ability to assign structures to the resulting oxidized peptides.

Elucidation of the collisional fragmentation patterns of oxidized peptides also pertains to a protein characterization method referred to as oxidative footprinting [35-47]. In this technique three-dimensional structures and conformational changes of proteins and protein complexes are examined by observing the oxidation reactivity of the solvent accessible amino acid side chains. The experiment is designed so that the time scale of oxidation exposure is shorter than the time necessary for major structural

rearrangement. Following the oxidation reaction, the target protein is then analyzed using traditional bottom-up proteomic methods in which the target undergoes enzymatic cleavage and the resulting peptides are sequenced using MS/MS. Specific information on the energetics and dynamics of oxidized peptide fragmentation could be useful in using collisional fragmentation of digest fragments to locate oxidation sites.

Qualitative studies of collisional fragmentation processes, even when the collision energy is varied, do not provide such important energetic and dynamic quantities as threshold energies and entropies of activation. These quantities can only come from measurements of rate constants as a function of internal energy. The results reported here were obtained using a unique method which combines energy-resolved Surface Induced Dissociation (SID) and Fourier Transform Ion Cyclotron Resonance Mass Spectrometry (FT-ICR MS). A packet of ions of selected translational energy collides with a prepared surface at a known collision time. The collisional reaction products are caught in the FT-ICR MS trap and sampled at known reaction times. The determination of fragmentation rate constants as a function of internal energy, and hence threshold energies and activation entropies from the resulting data, has been described [48]. The methodology has been applied to the dissociation reactions of a number of model peptides providing a context for the present results [49-59]. Particularly relevant are results for the model peptides LDIFSDF, LDIFSDFR, RLDIFSDF, and LEIFSEFR [56] as well as angiotensin II (DRVYIHPF) and the relative analogs RVYIHPF, RVYIHAF, and RVYIHDF [55]. These studies provide particular insight into selective charge-remote fragmentations involving aspartic acid amino acid residues. Dissociation thresholds (E_0) for charge-

remote selective cleavages involving aspartic acid were found to be similar to E_0 for nonselective charge-directed dissociation pathways. In addition, large negative entropy values are observed for peptides with arginine residues due to the extensive rearrangements associated with selective fragmentation mechanisms. Similarly, arginine containing peptides with methionine sulfoxide modifications were found to fragment selectively at the methionine sulfoxide in a charge-remote process associated with a large negative activation entropy. Given the structures postulated for the oxidized peptides, charge-remote mechanisms might account for several of the unusual selective fragment ions observed for the ozonolysis reaction products of angiotensin II. In the present study when a negative entropy of activation was observed, suggesting a constrained transition state, molecular dynamics calculations were done to probe primary ion conformations for the proposed structures of the oxidation products that could lead to the observed fragmentation patterns. The activation entropy and the molecular dynamics thus provided constraints on the proposed mechanism that strengthen the validity of the assigned oxidized peptide structure.

Applicable to the field of mass spectrometry for the analysis of both environmentally significant biomolecular ozonolysis products and bioanalytically significant protein-footprinting experiments, this study aims to build on the current literature by addressing the need for understanding gas-phase dissociation mechanisms of oxidized peptides during MS/MS experiments. Our focus is centered on how oxidative stress, resulting in modification to Tyr and His residues, affect selective fragmentation patterns of angiotensin II from an energetic and mechanistic perspective.

3.2 Experimental

Angiotensin II (DRVYIHPF) was purchased from Sigma-Aldrich (St. Louis, MO) and HPLC grade acetonitrile and methanol were purchased from Fisher Scientific (Fair Lawn, NJ). Aqueous peptide solutions (~143 μM) were prepared using deionized water (Millipore, Bedford, MA). Oxidation reactions were conducted by flowing ozone over peptide solutions for up to 21 min with a flow rate of ~1.2 L/min. Ozone was generated using an ozone generator model PZ5 (Prozone International, Inc., Huntsville, Al). Peptide solutions were diluted 1:1 with methanol or acetonitrile for electrospray experiments.

Analysis was done using a specially fabricated 6T FT-ICR mass spectrometer (Pacific Northwest National Laboratory, Richland, WA). Ions are produced using electrospray ionization (ESI emitter, 2.2 kV) at atmospheric pressure and enter through a heated stainless steel capillary (270 V). An ion funnel [60] is then used to efficiently transfer the ions to the high vacuum region of the instrument where they pass through a series of quadrupoles used for collisional focusing, mass selection and ion accumulation. The front plate of the funnel is kept at 270 V while the back plate is set to 25-35 V. The dc offsets for the three quadrupoles are set to 15-25 V, 5-10 V and 2-6 V respectively. Typical accumulation times range from 0.1-0.3 seconds and is done at elevated pressure (2x10-3 Torr) to allow internally excited ions to collisionally relax prior to entering the ICR cell. Ions are then extracted from the accumulation quadrupole and enter the ICR cell where they collide with the SID surface in MS/MS experiments. After collision, ions are captured by raising the trapping potentials (10-20 V). Ion collision energy is determined by the difference in potential between the accumulation quadrupole and the rear trapping plate of the ICR

cell. SID experiments were done using a surface composed of a 2 μm film of carbon vapor deposited diamond on a titanium surface prepared by P1 Diamond Inc. (Santa Clara, CA). A reaction delay of 1 s was used for fragmentation reactions over a range of collision energies from 23-81 eV using 2 eV increments. Energy-resolved fragmentation efficiency curves were generated from experimental mass spectra by plotting the relative abundance of primary ions and the resulting fragment ions as a function of collision energy. A more detailed description of the instrument can be found elsewhere [61]. Given the known structures of the precursor ions, most of the fragments can be unambiguously identified from their mass numbers. We note, however, that the agreement between the observed and theoretical fragment masses is consistent with the estimated 5 ppm accuracy of the calibrated mass scale of the SID spectra.

3.2.1 RRKM Modeling

Collision energy-resolved fragmentation efficiency curves (FECs) were modeled by Dr. Julia Laskin (Pacific Northwest National Laboratory, U.S. Department of Energy, Richland, WA) using a previously discussed RRKM-based method [62, 63]. Two dissociation rate constants were used for the total ion decomposition to account for the slow and fast fragmentation, as indicated schematically below:

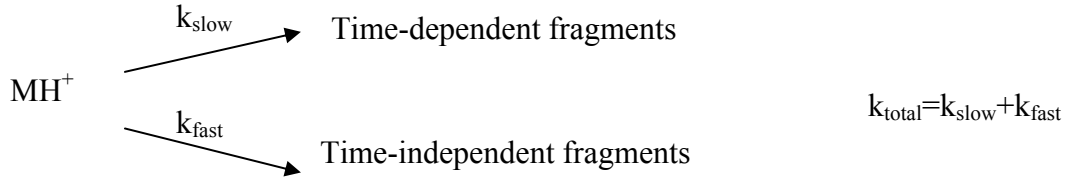

Microcanonical rate constants as a function of internal energy for the slow channel were calculated using the RRKM expression. For the fast reaction pathway the rate-energy dependence is very sharp and is best described by a step-function originating from the assumed threshold energy [57].

Fragmentation probability as a function of the internal energy of the primary ion and the experimental observation time (t_r), $F(E, t_r)$, is given by:

$$F(E,t_r) = e^{-(k_{total}(E)-k_{rad})t_r} \qquad 3.1$$

where k_{rad} is the rate constant for radiative cooling of the excited ion. The energy deposition function was described by the following analytical expression:

$$P(E,E_{coll}) = \frac{(E-\Delta)^l \exp(-(E-\Delta)/f(E_{coll}))}{C} \qquad 3.2$$

where l and Δ are parameters, $C = \Gamma(l+1)[f(E_{coll})]l+1$ is a normalization factor, and $f(E_{coll})$ has the form:

$$f(E_{coll}) = A_2E^2_{coll} + A_1E_{coll} + A_0 \qquad 3.3$$

where A_0, A_1, and A_2 are parameters, and E_{coll} is the collision energy. Finally, the normalized signal intensity for a particular reaction channel is given by the equation:

$$I_i(E_{coll}) = \int_0^\infty F_i(E,t)P(E,E_{coll})dE \qquad 3.4$$

Collision energy-resolved survival curves were constructed using the above procedure and compared to the experimental data. The energy deposition function, based on time and energy-resolved FEC data of angiotensin II from previous studies [56], was held constant for each oxidation product. Fitting parameters included the critical energy and the activation entropy for the total decomposition of the precursor ion. The quality of the fits was confirmed using sensitivity analysis described previously [63].

Vibrational frequencies of precursor ions were obtained from the frequency model provided by Christie and co-workers [64]. Vibrational frequencies for the transition state were varied by adjusting vibrational frequencies for the transition state which were estimated by removing one C-N stretch (reaction coordinate) from the parent ion frequencies as well as adjusting all frequencies in the range of 500-1000 cm^{-1} to obtain the best fit with experimental data. The resulting frequencies were used to calculate entropies of activation at 450 K.

3.2.2 Molecular Dynamics Calculations

Molecular dynamics calculations were done using the Insight II software package from Biosym Technologies (San Diego, CA). Peptides were constructed using the amino acid database of the Biopolymer module. Both the N- and C-terminus of all peptides were capped with hydrogen atoms and left neutral. A proton was placed on the most basic site ($D\underline{R}^{+}VYIHPF$) or as indicated below on a site appropriate for a particular charge driven decomposition mechanism. Peptide modification was done using the Fragment Library within the Biopolymer module. Modification to the Tyr residue was done by replacing the appropriate hydrogen atom

of the side chain with a hydroxyl group while His modification was done by substituting an Ala residue for His and constructing the oxidized His* residue from Ala using aldehyde and amide functionalities. Minimization and dynamics calculations were performed using the Discover Module. Steepest decent minimization was done for 1500 iterations using the CFF91 force field. Following minimization, molecular dynamics experiments were performed at 400 K for 100,000 cycles (100 ps). Intramolecular hydrogen bonds were observed by turning on the hydrogen bonding feature using default parameters.

3.3 Results and Disscussion

3.3.1 Fragmentation Pathways

Singly charged ESI FT-ICR mass spectra of angiotensin II and the oxidation products resulting from ozonolysis along with surface-induced dissociation mass spectra (43 eV) for angiotensin II and the AngII+O, AngII+3O, and AngII+4O adducts—$DR^{+}VYIHPF$, $DR^{+}VY^{*}IHPF$, $DR^{+}VYIH^{*}PF$, and $DR^{+}VY^{*}IH^{*}PF$—are shown in Figure 3.1. Additionally, detailed peak lists for 60 eV spectra can be found in Appendix B. The parent ion spectrum of the reaction solution shows the major oxidation products to be AngII+O, AngII+3O, and AngII+4O (Figure 3.1a). Accurate mass measurements confirmed the molecular formula of each ozonolysis adduct. SID data shows AngII and all oxidation products selectively fragment C-terminal to the aspartic acid residue (D) forming the $\mathbf{y_7}$, $\mathbf{y_7+O}$, $\mathbf{y_7+3O}$, and $\mathbf{[y_7+4O]^{+}-71}$ dissociation products respectively (Figure 3.1b-d). Selective fragmentation C-terminal to acidic residues (aspartic or glutamic acids) is typical of peptides when the number of ionizing protons is less than or equal to the number of basic sites [34]. Modification to the Tyr

residue, DRVY*IHPF (AngII+O), results in the selective formation of the **b_4+O** (Figure 3.1c) ion while oxidation of the His residue, DRVYIH*PF (AngII+3O), opens selective fragmentation channels resulting in the formation of the **$[MH+3O]^+$-45**, **$[MH+3O]^+$-71**, **b_5**, and **$[MH+3O]^+$-88** ions (Figure 3.1d). The AngII+4O oxidation product fragments to form ions associated with modification to both Tyr and His, DRVY*IH*PF, including the **$[MH+4O]^+$-45**, **$[MH+4O]^+$-71**, **$[MH+4O]^+$-88, b_5+O** and **b_4+O** fragments.

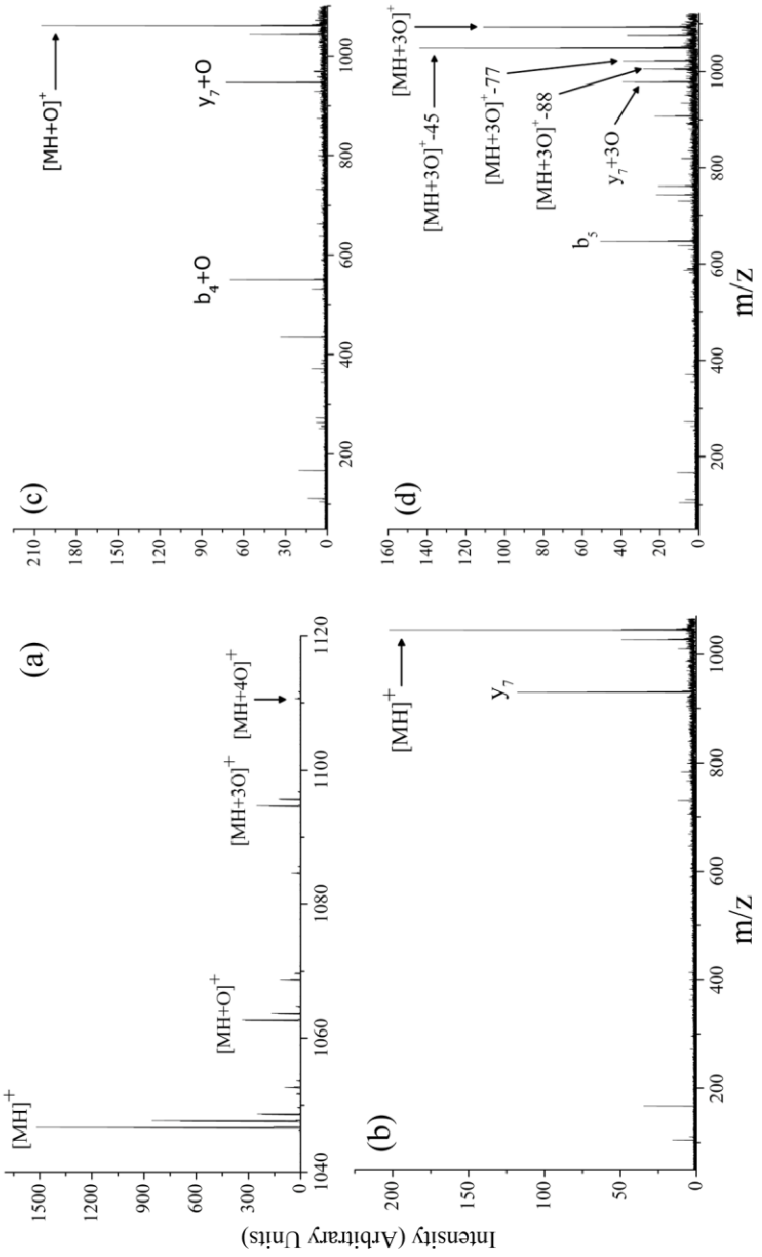

Figure 3.1. ESI FT-ICR mass spectra of (a) AngII and the oxidation products resulting from reaction with ozone, (b) the 43eV SID spectrum of unmodified AngII (MH^+), (c) the 43eV SID spectrum of AngII+O oxidation product ($MH+O^+$), and (d) the 43eV SID spectrum of AngII+3O oxidation product ($MH+3O^+$).

Unmodified angiotensin II selectively fragments to form the y_7 ion resulting from charge-remote cleavage C-terminal to the aspartic acid residue

(Figure 3.1b). This cleavage has been rationalized in terms of the "mobile" proton model [65, 66]. According to the model, arginine (R), being the most basic site on the molecule, sequesters the single ionizing proton preventing unselective charge-directed fragmentations at low collision energies. With the charge on the guanidine functionality of the Arg^+ side chain, the acidic side chain of aspartic acid can induce selective fragmentation through interaction with the peptide backbone. This common dissociation pathway has been described mechanistically in a number of studies [65-71]. According to one frequently proposed charge-remote fragmentation mechanism involving Asp residues, the hydroxyl hydrogen of the aspartic acid side chain can hydrogen bond with the carbonyl oxygen of the peptide backbone promoting a cis-1,2-elimination reaction leading to backbone cleavage C-terminal to the acidic side chain [66-68, 71]. In this mechanism the Asp residue plays no part in the solvation of the charge sequestered on the Arg side chain (Scheme 3.1a). Alternatively, others have proposed that the selective fragmentation C-terminal to aspartic acid is driven by the formation of a salt bridge between the protonated Arg residue and the Asp side chain [66, 69, 70]. This mechanism is still charge-remote with the proton sequestered at the guanidine of the Arg^+ residue, however, the charge is solvated by the Asp side chain resulting in an intramolecular salt-bridge intermediate (Scheme 3.1b). In both cases, the charge remains with the protonated Arg^+ residue which is C-terminal to the dissociated peptide bond, resulting in a y-type fragment ion. Aside from the y_7 fragment, the SID spectrum of AngII also shows a significant peak resulting from the loss of water from the parent ion (MH^+-H_2O). Additional peaks are a result of minor non-selective fragment ions.

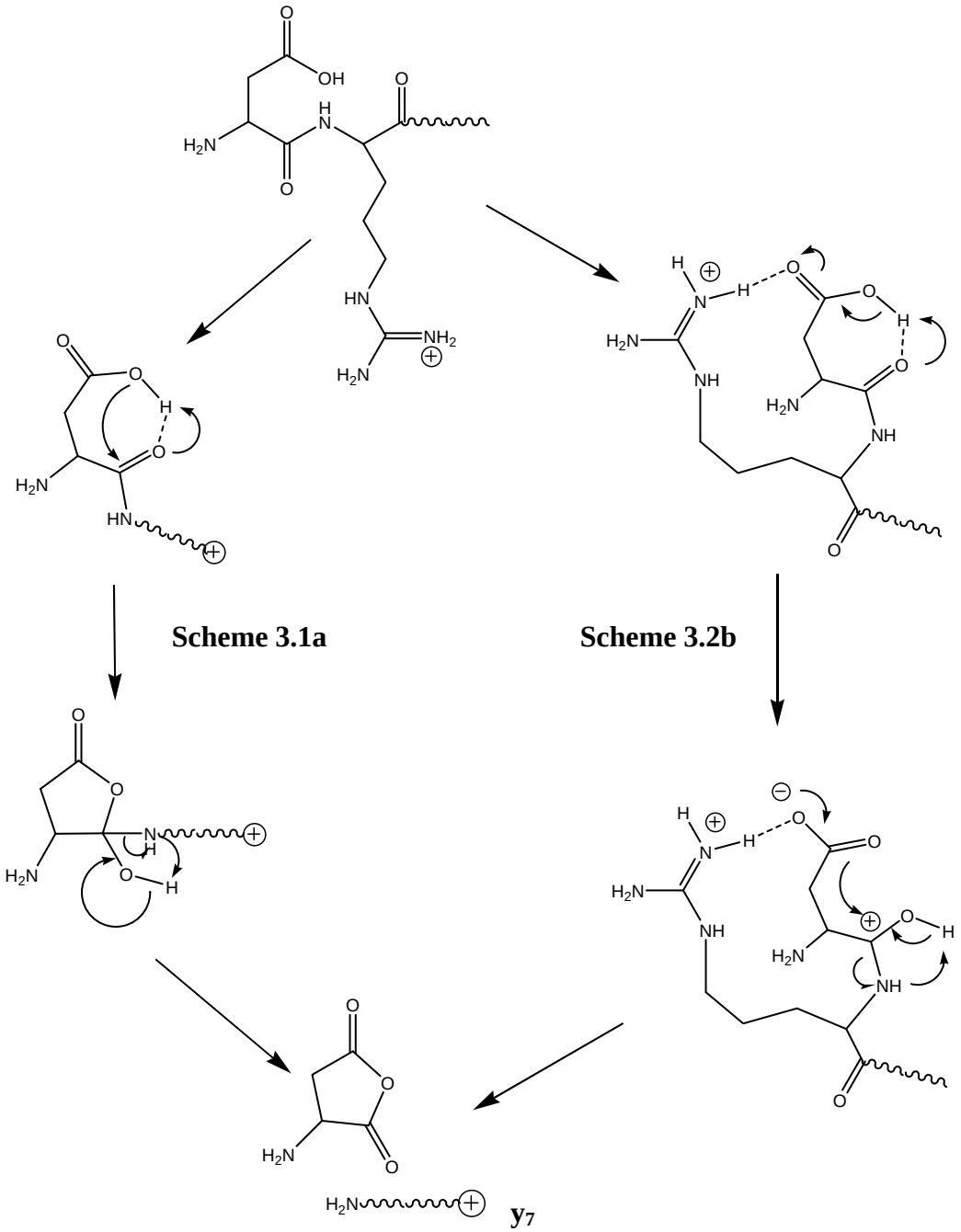
Scheme 3.1a
Scheme 3.2b
y7

SID of the AngII+O oxidation product results in the selective formation of the $\mathbf{y_7+O}$ and $\mathbf{b_4+O}$ fragment ions (Figure 3.1c). As observed in unmodified AngII, the most basic site of the AngII+O adduct is Arg making it the most likely site to accept the single ionizing proton resulting in charge-remote dissociation processes at low energies. The $\mathbf{y_7+O}$ ion, just as it is in unmodified AngII, is driven by the interaction between the Asp sidechain and the peptide backbone. Addition of one oxygen atom in the ozonolysis of AngII results from the oxidation of Tyr forming 3,4- or 2,4-dihydroxyphenylalanine [28]. The additional hydroxyl group of the modified Tyr^* residue can mimic aspartic acid by interacting with the peptide backbone C-terminal to the Tyr^* residue resulting in charge-remote dissociation of the peptide bond between Tyr^* and Ile. This is shown in Scheme 3.2 and results in the formation of the $\mathbf{b_4+O}$ fragment ion. This mechanism parallels the process shown in Scheme 3.1a for the formation of the $\mathbf{y_7}$ fragment. It is noteworthy that the Scheme 3.2 mechanism requires oxidation of the Tyr at the 2-position forming the 2,4-dihydroxyphenylalanine oxidation reaction product. A hydroxyl group at the 3-position could not interact with the peptide backbone C-terminal to Tyr^*.

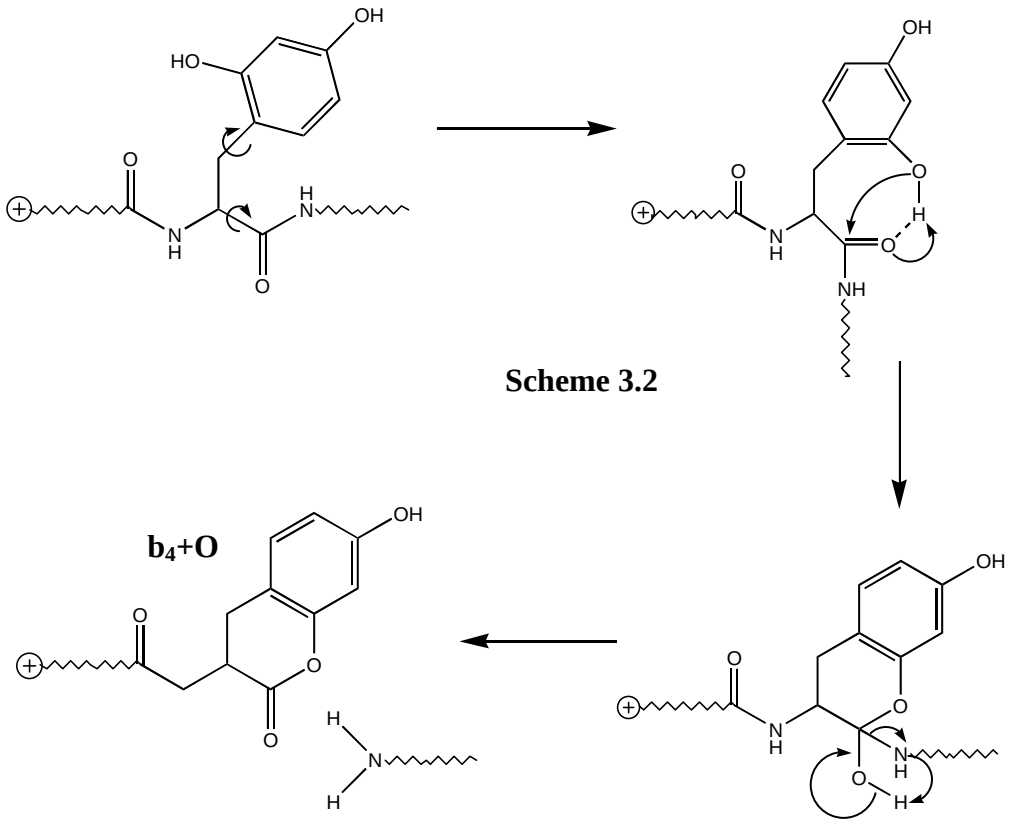

Scheme 3.2

The selective **b_4+O** cleavage is pertinent to the two mechanisms shown in Schemes 3.1a and 3.1b for charge-remote processes involving aspartic acid. The modified Tyr* residue, similarly to aspartic acid, can drive C-terminal charge-remote dissociation mechanisms at low internal energies. However, unlike the Asp residue, Tyr* cannot form a salt bridge with the protonated Arg^+ residue suggesting that the salt-bridge intermediate is unnecessary for fragmentation C-terminal to Asp residues. Other ions present in the 43 eV SID spectrum of AngII+O are the loss of water (**[MH+O^+]-H_2O**), the internal fragment **RVY+O**, and minor non-selective fragment ions.

Fragmentation of the AngII+3O oxidation product results in the selective formation of the **y_7+3O**, **[MH+3O]$^+$-45**, **[MH+3O]$^+$-71**, **b_5**, and **[MH+3O]$^+$-88** ions (Figure 3.1d). Fragmentation patterns using SID are consistent with previous studies that have shown the AngII+3O ozonolysis product to stem primarily from oxidation of the His residue in which three oxygen atoms are inserted into the side chain, opening the His ring, finally resulting in the 2-amino-4-oxo-4-(3-formylureido)butanoic acid structure [28]. The most basic site on the DRVYIH*PF is still the Arg residue, however, the modified His* side chain is also capable of delocalizing the charge associated with protonation and might compete for the single ionizing proton. As in the case of unmodified angiotensin II, the **y_7+3O** fragmentation pathway is a charge remote process resulting from acidic interaction between the hydroxyl hydrogen of the aspartic acid side chain and the peptide backbone with the charge localized on either the Arg or the His* residues.

Scheme 3.3 shows the proposed charge-remote mechanisms for the formation of the **[MH+3O]$^+$-45** and **[MH+3O]$^+$-71** fragment ions. With the singly ionizing proton sequestered by the Arg$^+$ residue, intramolecular hydrogen bonding can occur within the His* side chain forming a hydrogen bond between the hydrogen atom of the first amide group of the His* side chain relative to the peptide backbone and the formyl oxygen atom of the His* side chain. The proton can then be transferred, breaking the peptide-like bond of the His* side chain between the second carbonyl carbon atom and the second amide nitrogen from the peptide backbone resulting in the loss of neutral CH_3NO and the formation of the **[MH+3O]$^+$-45** fragment ion. Similarly, a hydrogen bond can form within the His* side chain between the hydrogen

atom of the second amide group and the oxygen atom of the first carbonyl group from the peptide backbone. This interaction drives the dissociation of the peptide-like bond between the nitrogen atom of the first amide nitrogen from the peptide backbone and the carbon atom of the second carbonyl group. This fragmentation pathway producing the **$[MH+3O]^+$-71** ion loses neutral C_2HNO_2.

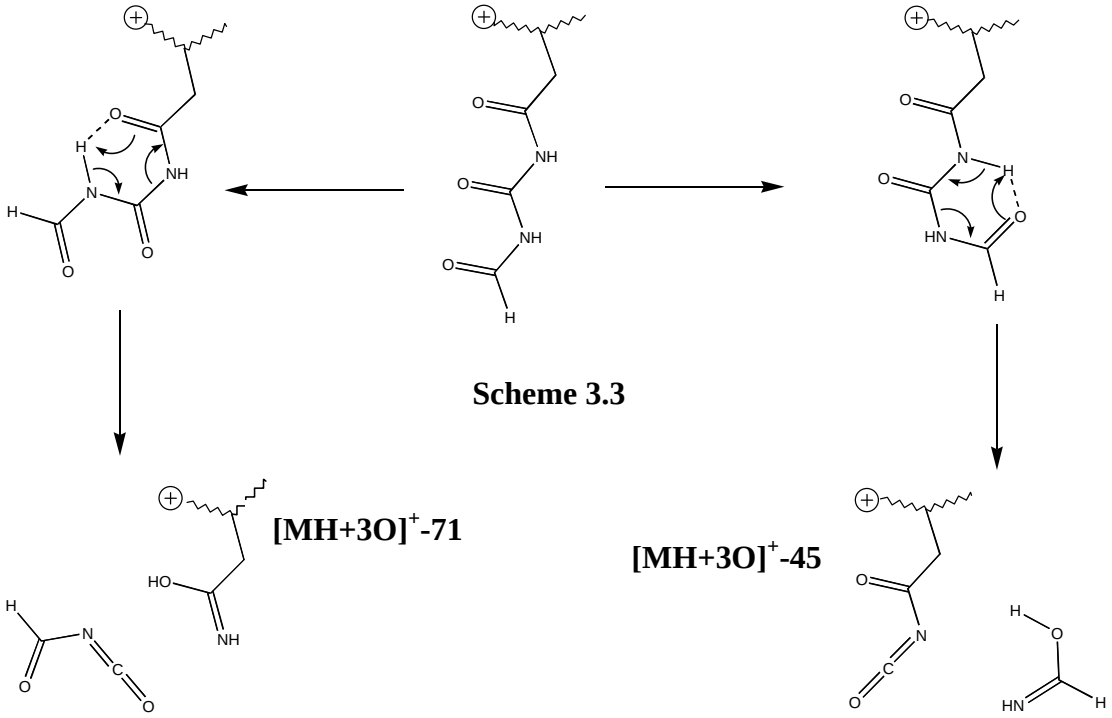

Scheme 3.3

As mentioned above, the relative basicity of oxidized His* allows it to compete with Arg for the single ionizing proton. It is proposed that as the collision energy increases sufficient internal energy becomes available to transfer the ionizing

proton to the modified His* side chain opening charge-directed fragmentation channels. Scheme 3.4 outlines the suggested mechanisms for the charge-directed formation of the $\mathbf{b_5}$ and $\mathbf{[MH+3O]^+}$**-88** fragment ions. Formation of the $\mathbf{b_5}$ secondary ion is driven by protonation of the first carbonyl oxygen of the His* side chain relative to the peptide backbone. The proton can then be transferred to the amide nitrogen of the peptide backbone N-terminal to the oxidized His* residue following the formation of a five member ring and cleavage of the peptide bond between Ile and His*. The C-terminal side of the peptide relative to the dissociated peptide bond is lost as a neutral and the charge is carried by the N-terminal fragment as a tertiary carbocation within the newly formed oxazolone ring structure resulting in a b-type ion [72]. On the other hand, proton transfer to the third carbonyl oxygen atom of the His* residue drives the formation of the $\mathbf{[MH+3O]^+}$**-88** fragment ion. Hydrogen bond formation between the additional proton and the first amide nitrogen of the modified His* residue relative to the peptide backbone promotes cleavage of the peptide-like bond between the first carbonyl carbon atom relative to the peptide backbone and the protonated amide nitrogen following the formation of a five member ring involving the carbonyl functional group C-terminal to the oxidized His* residue. The charge is carried by the peptide as a tertiary carbocation within the newly formed oxazolone ring while the His* side chain is lost as the neutral $C_2H_4N_2O_2$ species [72]. We note that these charge-driven fragmentation mechanisms are completely analogous to the well characterized backbone fragmentation mechanisms leading to $\mathbf{b_n}$ ions with oxazolone ring structures [72].

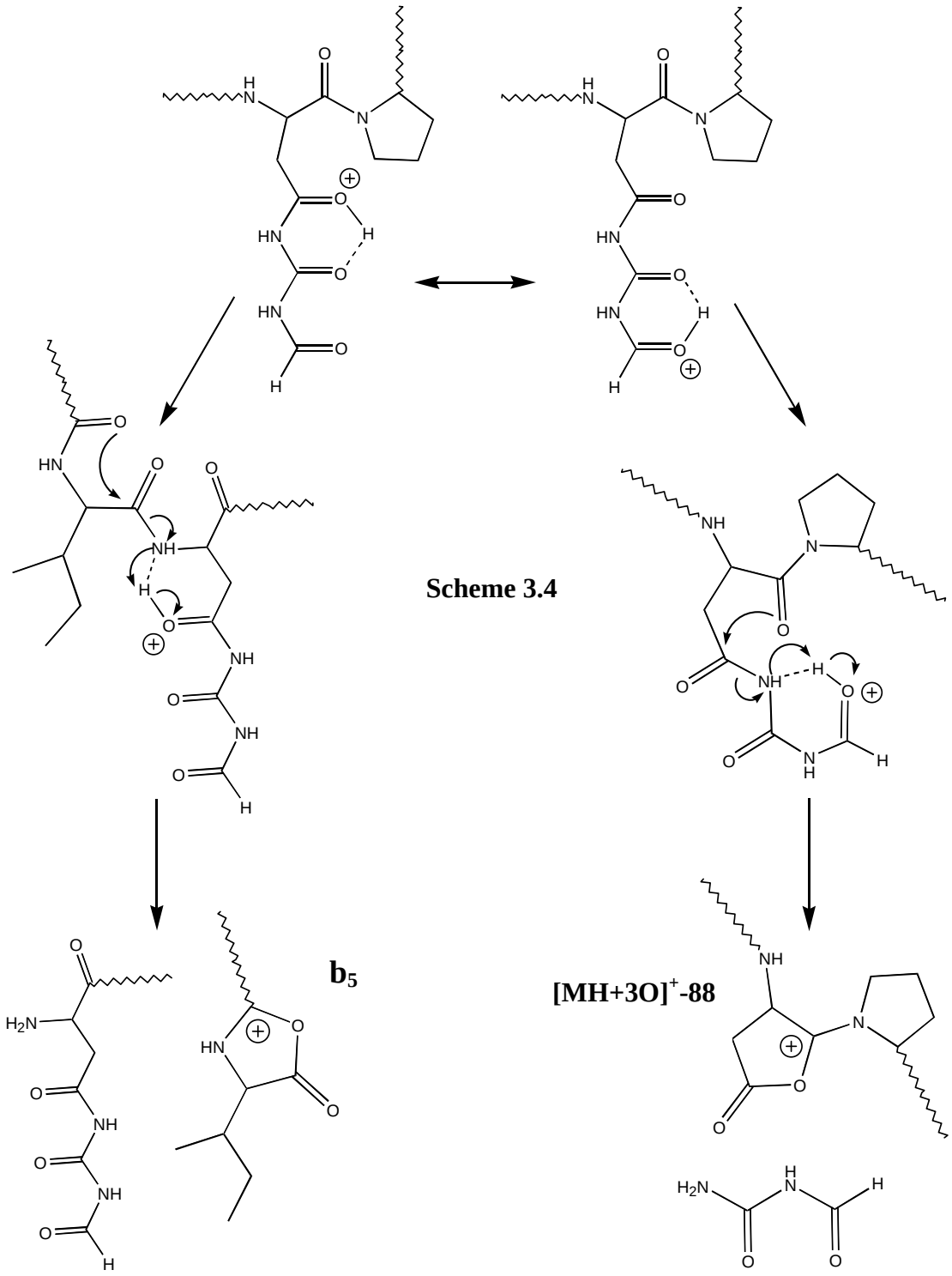

Scheme 3.4

3.3.2 Fragmentation Energetics

Fragmentation energetic studies were conducted by monitoring ion signal as a function of SID collision potential with a time delay of 1s between ion collision and detection. Parent ion survival curves for angiotensin II and the primary oxidation products can be found in Figure 3.2a. Oxidation resulting from reaction with ozone results in destabilization of the respective parent ions relative to collisional fragmentation. The collision energy needed for fragmentation decreases with increased oxidation as follows: AngII > AngII+O > AngII+3O/AngII+4O. This trend is evident from the shift in energy-resolved survival curves to lower collision energies with increased oxidation (Figure 3.2a). The AngII+3O and AngII+4O adducts have overlapping collision-energy-resolved FECs which suggests the lowest energy fragmentation channel of the AngII+4O species is associated with oxidative modification to the His residue. The gradual drop of each of the survival curves has been shown to suggest that the dominant dissociation pathways are kinetically unfavored with large negative reaction entropies [56].

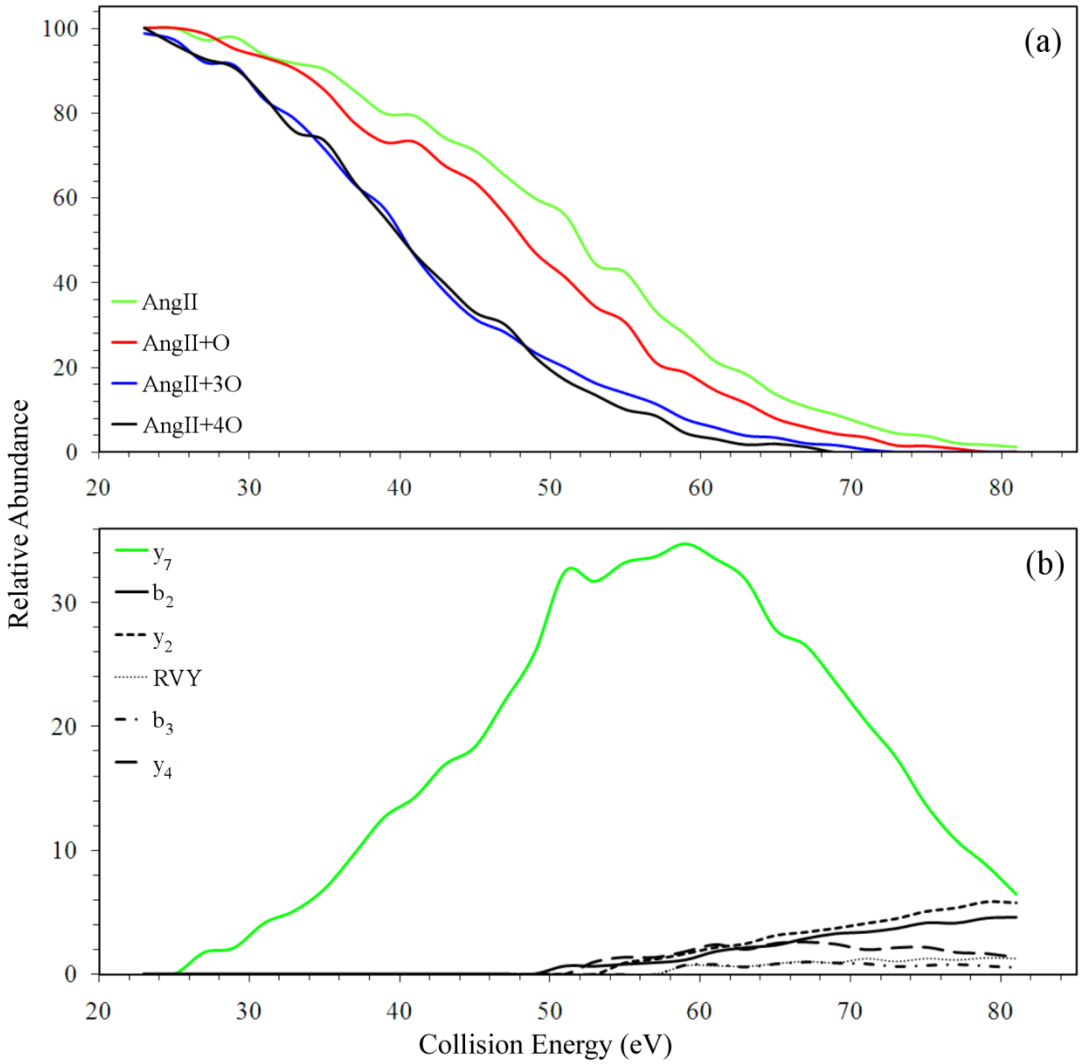

Figure 3.2. Energy-resolved SID FT-ICR MS data for AngII and the oxidation products resulting from ozonolysis representing (a) the parent ion survival curves for AngII, AngII+O, AngII+3O and AngII+4O, (b) FECs of the fragments resulting from AngII, (c) FECs of the fragments resulting from AngII+O, and (d) FECs of the fragments resulting from AngII+3O. ***Figure continued on page 59.***

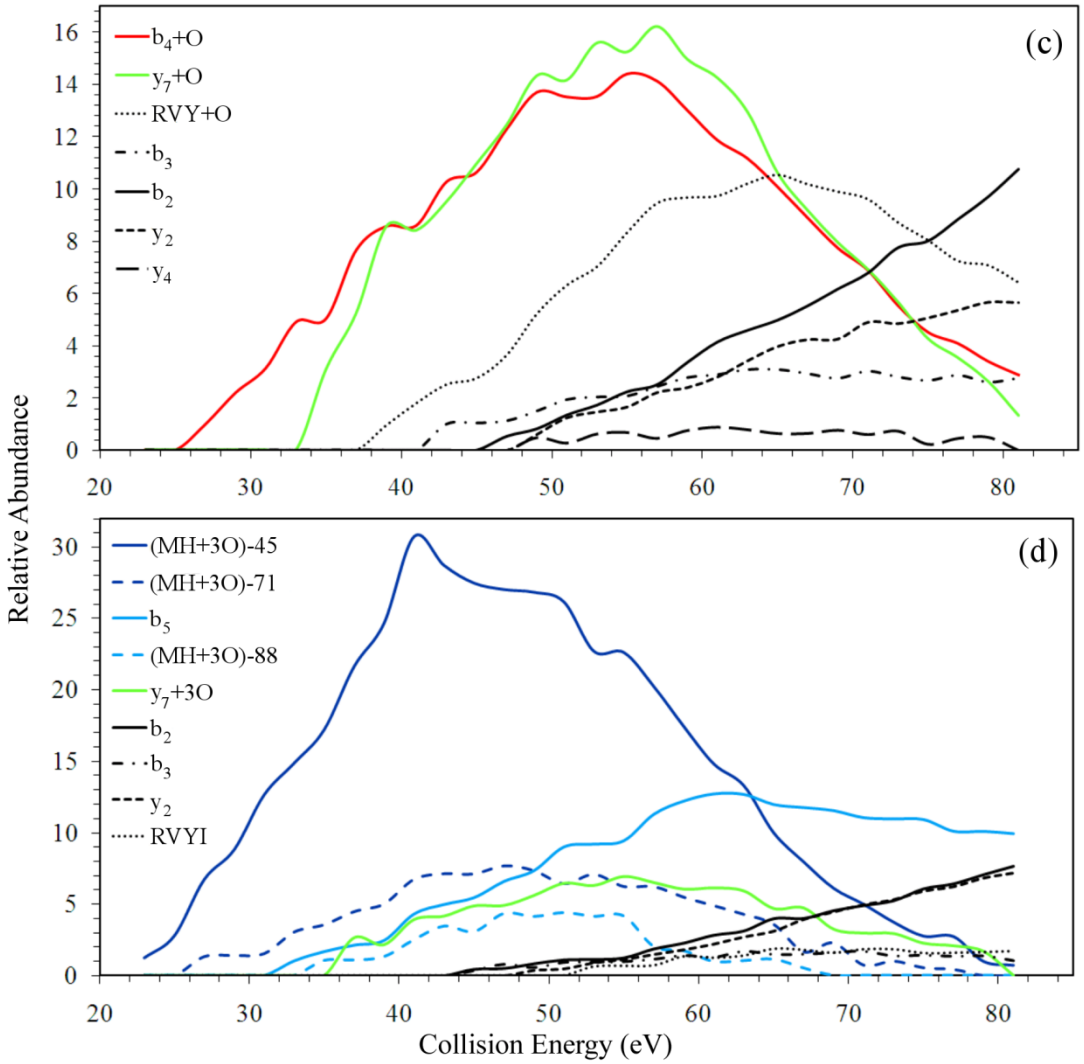

Figure 3.2. Energy-resolved SID FT-ICR MS data for AngII and the oxidation products resulting from ozonolysis representing (a) the parent ion survival curves for AngII, AngII+O, AngII+3O and AngII+4O, (b) FECs of the fragments resulting from AngII, (c) FECs of the fragments resulting from AngII+O, and (d) FECs of the fragments resulting from AngII+3O.

The fragment ion onset curves for unmodified angiotensin II (Figure 3.2b) show the minimum collision energy required to open the primary selective fragmentation channel resulting in the formation of the $\mathbf{y_7}$ ion to be 27 eV. This fragmentation pathway dominates until 50 eV at which high energy non-selective fragmentation channels associated with the transfer of the ionizing proton to the peptide backbone are unlocked. This observation of selective charge-remote fragmentation at low internal energies followed by non-selective fragment ions at high internal energies is consistent with the previously discussed mobile proton model [73].

Oxidation of the Tyr residue following ozonolysis of AngII opens the $\mathbf{b_4+O}$ selective fragmentation pathway. The onset curves for $DR^{+}VY^{*}IHPF$ (Figure 3.2c) show the lowest energy fragmentation channel to be the $\mathbf{b_4+O}$ pathway at 27 eV with the other selective dissociation mechanism ($\mathbf{y_7+O}$) shifted to 35 eV. It should be noted that oxidation of Tyr has little affect on the overall peptide structure and no apparent affect on the structure of the transition state for the $\mathbf{y_7+O}$ dissociation reaction. Additionally, the onset energies for both the $\mathbf{b_4+O}$ fragment in AngII+O and the $\mathbf{y_7}$ fragment in unmodified AngII occur at 27 eV. This suggests the shift to higher collision energies for the $\mathbf{y_7+O}$ fragment ion in AngII+O, in relation to the $\mathbf{y_7}$ fragmentation channel in unmodified AngII, is due to competition with the more entropically favorable $\mathbf{b_4+O}$ dissociation mechanism in the oxidized form of the peptide. This is borne out by the RRKM results discussed below. All other fragments appear at high collision energies driven by non-selective charge-directed pathways.

The onset curves for the fragmentation channels of AngII+3O (Figure 3.2d) highlight a much different fate for the parent ion in comparison to unmodified AngII and AngII+O. The onset energies of each of the primary fragment

ions for the AngII+3O oxidation product suggest that there are three different families of dissociation mechanisms taking place as the collision energy increases. The lowest energy pathways are the dissociation channels producing the **$[MH+3O]^+$-45** and **$[MH+3O]^+$-71** fragment ions. The **$[MH+3O]^+$-45** species is formed immediately at the lowest sampled collision energy (23 eV) while the **$[MH+3O]^+$-71** ion is first observed at 27 eV. The second family of curves are for the **b_5** and **$[MH+3O]^+$-88** fragment ions at onset energies of 33 and 35 eV respectively. The third family of ions includes all other fragments that appear at high collision energies resulting from non-selective charge-directed fragmentation pathways. The **y_7+3O** observed in unmodified AngII at 27 eV is shifted to higher onset energies (37 eV) due to competition with more entropically favorable fragmentation mechanisms just as it is in AngII+O.

From a qualitative perspective, the onset curves of AngII+3O describe the behavior of the extra proton as the collision increases. At very low energies, the proton resides on the most basic site of the molecule (Arg) so that that the first family of fragment ions results from charge-remote selective fragmentation channels (**$[MH+3O]^+$-45**, **$[MH+3O]^+$-71**, and **y_7+3O**). As the internal energy increases the proton can then move to the relatively basic modified His residue (His^*) opening charge-directed fragmentation pathways associated with His^* resulting in the second family of fragment ions (**b_5** and **$[MH+3O]^+$-88**). Finally, at high collision energies the internal energy is great enough that the proton can move to the peptide backbone allowing for nonselective charge-directed fragmentations leading to the third family of secondary ions. The onset curves are thus consistent with the proposed fragmentation mechanisms proposed above and with the mobile proton model.

3.3.3 RRKM Modeling of Experimental Data

Parameters giving the best fit to the parent ion survival curves are summarized in Table 3.1. The reaction barrier (E_o), the pre-exponential factor (A), and the activation entropy ($\Delta S^{\ddagger}$) for the dissociation parent ions all increase with increased oxidation, that is in the order: AngII < AngII+O < AngII+3O < AngII+4O. The quantitative kinetic parameters thus confirm that the shift of the survival curves to lower collision energy with increasing oxidation is completely entropy controlled.

Table 3.1. RRKM modeling results of the parent ion survival curves.

$[MH+nO]^+$	*DRVYIHPF*	*DRVY*IHPF*	*DRVYIH*PF*	*DRVY*IH*PF*
M/Z	1046	1062	1110	1126
E_0(eV)	1.14	1.20	1.21	1.24
$\Delta S^{\ddagger}$(cal/mol K)	-25.9	-21.6	-17.0	-15.3
Relative E_0	0	0.06	0.07	0.11
A, s^{-1}	$5.6x10^7$	$4.8x10^8$	$4.8x10^9$	$1.2x10^{10}$
Log (A)	7.7	8.7	9.7	10.1

E_o is the threshold energy, $\Delta S^{\ddagger}$ is the entropy change for the transition state at 450 K, A is the pre-exponential factor at 450 K, 18.1% of each of the kinetic energy was converted to internal energy upon collision and the radiative decay rate was set at 55 s^{-1} for each of the ions.

The fragmentation of each of the parent ions is dominated by a single process, particularly at low energies. For AngII the dominant process is formation of the y_7 ion, for AngII+O it is the b_4+O ion and for AngII+3O it is the (MH+3O)-45 ion. If correct the mechanisms proposed for these processes should therefore be consistent with the observed activation entropies. Consideration of the proposed transition states confirms that the observed activation entropy decreases as expected with the number of free rotations lost on transition state formation. AngII with an activation entropy of

-25.9 cal/mol K loses four side chain internal rotations on formation of the transition state for the $\mathbf{y_7}$ fragmentation pathway (Scheme 3.1a), as indicated in Scheme 3.5a (black arrows indicate internal rotations lost). In comparison, the $\mathbf{b_4}$**+O** dissociation pathway of AngII+O has a more positive entropic value (-21.6 cal/mol K, Table X.1) associated with a transition state characterized by the loss of three side chain internal rotations (black arrows in Scheme 3.5b) and one backbone rotation (red arrow in Scheme 3.5b). Although four total rotations are lost, the backbone rotation is a sterically hindered internal rotation making the entropic effect more positive in relation to the four free rotations lost upon formation of the transition state of the $\mathbf{y_7}$ mechanism. AngII+3O has the most positive activation entropy, -17.0 cal/mol K (Table 3.1), and formation of the transition state leading to the $\mathbf{[MH+3O]^+}$**-45** is associated with the loss of three amide bond rotations of the His^* side chain (blue arrows in Scheme 3.5c). The further positive shift in entropy, in relation to the transition states for the $\mathbf{y_7}$ and $\mathbf{b_4}$**+O** mechanisms, highlights the double bond characteristics of the peptide-like amide bonds of the His^* side chain. Delocalization of the electron cloud between the amide and carbonyl bonds does not allow for free rotation.

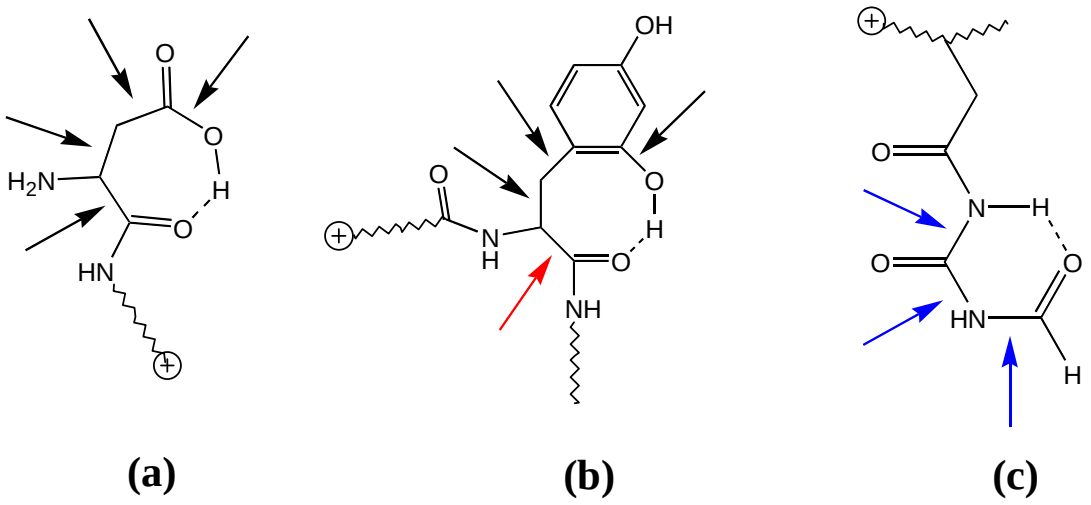

Scheme 3.5

The entropies of activation are also pertinent to the question raised above concerning the possibility of a salt bridge mechanism (Scheme 3.1b) for $\mathbf{y_7}$ fragmentation. The salt bridge mechanism involves closing two rings simultaneously which should result in a much greater negative shift in entropy, particularly in comparison to the entropy of the $\mathbf{b_4}$ mechanism than is observed.

3.3.4 Molecular Dynamics

Molecular dynamics experiments were done to probe how the observed fragmentation mechanisms follow from the intramolecular interactions for AngII and the primary oxidation products AngII+O and AngII+3O prior to dissociation. Figures 3.3 and 3.4 provide examples of results for 100 ps calculations of AngII+O and AngII+3O respectively. Unmodified angiotensin II was first run to understand the interactions taking place between the protonated guanidine functionallity of the Arg^+

residue and the rest of the peptide. It was apparent in all cases where the ionizing proton was placed on Arginine – $DR^{+}VYIHPF$, $DR^{+}VY^{*}IHPF$, and $DR^{+}VYIH^{*}PF$ – that the peptide delocalizes the charge by wrapping itself around the side chain of the protonated Arg^{+} residue forming multiple hydrogen bonds between the amide hydrogen atoms of Arg^{+} and carbonyl oxygen atoms of the peptide backbone (Figure 3.3). Scheme 3.6 highlights the observed hydrogen bonding interactions for the molecular dynamics calculation results of AngII+O shown in Figure 3.3. Graphs of the bond distance (Å) vs. time (ps) for each of the hydrogen bonds of interest (Figure 3.3) show that the bonds form very quickly and are very stable over the length of the experiment. At no point during the length of the experiment was a salt bridge interaction observed between the protonated Arg^{+} residue and aspartic acid side chain. The molecular dynamics results highlight the ability of peptides having the same number of ionizing protons as basic sites to sequester the charge making the lowest energy dissociation pathways the charge-remote fragmentation channels.

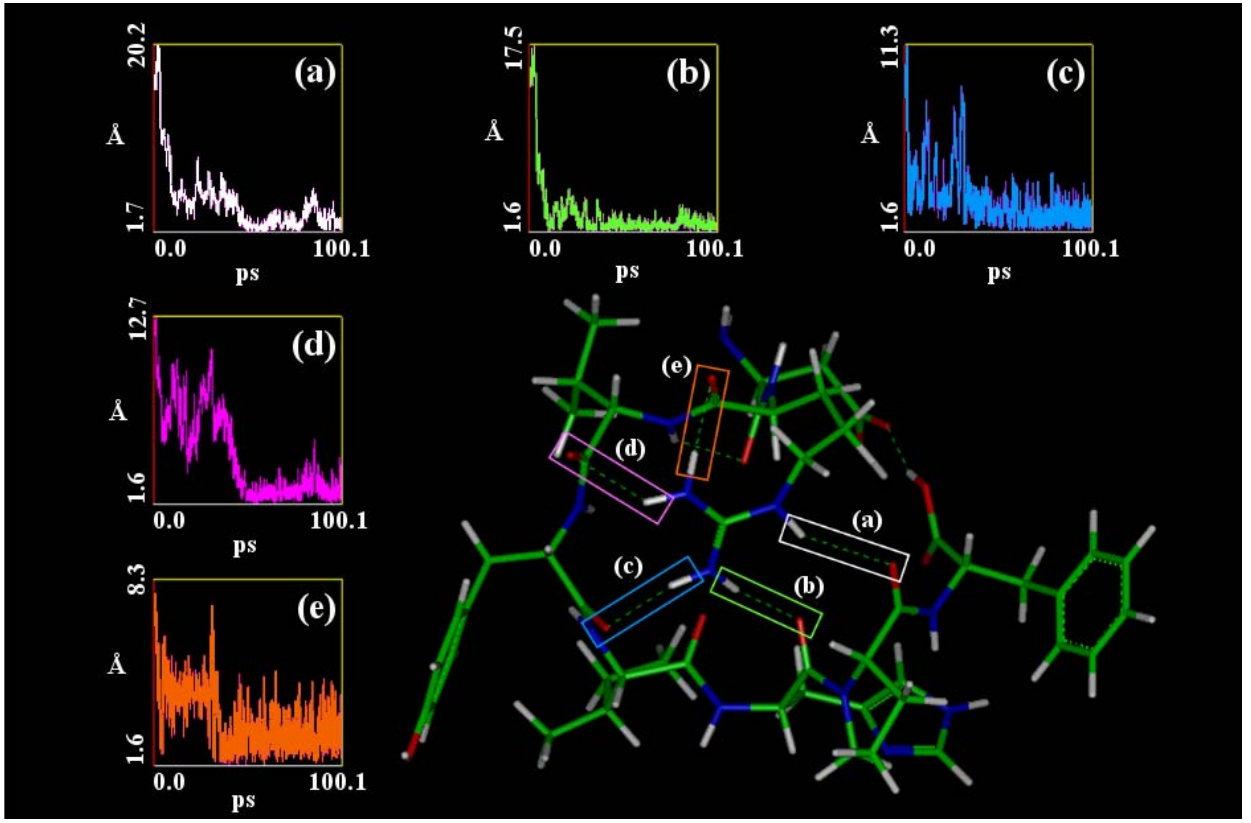

Figure 3.3. Molecular dynamics results for AngII+O ($DR^{+}VY^{*}IHPF$) highlighting the delocalization of charge resulting from protonation of the Arg residue. Hydrogen bonds formed between amide hydrogen atoms of the protonated Arg residue and carbonyl oxygen atoms of the peptide backbone and the plots of bond distance (Å) as a function of time (ps) associated with each hydrogen bond are labeled (a), (b), (c), (d) and (e).

Scheme 3.6

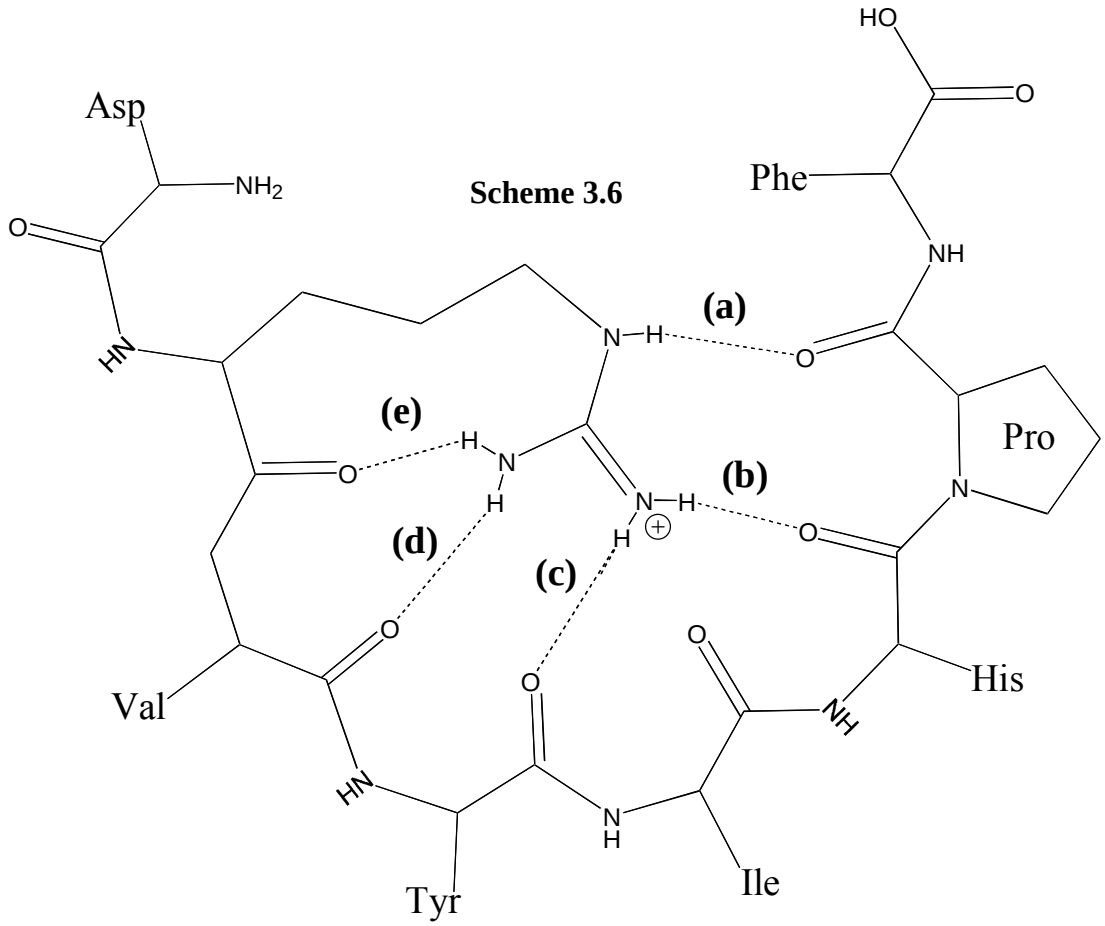

Molecular dynamics was also used to monitor the parent ion conformations for the proposed charge-remote fragmentation mechanisms shown in Schemes 3.2 and 3.3. The molecular dynamics results for $DR^{+}VY^{*}IHPF$ show strong interaction between the hydrogen atom of the additional hydroxyl group in the 2-position and the carbonyl oxygen atom of the peptide backbone between the Tyr^{*} and Ile residues (Figure 3.4). This interaction competes successfully with hydrogen bonding between protonated Arg and that same backbone carbonyl. The minimum hydrogen bonding distance measured during the length of the experiment was 1.92 Å and hydrogen bond formed multiple times during the first 60 ps of the dynamics

calculation. This intramolecular hydrogen bond is necessary for the formation of the **b_4+O** fragment ion via the proposed mechanism in Scheme 3.2.

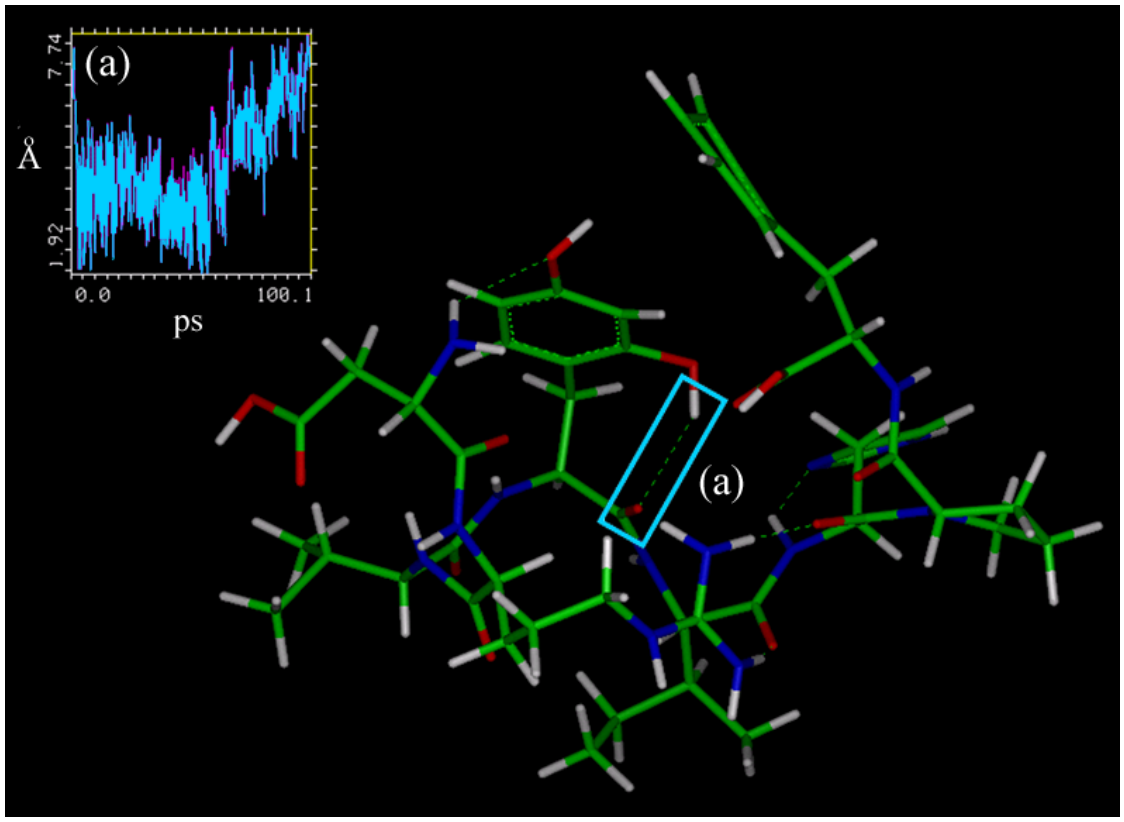

Figure 3.4. Molecular dynamics results for the AngII+O oxidation product ($DR^{+}VY^{*}IHPF$) highlighting the hydrogen bond formed between the carbonyl oxygen atom of the peptide backbone C-term to Tyr^{*} and the hydroxyl hydrogen atom of the modified Tyr residue. This hydrogen bond and the plot of bond distance (Å) as a function of time (ps) associated with this interaction are labeled (a).

Probing parent ion conformations of the AngII+3O oxidation product with the ionizing proton on the Arg residue – $DR^{+}VYIH^{*}PF$ – showed very strong interactions within the modified His^{*} residue itself. Two primary side chain conformations emerged in the molecular dynamics experiment. The first conformation involved hydrogen bonding between the hydrogen atom of the first amide group from the peptide backbone and the oxygen atom of the formyl end group (Figure 3.5). The plot of bond distance (Å) vs. time (ps) shows a very strong hydrogen bond that once formed is locked in for the length of the experiment only occasionally stretching beyond 2.5 Å. This strong interaction drives the low energy charge-remote **$[MH+3O]^{+}$-45** mechanism shown in Scheme 3.3. Secondly, a similar strong hydrogen bond associated with the formation of the **$[MH+3O]^{+}$-71** ion (Scheme 3.3) can form between the hydrogen atom of the second amide group and the oxygen atom of the first carbonyl relative to the peptide backbone (Figure 3.6). When formed, this interaction has a minimum bonding distance of 1.72 Å and is consistently between 2.0 and 2.5 Å over the length of the calculation.

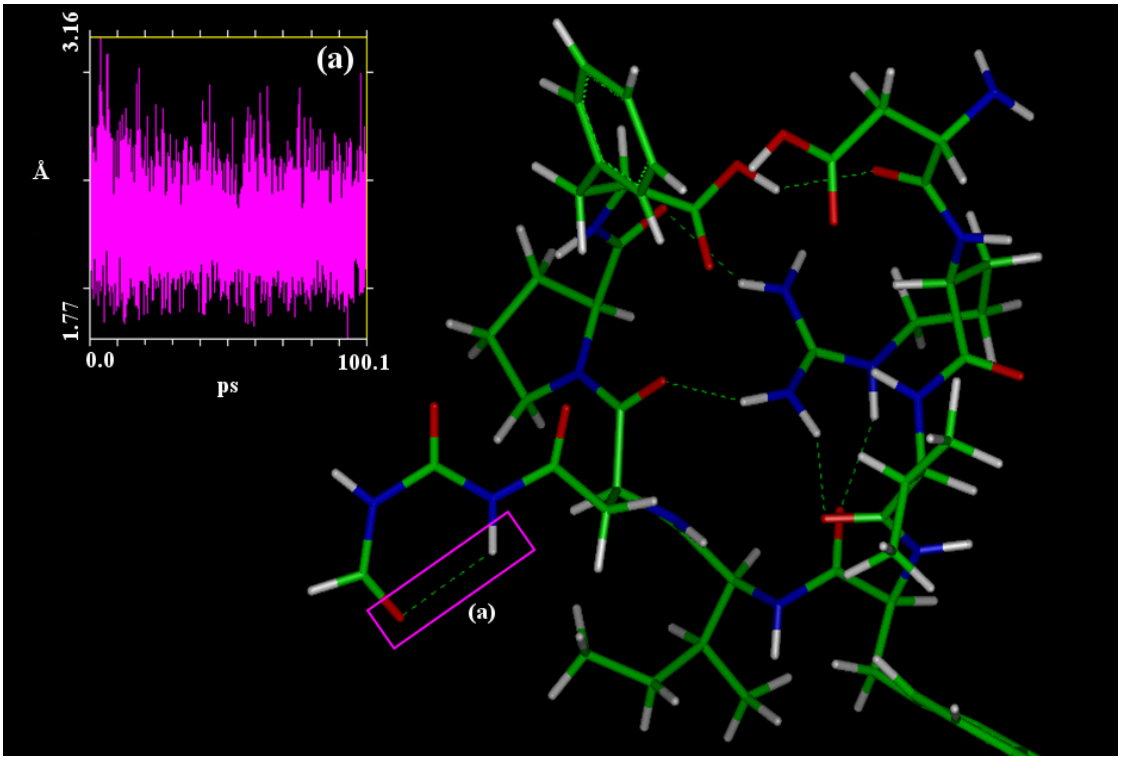

Figure 3.5. Molecular dynamics results for the AngII+3O oxidation product ($DR^{+}VYIH^{*}PF$) highlighting the hydrogen bond formed between the third carbonyl oxygen atom and the first amide hydrogen atom of the modified His residue. This hydrogen bond and the plot of bond distance (Å) as a function of time (ps) associated with this interaction are labeled (a).

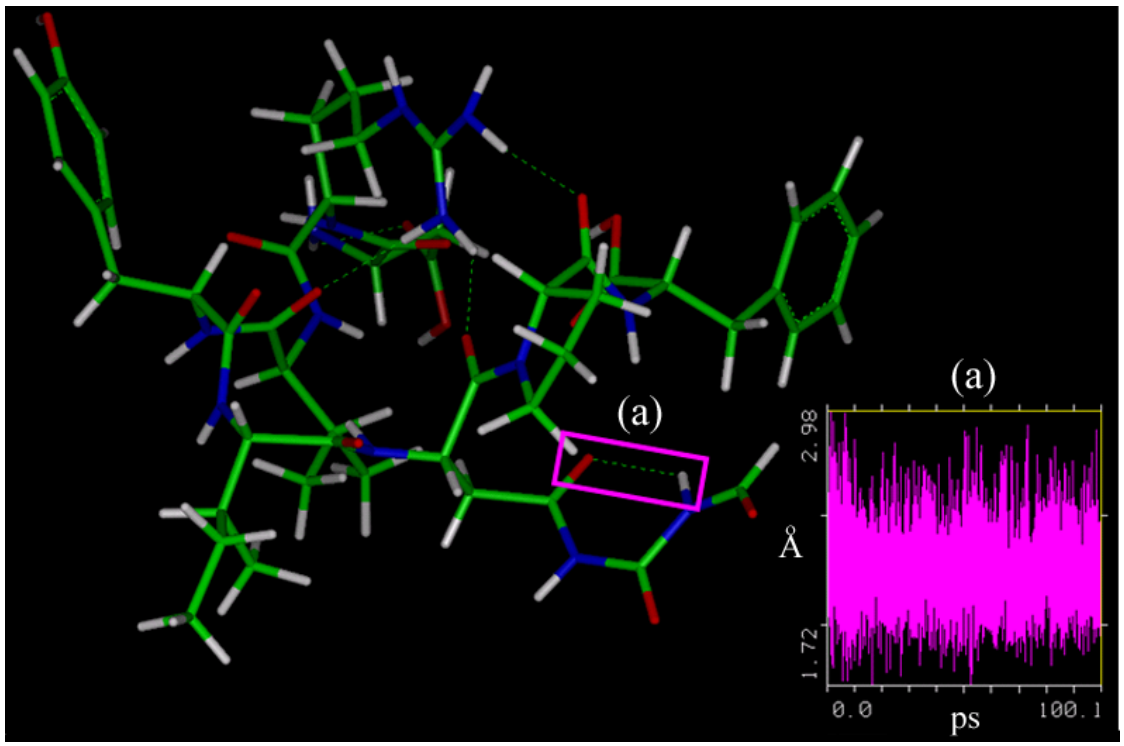

Figure 3.6. Molecular dynamics results for the AngII+3O oxidation product ($DR^{+}VYIH^{*}PF$) highlighting the hydrogen bond formed between the first carbonyl oxygen atom and the second amide hydrogen atom of the modified His residue. This hydrogen bond and the plot of bond distance (Å) as a function of time (ps) associated with this interaction are labeled (a).

Finally, molecular dynamics calculations were done to understand steric limitations of the proposed charge-directed fragmentation processes of AngII+3O ($DRVYIH^{*+}PF$) leading to the $\mathbf{b_5}$ and $\mathbf{[MH+3O]^{+}}$**-88** fragment ions (Sheme 3.4). It should be noted that for these calculations the ionizing proton was not able to be added to the modified His residue due to software limitations, therefore, the peptides were left neutral. A decrease in structural organization for the conformations sampled for unprotonated $DRVYIH^{*}PF$ were observed in comparison to the highly folded

structures required to delocalize the charge for cases with a proton placed on the Arg residue ($DR^{+}VYIHPF$, $DR^{+}VY^{*}IHPF$, and $DR^{+}VYIH^{*}PF$). Results for unprotonated AngII+3O show the formation of a hydrogen bond between the amide nitrogen atom of the peptide backbone between Ile and His^{*} and the hydrogen atom of the first amide group of the modified His side chain relative to the peptide backbone. This hydrogen bonding interaction occurs multiple times over the 100 ps calculation with a minimum distance of 2.16 Å (Figure 3.7). This interaction suggests that if a proton was placed on the first carbonyl His*, the proton would be conformationally caplable of being transfered to the backbone amide nitrogen resulting in cleavage of the peptide bond and driving the proposed charge-directed $\mathbf{b_5}$ mechanism (Sheme 3.4). Additionally, the required interaction for the proposed $\mathbf{[MH+3O]^{+}}$**-88** mechanism between the carbonyl oxygen atom of the backbone C-terminal to His* and the first carbonyl carbon atom of the modified His residue relative to the peptide backbone was observed during molecular dynamics calculations with a minimum distance of 2.48 Å (Figure 3.8). It is suggested that each of these interactions would be enhanced if the proton was able to be placed on the modified His residue.

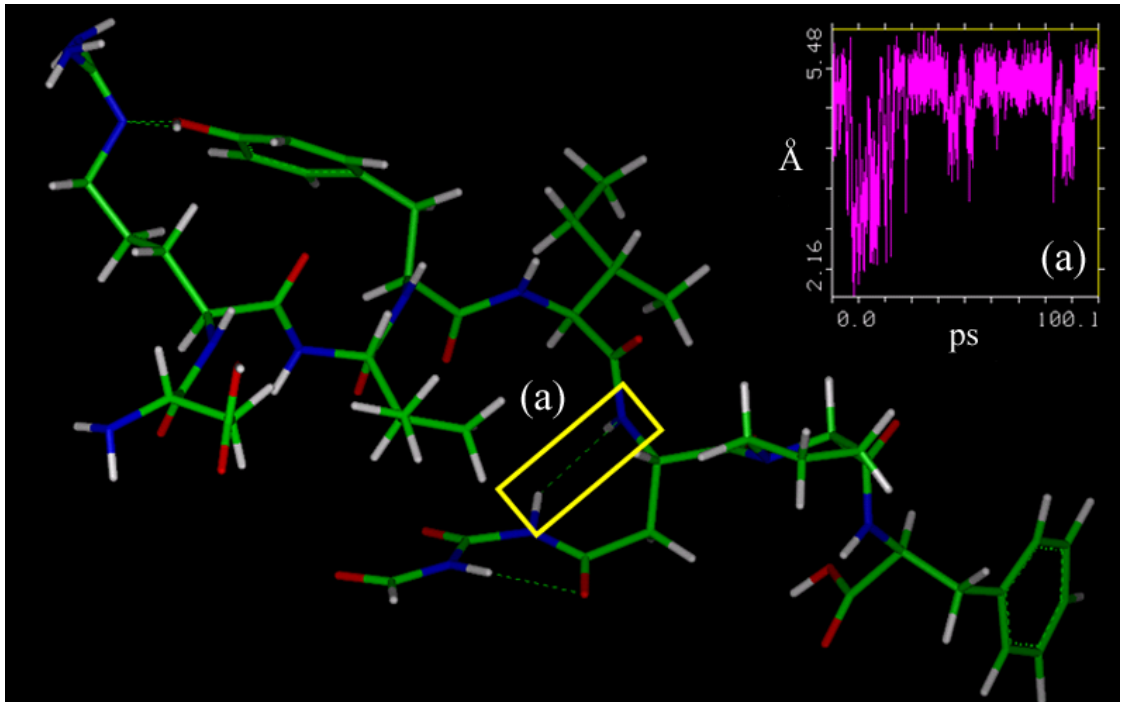

Figure 3.7. Molecular dynamics results for the AngII+3O (DRVYIH*PF) oxidation product highlighting the interaction between the amide nitrogen atom of the backbone N-terminal to the modified His residue and the hydrogen atom of the first amide group of the His* side chain. This hydrogen bond and the plot of bond distance (Å) as a function of time (ps) are labeled (a).

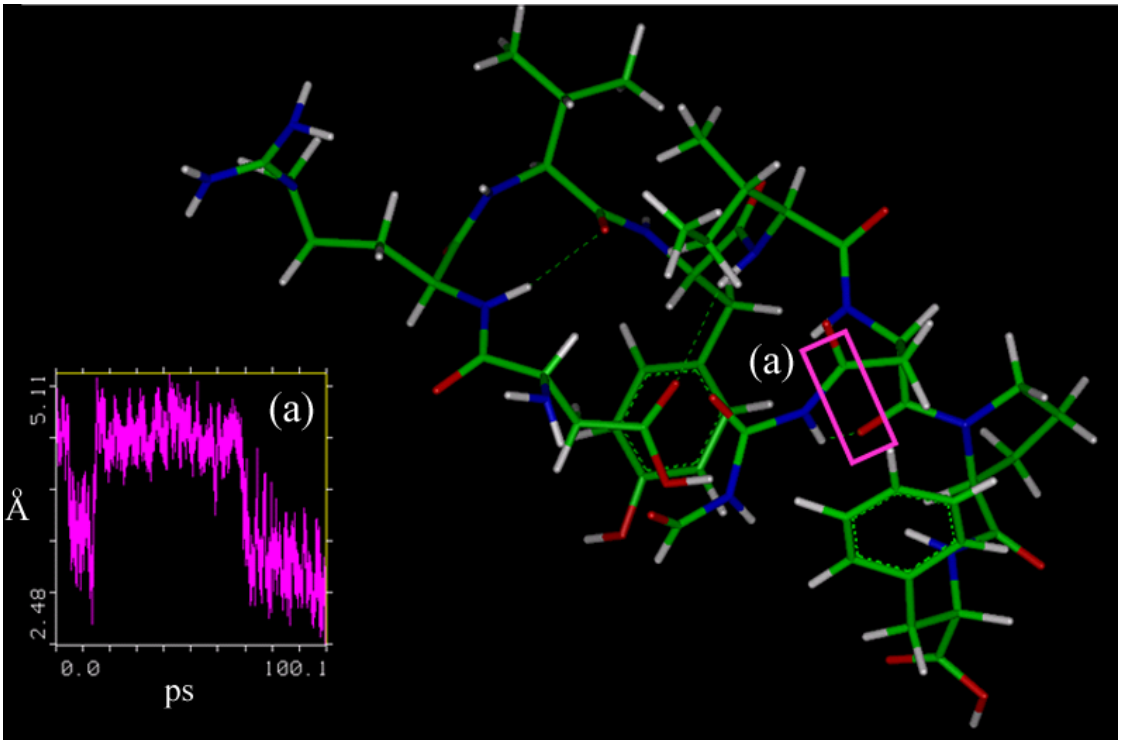

Figure 3.8. Molecular dynamics results for the AngII+3O (DRVYIH*PF) oxidation product highlighting the interaction between the carbonyl oxygen atom C-terminal to the modified His residue and the carbon atom of the first carbonyl of the His* residue. This interaction and the plot of bond distance (Å) as a function of time (ps) are labeled (a).

3.4 Conclusions

Oxidation of Tyr and His in angiotensin II, due to exposure to ozone, leads to new, low-energy selective fragmentation channels in MS/MS experiments. A detailed approach using energy-resolved SID FT-ICR MS experiments, RRKM modeling, and molecular dynamics calculations was used to characterize the selective fragmentation channels for AngII ($DR^{+}VYIHPF$) and the resulting primary ozonolysis

products AngII+O ($DR^{+}VY^{*}IHPF$), AngII+3O ($DR^{+}VYIH^{*}PF$) and AngII+4O ($DR^{+}VY^{*}IH^{*}PF$). This strategy was used to shed light on the mechanistic details of the unimolecular gas phase dissociation reactions of each of these singly charged species. Oxidation of Tyr opens a new low-energy charge-remote fragmentation pathway (**b_4+O**). The present results show that fragmentation to be consistent with oxidation of Tyr in the 2-position. Both the RRKM and molecular dynamics results support a mechanism for this fragmentation analogous to the acidic attack on the peptide backbone that takes place within Asp containing peptides with no "mobile" protons. Ozonolysis of His leads to a series of low-energy charge-remote dissociation channels (**$[MH+3O]^{+}$-45** and **$[MH+3O]^{+}$-71**) followed by charge-directed fragmentation pathways at slightly higher energies (**b_5** and **$[MH+3O]^{+}$-88**). Both the RRKM and molecular dynamics results support mechanisms for the charge-remote dissociations originating with the formation of hydrogen bonds between amide hydrogens and carbonyl oxygens in the oxidized side chain. The results are thus consistent with the structure of oxidized histidine proposed in earlier studies. Note that the dominance of charge-remote pathways for all the oxidation products is consistent with the "mobile" proton model since the proton is sequestered by the Arg side chain in the oxidation products as well as in AngII itself [65, 66]. The AngII+4O adduct, containing both Tyr^{*} and His^{*}, shows gas phase dissociation characteristics of both the AngII+O and AngII+3O oxidation products. The energy thresholds for decomposition of the energy-resolved FECs show that the overall stability of the individual parent ions with respect to SID fragmentation decreases with an increase in oxidative stress (AngII>AngII+O>AngII+3O/AngII+4O). RRKM modeling gives reaction barriers and pre-exponential factors that increase with oxidative stress

(AngII<AngII+O<AngII+3O/AngII+4O). Thus the threshold behavior is controlled by the pre-exponential factors which in turn depend on the entropies of activation. These results indicate that the primary reaction channels require significant conformational rearrangement in the formation of the transition states for each reaction pathway. Molecular dynamics calculations suggest reaction pathways involving hydrogen-bonded, closed-ring structures accounting for the importance of entropy in controlling the unimolecular kinetics of decomposition. Comparison between results for cleavage C-terminal to aspartic acid ($\mathbf{y_7}$) in unmodified angiotensin II and the selective charge-remote $\mathbf{b_4}$ dissociation pathway involving oxidized Tyr* (AngII+O) suggests intramolecular salt bridge interactions are unnecessary for charge-remote fragmentation involving acidic amino acid residues.

3.5 References

1. Bosson, J.; Barath, S.; Pourazar, J.; Behndig, A. F.; Sandstroem, T.; Blomberg, A.; Aedelroth, E. Diesel Exhaust Exposure Enhances the Ozone-Induced Airway Inflammation in Healthy Humans. *European Respiratory Journal.* **2008**, *31*, 1234-1240.

2. Iriti, M.; Faoro, F. Oxidative Stress, the Paradigm of Ozone Toxicity in Plants and Animals. *Water, Air, & Soil Pollution.* **2008**, *187*, 285-301.

3. Tzortzakis, N.; Singleton, I.; Barnes, J. Impact of Low-Level Atmospheric Ozone-Enrichment on Black Spot and Anthracnose Rot of Tomato Fruit. *Postharvest Biol. Technol.* **2008**, *47*, 1-9.

4. Burkey, K. O.; Booker, F. L.; Pursley, W. A.; Heagle, A. S. Elevated Carbon Dioxide and Ozone Effects on Peanut: II. Seed Yield and Quality. *Crop Sci.* **2007**, *47*, 1488-1497.

5. Chen, C.; Arjomandi, M.; Balmes, J.; Tager, I.; Holland, N. Effects of Chronic and Acute Ozone Exposure on Lipid Peroxidation and Antioxidant Capacity in Healthy Young Adults. *Environ. Health Perspect.* **2007**, *115*, 1732-1737.

6. Chuang, K.; Chan, C.; Su, T.; Lee, C.; Tang, C. The Effect of Urban Air Pollution on Inflammation, Oxidative Stress, Coagulation, and Autonomic Dysfunction in Young Adults. *American Journal of Respiratory and Critical Care Medicine.* **2007**, *176*, 370-376.

7. Hollingsworth, J. W.; Maruoka, S.; Li, Z.; Potts, E. N.; Brass, D. M.; Garantziotis, S.; Fong, A.; Foster, W. M.; Schwartz, D. A. Ambient Ozone Primes Pulmonary Innate Immunity in Mice. *Journal of Immunology.* **2007**, *179*, 4367-4375.

8. Leitao, L.; Bethenod, O.; Biolley, J. -. The Impact of Ozone on Juvenile Maize (Zea Mays L.) Plant Photosynthesis: Effects on Vegetative Biomass, Pigmentation, and Carboxylases (PEPc and Rubisco). *Plant Biology (Stuttgart, Germany).* **2007**, *9*, 478-488.

9. Zou, Z.; Liu, Y.; Wu, Y.; Li, Q.; Chen, M.; Sun, H.; Lee, I. Surface-Enhanced Raman Spectra of Oxidation Damage of Fetal Bovine Serum by Ozone. *Guangpuxue Yu Guangpu Fenxi.* **2007**, *27*, 1140-1142.

10. Chen, C.; Arjomandi, M.; Qin, H.; Balmes, J.; Tager, I.; Holland, N. Cytogenetic Damage in Buccal Epithelia and Peripheral Lymphocytes of Young Healthy Individuals Exposed to Ozone. *Mutagenesis.* **2006**, *21*, 131-137.

11. Cataldo, F. On the Action of Ozone on Proteins. *Polym. Degrad. Stab.* **2003**, *82*, 105-114.

12. Ashmore, M. R.; Marshall, F. M. Ozone Impacts on Agriculture: An Issue of Global Concern. *Adv. Bot. Res.* **1999**, *29*, 31-52.

13. Dell'era, R.; Brambilla, E.; Ballarin-Denti, A. Ozone and Air Particulate Measurements in Mountain Forest Sites. *Chemosphere.* **1998**, *36*, 1083-1088.

14. Mudd, J. B.; Dawson, P. J.; Tseng, S.; Liu, F. Reaction of Ozone with Protein Tryptophans: Band III, Serum Albumin, and Cytochrome c. *Arch. Biochem. Biophys.* **1997**, *338*, 143-149.

15. Berlett, B. S.; Levine, R. L.; Stadtman, E. R. Comparison of the Effects of Ozone on the Modification of Amino Acid Residues in Glutamine Synthetase and Bovine Serum Albumin. *J. Biol. Chem.* **1996**, *271*, 4177-4182.

16. Mudd, J. B.; Dawson, P. J.; Adams, J. R.; Wingo, J.; Santrock, J. Reaction of Ozone with Enzymes of Erythrocyte Membranes. *Arch. Biochem. Biophys.* **1996**, *335*, 145-151.

17. Uppu, R. M.; Cueto, R.; Squadrito, G. L.; Pryor, W. A. What does Ozone React with at the air/lung Interface? Model Studies using Human Red Blood Cell Membranes. *Arch. Biochem. Biophys.* **1995**, *319*, 257-266.

18. Weisel, C. P.; Cody, R. P.; Lioy, P. J. Relationship between Summertime Ambient Ozone Levels and Emergency Department Visits for Asthma in Central New Jersey. *Environ. Health Perspect.* **1995**, *103 Suppl 2*, 97-102.

19. Schmut, O.; Gruber, E.; el-Shabrawi, Y.; Faulborn, J. Destruction of Human Tear Proteins by Ozone. *Free Radic. Biol. Med.* **1994**, *17*, 165-169.

20. Uppu, R. M.; Pryor, W. A. The Reactions of Ozone with Proteins and Unsaturated Fatty Acids in Reverse Micelles. *Chem. Res. Toxicol.* **1994**, *7*, 47-55.

21. O'Neill, C. A.; van der Vliet, A.; Hu, M. L.; Kaur, H.; Cross, C. E.; Louie, S.; Halliwell, B. Oxidation of Biologic Molecules by Ozone: The Effect of pH. *J. Lab. Clin. Med.* **1993**, *122*, 497-505.

22. Pryor, W. A.; Uppu, R. M. A Kinetic Model for the Competitive Reactions of Ozone with Amino Acid Residues in Proteins in Reverse Micelles. *J. Biol. Chem.* **1993**, *268*, 3120-3126.

23. Kanofsky, J. R.; Sima, P. Singlet Oxygen Production from the Reactions of Ozone with Biological Molecules. *J. Biol. Chem.* **1991**, *266*, 9039-9042.

24. Knight, K. L.; Mudd, J. B. The Reaction of Ozone with Glyceraldehyde-3-Phosphate Dehydrogenase. *Arch. Biochem. Biophys.* **1984**, *229*, 259-269.

25. Menzel, D. B. Ozone: An Overview of its Toxicity in Man and Animals. *J. Toxicol. Environ. Health.* **1984**, *13*, 183-204.

26. Dooley, M. M.; Mudd, J. B. Reaction of Ozone with Lysozyme Under Different Exposure Conditions. *Arch. Biochem. Biophys.* **1982**, *218*, 459-471.

27. Kuroda, M.; Sakiyama, F.; Narita, K. Oxidation of Tryptophan in Lysozyme by Ozone in Aqueous Solution. *Journal of Biochemistry (Tokyo, Japan).* **1975**, *78*, 641-651.

28. Kotiaho, T.; Eberlin, M. N.; Vainiotalo, P.; Kostiainen, R. Electrospray Mass and Tandem Mass Spectrometry Identification of Ozone Oxidation Products of Amino Acids and Small Peptides. *J. Am. Soc. Mass Spectrom.* **2000**, *11*, 526-535.

29. Pryor, W. A.; Giamalva, D. H.; Church, D. F. Kinetics of Ozonation. 2. Amino Acids and Model Compounds in Water and Comparisons to Rates in Nonpolar Solvents. *J. Am. Chem. Soc.* **1984**, *106*, 7094-7100.

30. Mudd, J. B.; Leavitt, R.; Ongun, A.; McManus, T. T. Reaction of Ozone with Amino Acids and Proteins. *Atmospheric Environment (1967-1989).* **1969**, *3*, 669-682.

31. Previero, A.; Scoffone, E.; Benassi, C. A.; Pajetta, P. Investigations on the Structure of Proteins. XI. Modification of the Tryptophan Residue in a Peptide Chain. *Gazzetta Chimica Italiana.* **1963**, *93*, 849-858.

32. Previero, A.; Scoffone, E.; Pajetta, P.; Benassi, C. A. The Structure of Proteins. X. the Behavior of Amino Acids in the Presence of Ozone. *Gazzetta Chimica Italiana.* **1963**, *93*, 841-848.

33. Lloyd, J. A.; Spraggins, J. M.; Johnston, M. V.; Laskin, J. Peptide Ozonolysis: Product Structures and Relative Reactivities for Oxidation of Tyrosine and Histidine Residues. *J. Am. Soc. Mass Spectrom.* **2006**, *17*, 1289-1298.

34. Summerfield, S. G.; Gaskell, S. J. Fragmentation Efficiencies of Peptide Ions Following Low Energy Collisional Activation. *International Journal of Mass Spectrometry and Ion Processes.* **1997**, *165/166*, 509-521.

35. Kamal, J. K. A.; Benchaar, S. A.; Takamoto, K.; Reisler, E.; Chance, M. R. Three-Dimensional Structure of Cofilin Bound to Monomeric Actin Derived by Structural Mass Spectrometry Data. *Proc. Natl. Acad. Sci. U. S. A.* **2007**, *104*, 7910-7915.

36. Kiselar, J. G.; Mahaffy, R.; Pollard, T. D.; Almo, S. C.; Chance, M. R. Visualizing Arp2/3 Complex Activation Mediated by Binding of ATP and WASp using Structural Mass Spectrometry. *Proc. Natl. Acad. Sci. U. S. A.* **2007**, *104*, 1552-1557, S1552/1-S1552/2.

37. Takamoto, K.; Chance, M. R. Radiolytic Protein Footprinting with Mass Spectrometry to Probe the Structure of Macromolecular Complexes. *Annu. Rev. Biophys. Biomol. Struct.* **2006**, *35*, 251-276.

38. Aye, T. T.; Low, T. Y.; Sze, S. K. Nanosecond Laser-Induced Photochemical Oxidation Method for Protein Surface Mapping with Mass Spectrometry. *Anal. Chem.* **2005**, *77*, 5814-5822.

39. Guan, J.; Chance, M. R. Structural Proteomics of Macromolecular Assemblies using Oxidative Footprinting and Mass Spectrometry. *Trends Biochem. Sci.* **2005**, *30*, 583-592.

40. Hambly, D. M.; Gross, M. L. Laser Flash Photolysis of Hydrogen Peroxide to Oxidize Protein Solvent-Accessible Residues on the Microsecond Timescale. *J. Am. Soc. Mass Spectrom.* **2005**, *16*, 2057-2063.

41. Sharp, J. S.; Guo, J.; Uchiki, T.; Xu, Y.; Dealwis, C.; Hettich, R. L. Photochemical Surface Mapping of C14S-Sml1p for Constrained Computational Modeling of Protein Structure. *Anal. Biochem.* **2005**, *340*, 201-212.

42. Guan, J.; Almo, S. C.; Chance, M. R. Synchrotron Radiolysis and Mass Spectrometry: A New Approach to Research on the Actin Cytoskeleton. *Acc. Chem. Res.* **2004**, *37*, 221-229.

43. Sharp, J. S.; Becker, J. M.; Hettich, R. L. Analysis of Protein Solvent Accessible Surfaces by Photochemical Oxidation and Mass Spectrometry. *Anal. Chem.* **2004**, *76*, 672-683.

44. Kiselar, J. G.; Maleknia, S. D.; Sullivan, M.; Downard, K. M.; Chance, M. R. Hydroxyl Radical Probe of Protein Surfaces using Synchrotron X-Ray Radiolysis and Mass Spectrometry. *Int. J. Radiat. Biol.* **2002**, *78*, 101-114.

45. Maleknia, S. D.; Downard, K. M. Radical Approaches to Probe Protein Structure, Folding, and Interactions by Mass Spectrometry. *Mass Spectrom. Rev.* **2002**, *20*, 388-401.

46. Maleknia, S. D.; Kiselar, J. G.; Downard, K. M. Hydroxyl Radical Probe of the Surface of Lysozyme by Synchrotron Radiolysis and Mass Spectrometry. *Rapid Commun. Mass Spectrom.* **2002**, *16*, 53-61.

47. Chance, M. R. Unfolding of Apomyoglobin Examined by Synchrotron Footprinting. *Biochem. Biophys. Res. Commun.* **2001**, *287*, 614-621.

48. Laskin, J. Energetics and Dynamics of Peptide Fragmentation from Multiple-Collision Activation and Surface-Induced Dissociation Studies. *European Journal of Mass Spectrometry.* **2004**, *10*, 259-267.

49. Laskin, J.; Yang, Z.; Chu, I. K. Energetics and Dynamics of Electron Transfer and Proton Transfer in Dissociation of MetalIII(Salen)-Peptide Complexes in the Gas Phase. *J. Am. Chem. Soc.* **2008**, *130*, 3218-3230.

50. Yang, Z.; Lam, C.; Chu, I. K.; Laskin, J. The Effect of the Secondary Structure on Dissociation of Peptide Radical Cations: Fragmentation of Angiotensin III and its Analogues. *J Phys Chem B.* **2008**, *112*, 12468-12478.

51. Lioe, H.; Laskin, J.; Reid, G. E.; O'Hair, R. A. J. Energetics and Dynamics of the Fragmentation Reactions of Protonated Peptides Containing Methionine Sulfoxide Or Aspartic Acid Via Energy- and Time-Resolved Surface Induced Dissociation. *Journal of Physical Chemistry A.* **2007**, *111*, 10580-10588.

52. Laskin, J. Energetics and Dynamics of Fragmentation of Protonated Leucine Enkephalin from Time- and Energy-Resolved Surface-Induced Dissociation Studies. *Journal of Physical Chemistry A.* **2006**, *110*, 8554-8562.

53. Laskin, J.; Bailey, T. H.; Futrell, J. H. Mechanisms of Peptide Fragmentation from Time- and Energy-Resolved Surface-Induced Dissociation Studies: Dissociation of Angiotensin Analogs. *International Journal of Mass Spectrometry.* **2006**, *249/250*, 462-472.

54. Laskin, J. Energetics and Dynamics of Peptide Fragmentation from Multiple-Collision Activation and Surface-Induced Dissociation Studies. *European Journal of Mass Spectrometry.* **2004**, *10*, 259-267.

55. Laskin, J.; Bailey, T. H.; Futrell, J. H. Fragmentation Energetics for Angiotensin II and its Analogs from Time- and Energy-Resolved Surface-Induced Dissociation Studies. *International Journal of Mass Spectrometry.* **2004**, *234*, 89-99.

56. Bailey, T. H.; Laskin, J.; Futrell, J. H. Energetics of Selective Cleavage at Acidic Residues Studied by Time- and Energy-Resolved Surface-Induced Dissociation in FT-ICR MS. *International Journal of Mass Spectrometry.* **2003**, *222*, 313-327.

57. Laskin, J.; Bailey, T. H.; Futrell, J. H. Shattering of Peptide Ions on Self-Assembled Monolayer Surfaces. *J. Am. Chem. Soc.* **2003**, *125*, 1625-1632.

58. Laskin, J.; Futrell, J. H. Surface-Induced Dissociation of Peptide Ions: Kinetics and Dynamics. *J. Am. Soc. Mass Spectrom.* **2003**, *14*, 1340-1347.

59. Laskin, J.; Bailey, T. H.; Denisov, E. V.; Futrell, J. H. On the Relative Stability of Singly Protonated Des-Arg1- and Des-Arg9-Bradykinins. *Journal of Physical Chemistry A.* **2002**, *106*, 9832-9836.

60. Shaffer, S. A.; Tang, K.; Anderson, G. A.; Prior, D. C.; Udseth, H. R.; Smith, R. D. A Novel Ion Funnel for Focusing Ions at Elevated Pressure using Electrospray Ionization Mass Spectrometry. *Rapid Communications in Mass Spectrometry.* **1997**, *11*, 1813-1817.

61. Laskin, J.; Denisov, E. V.; Shukla, A. K.; Barlow, S. E.; Futrell, J. H. Surface-Induced Dissociation in a Fourier Transform Ion Cyclotron Resonance Mass Spectrometer: Instrument Design and Evaluation. *Anal. Chem.* **2002**, *74*, 3255-3261.

62. Laskin, J.; Byrd, M.; Futrell, J. Internal Energy Distributions Resulting from Sustained Off-Resonance Excitation in FTMS. I. Fragmentation of the Bromobenzene Radical Cation. *International Journal of Mass Spectrometry.* **2000**, *195/196*, 285-302.

63. Laskin, J.; Futrell, J. Internal Energy Distributions Resulting from Sustained Off-Resonance Excitation in Fourier Transform Ion Cyclotron Resonance Mass Spectrometry. II. Fragmentation of the 1-Bromonaphthalene Radical Cation. *Journal of Physical Chemistry A.* **2000**, *104*, 5484-5494.

64. Derrick, P. J.; Lloyd, P. M.; Christie, J. R. Physical Chemistry of Ion Reactions. *Advances in Mass Spectrometry.* **1995**, *13*, 23-52.

65. Tsaprailis, G.; Somogyi, A.; Nikolaev, E. N.; Wysocki, V. H. Refining the Model for Selective Cleavage at Acidic Residues in Arginine-Containing Protonated Peptides. *International Journal of Mass Spectrometry.* **2000**, *195/196*, 467-479.

66. Tsaprailis, G.; Nair, H.; Somogyi, A.; Wysocki, V. H.; Zhong, W.; Futrell, J. H.; Summerfield, S. G.; Gaskell, S. J. Influence of Secondary Structure on the Fragmentation of Protonated Peptides. *J. Am. Chem. Soc.* **1999**, *121*, 5142-5154.

67. Herrmann, K. A.; Wysocki, V. H.; Vorpagel, E. R. Computational Investigation and Hydrogen/Deuterium Exchange of the Fixed Charge Derivative Tris(2,4,6-Trimethoxyphenyl) Phosphonium: Implications for the Aspartic Acid Cleavage Mechanism. *J. Am. Soc. Mass Spectrom.* **2005**, *16*, 1067-1080.

68. Gu, C.; Tsaprailis, G.; Breci, L.; Wysocki, V. H. Selective Gas-Phase Cleavage at the Peptide Bond C-Terminal to Aspartic Acid in Fixed-Charge Derivatives of Asp-Containing Peptides. *Anal. Chem.* **2000**, *72*, 5804-5813.

69. Lee, S.; Kim, H. S.; Beauchamp, J. L. Salt Bridge Chemistry Applied to Gas-Phase Peptide Sequencing: Selective Fragmentation of Sodiated Gas-Phase Peptide Ions Adjacent to Aspartic Acid Residues. *J. Am. Chem. Soc.* **1998**, *120*, 3188-3195.

70. Summerfield, S. G.; Whiting, A.; Gaskell, S. J. Intra-Ionic Interactions in Electrosprayed Peptide Ions. *International Journal of Mass Spectrometry and Ion Processes.* **1997**, *162*, 149-161.

71. Yu, W.; Vath, J. E.; Huberty, M. C.; Martin, S. A. Identification of the Facile Gas-Phase Cleavage of the Asp-Pro and Asp-Xxx Peptide Bonds in Matrix-Assisted Laser Desorption Time-of-Flight Mass Spectrometry. *Anal. Chem.* **1993**, *65*, 3015-3023.

72. Yalcin, T.; Khouw, C.; Csizmadia, I. G.; Peterson, M. R.; Harrison, A. G. Why are B Ions Stable Species in Peptide Spectra? *J. Am. Soc. Mass Spectrom.* **1995**, *6*, 1165-1174.

73. Dongre, A. R.; Jones, J. L.; Somogyi, A.; Wysocki, V. H. Influence of Peptide Composition, Gas-Phase Basicity, and Chemical Modification on Fragmentation Efficiency: Evidence for the Mobile Proton Model. *J. Am. Chem. Soc.* **1996**, *118*, 8365-8374.

Chapter 4

METAL SULFIDE CLUSTERS: BACKGROUND

4.1 Clusters in the Environment

Environmentally, metal sulfide particles are of particular importance in the speciation and bioavailability of metals in aquatic systems [1,2]. Although there are a number of environmentally significant heavy metals, cadmium has been chosen as a model system for a number of reasons. From the perspective of our collaborators, as will be discussed below, the semiconducting properties of CdS allow for particle size to be extracted from UV/Vis absorption data [3]. For mass spectrometry experiments, the single oxidation state of cadmium (Cd^{2+}) simplifies analysis in comparison to other metals of interest ($Fe^{2+/3+}$ and $Cu^{+/2+}$). Finally, cadmium binds strongly to sulfide thus metal sulfides are likely to play an important role in its speciation [4].

As described by Pearson [5], hard-soft acid-base theory predicts that a "soft" Lewis base, such as sulfide, will strongly bind to "soft" acids including many environmentally significant heavy metals (Cd^{2+}, Zn^{2+}, Hg^{2+}, Pb^{2+}, $Cu^{+/2+}$, Ag^{+} and Au^{+}). With that said, this favorable interaction drives the formation of metal sulfide species in sulfur rich (H_2S, HS^-) aquatic environments when metals are present. Both abiotic and biotic sources have been shown to produce dissolved metal sulfide species in aqueous systems. Some abiotic sources include hydrothermal vents, anoxic waterways and sewage treatment plants. Researchers have suggested that, as

hydrothermal fluids mix with seawater, reduced forms of sulfur are stabilized when bound to metal sulfide clusters at hydrothermal vent sites [6]. In an anaerobic treatment wetland in Montana, high concentrations of dissolved Cd, Zn and Cu in the presence of H_2S were attributed to molecular metal sulfide clusters [7]. Even under oxic conditions, molecular clusters of zinc and copper were shown to persist due to their resistance to oxidation and dissociation in freshwater rivers [8].

In addition to abiotic sources, biomineralization is known to be a significant source of metal sulfide clusters in the environment. Walsh and co-workers found that phytoplankton produce dissolved sulfides in response to toxic metal exposure forming biologically inert metal sulfide species [9]. Sulfate-reducing bacteria have also shown the ability to produce metal sulfide clusters (ZnS) in deposited natural biofilms as a defense against elevated metal concentrations in groundwater and wetland systems [10]. Finally, at the East Pacific Rise mercury resistant extremophiles living in hydrothermal vent fluids were shown to produce HgS as a detoxification mechanism [11].

4.2 Complexes, Clusters and Particles

4.2.1 Definitions

Essential to a discussion of metal sulfide species in aqueous environments is a fundamental understanding of nucleation mechanisms and clarification of the species involved in this process. As illustrated in Figure 4.1, along the continuum from dissolved ions to bulk solid state material there are thought to be a variety of

species classified as dissolved with properties that are unique from either extreme [12]. In the following chapters, a complex is defined as a mononuclear species with a number of ligands bound to a single central metal atom. As established by our collaborators, a cluster is characterized as having multiple metal centers (polynuclear) bound by ligating atoms and is small enough to be considered a molecular species [13]. Finally, nanoparticles have diameters between 1-100 nm and can be described as solid materials [12].

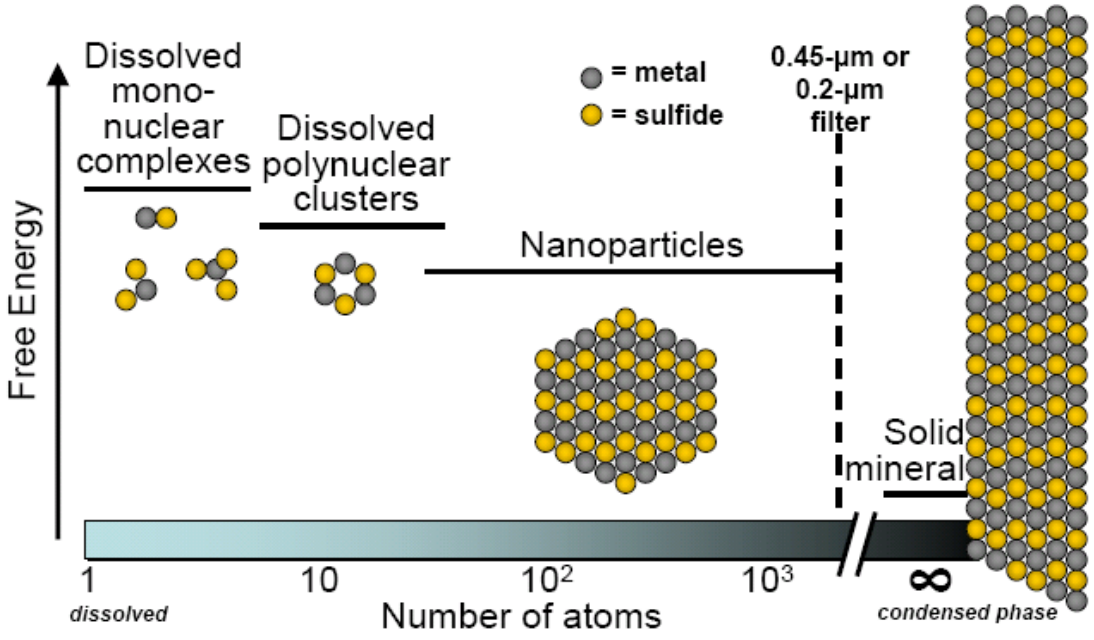

Figure 4.1. Definitions of species along the continuum between dissolved ions and solid state material for metal sulfide systems (Reproduced with permission from Katherine M. Mullaugh [3]).

4.2.2 Nucleation of Metal Sulfides

Although there are a number of classical theories of crystallization, more directly related to the work presented herein is an alternative mechanism based on dissolved molecular metal sulfide clusters [14]. Luther and Rickard suggest that nucleation proceeds through aggregation of small molecular clusters which build up to form larger particles [13]. Molecular modeling has shown the configuration of the first condensed phase to be established by the structure of the dissolved molecular clusters [13]. Experimentally this mechanism has been supported by the observation of persistent molecular clusters in laboratory solutions of CuS [15], FeS in sulfidic seawater [16], and ZnS observed in laboratory samples and field samples taken from the Black Sea [17].

4.3 Multidisciplinary Approach

While much work has been done to understand the formation of metal sulfide particles research is still needed to fully describe this process. The following chapters focus on the use of electrospray ionization FT-ICR mass spectrometry (See Chapter 2) to characterize cadmium sulfide clusters, however, these experiments are part of a larger multidisciplinary project in collaboration with the Luther group in the College of Marine Studies at the University of Delaware. The overall goal was to use a multifaceted approach to describe metal sulfide precipitation using ESI mass spectrometry, UV/VIS spectroscopy, and voltammetry (Figure 4.2). Molecular capping agents, particularly organic thiols, were used to interrupt cluster growth at different stages as described in Chapter 6. Adapted from previous studies on the synthesis of CdS nanoparticles in aqueous solutions [18-21], it was believed that the

capping agents would freeze nucleation events allowing chemical ‘snap-shots’ to be taken by the various analytical techniques. Using UV/VIS spectroscopy and voltammetry, our collaborators worked to elucidate metal:sulfide ratios and particle size of cadmium sulfide reactions [3]. Our task was to simply characterize metal sulfide complexes and clusters using ESI FT-ICR mass spectrometry. However, this project evolved to take advantage of the many capabilities of FT-ICR MS, not only through analysis of solution based reactions, but also moving the experiment into the gas phase (Chapter 7) where the ion-molecule reactions between metal salt clusters and hydrogen sulfide provided an entirely new perspective on this process.

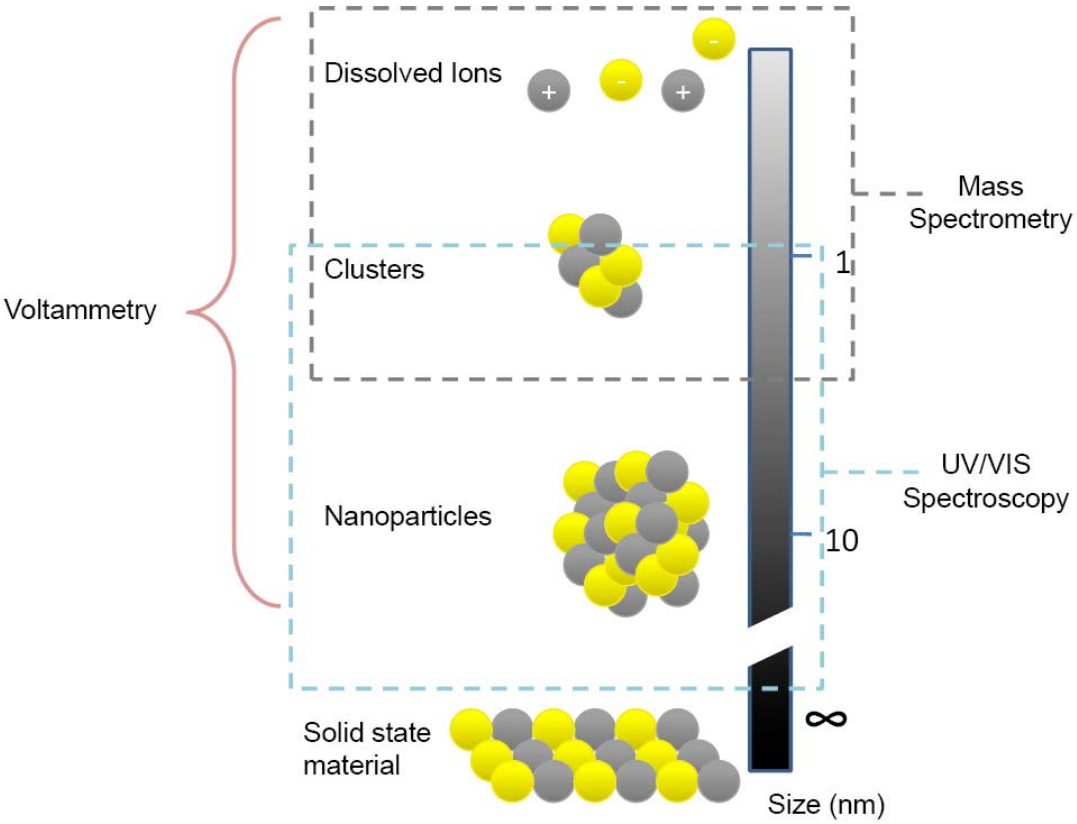

Figure 4.2. The study of metal sulfide precipitation using a multifaceted analytical approach. ESI mass spectrometry is used to characterize metal sulfide complexes and clusters, UV/VIS spectroscopy can determine size of larger clusters and nanoparticles, and voltammetry can determine metal:sulfide ratios (Adapted from Figure 4.1 [3]).

4.4 References

1. Bianchini, A.; Bowles, K. C. Metal Sulfides in Oxygenated Aquatic Systems: Implications for the Biotic Ligand Model. *Comp. Biochem. Physiol., Part C: Toxicol. Pharmacol.* **2002***, 133C*, 51-64.

2. Smith, D. S.; Bell, R. A.; Kramer, J. R. Metal Speciation in Natural Waters with Emphasis on Reduced Sulfur Groups as Strong Metal Binding Sites. *Comp. Biochem. Physiol., Part C: Toxicol. Pharmacol.* **2002***, 133C*, 65-74.

3. Mullaugh, K. M. A Spectroscopic and Votammetric Study of Dissolved Cadmium Sulfide Nanoparticles and Clusters: Formation and Persistence in Aqueous Solution. *Dissertation submitted to the Dept. of Chemistry and Biochemistry, University of Delaware.* **2009**.

4. Rickard, D.; Luther, G. W.,III. Metal Sulfide Complexes and Clusters. *Reviews in Mineralogy & Geochemistry.* **2006***, 61*, 421-504.

5. Pearson, R. G. Hard and Soft Acids and Bases. *J. Am. Chem. Soc.* **1963***, 85*, 3533-3539.

6. Hsu-Kim, H.; Mullaugh, K. M.; Tsang, J. J.; Yucel, M.; Luther, G. W.,III. Formation of Zn- and Fe-Sulfides Near Hydrothermal Vents at the Eastern Lau Spreading Center: Implications for Sulfide Bioavailability to Chemoautotrophs. *Geochem. Trans.* **2008***, 9*, No pp. given.

7. Gammons, C. H.; Frandsen, A. K. Fate and Transport of Metals in H2S-Rich Waters at a Treatment Wetland. *Geochem. Trans.* **2001***, 2*, 1-15.

8. Rozan, T. F.; Lassman, M. E.; Ridge, D. P.; Luther, G. W.,III. Evidence for Iron, Copper and Zinc Complexation as Multinuclear Sulfide Clusters in Oxic Rivers. *Nature (London).* **2000***, 406*, 879-882.

9. Walsh, R. S.; Cutter, G. A.; Dunstan, W. M.; Radford-Knoery, J.; Elder, J. T. The Biogeochemistry of Hydrogen Sulfide: Phytoplankton Production in the Surface Ocean. *Limnol. Oceanogr.* **1994***, 39*, 941-948.

10. Labrenz, M.; Druschel, G. K.; Thomsen-Ebert, T.; Gilbert, B.; Welch, S. A.; Kemner, K. M.; Logan, G. A.; Summons, R. E.; De, S. G.; Bond, P. L.; Lai, B.; Kelly, S. D.; Banfield, J. F. Formation of Sphalerite (ZnS) Deposits in Natural Biofilms of Sulfate-Reducing Bacteria. *Science.* **2000***, 290*, 1744-1747.

11. Crespo-Medina, M.; Chatziefthimiou, A. D.; Bloom, N. S.; Luther, G. W.,III; Wright, D. D.; Reinfelder, J. R.; Vetriani, C.; Barkay, T. Adaptation of Chemosynthetic Microorganisms to Elevated Mercury Concentrations in Deep-Sea Hydrothermal Vents. *Limnol. Oceanogr.* **2009***, 54*, 41-49.

12. Wigginton, N. S.; Haus, K. L.; Hochella, M. F.,Jr. Aquatic Environmental Nanoparticles. *J Environ Monit.* **2007***, 9*, 1306-1316.

13. Luther, G. W.,I.I.I.; Rickard, D. T. Metal Sulfide Cluster Complexes and their Biogeochemical Importance in the Environment. *Journal of Nanoparticle Research.* **2005***, 7*, 389-407.

14. Rickard, D.; Luther, G. W.,III. Metal Sulfide Complexes and Clusters. *Rev. Mineral. Geochem.* **2006***, 61*, 421-504.

15. Luther, G. W.,III; Theberge, S. M.; Rozan, T. F.; Rickard, D.; Rowlands, C. C.; Oldroyd, A. Aqueous Copper Sulfide Clusters as Intermediates during Copper Sulfide Formation. *Environmental Science and Technology.* **2002***, 36*, 394-402.

16. Theberge, S. M.; Luther, G. W.,III. Determination of the Electrochemical Properties of a Soluble Aqueous FeS Species Present in Sulfidic Solutions. *Aquat. Geochem.* **1997***, 3*, 191-211.

17. Luther, G. W.,III; Theberge, S. M.; Rickard, D. T. Evidence for Aqueous Clusters as Intermediates during Zinc Sulfide Formation. *Geochim. Cosmochim. Acta.* **1999***, 63*, 3159-3169.

18. Winter, J. O.; Gomez, N.; Gatzert, S.; Schmidt, C. E.; Korgel, B. A. Variation of Cadmium Sulfide Nanoparticle Size and Photoluminescence Intensity with Altered Aqueous Synthesis Conditions. *Colloids Surf. , A.* **2005***, 254*, 147-157.

19. Murphy, C. J. CdS Nanoclusters Stabilized by Thiolate Ligands: A Mini-Review. *Journal of Cluster Science.* **1996***, 7*, 341-350.

20. Nosaka, Y.; Ohta, N.; Fukuyama, T.; Fujii, N. Size Control of Ultrasmall Cadmium Sulfide Particles in Aqueous Solution by using various Thiols. *J. Colloid Interface Sci.* **1993***, 155*, 23-29.

21. Swayambunathan, V.; Hayes, D.; Schmidt, K. H.; Liao, Y. X.; Meisel, D. Thiol Surface Complexation on Growing Cadmium Sulfide Clusters. *J. Am. Chem. Soc.* **1990***, 112*, 3831-3837.

Chapter 5

METAL SALT NUCLEATION OBSERVED USING ESI FT-ICR MASS SPECTROMETRY

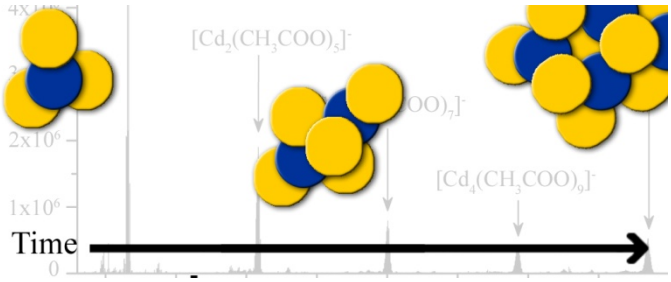

5.1 Introduction

As part of a collaborative research project to understand fundamental chemical processes taking place at deep-sea hydrothermal vents, our research focus shifted to the elucidation of metal sulfide cluster formation using mass spectrometry. As will be discussed in the following chapter (Chapter 6), attempts were made to react metal salts with hydrogen sulfide in aqueous solution while introducing a capping agent, such as 2-mercaptopyridine, to interrupt cluster growth at various stages allowing 'snap-shots' of the nucleation process to be sampled. Although this work resulted in limited success an interesting observation was made. The relative intensities of the metal salt clusters that were detected changed over time. The addition of methanol, to provide stable electrospray ionization (ESI) conditions, was found to initiate the change in the sampled aqueous salt solutions. This observation, which at first seemed to relate only

to electrospray fundamentals, may in fact provide insight into hydrothermal vent chemistry.

Understanding the solvent properties of water is of critical importance in understanding hydrothermal vent chemistry and the chemical environment of ions in aqueous solution. The ability of water to effectively solvate ionic and dipolar species in combination with its ineffectiveness in solvating nonpolar molecules has a drastic affect on the chemistry of our planet. There are instances, however, when this 'hydrophobic effect' breaks down and the solvent properties of water can change dramatically. As water approaches its super critical point (647.1 K, 22.1 MPa) [1], the hydrogen bonding network that drives the physical properties of water dissipates causing water to behave more like a nonpolar solvent. A number of studies highlighted in a recent review by Weingartner and Franck [2] have focused on understanding the properties of water as it approaches and exceeds the supercritical region.

The transition of water from polar to nonpolar solvent as it passes through the supercritical region has particular importance in the ability of water to effectively solvate ionic species. Under 'normal conditions' the highly dipolar nature of water allows it to form solvent shells surrounding dissociated salt ions. The solvent shells effectively shield the ion's charge disrupting the ionic interaction [3]. Formation of the solvent separated ion pair is driven by the hydrogen bonding network of water. As the temperature of the solution increases, kinetic energy of the water molecules

increase causing the hydrogen bonding network to deteriorate. The inability of water to shield the ions, brought about by reduction of solvent structure, results in salt precipitation. This process has also been placed in an environmental context relating to the observation of salt deposits and gyser-like brine discharges from the sea floor [4] in addition to the formation of 'salt diapirs' which seem to form as a result of hydrothermal seepage products created by supercritical water at depth [5].

Nucleation of ionic species, due to disruption of the hydrogen bonding network, can also be observed in binary water-alcohol solvent systems. One perspective as to why this happens is that as an alcohol, such as methanol, is mixed with water; hydrogen bonds are formed as the protic hydrogen atom of methanol interacts with an oxygen atom of a water molecule. At the same time, a hydrogen atom of a water molecule can hydrogen bond with the oxygen atom of methanol. The combination of these interactions pull methanol into aqueous solutions. Working against this process is the interaction between the hydrophobic methyl functionality of methanol and water. To minimize interaction with the hydrophobic end of methanol, it is suggested that water forms highly structured 'cages' around the methyl group [6-9]. This reordering of water molecules as a result of addition of methanol causes a decrease in 'free' water molecules that can participate in ionic shielding as part of the solvent shells. This, in turn, leads to association of ionic clusters in water-methanol solutions.

Quantitatively this process can be described in terms of the dielectric constant (ε) of the solvent. At ambient conditions the static dielectric constant of water is approximately 80, however, under supercritical conditions this value can range from ε≈10 to ε≈23 at high densities [2,10-12]. Although the effects are less dramatic, the static dielectric constants of water methanol mixtures have been experimentally determined [13-16]. For example, at 298 K the static dielectric constant of a 1:1 molar ratio of a water-methanol solution is 61 while a 1:9 solution has a static dielectric constant of 40. We suggest that these quantitative differences in the dielectric constants between 'neat' aqueous solutions and binary water-methanol solutions, which result from substantially altered qualitative physical properties of the aqueous solution upon addition of methanol, is observable in the time-dependent analysis of salt solutions using mass spectrometry.

5.2 Experimental

Analysis of cadmium acetate ($Cd(CH_3COO)_2 \cdot 4H_2O$: Fisher Scientific, Fair Lawn, NJ) solutions was done using ESI FT-ICR mass spectrometry in negative mode. Solutions were prepared using deionized water (Millipore, Bedford, MA) and then diluted 1:1 by volume with methanol (HPLC grade: Fisher Scientific, Fair Lawn, NJ) to a final concentrations ranging from 0.1 mM to 3.0 mM. The final solutions had a 0.3 molar ratio of methanol. Time-dependent sampling was done at various times following dilution with methanol. Analysis was done using a 7 tesla Bruker Apex Qe FT-ICR mass spectrometer (Section 2.3.2). The capilary flow rate was set to

160 μL/hr and the ESI emmitter voltage was 3.8 kV for all experiments. Ions produced by ESI are focused using a series of ion funnels and a hexapole. The focused ion beam can then be accumulated in a second hexapole prior to transfer to the ICR cell to increase ion signal. The collision voltage used to transfer ions into the accumulation hexapole was set to 1.0 V to minimize dissociaiton of larger salt clusters. Accumulation times ranging from 0.1-1.5 sec were used to optimize signal. All other instrumental parameters were held constant over all experiments. Stoichiometric identification of observed cadmium salt clusters was achieved using both theoretical isotopic distributions and mass accuracy (<5ppm).

5.3 Results and Disscussion

Figure 5.1 shows an example mass spectrum taken 30 minutes after dilution with methanol to a final concentration of 0.3 mM cadmium acetate. The major species observed are of the form $[Cd_x(CH_3COO)_{2x+1}]^-$ (x=1-5) with minor products resulting from chloride substitution or loss of CO_2 from acetate. The expanded view for the $[Cd_2(CH_3COO)_5]^-$ cluster highlights the consistency between experimental results and theoretical values for both isotopic distribution and mass accuracy (0.3 ppm). Interestingly, time dependent spectra show that the relative abundances of each of the observed clusters changes as a function of time. Although multiple sample concentrations were tested, 0.3 mM cadmium salt samples provided the best results. As time proceeds after dilution with methanol, the intensity of the mononuclear species decreases relative to the larger cadmium clusters as shown in Figure 5.2. This

result is consistent over various sampling techniques. The results are similar regardless of whether separate aliquots are taken from the diluted solution and loaded into the syringe for ESI analysis (Figure 5.2A) or if a single aliquot is loaded into the syringe and spectra are taken repeatedly as ions are continuously injected into the instrument (Figure 5.2B). This suggests that a nucleation process, distinct from the ESI process, is taking place in solution as a result of methanol addition.

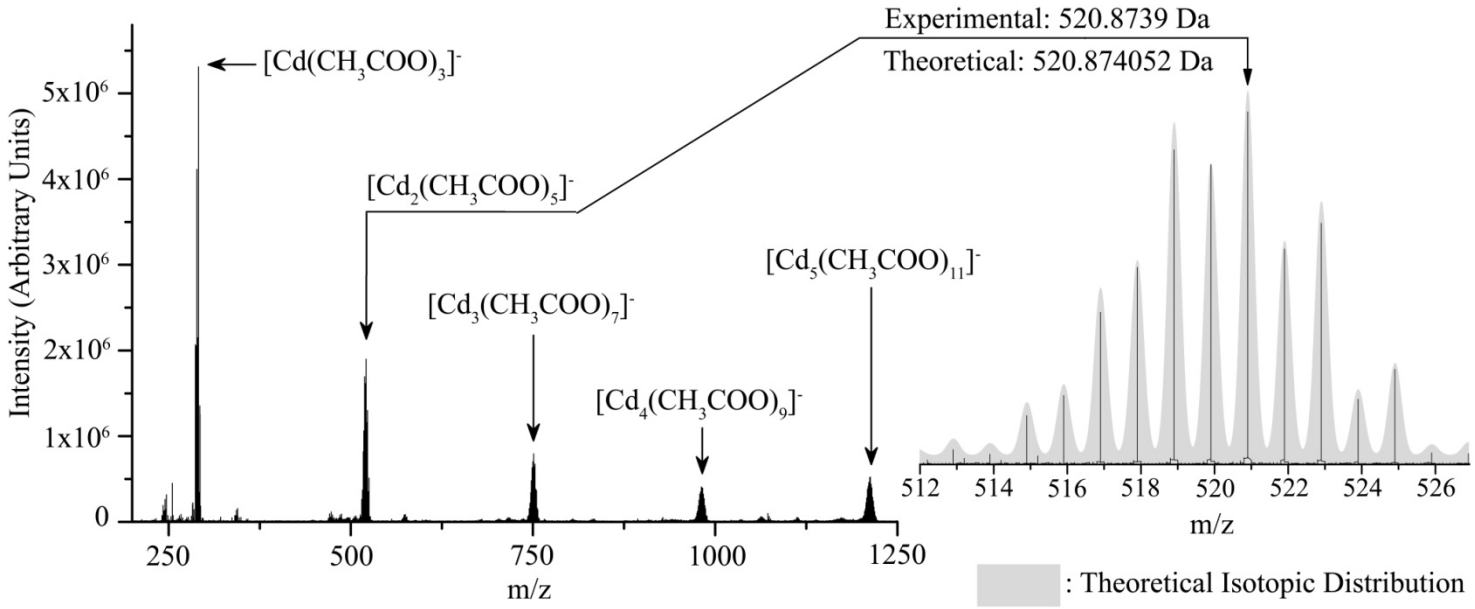

Figure 5.1. ESI mass spectrum of a 0.3 mM cadmium acetate solution taken 30 min. following dilution with methanol (final concentration 0.3mM). The expanded view of the $[Cd_2(CH_3COO)_5]^-$ cluster highlights experimental consistency with both theoretical isotopic distributions and mass accuracy.

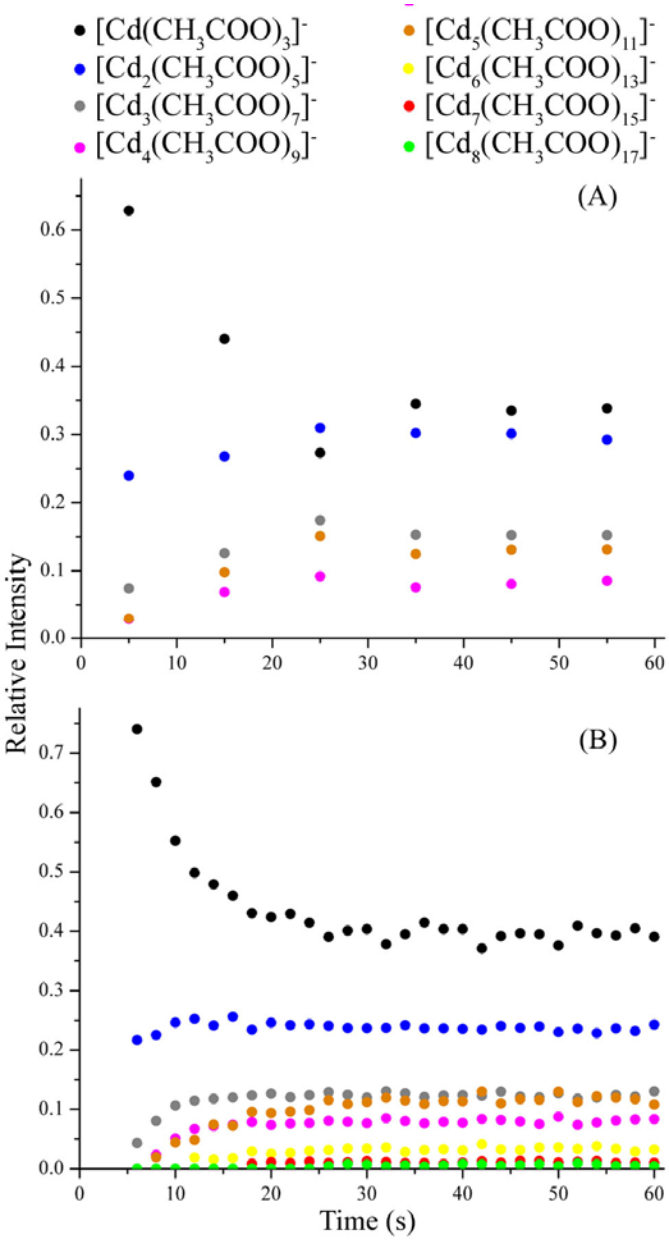

Figure 5.2. Time-dependence ESI mass spectroscopy data relating relative intensities of observed anionic cadmium acetate clusters as a function of time following dilution of solutions with methanol for a 0.3 mM cadmium acetate solution. (A) Sampling was done using separate aliquots for each spectrum and (B) a single aliquot was continually injected as spectra were repeatedly taken.

Further explanation of this distinction from cluster formation due to the ESI process is necessary. As described earlier (Section 2.2), much work has been done in understanding the ESI process using salt solutions [17-25]. Two major models have been developed for the explanation of ESI data [26]. The first of which, described as the ion evaporation model (IEM) developed by Iribarn and Thomson [27,28] suggests that a sequence of coulombic explosions caused by evaporation of charged droplets results in very small droplets in which the field strength at the surface is great enough to promote field desorption of charged solute molecules. On the other hand, Dole et al. [29] described the charged residue model (CRM) in which electrospray droplets undergo multiple evaporation and coulombic explosion cycles until the droplet, on average, contains one solute ion. The transition to the gas-phase is complete when all the remaining solvent molecules evaporate leaving the charged solute ion. Either model, or combination models, can explain the formation of charged clusters from fully dissolved electrolyte solutions. However, neither model would predict that time would have any effect on the relative intensities of the observed clusters. Our results do, conversely, show that the relative intensities of the different sized clusters are changing as a function of time suggesting that the composition of the solution is changing once diluted with methanol. Moreover, the shift to larger clusters, even though the salt concentration decreases with addition of methanol, indicates that to some extent clustering is taking place in solution before ESI analysis.

The detection of metal salt nucleation using ESI mass spectrometry is a unique observation. Although the dilelectric constant of aqueous binary solutions with a 0.3 molar ratio of methanol (ε=66) [13-16] is sufficiently high enough so that ionic species would remain dissolved, it would be expected that the solubility of cadmium acetate would decrease as the dielectric constant decreases. Decreasing solubility lends to the notion that association of ionic species would occur in water-methanol binary solutions and, in turn, the observed clusters would represent the beginning stages of precipitation. As previously mentioned, Hovland and co-workers [4,5] have shown that precipitation of salts and the concentration of metals occurs at deep-sea hydrothermal sites. Our results then imply that the small clusters we are observing in the mass spectra of cadmium salt solutions may be more similar to the form that metals take under supercritical conditions in hydrothermal vents prior to reaction with hydrogen sulfide than fully solvated individual metal ions. It would then more accurate to study these reactions, not using fully dissolved ionic systems as starting points, but instead, utilizing metal salt clusters as the initial reactants.

5.4 Conclusions

Although much work needs to be done to fully understand the mechanism of cadmium salt precipication in low dielectric constant solvents, the observation of cluster growth in solution using ESI mass spectrometry is a unique finding. The time-dependent variance of the relative signal intensity, consistent over different sampling approaches, provides evidence of salt nucleation in water-methanol binary solvent

systems. This result suggests that ion association is occurring in solution prior to the electrospray ionization process. Furthermore, this work has provided important insight into experimental approaches for studying metal sulfide formation in deep-sea hydrothermal vents.

5.5 References

1. Wagner, W.; Pruss, A. The IAPWS Formulation 1995 for the Thermodynamic Properties of Ordinary Water Substance for General and Scientific use. *J. Phys. Chem. Ref. Data.* **2002***, 31*, 387-535.

2. Weingartner, H.; Franck, E. U. Supercritical Water as a Solvent. *Angew Chem Int Ed Engl.* **2005***, 44*, 2672-2692.

3. Debye, P.; Huckel, E. The Theory of Electrolytes. I. Lowering of Freezing Point and Related Phenomena. *Phys. Z.* **1923***, 24*, 185-206.

4. Hovland, M.; Rueslatten, H. G.; Johnsen, H. K.; Kvamme, B.; Kuznetsova, T. Salt Formation Associated with Sub-Surface Boiling and Supercritical Water. *Mar. Pet. Geol.* **2006***, 23*, 855-869.

5. Hovland, M.; Fichler, C.; Rueslatten, H.; Johnsen, H. K. Deep-Rooted Piercement Structures in Deep Sedimentary Basins - Manifestations of Supercritical Water Generation at Depth? *J. Geochem. Explor.* **2006***, 89*, 157-160.

6. Soper, A. K.; Dougan, L.; Crain, J.; Finney, J. L. Excess Entropy in Alcohol-Water Solutions: A Simple Clustering Explanation. *J. Phys. Chem. B.* **2006***, 110*, 3472-3476.

7. Laaksonen, A.; Kusalik, P. G.; Svishchev, I. M. Three-Dimensional Structure in Water-Methanol Mixtures. *J. Phys. Chem. A.* **1997***, 101*, 5910-5918.

8. Soper, A. K.; Finney, J. L. Hydration of Methanol in Aqueous Solution. *Phys. Rev. Lett.* **1993***, 71*, 4346-4349.

9. Micali, N.; Trusso, S.; Vasi, C.; Blaudez, D.; Mallamace, F. Dynamical Properties of Water-Methanol Solutions Studied by Depolarized Rayleigh Scattering.

Phys. Rev. E: Stat. Phys. , Plasmas, Fluids, Relat. Interdiscip. Top. **1996**, *54*, 1720-1724.

10. Deul, R.; Franck, E. U. The Static Dielectric Constant of the Water-Benzene Mixture System to 400Â°C and 2800 Bar. *Ber. Bunsen-Ges. Phys. Chem.* **1991**, *95*, 847-853.

11. Franck, E. U.; Rosenzweig, S.; Christoforakos, M. Calculation of the Dielectric Constant of Water to 1000Â°C and very High Pressures. *Ber. Bunsen-Ges. Phys. Chem.* **1990**, *94*, 199-203.

12. Heger, K.; Uematsu, M.; Franck, E. U. The Static Dielectric Constant of Water at High Pressures and Temperatures to 500 MPa and 550Â°C. *Ber. Bunsenges. Phys. Chem.* **1980**, *84*, 758-762.

13. Kanse, K. S.; Chavan, S. D.; Mali, C. S.; Kumbharkhane, A. C.; Mehrotra, S. C. Structural Study of Methanol-Water Mixture from Dielectric Parameters. *Indian J. Phys.* **2006**, *80*, 265-269.

14. Puranik, S. M.; Kumbharkhane, A. C.; Mehrotra, C. The Static Permittivity of Binary Mixtures using an Improved Bruggeman Model. *J. Mol. Liq.* **1994**, *59*, 173-177.

15. Puranik, S. M.; Kumbharkhane, A. C.; Mehrotra, S. C. The Dielectric Relaxation Study of Primary Alcohol-Water Mixtures using Time Domain Reflectometry Technique. *Proc. Natl. Acad. Sci. , India, Sect. A.* **1993**, *63*, 415-426.

16. Akerlof, G. Dielectric Constant of some Organic Solvent-Water Mixtures at various Temperatures. *J. Am. Chem. Soc.* **1932**, *54*, 4125-4139.

17. Sunner, J.; Beech, I. B.; Hiraoka, K. On the Distributions of Ion/Neutral Molecule Clusters in Electrospray and Laser Spray. A Cluster Division Model for the Electrospray Process. *J. Am. Soc. Mass Spectrom.* **2006**, *17*, 151-162.

18. Hao, C.; March, R. E.; Croley, T. R.; Smith, J. C.; Rafferty, S. P. Electrospray Ionization Tandem Mass Spectrometric Study of Salt Cluster Ions. Part 1-Investigations of Alkali Metal Chloride and Sodium Salt Cluster Ions. *Journal of Mass Spectrometry.* **2001**, *36*, 79-96.

19. Charles, L.; Pepin, D.; Gonnet, F.; Tabet, J. -. Effects of Liquid Phase Composition on Salt Cluster Formation in Positive Ion Mode Electrospray

Mass Spectrometry: Implications for Clustering Mechanism in Electrospray. *J. Am. Soc. Mass Spectrom.* **2001***, 12*, 1077-1084.

20. Zhou, S.; Cook, K. D. A Mechanistic Study of Electrospray Mass Spectrometry: Charge Gradients within Electrospray Droplets and their Influence on Ion Response. *J. Am. Soc. Mass Spectrom.* **2001***, 12*, 206-214.

21. Fernandez de la Mora, J. Electrospray Ionization of Large Multiply Charged Species Proceeds Via Dole's Charged Residue Mechanism. *Anal. Chim. Acta.* **2000***, 406*, 93-104.

22. Gamero-Castano, M.; Fernandez de la Mora, J. Modulations in the Abundance of Salt Clusters in Electrosprays. *Anal. Chem.* **2000***, 72*, 1426-1429.

23. Gamero-Castano, M.; Fernandez de la Mora, J. Mechanisms of Electrospray Ionization of Singly and Multiply Charged Salt Clusters. *Anal. Chim. Acta.* **2000***, 406*, 67-91.

24. Kebarle, P.; Peschke, M. On the Mechanisms by which the Charged Droplets Produced by Electrospray Lead to Gas Phase Ions. *Anal. Chim. Acta.* **2000***, 406*, 11-35.

25. Wang, G.; Cole, R. B. Charged Residue Versus Ion Evaporation for Formation of Alkali Metal Halide Cluster Ions in ESI (Electrospray Ionization). *Anal. Chim. Acta.* **2000***, 406*, 53-65.

26. Kebarle, P. A Brief Overview of the Present Status of the Mechanisms Involved in Electrospray Mass Spectrometry. *Journal of Mass Spectrometry.* **2000***, 35*, 804-817.

27. Iribarne, J. V.; Thomson, B. A. On the Evaporation of Small Ions from Charged Droplets. *J. Chem. Phys.* **1976***, 64*, 2287-2294.

28. Thomson, B. A.; Iribarne, J. V. Field-Induced Ion Evaporation from Liquid Surfaces at Atmospheric Pressure. *J. Chem. Phys.* **1979***, 71*, 4451-4463.

29. Dole, M.; Mack, L. L.; Hines, R. L.; Mobley, R. C.; Ferguson, L. D.; Alice, M. B. Molecular Beams of Macroions. *J. Chem. Phys.* **1968***, 49*, 2240-2249.

Chapter 6

MONITORING METAL SULFIDE FORMATION IN SOLUTION USING MOLECULAR CAPPING AGENTS

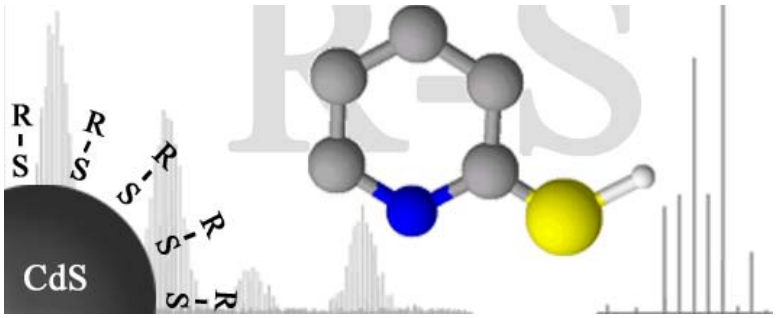

6.1 Introduction

Metal sulfides represent an important family of nanoparticles which play an integral role in the speciation and bioavailability of metals in aquatic ecosystems [1,2]. Nonetheless, the details of how these environmentally significant particles are formed are still yet to be fully understood. Along the continuum going from dissolved ionic species to condensed phase material there are thought to be any number of dissolved polynuclear clusters representing the intermediates of precipitation [3]. Although metal sulfides are considered scarcely soluble in water, these intermediate clusters have been found to be prevalent in the environment [3,4]. From this observation, our collaborators have suggested a mechanism for the nucleation of metal sulfide particles in which the first condensed phase results from aggregation of dissolved polynuclear clusters with a molecular structure similar to that found in the bulk material [5]. Support for this hypothesis of small molecular metal sulfide clusters

as ‘building-blocks’ has been demonstrated for FeS [6], CuS [7] and ZnS systems [8]. These studies represent only the starting point and much work is needed to fully explain the process of metal sulfide particle formation.

FT-ICR Mass spectrometry is an optimal analytical technique for the analysis of metal sulfide clusters in that stoichiometric identification can be made based on mass accuracy and structural information can be obtained through fragmentation experiments. Past work by our research group has focused on the use of laser desorption ionization FT-ICR mass spectrometry to identify ZnS, CuS and FeS clusters present in both laboratory and natural water samples [3] and PbS clusters in laboratory samples [9]. This work was part of the foundation for the polynuclear ‘building-block model’ discussed above. However, one of the major criticisms of this work was that, between the freeze drying process as part of sample preparation and the harsh laser ablating/ionization process, the observed metal sulfide clusters may not represent those present in solution [10]. To circumvent these criticisms we set out to use ESI FT-ICR mass spectrometry. Direct sampling from solution and the inherently soft ionization mechanism of ESI makes this technique optimal for analyzing molecular metal sulfide cluster intermediates.

A major hurdle in using electrospray ionization with metal sulfide systems, as mentioned earlier, is that most metal sulfides are only sparingly soluble in aqueous solutions. At reasonable concentrations for the technique, synthesis results in very fast precipitation reactions. In order trap the intermediates of this process our method, in this case, was to introduce a capping agent to a reaction between Cd^{2+} and HS^- in aqueous solution. Our ambitious hypothesis was that the capping agent would bind to the forming CdS clusters halting growth. Ideally, analysis of the various

capped species using mass spectrometry would be like flipping through a series of 'snap-shots' at various mechanistic stages of mineral precipitation. Molecular candidates for capping agents were small organic thiols. The thiol functionality can bind to metal sulfide clusters while the organic "greasy" end group was expected to passivate the surface preventing further cluster growth. This approach was adapted from previous studies on the synthesis of CdS nanoparticles in aqueous solutions [11-14] and was designed to mimic the behavior of bacteria that excrete both sulfide and thiol-rich peptides in the presence of toxic metals [15,16].

6.2 Experimental

Cadmium Nitrate ($Cd(NO_3)_2 \bullet 4H_2O$), glutathione and 2-mercaptopyridine (**mpH**: C_5H_5NS) were purchased from Sigma-Aldrich (St. Louis, MO) while sodium sulfide ($Na_2S \bullet 9H_2O$), hydrochloric acid (HCl) and HPLC grade methanol were purchased from Fisher Scientific (Fair Lawn, NJ). Aqueous stock solutions (10 mM) of cadmium nitrate, 2-mercaptopyridine, glutathione and sodium sulfide were prepared using deionized water (Millipore, Bedford, MA). Prior to use, all solvents were degassed with high purity argon gas for at least 1 hour. Elecrospray solutions of cadmium nitrate were prepared by diluting the stock solution using deionized water and methanol to a final concentration of 3 mM and a 1:1 water to methanol ratio (Solution A). Introduction of the capping agent (2-mercaptopyridine and glutathione) was done by mixing Solution A with a similar 3 mM 2-mercaptopyridine or glutathione water/methanol solution. Cd/**mpH** ratios were 1:1 for all reactions. Cadmium sulfide reactions were performed by bubbling H_2S (g), generated by

reaction of Na_2S with HCl and transferred using argon pressure, through solutions of $Cd(NO_3)_2$ as the capping agent was added.

Solutions were analyzed using a 7 tesla Bruker Apex Qe FT-ICR mass spectrometer in negative mode (Section 2.3.2). Ions produced by electrospray ionization enter the instrument through a glass capillary and are then focused into a beam using two consecutive ion funnels followed by a linear hexapole operated in r.f. mode only. As the ions enter the Qh Interface, if necessary, they were accumulated (0.1-1.0 s) in the hexapole collision cell to increase signal strength before transfer to the ICR cell where they are trapped, excited and detected. Comparison to theoretical isotopic distributions and mass accuracy (<5 ppm) allowed for unambiguous identification of observed clusters (See Figure 6.1).

6.3 Results and Disscussion

Analysis of cadmium nitrate solutions using ESI mass spectrometry in negative mode resulted in the observation of cadmium clusters of the type $[Cd_x(NO_3)_{2x+1}]^-$ (x=1-5) as seen in Spectrum A (Figures 6.1-6.5). This series of figures, Figures 6.1-6.5, represent different m/z ranges based on the number of cadmium atoms in the observed clusters. Stoichiometric identification was made using mass accuracy and comparison to theoretical isotopic distributions as highlighted in Figure 6.1 for the single cadmium complex. Minor unlabeled species are solvated clusters, chloride substitution of nitrate ligands, or electronic noise. Reaction of cadmium nitrate with **mpH** (Spectrum B: Figures 6.1-6.5) leads to successive substitution of nitrate ligands for deprotonated 2-mercaptopyridine (**mp**).

Minor reaction products including sulfate ligands are observed which seem to result from oxidation of the thiol capping agent by nitrate. These products are seen in greater abundance following reaction with H_2S (g) as observed in Spectrum C (Figures 6.2-6.5). Similar to 2-mercaptopyridine, the sulfidic species resulting from H_2S are oxidized to sulfate ligands. Likewise, oxidation of sulfidic ligands to form sulfate in the presence of nitrate anions was observed in a study by Jacobson and co-workers for silver systems [17]. It should be noted that the m/z range for the H_2S reaction spectrum (Spectrum C: Figures 6.2-6.5) is not provided for the mononuclear complex (Figure 6.1) because it was identical to Spectrum B in Figure 6.1. Unlike the larger cadmium clusters, there was no change in the observed mononuclear cadmium complexes or the relative abundance of $[Cd(NO_3)_3]^-$ in comparison to $[Cd(NO_3)_2(mp)]^-$ upon reaction with H_2S (g). No H_2S (g) reaction products were observed for reactions using glutathione as the capping agent. Additionally, it should be noted that positive mode ESI of cadmium nitrate solutions resulted in too many unidentifiable ions to move forward with H_2S reactions. See Appendix C for example spectrum.

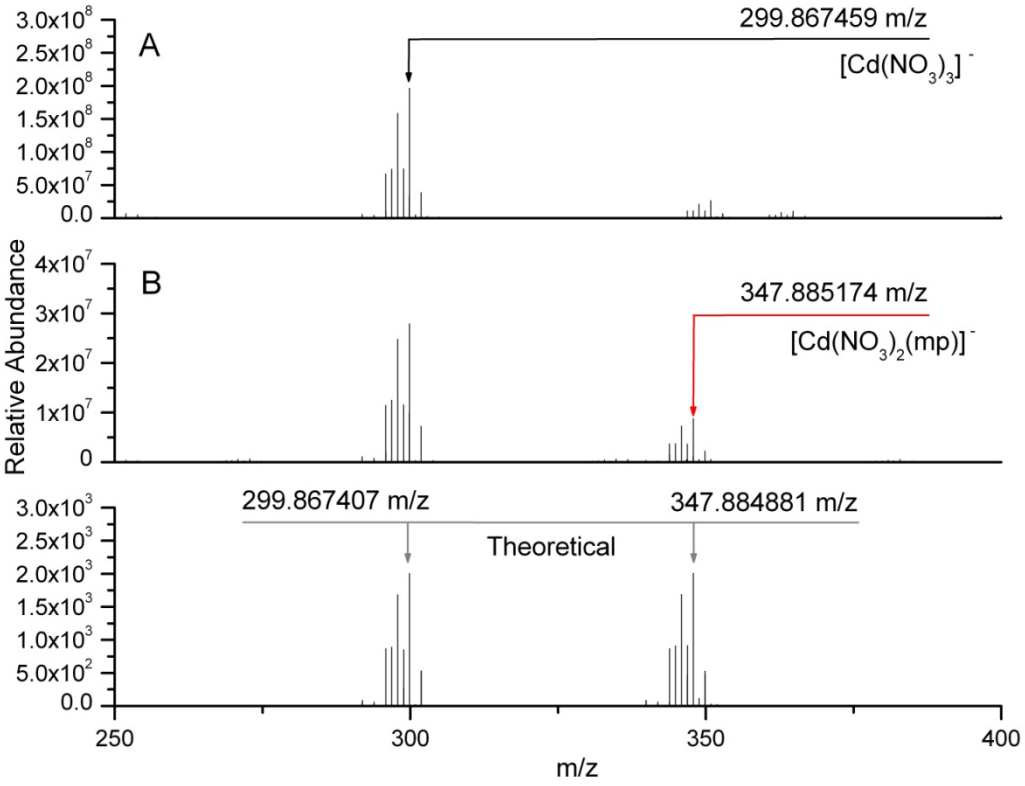

Figure 6.1. The single cadmium region of the anionic ESI FT-ICR mass spectrum taken for (A) a 3 mM solution of cadmium nitrate and (B) the same solution following reaction with 2-mercaptopyridine. Substitution of a nitrate ligand for deprotonated 2-mercaptopyridine (mp) is observed. The theoretical spectrum highlights the mass accuracy and consistency in isotopic distribution for the experiment.

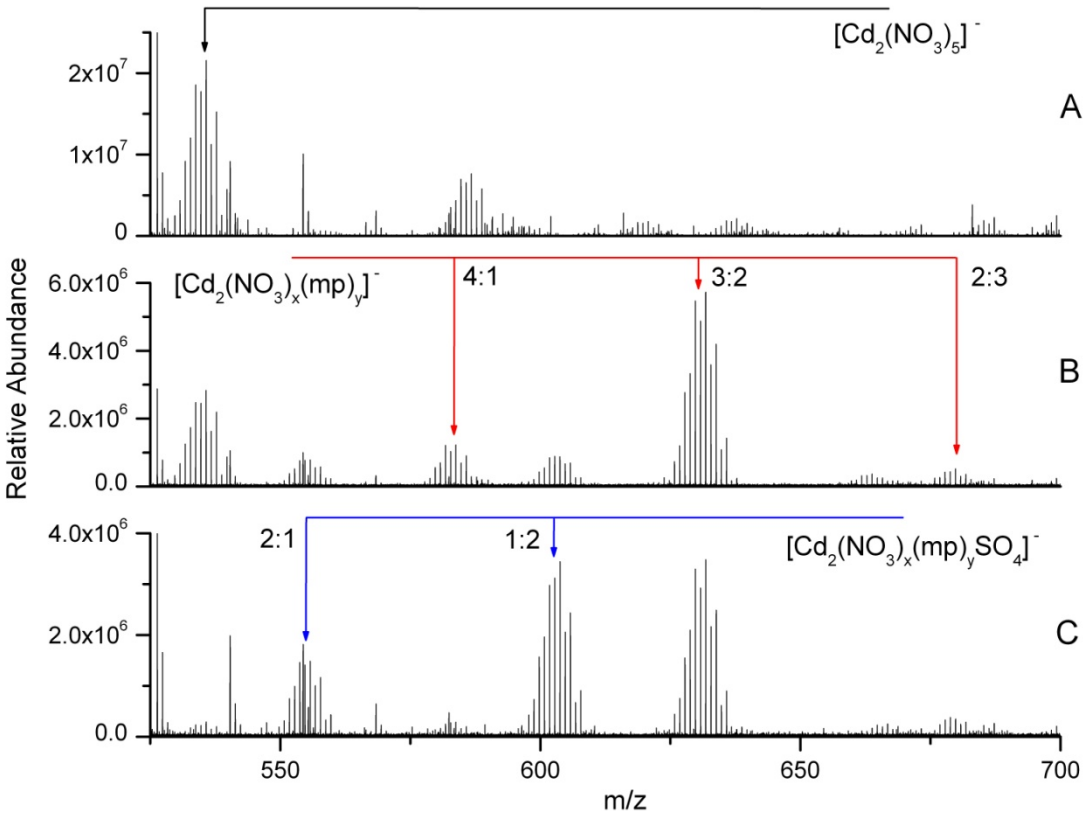

Figure 6.2. The Cd_2 region of the anionic ESI FT-ICR mass spectrum taken for (A) a 3 mM solution of cadmium nitrate (B) the same solution following reaction with 2-mercaptopyridine and (C) the introduction of H_2S (g) to a 1.5 mM solution of cadmium nitrate and 2-mercaptopyridine (1:1).

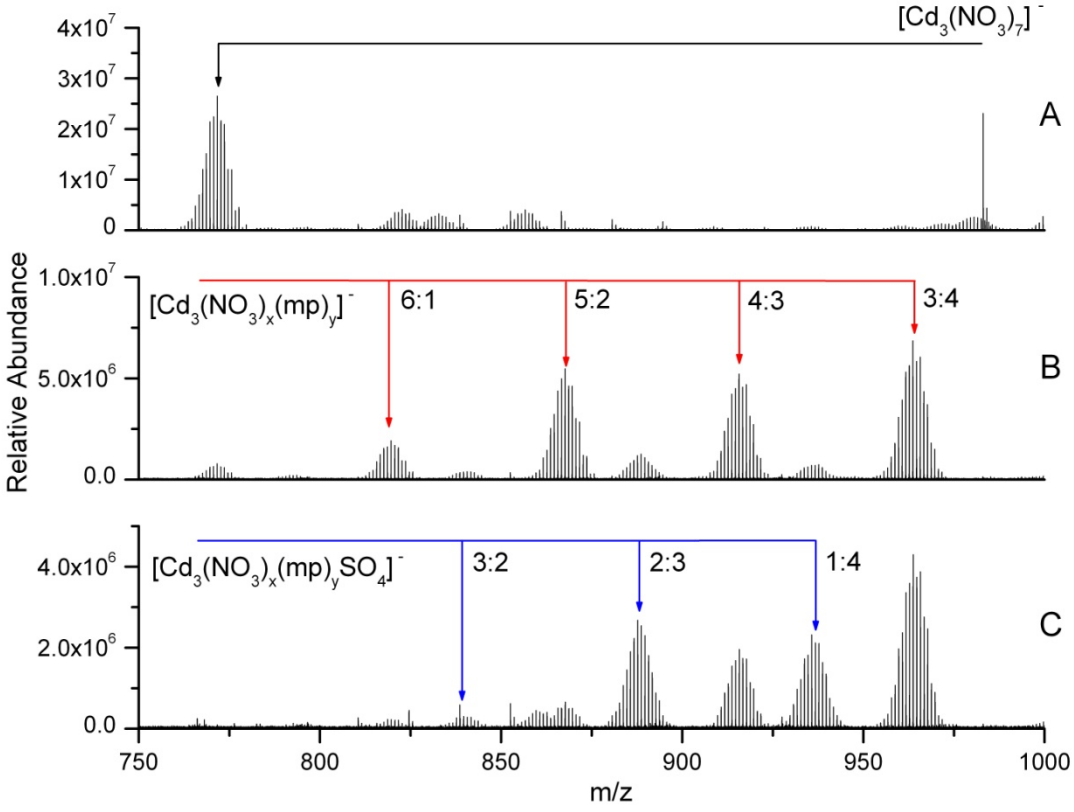

Figure 6.3. The Cd_3 region of the anionic ESI FT-ICR mass spectrum taken for (A) a 3 mM solution of cadmium nitrate (B) the same solution following reaction with 2-mercaptopyridine and (C) the introduction of H_2S (g) to a 1.5 mM solution of cadmium nitrate and 2-mercaptopyridine (1:1).

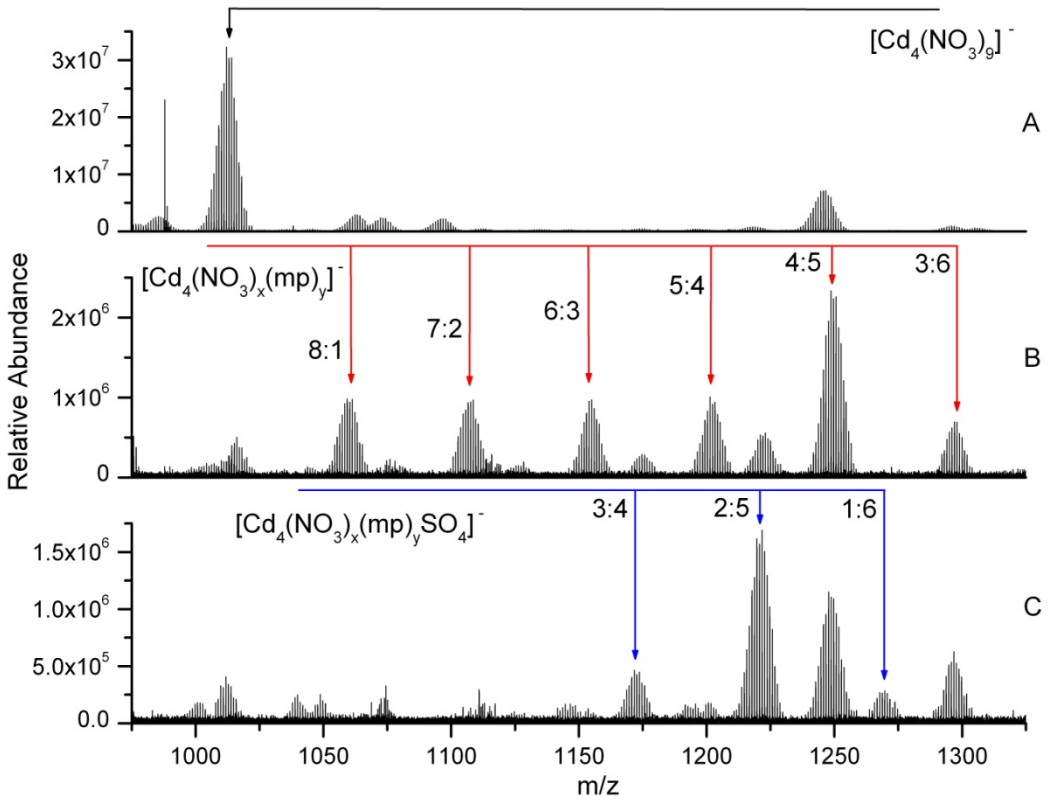

Figure 6.4. The Cd_4 region of the anionic ESI FT-ICR mass spectrum taken for (A) a 3 mM solution of cadmium nitrate (B) the same solution following reaction with 2-mercaptopyridine and (C) the introduction of H_2S (g) to a 1.5 mM solution of cadmium nitrate and 2-mercaptopyridine (1:1).

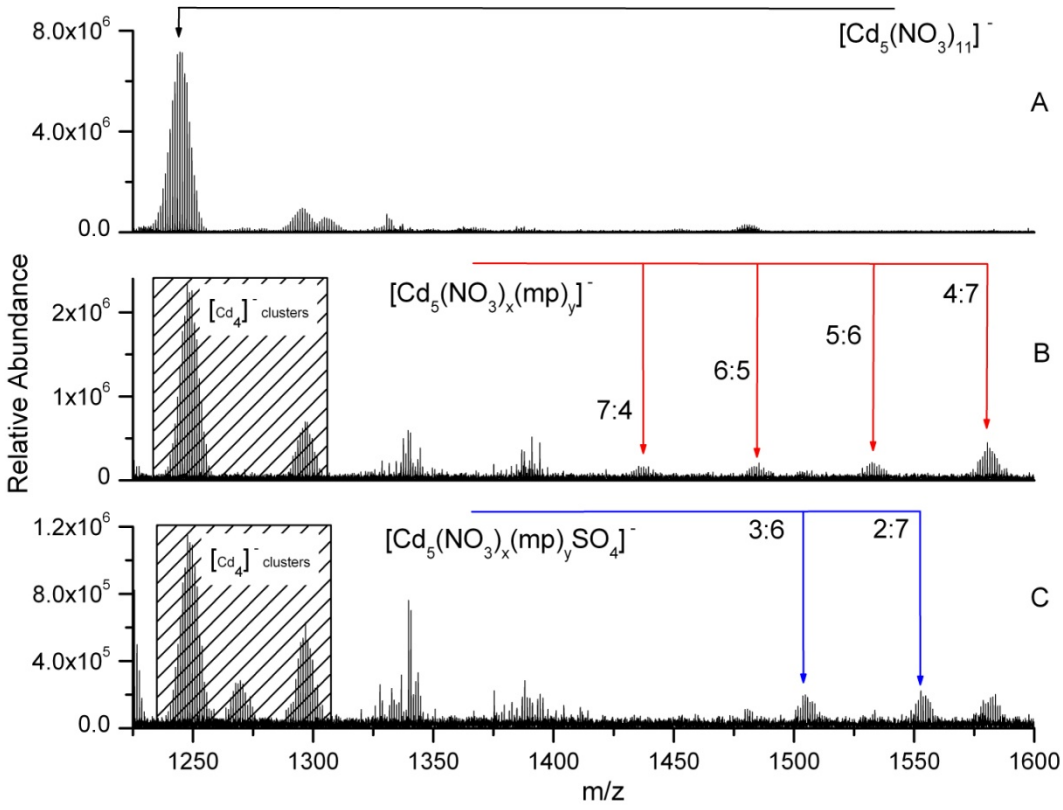

Figure 6.5. The Cd_5 region of the anionic ESI FT-ICR mass spectrum taken for (A) a 3 mM solution of cadmium nitrate (B) the same solution following reaction with 2-mercaptopyridine and (C) the introduction of H_2S (g) to a 1.5 mM solution of cadmium nitrate and 2-mercaptopyridine (1:1).

Although results using 2-mercaptopyridine as a capping agent provided limited information as to the formation of metal sulfide clusters they do provide a foundation for observing sulfidic species using ESI mass spectrometry. The primary hurdle when studying environmentally significant metal sulfides (FeS, CuS, CdS, ZnS) using ESI mass spectrometry is the insolubility of these species in aqueous solutions. While much of the sample is still lost as precipitate using **mpH** as a capping agent, the observation of sulfidic cadmium clusters suggest that metal salt

reactions with H_2S (g) can be interrupted and nucleation intermediates can be sampled using electrospray ionization.

These results also build off of those discussed in Chapter 5 regarding sampling solution nucleation processes for metal salts using electrospray ionization. Of particular interest are the results for the mononuclear cadmium nitrate reactions (Figure 6.1). The lack of observable H_2S (g) reaction products for the single cadmium complexes is evidence that a solution based chemical process is being sampled. For the larger clusters (Figures 6.2-6.5), it can be seen from the relative abundances of the observable species that the reaction products including sulfate are the majority family of clusters following reaction with H_2S (g). This suggests that there is a relatively high concentration of sulfide (oxidized to sulfate) present in solution. If the observed clusters were simply aggregates of the ions present in the electrospray droplets prior to final evaporation steps (See Section 2.2), we would fully expect to see mononuclear species with sulfate as well. The lack of these clusters points to a solution based process in which ESI mass spectrometry is able to observe the unique chemistry that takes place for different sized metal clusters. These results will be illuminated further in the next chapter (Chapter 7) on the gas-phase reactions of cadmium nitrate with H_2S (g).

6.4 Conclusions

In Conclusion, sulfidic metal clusters were observed for reactions of cadmium nitrate with hydrogen sulfide using 2-mercaptopyridine as a molecular capping agent. Sulfidic ligands were seen as sulfate suggesting oxidation by excess nitrate in aqueous solutions of $Cd(NO_3)_2$. Although these results provided limited

insight into the mechanism of metal sulfide particle formation, they do provide additional evidence that electrospray ionization can sample nucleation reactions of metal salts in aqueous solutions. The observed differences in reactivity for cadmium nitrate clusters of different stoichiometries in aqueous solution are consistent with the observed gas phase ion-molecule reactions that will be discussed in the following chapter.

6.5 References

1. Bianchini, A.; Bowles, K. C. Metal Sulfides in Oxygenated Aquatic Systems: Implications for the Biotic Ligand Model. *Comp. Biochem. Physiol. , Part C: Toxicol. Pharmacol.* 2002*, 133C*, 51-64.

2. Smith, D. S.; Bell, R. A.; Kramer, J. R. Metal Speciation in Natural Waters with Emphasis on Reduced Sulfur Groups as Strong Metal Binding Sites. *Comp. Biochem. Physiol. , Part C: Toxicol. Pharmacol.* 2002*, 133C*, 65-74.

3. Rozan, T. F.; Lassman, M. E.; Ridge, D. P.; Luther, G. W.,III. Evidence for Iron, Copper and Zinc Complexation as Multinuclear Sulfide Clusters in Oxic Rivers. *Nature (London).* 2000*, 406*, 879-882.

4. Rickard, D.; Luther, G. W.,III. Metal Sulfide Complexes and Clusters. *Reviews in Mineralogy & Geochemistry.* 2006*, 61*, 421-504.

5. Luther, G. W.,I.I.I.; Rickard, D. T. Metal Sulfide Cluster Complexes and their Biogeochemical Importance in the Environment. *Journal of Nanoparticle Research.* 2005*, 7*, 389-407.

6. Theberge, S. M.; Luther, G. W.,III. Determination of the Electrochemical Properties of a Soluble Aqueous FeS Species Present in Sulfidic Solutions. *Aquat. Geochem.* 1997*, 3*, 191-211.

7. Luther, G. W.,III; Theberge, S. M.; Rozan, T. F.; Rickard, D.; Rowlands, C. C.; Oldroyd, A. Aqueous Copper Sulfide Clusters as Intermediates during Copper

Sulfide Formation. *Environmental Science and Technology.* 2002*, 36*, 394-402.

8. Luther, G. W.,III; Theberge, S. M.; Rickard, D. T. Evidence for Aqueous Clusters as Intermediates during Zinc Sulfide Formation. *Geochim. Cosmochim. Acta.* 1999*, 63*, 3159-3169.

9. Rozan, T. F.; Luther, G. W.; Ridge, D.; Robinson, S. Determination of Pb Complexation in Oxic and Sulfidic Waters using Pseudovoltammetry. *Environmental Science and Technology.* 2003*, 37*, 3845-3852.

10. Sukola, K.; Wang, F.; Tessier, A. Metal-Sulfide Species in Oxic Waters. *Anal. Chim. Acta.* 2005*, 528*, 183-195.

11. Winter, J. O.; Gomez, N.; Gatzert, S.; Schmidt, C. E.; Korgel, B. A. Variation of Cadmium Sulfide Nanoparticle Size and Photoluminescence Intensity with Altered Aqueous Synthesis Conditions. *Colloids Surf. , A.* 2005*, 254*, 147-157.

12. Murphy, C. J. CdS Nanoclusters Stabilized by Thiolate Ligands: A Mini-Review. *Journal of Cluster Science.* 1996*, 7*, 341-350.

13. Nosaka, Y.; Ohta, N.; Fukuyama, T.; Fujii, N. Size Control of Ultrasmall Cadmium Sulfide Particles in Aqueous Solution by using various Thiols. *J. Colloid Interface Sci.* 1993*, 155*, 23-29.

14. Swayambunathan, V.; Hayes, D.; Schmidt, K. H.; Liao, Y. X.; Meisel, D. Thiol Surface Complexation on Growing Cadmium Sulfide Clusters. *J. Am. Chem. Soc.* 1990*, 112*, 3831-3837.

15. Labrenz, M.; Druschel, G. K.; Thomsen-Ebert, T.; Gilbert, B.; Welch, S. A.; Kemner, K. M.; Logan, G. A.; Summons, R. E.; De, S. G.; Bond, P. L.; Lai, B.; Kelly, S. D.; Banfield, J. F. Formation of Sphalerite (ZnS) Deposits in Natural Biofilms of Sulfate-Reducing Bacteria. *Science.* 2000*, 290*, 1744-1747.

16. Reese, R. N.; Winge, D. R. Sulfide Stabilization of the Cadmium-Î³-Glutamyl Peptide Complex of Schizosaccharomyces Pombe. *J. Biol. Chem.* 1988*, 263*, 12832-12835.

17. Jacobson, A. R.; Martínez, C. E.; Spagnuolo, M.; McBride, M. B.; Baveye, P. Reduction of Silver Solubility by Humic Acid and Thiol Ligands during Acanthite (β-Ag2S) Dissolution. *Environmental Pollution.* 2005*, 135*, 1-9.

Chapter 7

GAS PHASE ION-MOLECULE REACTIONS OF METAL SALT CLUSTERS WITH HYDROGEN SULFIDE

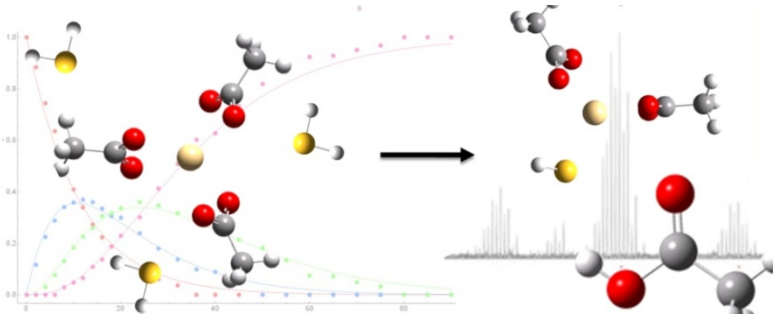

7.1 Introduction

This chapter represents a fundamental shift in our approach to understanding metal sulfide nucleation using mass spectrometry. To this point our method have focused on attempts to control solution processes, however, the ability to produce salt clusters of various stoichiometries in combination with our group's experience in the field of gas phase ion-molecule reactions proved to be an ideal combination leading to this shift in methodology. As described in previous chapters, metal clusters have been shown to play an vital role in the speciation and bioavailability of metals in aqueous environments [1,2]. Although much work has been done focusing on these systems, little is known regarding the chemical processes that control the transformation of dissolved ions to solid state materials. A model developed from the observations of persistent molecular clusters in dilute aqueous environments suggests that metal sulfide particles form through aggregation of

dissolved polynuclear clusters [3-5]. A few of the analytical approaches deployed to characterize these elusive species have included voltametry [3,4,6], transmission electron microscopy [7], powder x-ray diffraction [8,9], dynamic light scattering [10,11] and UV/vis spectroscopy [12-14]. Although these techniques provide useful information such as stoichiometric ratios and particle size, mass spectrometry may be the tool necessary to truly characterize these clusters on a molecular level and clarify the process of metal sulfide formation.

Fourier Transform Ion Cyclotron Resonance (FT-ICR) mass spectrometry provides the ideal combination of instrumental advantages to directly characterize metal sulfide clusters. In addition to being able to elucidate chemical structure based on mass-to-charge ratio and fragmentation experiments, monitoring gas phase ion-molecule reactions using mass spectrometry has the potential to describe metal sulfide nucleation reactions. FT-ICR mass spectrometry provides the advantages of mass accuracy and variable trapping times ideal for studying rate constants of gas phase ion-molecule reactions [15,16]. Long trapping times enable single collision interactions to be monitored allowing elementary reaction steps to be monitored in the gas phase. Ions are trapped in the ICR cell where they are exposed to the neutral reactant gas. As the reaction proceeds, the identity and relative concentrations of both the reactant and product ions are followed allowing kinetic information to be extracted. The Ridge group has extensive experience applying this technique to metal systems [17-34], however, the use of gas phase ion-molecule reactions to study environmentally significant metal sulfide clusters is a novel application of the technique.

The work with solution based systems described in Chapters 5 and 6 have set the foundation for making gas phase metal salt clusters of various sizes using

electrospray ionization. The observation of salt cluster growth has been placed in an environmental context suggesting larger clusters may represent initial reactant species in hydrothermal systems with low dielectric constant solutions while smaller clusters most likely represent clusters found in dilute surface water environments (Chapter 5). This final section on metal sulfide clusters describes the gas phase ion-molecule reactions between metal salt clusters and hydrogen sulfide with the goal of elucidating the process of metal sulfide formation in aqueous environments.

7.2 Experimental

Reagent grade cadmium nitrate ($Cd(NO_3)_2 \bullet 4H_2O$), cadmium acetate ($Cd(CH_3COO)_2 \bullet 2H_2O$), cadmium chloride ($CdCl_2$), and zinc chloride ($ZnCl_2$) were purchased from Sigma-Aldrich (St. Louis, MO). HPLC grade methanol was purchased from Fisher Scientific (Fair Lawn, NJ) and H_2S (gas: 99.5% purity) was purchased from Matheson Tri Gas (Basking Ridge, NJ). Stock solutions (10 mM) of each of the metal salts were prepared using deionized water (Millipore, Bedford, MA). These solutions were then diluted to 0.3 mM using deionized water and methanol (final solution 1:1) for electrospray experiments.

Experiments were done using a 7 Tesla Bruker Apex Qe FT-ICR mass spectrometer (Section 2.3.2). Ions produced by electrospray ionization enter the instrument through a glass capillary and are then focused into a beam using two consecutive ion funnels followed by a linear hexapole operated in rf mode only. As the ions enter the Qh Interface a reactant ion of choice can be mass selected using the mass resolving quadrupole and accumulated (0.1-1.0 s) in the hexapole collision cell where they are collisionally cooled so they can be injected into the ICR cell. Ion-

molecule reactions (Section 2.1.4) are performed by trapping the ions in the ICR cell for various reaction times at elevated H_2S (g) pressure prior to excitation and detection. Operating in SORI MS/MS mode with the SORI power at 0%, the reaction time is controlled using the delay time associated with the SORI pulse length. The neutral reactant gas is introduced through a high precision variable leak valve allowing for constant elevated pressures (H_2S: $4x10^{-9}$ Torr or $9x10^{-9}$ Torr) to be maintained throughout the experiment.

Kinetic studies of gas phase ion-molecule reactions in the ICR cell were performed under pseudo first-order conditions. The reactant gas pressure, in this case H_2S, is in great excess relative to the number of ions trapped in the ICR cell making [H_2S] constant over the course of the experiment. The rate equation can then be written

$$rate = k_x^1[\text{Cluster}] \qquad 7.1$$

in terms of the pseudo first-order rate constant (k_x^1) and the concentration of the reactant cluster ion ([Cluster]). Adjusted for differences in isotopic distributions, the relative intensity of a single isotope ([Cluster]) for reactant and product clusters were used to generate plots as a function of time. The integrated form of the rate equation can be fit to the plot of [Cluster] vs. time using nonlinear regression in Mathematica (Wolfram Research, Champaign, IL) to determine the pseudo first-order rate constant (See Appendix D for examples). It should be noted that for consistency, product clusters were grouped into families of ions based on the number of sulfur atoms added upon reaction (See Scheme 7.2 for example). This treatment allows all reactions to be considered sequential reactions simplifying the derivation of the integrated rate

equations for complex branching reaction schemes. Taking into consideration differences in reduced mass (μ'_x) and H_2S pressure (P_x), the experimentally determined pseudo first-order rate (k_x^1) constants were then converted to reaction efficiencies (k/k_c) relative to k_1^1 for the fastest observed reaction

Scheme 7.1

$$[Cd(NO_3)(CH_3OH)]^+ + H_2S(g) \xrightarrow[4\times10^{-9}\text{torr}]{} [Cd(SH)(CH_3OH)]^+ + HNO_3$$

$$k_1^1 = 2.85 \pm 0.27\text{s}^{-1}$$

$$\frac{k}{k_c} = \frac{k_x^1}{2.85\ \text{s}^{-1}}\left(\frac{\mu_x'}{29.19\ \text{Da}}\right)^{1/2}\left(\frac{4\times10^{-9}\text{torr}}{P_x}\right) \qquad 7.2$$

which was assumed to proceed at the collision rate. It is important to point out that the error associated with k_1^1 ($2.85 \pm 0.27\text{s}^{-1}$) is far larger than that for most other determined pseudo first-order rate constants; therefore, the accuracy of all reported k/k_c values is limited to 9.5% unless otherwise specified. Further explanation of this approach and the instrumental design can be found in Chapter 2.

When possible, Gaussian (Wallingford, CT) was used by Kaitlin Papson to examine the thermodynamic properties of the observed reactions between metal salt clusters and hydrogen sulfide. Gaussian is able to characterize the potential energy surface of a reaction allowing the change in reaction energy (ΔE) to be calculated. This information is used for comparison to experimental results. All theoretical results are ground state density functional theory (DFT) calculations done using the B3LYP hybrid functional and LANL2DZ basis set.

7.3 Results and Disscussion

7.3.1 Anionic Reactions

Electrosprayed solutions of cadmium salts ($Cd(NO_3)_2$, $Cd(CH_3COO)_2$ and $CdCl_2$) produce ions of the type $[Cd_xL_{2x+1}]^-$ (x = 1-4, L = NO_3, CH_3COO, or Cl) in negative ion mode. Individual clusters were isolated in the source region of the instrument and exposed to H_2S (g) in the ICR cell. Both cadmium nitrate and cadmium acetate anionic clusters were shown to react readily with hydrogen sulfide in the gas phase. Cadmium chloride clusters ($[Cd_xCl_{2x+1}]^-$, x=1-4), although able to be observed using electrospray, did not display any reactivity under the conditions of the experiment. A representative set of mass spectra can be found in Figure 7.1 for the reaction of $[Cd_2(NO_3)_5]^-$ with hydrogen sulfide. It can be seen that the first reaction product is the sulfidic cluster $[Cd_2SH(NO_3)_4]^-$ resulting from substitution of NO_3^- by SH^- losing HNO_3 as a neutral. As reaction time proceeds, a second bisulfide can replace a nitrate ligand or $[Cd_2SH(NO_3)_4]^-$ can lose HNO_3 to make $[Cd_2S(NO_3)_3]^-$. Although unlikely, the possibility of $[Cd_2S(NO_3)_3]^-$ being a direct product of $[Cd_2(NO_3)_5]^-$ through a loss of $2HNO_3$ cannot be ruled out. This reaction sequence is highlighted in Scheme 7.2. As mentioned earlier, the observed reaction products were grouped into families of clusters based on the number of sulfur atoms added upon reaction with H_2S. The simplified sequential reaction scheme (See Scheme 7.2) is then used to generate kinetic plots as seen in Figure 7.2. The data points represent the sum of isotopically adjusted relative intensities for all clusters associated with each cluster family. For example, the orange data set (Cd_2S_1 cluster family) in Figure 7.2 represents all observed clusters with one sulfur added ($[Cd_2SH(NO_3)_4]^-$ and $[Cd_2S(NO_3)_3]^-$) for the reaction of $[Cd_2(NO_3)_5]^-$ with H_2S. The lines are fit to the data

using the appropriate integrated rate equations to determine the pseudo first-order rate constants for the simplified sequential reaction scheme. Pseudo first-order rate constants are converted to reaction efficiencies which, for all reported anionic gas phase ion-molecule reactions, can be found in Table 7.1.

Scheme 7.2

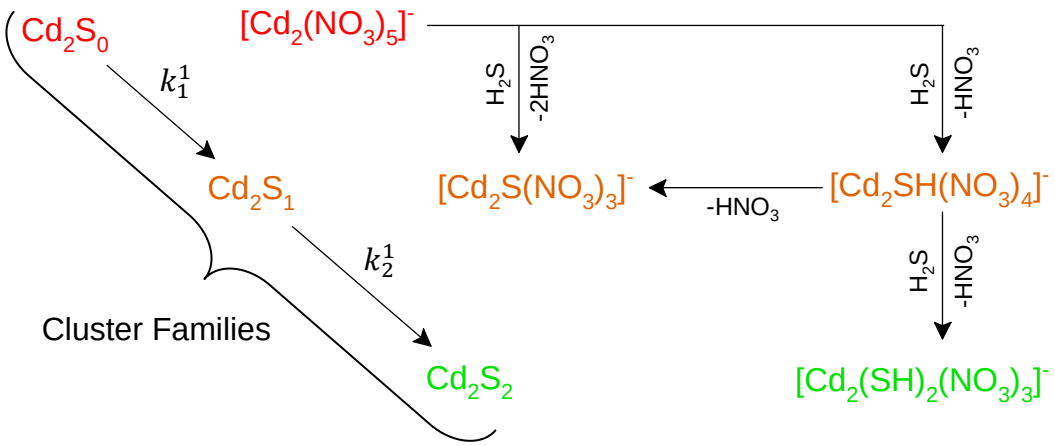

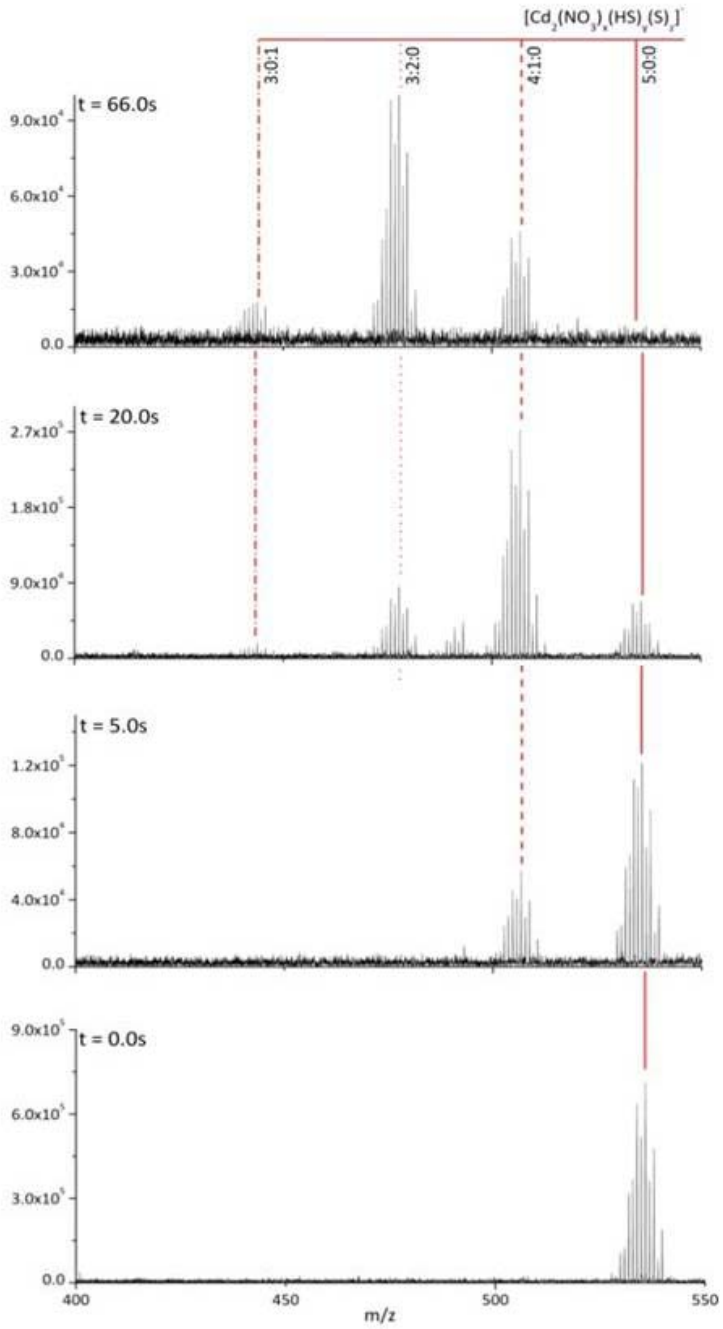

Figure 7.1. Mass spectra taken at different reaction times for the reaction between $[Cd_2(NO_3)_5]^-$ and H_2S (g). Results show the formation of various sulfidic product ions over time (Pressure = $4x10^{-9}$ Torr).

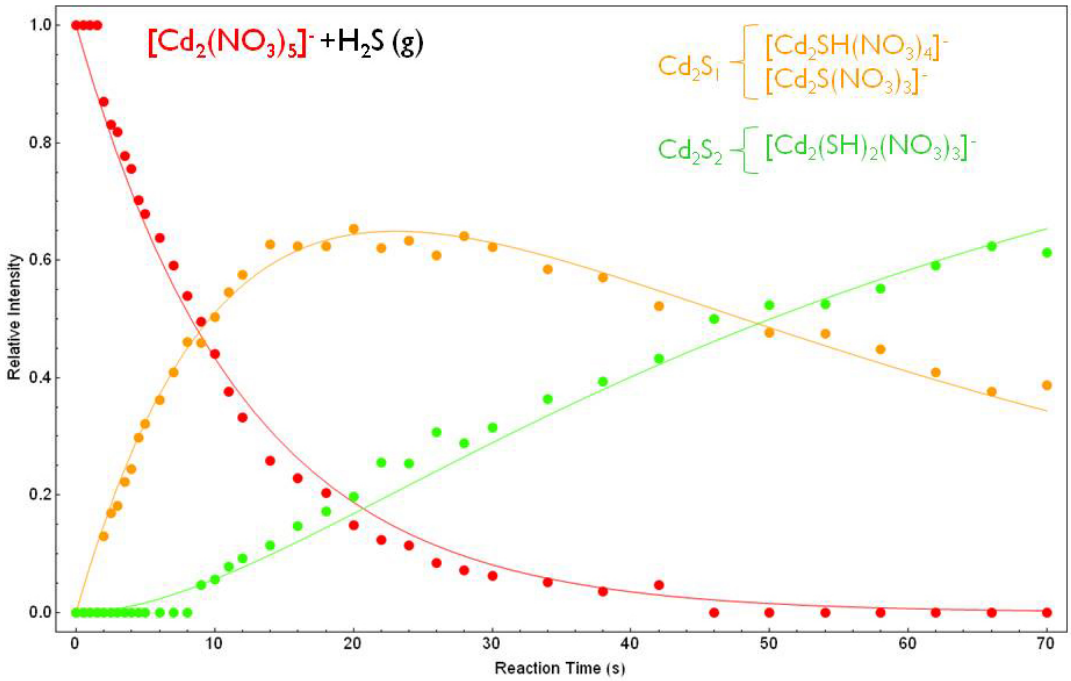

Figure 7.2. Kinetic plot for the substitution reaction of $[Cd_2(NO_3)_5]^-$ with hydrogen sulfide using a simplified sequential pseudo first-order model (Pressure = 4.0×10^{-9} Torr).

Table 7.1. Reaction efficiencies experimentally determined assuming sequential pseudo first-order kinetics for the reaction of anionic cadmium salt clusters with hydrogen sulfide.

Reactant	H_2S (torr)	k_1/k_c	k_2/k_c	k_3/k_c	k_4/k_c	k_5/k_c	k_6/k_c	k_7/k_c
$[Cd(CH_3COO)_3]^-$	$4x10^{-9}$	0.032	0.034	0.023				
$[Cd(CH_3COO)_3]^-$	$9x10^{-9}$	0.035	0.042	0.030				
$[Cd_2(CH_3COO)_5]^-$	$4x10^{-9}$	0.018	0.015	0.010	0.0020			
$[Cd_2(CH_3COO)_5]^-$	$9x10^{-9}$	0.019	0.015	0.0095	0.0034			
$[Cd_3(CH_3COO)_7]^-$	$4x10^{-9}$	0.015	0.14	0.038	0.011	0.019	0.0073	
$[Cd_3(CH_3COO)_7]^-$	$9x10^{-9}$	0.016	0.24	0.061	0.012	0.035	0.0082	
$[Cd_4(CH_3COO)_9]^-$	$4x10^{-9}$	0.013	0.034 (24) $^{\intercal}$	1.00*	1.00*	1.00*	0.0079	0.0097 (15) $^{\intercal}$
$[Cd_4(CH_3COO)_9]^-$	$9x10^{-9}$	0.013	0.042 (15)†	1.00*	1.00*	1.00*	0.0080	0.015
$[Cd(NO_3)_3]^-$	No Reaction Products Observed at $4x10^{-9}$ or $9x10^{-9}$ torr							
$[Cd_2(NO_3)_5]^-$	$4x10^{-9}$	0.031	0.0069					
$[Cd_3(NO_3)_7]^-$	$4x10^{-9}$	0.046	0.035	0.00090				
$[Cd_4(NO_3)_9]^-$	$4x10^{-9}$	0.0094	0.0090	0.017				
$[Cd_xCl_{2x+1}]^-$ (x = 1- 4)	No Reaction Products Observed at $4x10^{-9}$ or $9x10^{-9}$ torr							

*Assumed to be collision rate limited in cases where intermediate species were not observed.
†In cases in which error is greater than 9.5 %, the % error is indicated in parenthesis.

The observed product ions for the reactions between anionic cadmium nitrate salt clusters and hydrogen sulfide can be found in Table 7.2. No reaction products were detected for the single cadmium complex, $[Cd(NO_3)_3]^-$, at either $4.0x10^{-9}$ or $9.0x10^{-9}$ torr of H_2S. For larger cadmium nitrate clusters ($[Cd_x(NO_3)_{2x+1}]^-$, x = 2-4), reaction with hydrogen sulfide results in the substitution of nitrate ligands for bisulfide losing HNO_3 as a neutral. Sulfide ligands are then formed with the additional loss of nitric acid. The kinetic plots for each of these reaction sequences can be found in Figures 7.2-7.4. As can be seen in Table 7.1, these reactions are generally inefficient (k_x/k_c < 5%) and fairly constant for all steps of the reaction. Although larger metal clusters were not susceptible to examination using Gaussian (See Table 7.3) with our computing resources, theoretical results for the single anionic cadmium nitrate complex are consistent with experimental results. DFT calculations confirmed that the reaction between $[Cd(NO_3)_3]^-$ and H_2S is an endothermic process. These results are of particular importance in comparison to the solution based chemistry as discussed in Chapter 6. Similar to the observed gas phase ion-molecule reactions, solution reactions between cadmium nitrate clusters and H_2S displayed substitution of nitrate for sulfate in larger clusters while no sulfidic reaction products were observed for the single cadmium nitrate complex. This suggests the chemistry that governs the formation of metal sulfide clusters is similar in both gas and condensed phases.

Table 7.2. Observed product ions for the reaction between cadmium nitrate clusters and hydrogen sulfide.

Cluster Families	$[Cd(NO_3)_3]^-$	$[Cd_2(NO_3)_5]^-$	$[Cd_3(NO_3)_7]^-$	$[Cd_4(NO_3)_9]^-$
Cd_xS_1		$[Cd_2SH(NO_3)_4]^-$	$[Cd_3SH(NO_3)_6]^-$	$[Cd_4SH(NO_3)_8]^-$
		$[Cd_2S(NO_3)_3]^-$	$[Cd_3S(NO_3)_5]^-$	$[Cd_4S(NO_3)_7]^-$
Cd_xS_2		$[Cd_2(SH)_2(NO_3)_3]^-$	$[Cd_3S(SH)(NO_3)_4]^-$	$[Cd_4S(SH)(NO_3)_6]^-$
				$[Cd_4S_2(NO_3)_5]^-$
Cd_xS_3			$[Cd_3S(SH)_2(NO_3)_3]^-$	$[Cd_4S_2(SH)(NO_3)_4]^-$

■: No reaction products observed

Table 7.3. Theoretical reaction energies for the reactions between mononuclear salt complexes and hydrogen sulfide in relation to experimentally determined reaction efficiencies.

Modeled Complexes	ΔE (kcal/mol)	k_1/k_c
$[Cd(NO_3)_3]^-$	9.7109	No Observed reaction
$[Cd(CH_3COO)_3]^-$	-6.2361	0.032
$[CdCl_3]^-$	8.8246	No Observed Reaction
$[CdNO_3]^+$	-17.4419	1.00*
$[CdOH]^+$	-27.1828	0.77*
$[CdCl]^+$	-11.1628	0.16*
$[ZnCl]^+$	-11.9029	0.037*

■: No reaction products observed; *k_1/k_c values are for solvated (CH_3OH) forms of these ions.

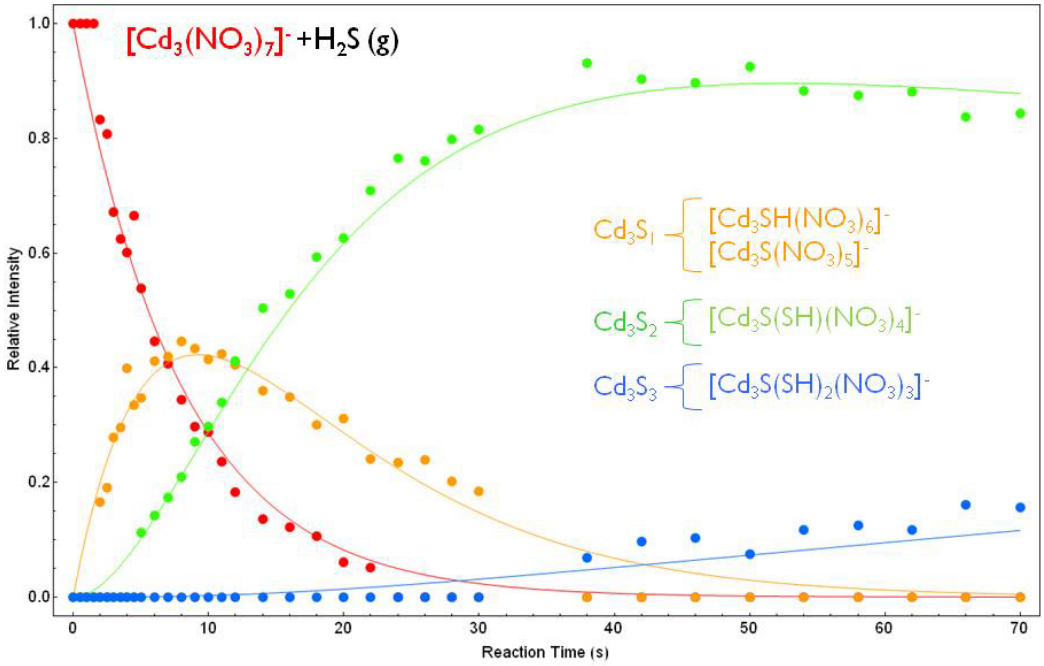

Figure 7.3. Kinetic plot for the substitution reaction of $[Cd_3(NO_3)_7]^-$ with hydrogen sulfide using a simplified sequential pseudo first-order model (Pressure = 4.0×10^{-9} Torr).

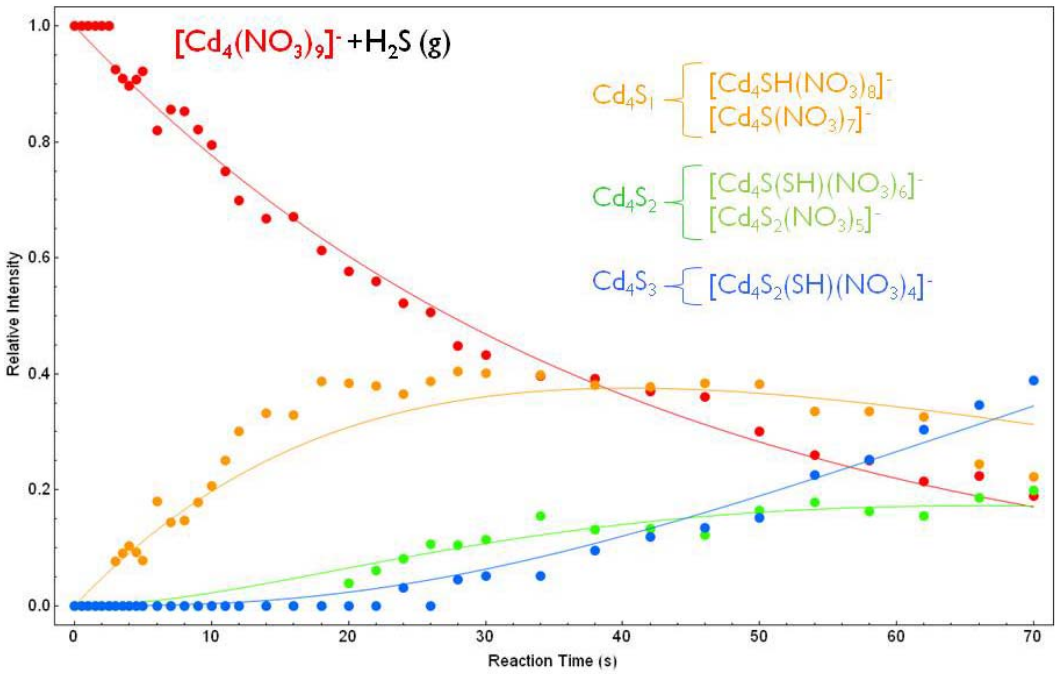

Figure 7.4. Kinetic plot for the substitution reaction of $[Cd_4(NO_3)_9]^-$ with hydrogen sulfide using a simplified sequential pseudo first-order model (Pressure = 4.0×10^{-9} Torr).

The detected products for the reaction between cadmium acetate clusters ($[Cd_x(CH_3COO)_{2x+1}]^-$, x=1-4) and H_2S can be found in Table 7.4. Unlike cadmium nitrate, hydrogen sulfide reactivity was observed for all examined anionic cadmium acetate clusters. As seen in Figure 7.5, the single cadmium acetate complex ($[Cd(CH_3COO)_3]^-$) displays successive acetate ligand substitutions for bisulfide displacing HOAc as a neutral. Experimentally determined reaction efficiencies (Table 7.1) show substitution of all three ligands to be a fairly slow process (k_x/k_c < 5%). Observed reactivity for this complex is rationalized by the theoretical results (Table 7.3) showing the first step of this reaction to be energetically favorable (ΔE = -6.2361). $[Cd_2(CH_3COO)_5]^-$ and $[Cd_3(CH_3COO)_7]^-$ exhibit similar reactivity to

their nitrate cluster counterparts (See Scheme 7.2) forming both bisulfide and sulfide ligated clusters with generally low reaction efficiencies for all steps in the reaction sequence (Table 7.1). Kinetic plots for these reactions can be found in Figures 7.6 and 7.7 respectively.

Table 7.4. Observed product ions for the reaction between cadmium acetate clusters and hydrogen sulfide.

Cluster Families	$[Cd(OAc)_3]^-$	$[Cd_2(OAc)_5]^-$	$[Cd_3(OAc)_7]^-$	$[Cd_4(OAc)_9]^-$
Cd_xS_1	$[CdSH(OAc)_2]^-$	$[Cd_2SH(OAc)_4]^-$ $[Cd_2S(OAc)_3]^-$	$[Cd_3S(OAc)_5]^-$	$[Cd_4S(OAc)_7]^-$
Cd_xS_2	$[Cd(SH)_2(OAc)]^-$	$[Cd_2(SH)_2(OAc)_3]^-$ $[Cd_2S(SH)\ OAc)_2]^-$	$[Cd_3S(SH)(\ OAc)_4]^-$	
Cd_xS_3	$[Cd(SH)_3]^-$	$[Cd_2S(SH)_2(OAc)]^-$	$[Cd_3S(SH)_2(OAc)_3]^-$	
Cd_xS_4		$[Cd_2S(SH)_3]^-$	$[Cd_3S(SH)_3(OAc)_2]^-$	
Cd_xS_5			$[Cd_3S(SH)_4(OAc)]^-$ $[Cd_3S_2(SH)_3]^-$	$[Cd_4S_2(SH)_3(OAc)_2]^-$
Cd_xS_6			$[Cd_3S(SH)_4]^-$	$[Cd_4S_2(SH)_4(OAc)]^-$ $[Cd_4S_3(SH)_3]^-$
Cd_xS_7				$[Cd_4S_2(SH)_5]^-$

OAc: Acetate Ligand (CH_3COO^-), ■: No reaction products observed

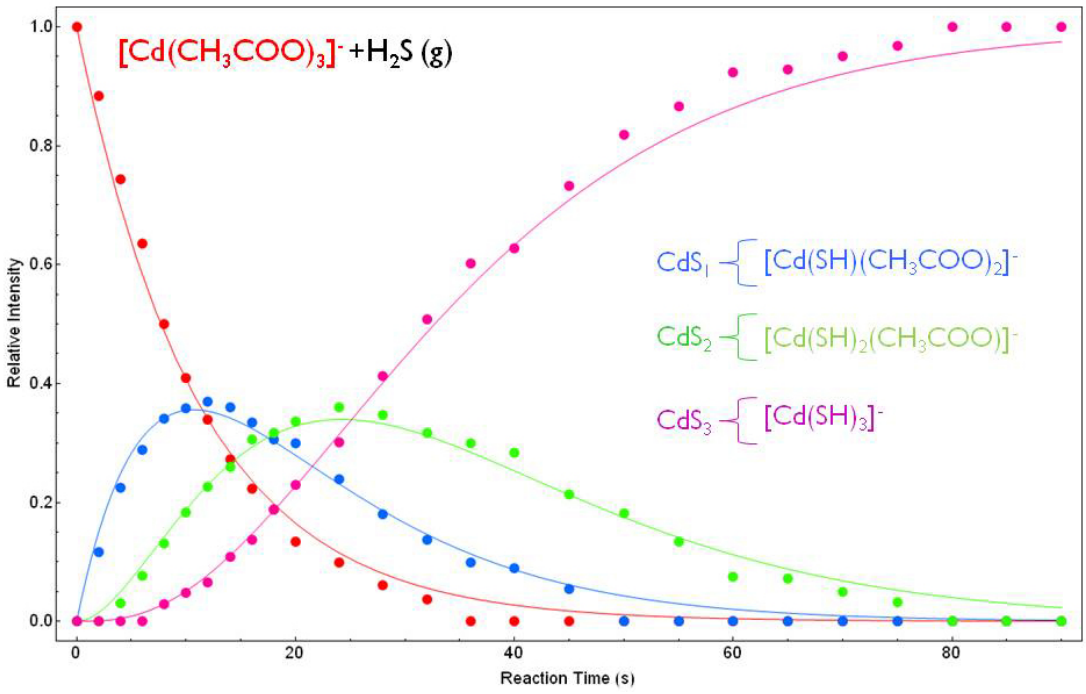

Figure 7.5. Kinetic plot for the substitution reaction of $[Cd(CH_3COO)_3]^-$ with hydrogen sulfide using a simplified sequential pseudo first-order model (Pressure = 4.0×10^{-9} Torr).

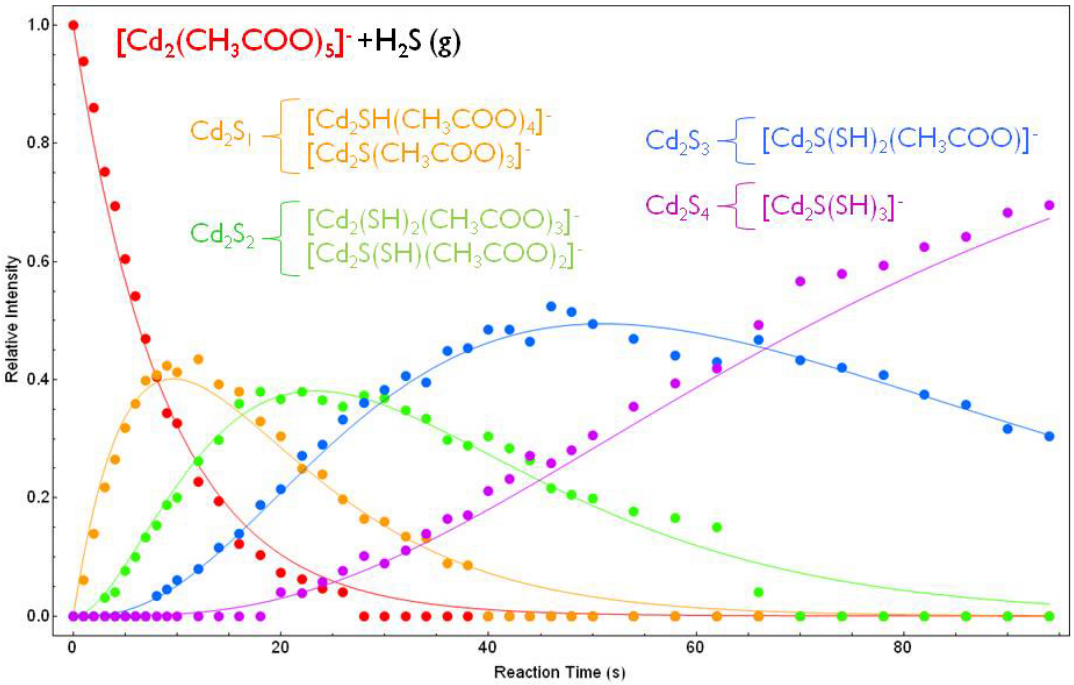

Figure 7.6. Kinetic plot for the substitution reaction of $[Cd_2(CH_3COO)_5]^-$ with hydrogen sulfide using a simplified sequential pseudo first-order model (Pressure = 4.0×10^{-9} Torr).

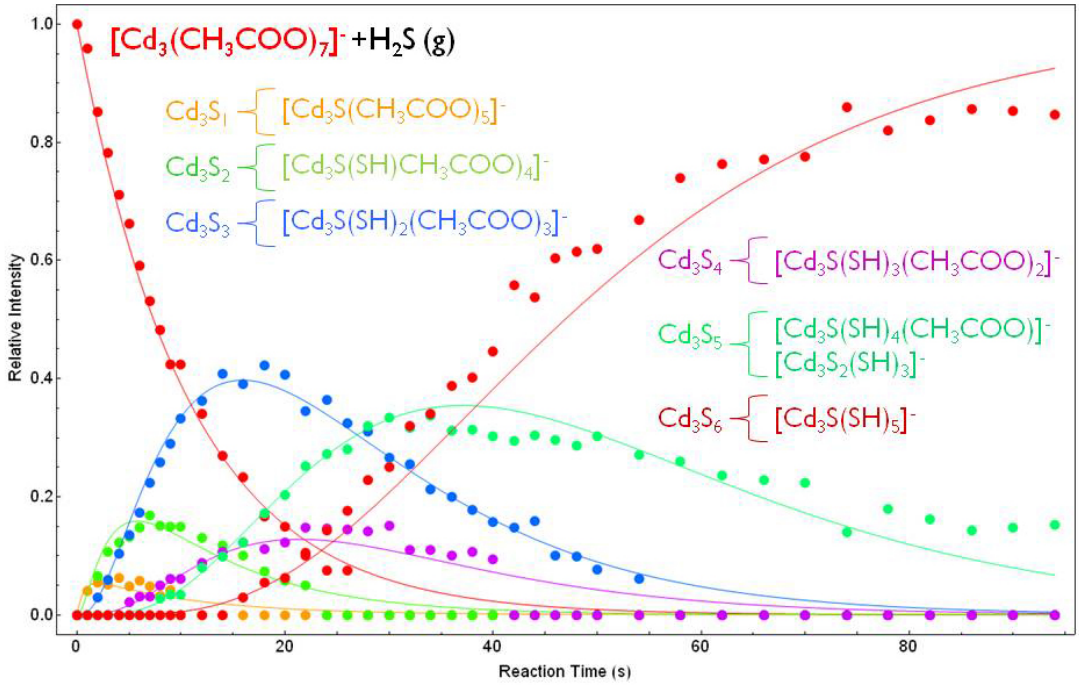

Figure 7.7. Kinetic plot for the substitution reaction of $[Cd_3(CH_3COO)_7]^-$ with hydrogen sulfide using a simplified sequential pseudo first-order model (Pressure = 4.0×10^{-9} Torr).

Unique in comparison to all other reactions reported is the interaction between $[Cd_4(CH_3COO)_9]^-$ and H_2S. Similar to other systems, $[Cd_4(CH_3COO)_9]^-$ reacts to form sulfidic clusters with both bisulfide and sulfide ligands with the initial steps of this process being rather inefficient (See Table 7.1). However, only initial (Cd_4S_1) and final (Cd_4S_5 - Cd_4S_7) product clusters are observed for this reaction sequence at both pressures tested (4.0×10^{-9} and 9.0×10^{-9} torr). The lack of intermediate species (Cd_4S_2, Cd_4S_3, and Cd_4S_4) suggests that the reaction efficiencies associated with these products (k_3/k_c, k_4/k_c and k_5/k_c) must be very high. A combination of high efficiency for these middle steps along with very slow initial

steps would not allow any significant build up of intermediate products. To model this system it was assumed that k_3/k_c, k_4/k_c and k_5/k_c were collision rate limited as highlighted in Scheme 7.3. The kinetic plot for this reaction (Figure 7.8) shows the fits using this model to be reasonable suggesting that it is an appropriate description of the reaction sequence. The fast intermediate reactions of this cluster are unusual in that they are the most efficient processes observed in larger clusters. Overall, anionic clusters are characterized by slower reactions which can be explained, in comparison to their cationic counterparts, in that they have fewer open metal coordination sites. Moreover, in the case of cadmium acetate, the additional ligands in the anionic clusters would be expected to further slow substitution reactions due to negative steric effects caused by the methyl groups. With that said, the enhanced reactivity of $[Cd_4(CH_3COO)_9]^-$ seems to point to unique structural features in comparison to similar systems.

Scheme 7.3

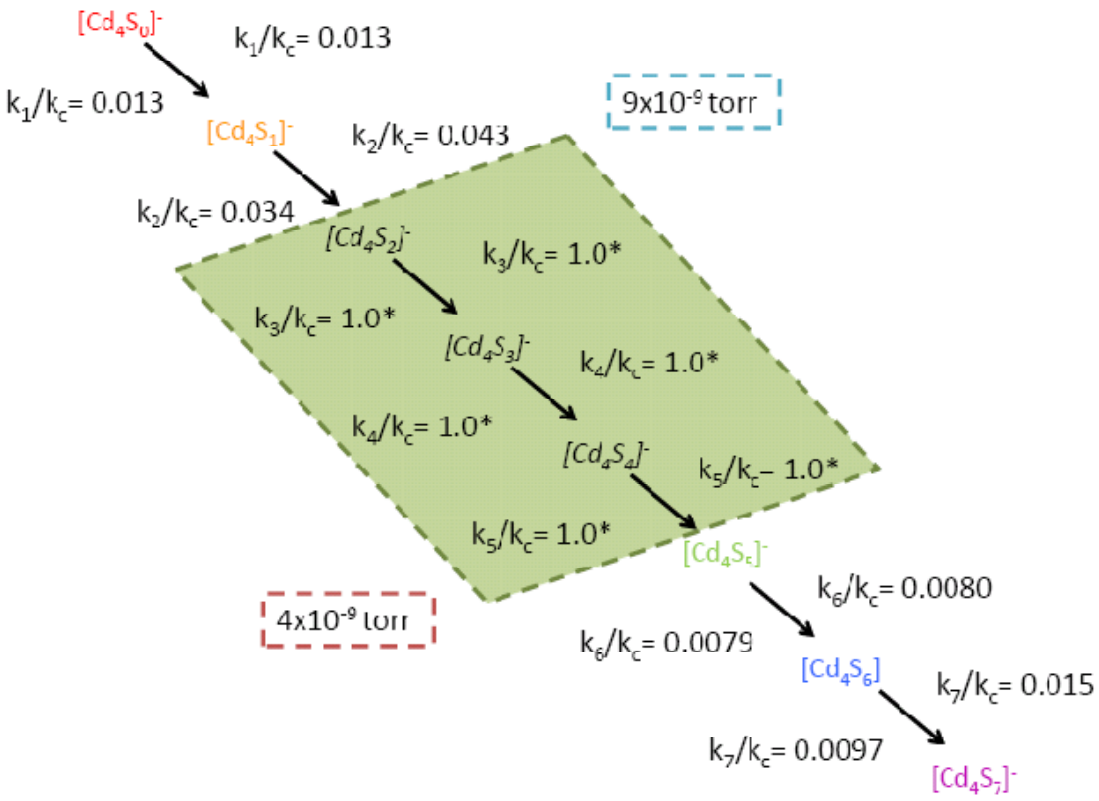
[Cd4S0]-
k1/kc= 0.013
k1/kc= 0.013
[Cd4S1]-
k2/kc= 0.043
9x10-9 torr
k2/kc= 0.034
[Cd4S2]-
k3/kc= 1.0*
k3/kc= 1.0*
[Cd4S3]-
k4/kc= 1.0*
k4/kc= 1.0*
[Cd4S4]-
k5/kc– 1.0*
k5/kc= 1.0*
[Cd4S5]-
4x10-9 torr
k6/kc= 0.0080
k6/kc= 0.0079
[Cd4S6]
k7/kc= 0.015
k7/kc= 0.0097
[Cd4S7]-

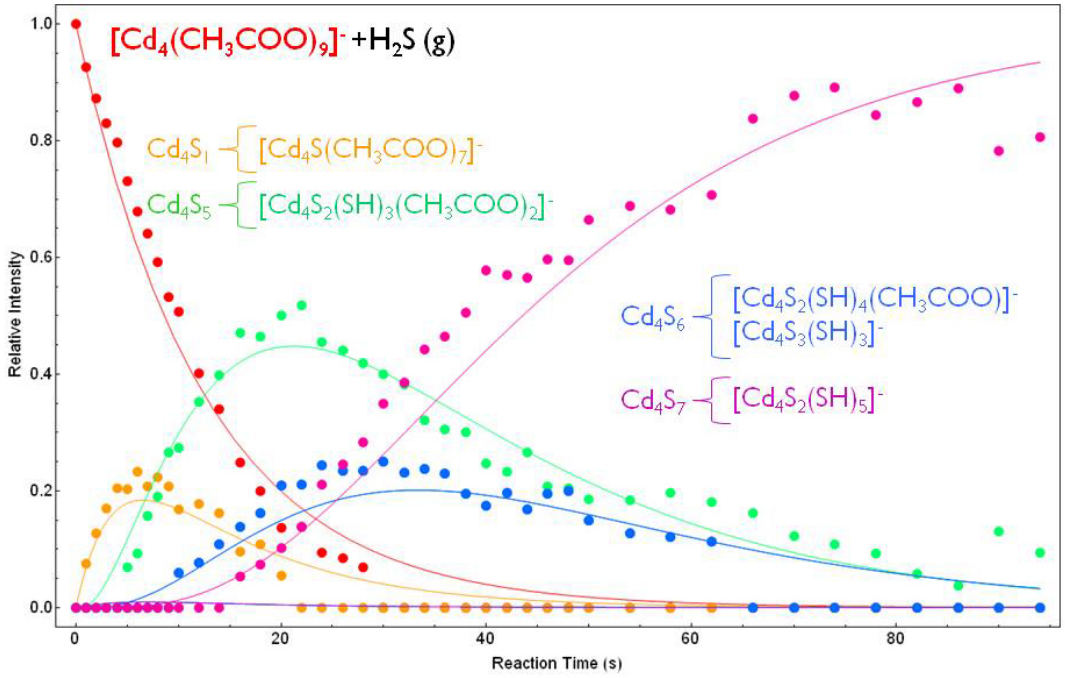

Figure 7.8. Kinetic plot for the substitution reaction of $[Cd_4(CH_3COO)_9]^-$ with hydrogen sulfide using a simplified sequential pseudo first-order model (Pressure = 4.0×10^{-9} Torr).

7.3.2 Cationic Reactions

Cationic clusters produced by positive mode electrospray vary greatly depending on the specific salt solution being analyzed. Similar to clusters observed in negative mode, ESI of cadmium acetate solutions generates a series of cationic clusters of the type $[Cd_x(CH_3COO)_{2x-1}]^+$ (x = 2-4). However, for cadmium acetate solutions no single cadmium complexes were detected while operating in positive mode. On the other hand, for all other metal salt solutions analyzed in positive mode ($Cd(NO_3)_2$, $CdCl_2$, and $ZnCl_2$) only solvated single metal complexes were able to be isolated for reaction with hydrogen sulfide. Additionally, $[CdOH(CH_3OH)]^+$ was

produced using cadmium nitrate solutions presumably from substitution of the nitrate ligand by water forming the hydroxy complex. Although solvated complexes were not able to be modeled using Gaussian, DFT calculations show reaction of all relevant cationic clusters to be energetically favorable (Table 7.3). As with the anionic reactions, all cationic systems were modeled as sequential pseudo first-order processes by organizing product ions into families based on the total number of sulfur atoms added. Reaction efficiencies for the cationic systems can be found in Table 7.5.

Table 7.5. Reaction efficiencies experimentally determined assuming sequential pseudo first-order kinetics for the reaction of anionic cadmium salt clusters with hydrogen sulfide.

Reactant	H_2S (torr)	k_1/k_c	k_2/k_c	k_3/k_c	k_4/k_c	k_5/k_c
$[Cd_2(CH_3COO)_3]^+$	$4x10^{-9}$	0.77	00.0033	0.0045		
$[Cd_3(CH_3COO)_5]^+$	$4x10^{-9}$	0.92	0.072	0.0045	0.0013	
$[Cd_3(CH_3COO)_5]^+$	$9x10^{-9}$	0.88	0.073	0.0062	0.0066	
$[Cd_4(CH_3COO)_7]^+$	$9x10^{-9}$	0.37	0.54	0.28	0.0029	0.0016
$[Cd\ NO_3(CH_3OH)(H_2O)]^+$	$4x10^{-9}$	0.61				
$[Cd\ NO_3(CH_3OH)]^+$	$4x10^{-9}$	1.00‡				
$[Cd\ OH(CH_3OH)]^+$	$4x10^{-9}$	0.77				
$[Cd\ Cl(CH_3OH)]^+$	$4x10^{-9}$	0.16				
$[Zn\ Cl(CH_3OH)]^+$	$4x10^{-9}$	0.037				

‡Assumed to be a collision rate limited process.

The observed product ions for the reaction between cationic cadmium acetate salt clusters and hydrogen sulfide can be found in Table 7.6. As mentioned earlier, no single cadmium complexes were detected using positive mode ESI. The product ions for the reaction between larger cationic cadmium acetate clusters ($[Cd_x(CH_3COO)_{2x-1}]^+$, x = 2-4) and hydrogen sulfide are much different than those seen for the similar anionic clusters. As can be seen in Table 7.5, the initial reaction steps are much more efficient ($k_x/k_c \geq 37\%$) for the cationic reactions. These first steps are associated with substitution of acetate by bisulfide ligands losing CH_3COOH as a neutral. Again, similar to anionic clusters, the cadmium bisulfide species undergo unimolecular reactions losing acetic acid to form sulfide ligands at longer reaction times. Unique to the cationic reactions, the reaction efficiency decreases greatly ($k_x/k_c < 7\%$) as the reaction proceeds. At longer time scales, these more inefficient processes are linked to H_2S addition reactions. It should be noted that it is unknown whether H_2S is simply being added to the cationic cluster or if the bisulfide species is formed and not enough energy is released to eject CH_3COOH. Scheme 7.4 illustrates this complex reaction sequence for $[Cd_4(CH_3COO)_7]^+$. This reaction scheme, in particular, highlights the necessity of the simplified 'cluster family' model. Kinetic plots for reactions between $[Cd_x(CH_3COO)_{2x-1}]^+$ (x = 2-4) and hydrogen sulfide can be found in Figures 7.9-7.11.

Table 7.6. Observed product ions for the reaction between cadmium acetate clusters and hydrogen sulfide.

Cluster Families	$[Cd_2(OAc)_3]^+$	$[Cd_3(OAc)_5]^+$	$[Cd_4(OAc)_7]^+$
Cd_xS_1	$[Cd_2SH(OAc)_2]^+$	$[Cd_3SH(OAc)_4]^+$ $[Cd_3(OAc)_3(H_2S)]^+$	$[Cd_4SH(OAc)_6]^+$
Cd_xS_2	$[Cd_2SH(OAc)_2(H_2S)]^+$	$[Cd_3(SH)_2(OAc)_3]^+$ $[Cd_3SH(OAc)_4(H_2S)]^+$	$[Cd_4(SH)_2(OAc)_5]^+$ $[Cd_4S(SH)(OAc)_4]^+$ $[Cd_4SH(OAc)_6(H_2S)]^+$
Cd_xS_3	$[Cd_2SH(OAc)_2(H_2S)_2]^+$	$[Cd_3(SH)_3(OAc)_2]^+$ $[Cd_3(SH)_2(OAc)_3(H_2S)]^+$	$[Cd_4(SH)_3(OAc)_4]^+$ $[Cd_4S(SH)_2(OAc)_3]^+$ $[Cd_4(SH)_2(OAc)_5(H_2S)]^+$
Cd_xS_4		$[Cd_3(SH)_3(OAc)_2(H_2S)]^+$	$[Cd_4(SH)_4(OAc)_3]^+$ $[Cd_4S(SH)_3(OAc)_2]^+$ $[Cd_4(SH)_3(OAc)_4(H_2S)]^+$
Cd_xS_5			$[Cd_4S(SH)_4(OAc)]^+$ $[Cd_4S(SH)_3(OAc)_2(H_2S)]^+$

OAc: Acetate Ligand (CH_3COO^-), ■: No reaction products observed

Scheme 7.4

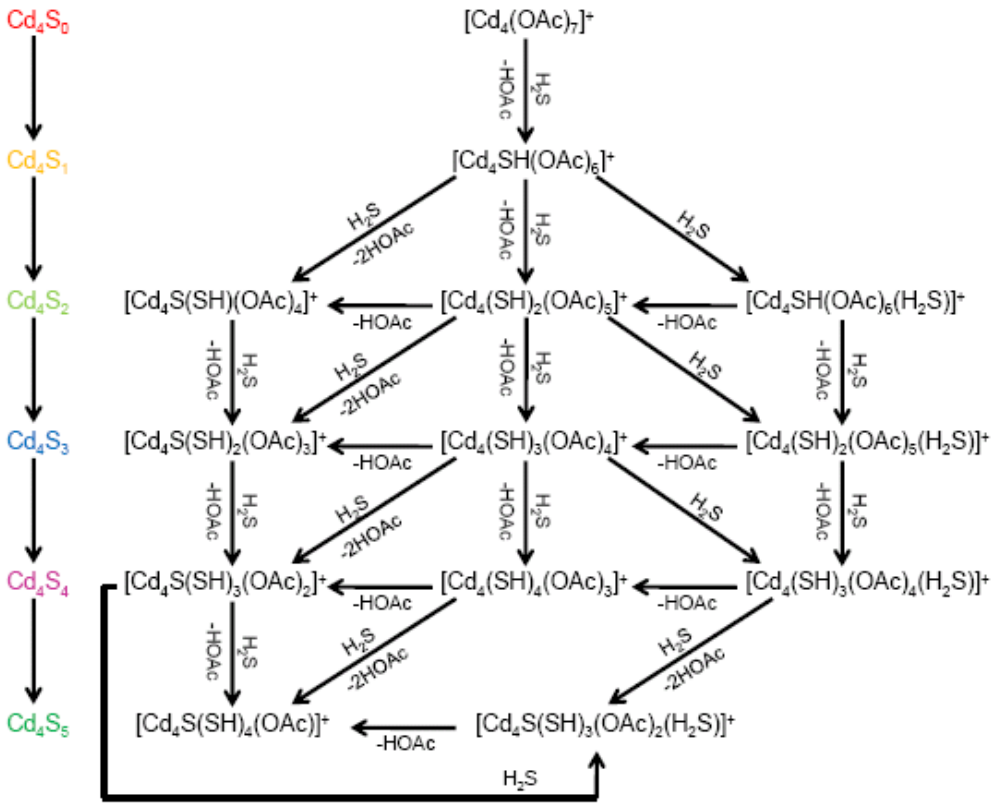
Cd4S0
Cd4S1
Cd4S2
Cd4S3
Cd4S4
Cd4S5
[Cd4(OAc)7]+
[Cd4SH(OAc)6]+
[Cd4S(SH)(OAc)4]+
[Cd4(SH)2(OAc)5]+
[Cd4SH(OAc)6(H2S)]+
[Cd4S(SH)2(OAc)3]+
[Cd4(SH)3(OAc)4]+
[Cd4(SH)2(OAc)5(H2S)]+
[Cd4S(SH)3(OAc)2]+
[Cd4(SH)4(OAc)3]+
[Cd4(SH)3(OAc)4(H2S)]+
[Cd4S(SH)4(OAc)]+
[Cd4S(SH)3(OAc)2(H2S)]+
-HOAc
H2S
-2HOAc
H2S

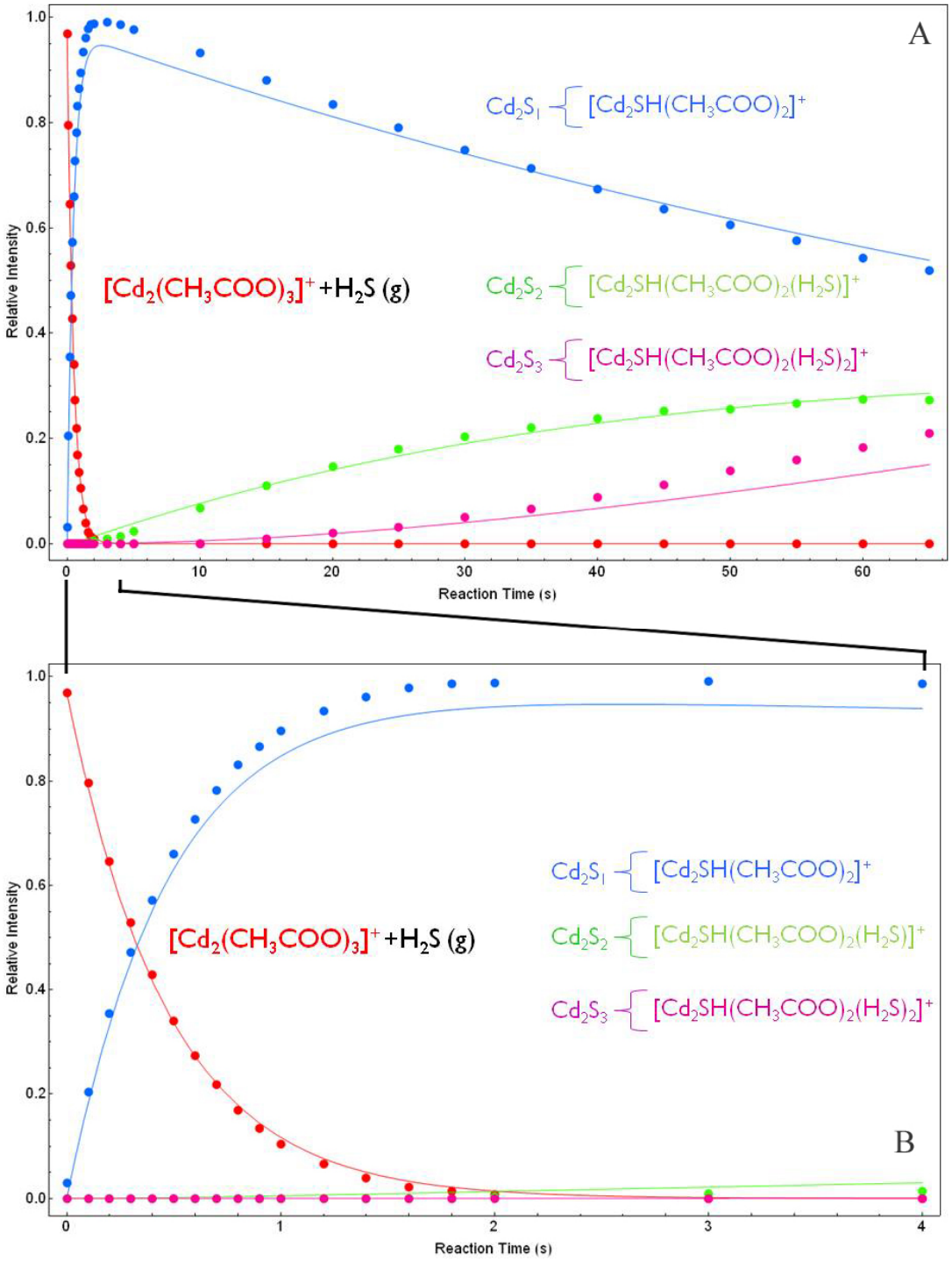

Figure 7.9. Kinetic plot for the substitution reaction of $[Cd_2(CH_3COO)_3]^+$ with hydrogen sulfide using a simplified sequential pseudo first-order model (Pressure = 4.0×10^{-9} Torr).

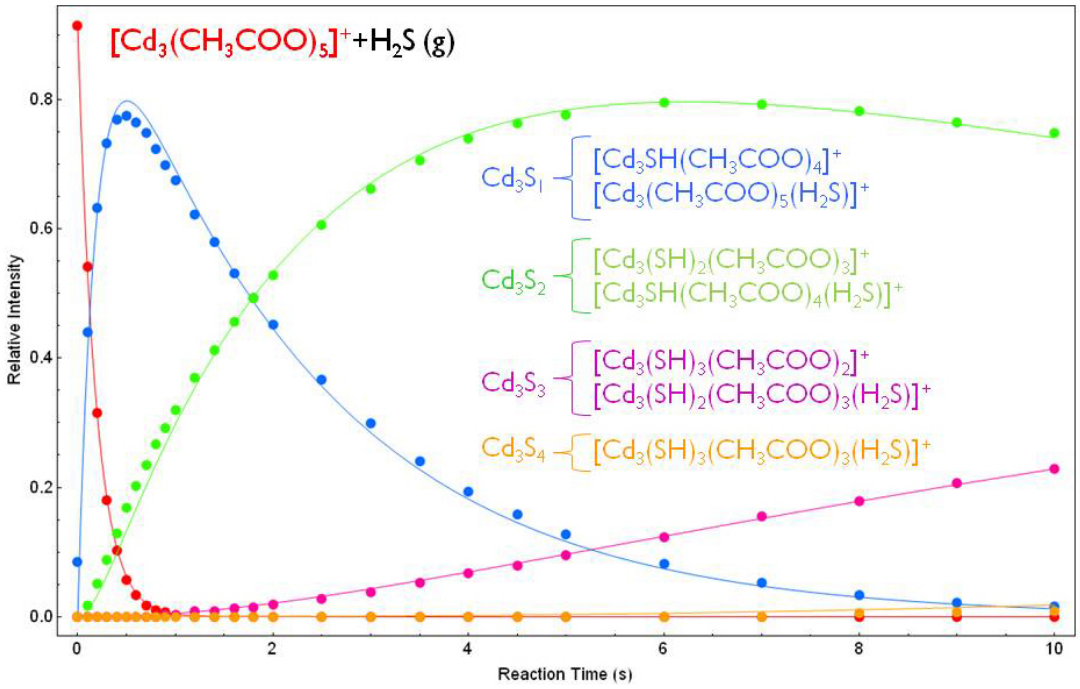

Figure 7.10. Kinetic plot for the substitution reaction of $[Cd_3(CH_3COO)_5]^+$ with hydrogen sulfide using a simplified sequential pseudo first-order model (Pressure = 9.0×10^{-9} Torr).

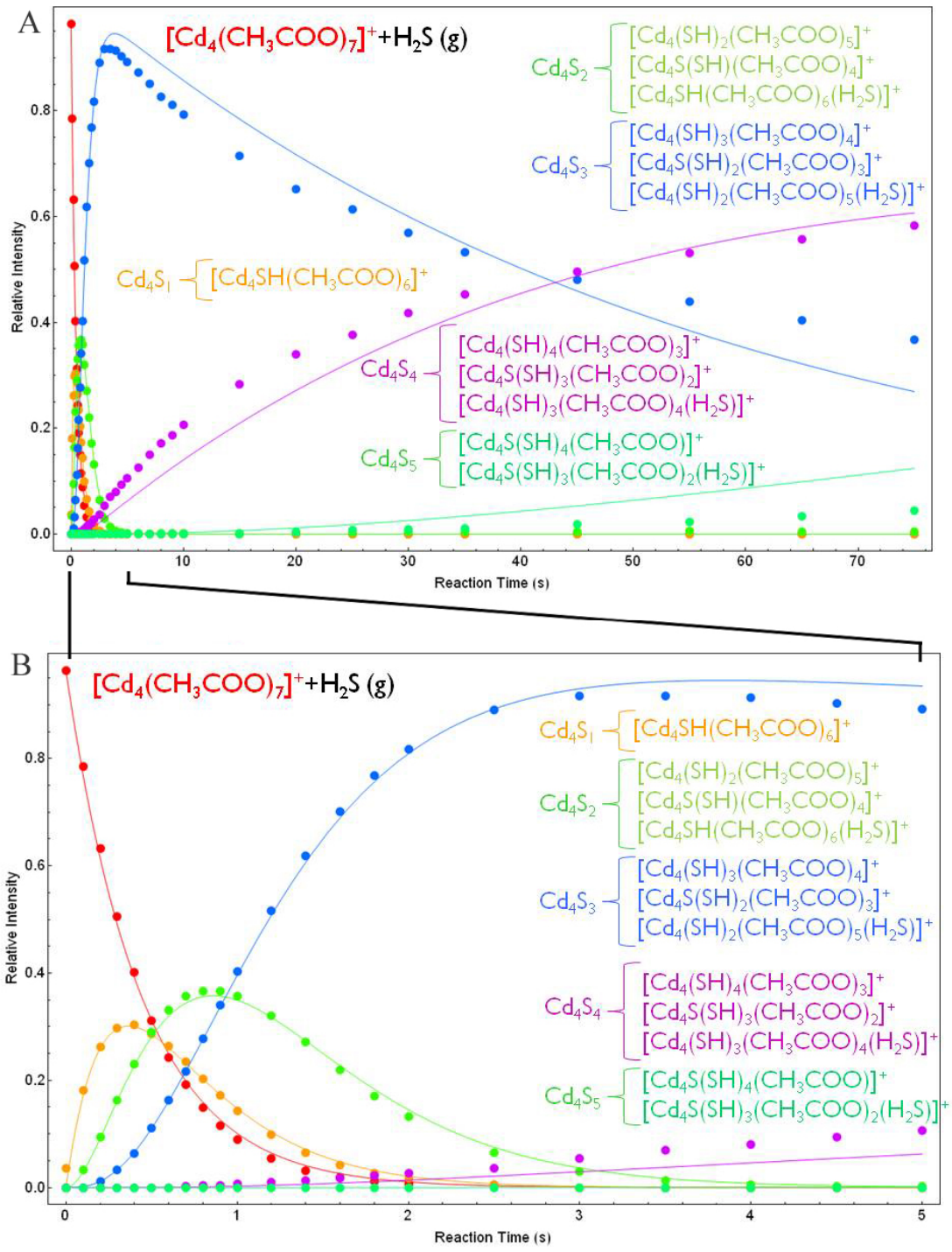

Figure 7.11. Kinetic plot for the substitution reaction of $[Cd_4(CH_3COO)_7]^+$ with hydrogen sulfide using a simplified sequential pseudo first-order model (Pressure = 9.0×10^{-9} Torr).

The last group of reactions studied was between solvated metal salt complexes and hydrogen sulfide. Observed reaction products can be found in Table 7.7 and kinetic plots can be found in Figures 7.12-7.15. In all cases, the primary reaction channel involves simple substitution of the lone anionic ligand for bisulfide with the bound solvent molecules remaining following the reaction. For the reaction between $[CdCl(CH_3OH)]^+$ and H_2S (Table 7.7, Figure 7.14) a minor channel stemming from substitution of the solvent molecule for H_2S is observed. It should be noted, however, that $[CdSH(CH_3OH)]^+$ is the dominate reaction product. The persistence of solvent molecules throughout the reaction suggests that they do not play a role in the chemistry of metal sulfide formation. This further demonstrates the suitability of gas phase ion-molecule reactions as models for aqueous metal sulfide reactions.

The reactions of cationic complexes allow for a number of important comparisons to be made. The cadmium nitrate complexes ($[CdNO_3(CH_3OH)(H_2O)]^+$ and $[CdNO_3(CH_3OH)]^+$) show a decrease in reaction efficiency (Table 7.5) with an increase in solvation highlighting solvent shell effects on reactivity. The cationic cadmium complexes also illustrate effects of counter ion on reactivity with the order being $NO_3^- > OH^- > Cl^-$ in terms of reaction efficiency (Table 7.5). Comparisons between cadmium and zinc were also made (Table 7.5) showing the reaction of H_2S with $[CdCl(CH_3OH)]^+$ to be much more efficient than $[ZnCl(CH_3OH)]^+$.

Table 7.7. Observed product ions for the reaction between cadmium acetate clusters and hydrogen sulfide.

Cluster Families	CdS_1	CdS_2
$[CdNO_3(CH_3OH)(H_2O)]^+$	$[CdSH(CH_3OH)(H_2O)]^+$	
$[CdNO_3(CH_3OH)]^+$	$[CdSH(CH_3OH)]^+$	
$[CdOH(CH_3OH)]^+$	$[CdSH(CH_3OH)]^+$	
$[CdCl(CH_3OH)]^+$	$[CdSH(CH_3OH)]^+$ $[CdCl(H_2S)]^+$ $[CdSH]^+$	$[CdSH(H_2S)]^+$
$[ZnCl(CH_3OH)]^+$	$[CdSH(CH_3OH)]^+$	

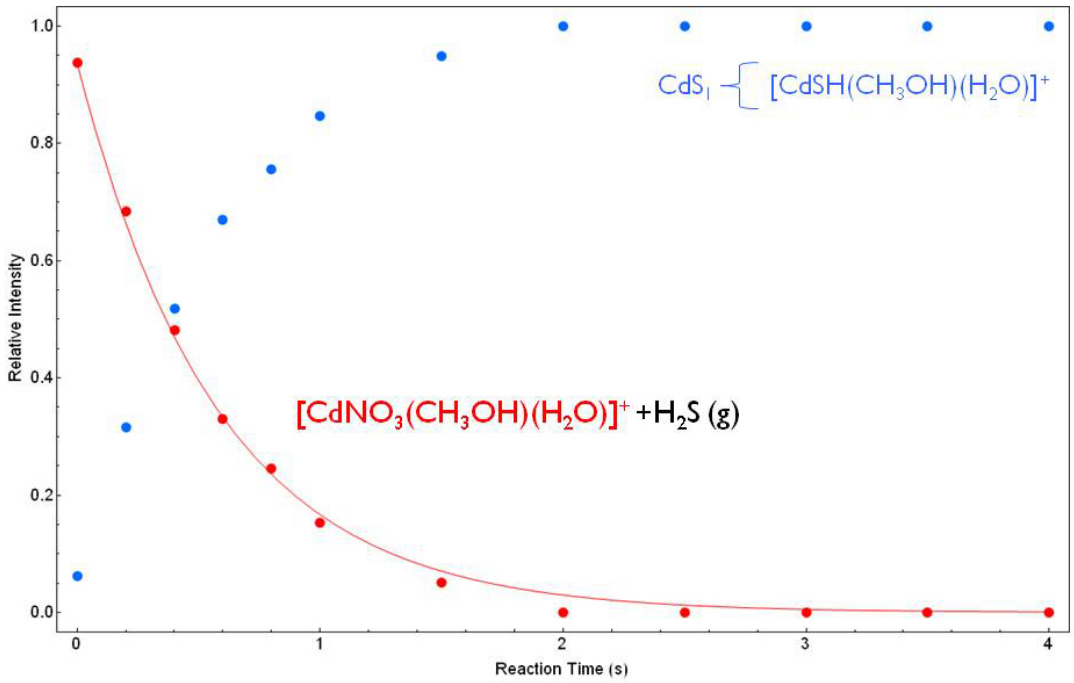

Figure 7.12. Kinetic plot for the substitution reaction of $[CdNO_3(CH_3OH)(H_2O)]^+$ with hydrogen sulfide (Pressure = 4.0×10^{-9} Torr).

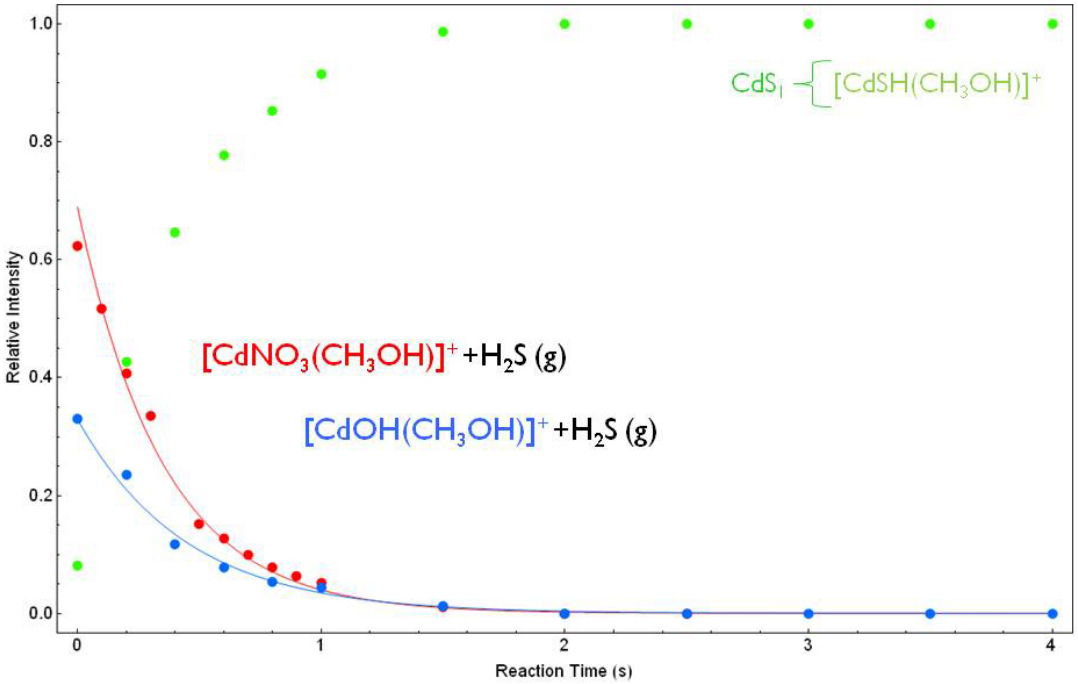

Figure 7.13. Kinetic plot for the substitution reaction of $[CdNO_3(CH_3OH)]^+$ and $[CdOH(CH_3OH)]^+$ with hydrogen sulfide using a simplified sequential pseudo first-order model (Pressure = 4.0×10^{-9} Torr).

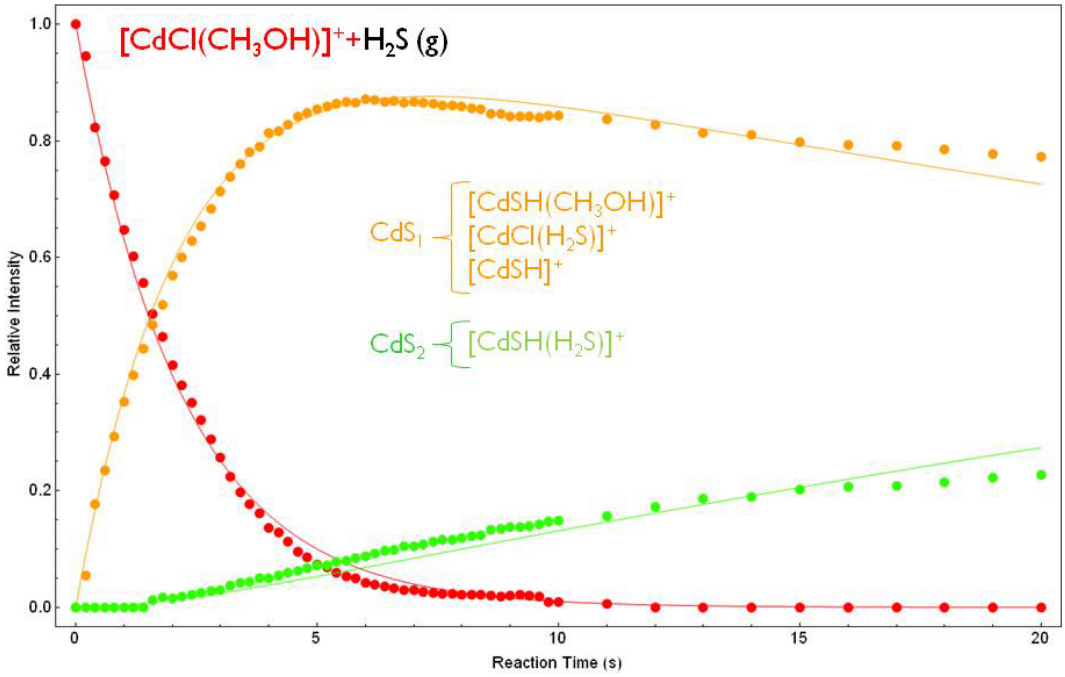

Figure 7.14. Kinetic plot for the substitution reaction of $[CdCl(CH_3OH)]^+$ with hydrogen sulfide using a simplified sequential pseudo first-order model (Pressure = 4.0×10^{-9} Torr).

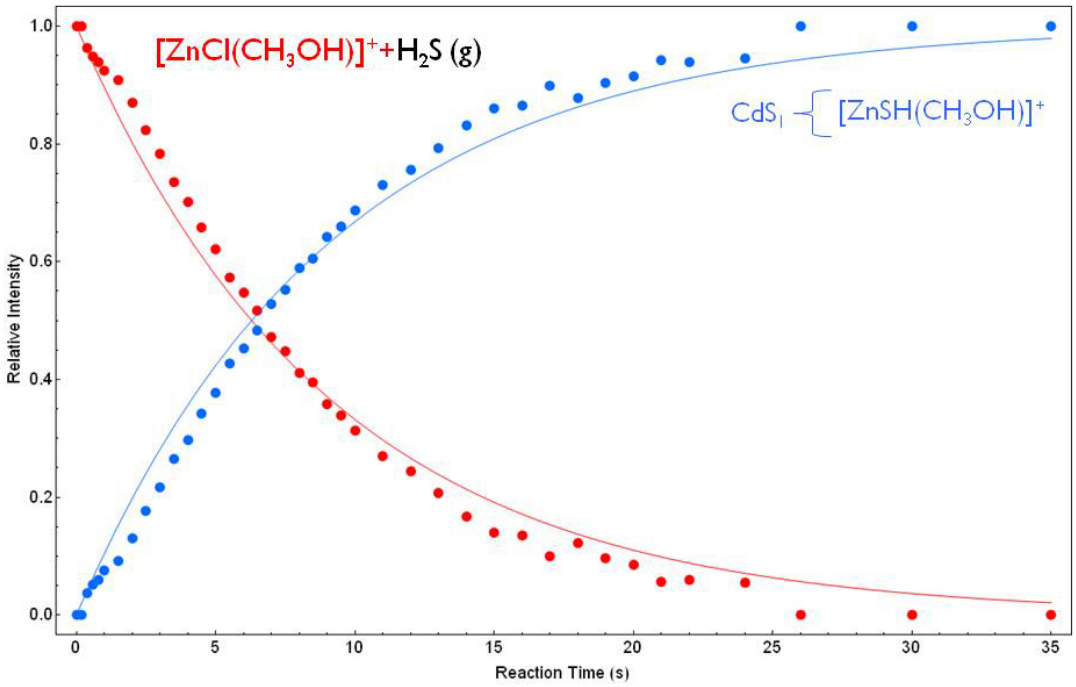

Figure 7.15. Kinetic plot for the substitution reaction of $[ZnCl(CH_3OH)]^+$ with hydrogen sulfide using a simplified sequential pseudo first-order model (Pressure = 4.0×10^{-9} Torr).

7.4 Conclusions

Gas phase ion-molecule reactions between metal salt clusters and hydrogen sulfide were described using a simplified sequential pseudo first-order kinetic model. Reaction energies, determined using DFT calculations, were consistent with all observed reactions. Anionic reactions were shown to proceed with low reaction efficiencies (k_x/k_c < 5%) except for the reaction between $[Cd_4(CH_3COO)_9]^-$ and H_2S in which intermediate steps were shown to proceed very rapidly after initial

sulfide substitution. No reaction products were observed for any anionic cadmium chloride cluster. Cationic metal salt clusters were shown to react with much higher efficiencies, however, reaction rates decrease substantially in later reaction steps. Although bound solvent molecules were shown to not participate in ligand substitution reactions, an increase in the number of solvent molecules resulted in a decrease in reaction efficiency presumably due to steric effects. Additionally, evaluation of the ligands tested showed $NO_3^- > OH^- > Cl^-$ in terms of reaction efficiency while higher reaction rates were observed for cadmium in comparison to zinc. Gas phase ion-molecule reactions were also found to be consistent with the observed solution phase reactivity of cadmium nitrate clusters. This comparison, in combination with the results for solvated cationic complexes, suggest that gas phase ion-molecule reactions of metal salt clusters with hydrogen sulfide can be used as models for metal sulfide formation in aqueous systems.

The reactions between metal salt clusters and hydrogen sulfide may represent the initial steps in the continuum going from dissolved ions to solid particulate matter and therefore are the foundation for understanding metal sulfide formation and nucleation. The direct observation of cadmium salt growth in aqueous solutions and the similarities between the gas-phase and solution-phase reactivity for cadmium nitrate clusters allow for speculation as to how metal sulfide nucleation reactions proceed. Particularly in hydrothermal systems where metal concentrations are high, our data suggests that small metal sulfide molecular species may not be the building blocks of particulate matter. Instead, at least initially, cluster growth seems to proceed through the addition of metal salt units. These salt clusters can then react with H_2S as highlighted in our results. Additionally, our results may point to anionic

metal sulfide species overshadowing both cationic and neutral species in initiating cluster growth in aquatic environments. Neutral and cationic clusters have open binding sites which would presumably be occupied by solvent molecules in solution. We propose that sulfidic ligands (HS^- or S^{2-}) would readily displace the bound neutral solvent molecules due to the strong binding energy associated with the formation of metal sulfide bonds. The strength of the metal-sulfur interaction is demonstrated by formation of HNO_3 and HCl as products of the reaction between metal salt clusters and H_2S despite the fact that these species are strong acids.

Finally, it should be noted that these studies outline methods for producing mass selected ion beams for further studies. Guided ion beam studies, for example, might provide accurate fragmentation energies of the clusters [35]. Multiphoton infrared dissociation studies using tunable free electron lasers might provide vibrational frequencies of the clusters [36]. Finally soft deposition methods have been developed that might provide a means for depositing the mass selected clusters on a surface for further studies and perhaps ultimately new kinds of semiconductor films [37]. The development of methodology for producing mass selected metal sulfide species provides an entirely new perspective on the study of these important materials.

7.5 References

1. Bianchini, A.; Bowles, K. C. Metal Sulfides in Oxygenated Aquatic Systems: Implications for the Biotic Ligand Model. *Comp. Biochem. Physiol. , Part C: Toxicol. Pharmacol.* **2002***, 133C*, 51-64.

2. Smith, D. S.; Bell, R. A.; Kramer, J. R. Metal Speciation in Natural Waters with Emphasis on Reduced Sulfur Groups as Strong Metal Binding Sites. *Comp. Biochem. Physiol. , Part C: Toxicol. Pharmacol.* **2002***, 133C*, 65-74.

3. Rickard, D.; Luther, G. W.,III. Metal Sulfide Complexes and Clusters. *Reviews in Mineralogy & Geochemistry.* **2006***, 61*, 421-504.

4. Luther, G. W.,I.I.I.; Rickard, D. T. Metal Sulfide Cluster Complexes and their Biogeochemical Importance in the Environment. *Journal of Nanoparticle Research.* **2005***, 7*, 389-407.

5. Rozan, T. F.; Lassman, M. E.; Ridge, D. P.; Luther, G. W.,III. Evidence for Iron, Copper and Zinc Complexation as Multinuclear Sulfide Clusters in Oxic Rivers. *Nature (London).* **2000***, 406*, 879-882.

6. Bianchi, A.; Domenech, A.; Garcia-Espana, E.; Luis, S. V. Electrochemical Studies on Anion Coordination Chemistry. Application of the Molar-Ratio Method to Competitive Cyclic Voltammetry. *Anal. Chem.* **1993***, 65*, 3137-3142.

7. Moreau, J. W.; Webb, R. I.; Banfield, J. F. Ultrastructure, Aggregation-State, and Crystal Growth of Biogenic Nanocrystalline Sphalerite and Wurtzite. *Am. Mineral.* **2004***, 89*, 950-960.

8. Borchert, H.; Shevchenko, E. V.; Robert, A.; Mekis, I.; Kornowski, A.; Gruebel, G.; Weller, H. Determination of Nanocrystal Sizes: A Comparison of TEM, SAXS, and XRD Studies of Highly Monodisperse CoPt3 Particles. *Langmuir.* **2005***, 21*, 1931-1936.

9. Burleson, D. J.; Driessen, M. D.; Penn, R. L. On the Characterization of Environmental Nanoparticles. *J Environ Sci Health A Tox Hazard Subst Environ Eng.* **2004***, 39*, 2707-2753.

10. Deonarine, A.; Hsu-Kim, H. Precipitation of Mercuric Sulfide Nanoparticles in NOM-Containing Water: Implications for the Natural Environment. *Environ. Sci. Technol.* **2009***, 43*, 2368-2373.

11. Pecora, R.; Editor. Dynamic Light Scattering: Applications of Photon Correlation Spectroscopy. **1985**, *Plenum Press, New York.*

12. Tiemann, M.; Marlow, F.; Hartikainen, J.; Weiss, O.; Linden, M. Ripening Effects in ZnS Nanoparticle Growth. *J. Phys. Chem. C.* **2008***, 112*, 1463-1467.

13. Brus, L. Electronic Wave Functions in Semiconductor Clusters: Experiment and Theory. *J. Phys. Chem.* **1986***, 90*, 2555-2560.

14. Brus, L. E. Electron-Electron and Electron-Hole Interactions in Small Semiconductor Crystallites: The Size Dependence of the Lowest Excited Electronic State. *J. Chem. Phys.* **1984***, 80*, 4403-4409.

15. McMahon, T. B.; Beauchamp, J. L. Determination of Ion Transit Times in an Ion Cyclotron Resonance Spectrometer. *Rev. Sci. Instrum.* **1972***, 43*, 509.

16. McIver, R. T., Jr.; Dunbar, R. C. Pulsed Ion Cyclotron Double Resonance for the Study of Ion-Molecule Reactions. *Int. J. Mass Spectrom. Ion Phys.* **1971***, 7*, 471-483.

17. Byrd, M.; Guttman, C. M.; Wallace, W. E.; Ridge, D. P. Gas-Phase Reactivity of Î·5-Cyclopentadienylcobalt Ion (CpCo+) Towards Saturated Hydrocarbons using Fourier-Transform Mass Spectrometry (FT-MS). *Abstracts of Papers, 223rd ACS National Meeting, Orlando, FL, United States, April 7-11, 2002.* **2002**, ANYL-079.

18. Luu, N. C.; Iyer, R. A.; Anders, M. W.; Ridge, D. P. Bioactivation Mechanisms of Haloalkene Cysteine S-Conjugates Modeled by Gas-Phase, Ion-Molecule Reactions. *Chem. Res. Toxicol.* **2000***, 13*, 610-615.

19. Luu, N. C.; Iyer, R. A.; Anders, M. W.; Ridge, D. P. Fourier-Transform Ion Cyclotron Resonance Mass Spectrometric Studies of Elimination Reactions of Anionic Bases with Metabolites of a Fluorinated Anesthetic Agent: Towards Modeling Bioactivation in the Gas Phase. *International Journal of Mass Spectrometry.* **2000***, 195/196*, 203-213.

20. Chen, O.; Groh, S.; Liechty, A.; Ridge, D. P. Binding of Nitric Oxide to Iron(II) Porphyrins: Radiative Association, Blackbody Infrared Radiative Dissociation and Gas-Phase Association Equilibrium. *J. Am. Chem. Soc.* **1999***, 121*, 11910-11911.

21. Ekeberg, D.; Uggerud, E.; Lin, H.; Sohlberg, K.; Chen, H.; Ridge, D. P. Dehydrogenation of Ethane by CpM+ (M = Fe, Co, Ni) in the Gas Phase. an FT-ICR-MS Study. *Organometallics.* **1999***, 18*, 40-44.

22. Bjarnason, A.; Ridge, D. P. Gas-Phase Reactions of M+ and MO+ (M = Sc, Ti, V) with Toluene. *Organometallics.* **1998***, 17*, 1889-1893.

23. Arnold, F. P.,Jr.; Ridge, D. P.; Rheingold, A. L. Reaction of Diantimony Anion with Mononuclear Metal Carbonyls. First Observed Instance of an Antimony-Transition-Metal Triple Bond. *J. Am. Chem. Soc.* **1995***, 117*, 4427-4428.

24. Pan, Y. H.; Ridge, D. P. Gas-Phase Reactions of Chromium, Iron, and Nickel Carbonyls of Cr(CO)5-, Fe(CO)4-, and Ni(CO)3- with Organic Electrophiles. *J. Am. Chem. Soc.* **1992***, 114*, 2773-2780.

25. Chen, H. L.; Hagan, T. E.; Groh, S. E.; Ridge, D. P. Gas-Phase Reactions of Iron Porphyrins with Nitrogen Oxide (NO2): Oxygen Atom Transfer to Anionic and Cationic Iron Porphyrins. *J. Am. Chem. Soc.* **1991***, 113*, 9669-9670.

26. Pan, Y. H.; Sohlberg, K.; Ridge, D. P. Reactions of Cobalt Ions Co1-4+ and Co4(CO)n+ with Cyclohexane: C-H Activation as a Function of Cluster Size and Ligand Substitution. *J. Am. Chem. Soc.* **1991***, 113*, 2406-2411.

27. Barry, R.; Strobel, F.; Haas, M.; Ridge, D.; Munson, B. Ion Molecule Reactions in Diisopropyl Ether. *Int. J. Mass Spectrom. Ion Processes.* **1989***, 89*, 133-148.

28. Ridge, D. P.; Meckstroth, W. K. Reactions in Ionized Metal Carbonyls: Clustering and Oxidative Addition. *Gas Phase Inorg.Chem.* **1989**, 93-113.

29. Ridge, D. P. Reactions of Transition Metal Ions with Cycloalkanes and Metal Carbonyls. *NATO ASI Series, Series C: Mathematical and Physical Sciences.* **1987***, 193*, 165-175.

30. Meckstroth, W. K.; Freas, R. B.; Reents, W. D., Jr.; Ridge, D. P. Relationship between Structure and Reactivity for Metal Clusters Formed in Ion-Molecule Reactions in Decacarbonyldimanganese and Pentacarbonyl(Pentacarbonylmanganio)Rhenium. *Inorg. Chem.* **1985***, 24*, 3139-3146.

31. Meckstroth, W. K.; Ridge, D. P. Very Large Metal Carbonyl Clusters Formed by ion/molecule Reactions in Decacarbonyldirhenium. *International Journal of Mass Spectrometry and Ion Processes.* **1984***, 61*, 149-152.

32. Peake, D. A.; Gross, M. L.; Ridge, D. P. Mechanism of the Reaction of Gas-Phase Iron Ions with Neutral Olefins. *J. Am. Chem. Soc.* **1984***, 106*, 4307-4316.

33. Wronka, J.; Ridge, D. P. Double Metal to Metal Bonds in Metal Carbonyl Clusters Formed in the Gas-Phase Negative Ion Chemistry of Iron Pentacarbonyl. *J. Am. Chem. Soc.* **1984***, 106*, 67-71.

34. Allison, J.; Ridge, D. P. Reactions of Atomic Metal Ions with Alkyl Halides and Alcohols in the Gas Phase. *J. Am. Chem. Soc.* **1979***, 101*, 4998-5009.

35. Armentrout, P. B. Guided Ion Beam Studies of Transition Metal-Ligand Thermochemistry. *Int. J. Mass Spectrom.* **2003***, 227*, 289-302.

36. Moore, D. T.; Oomens, J.; Eyler, J. R.; Meijer, G.; von Helden, G.; Ridge, D. P. Gas-Phase IR Spectroscopy of Anionic Iron Carbonyl Clusters. *J. Am. Chem. Soc.* **2004***, 126*, 14726-14727.

37. Laskin, J.; Wang, P.; Hadjar, O. Soft-Landing of Peptide Ions Onto Self-Assembled Monolayer Surfaces: An Overview. *Physical Chemistry Chemical Physics*. **2008***, 10*, 1079-1090.

Chapter 8

CONCLUDING REMARKS

The unique and powerful capabilities of ESI FT-ICR mass spectrometry have been utilized for the analysis of complex environmental samples. The research featured in this dissertation is a true example of modern multidisciplinary research covering environmental, analytical, physical, inorganic and biochemistry. From an analytical perspective, this work provided training in traditional mass spectrometry analysis characterizing samples based on mass accuracy and fragmentation experiments in addition to more innovative techniques such as energy-resolved SID experiments and gas phase ion-molecule reactions. The following is a synopsis of my finding and thoughts on how they may fit into a broader range of applications.

Following an overview of the experimental methods, Chapter 3 describes the affect of oxidation on fragmentation patterns of peptides using energy-resolved surface-induced dissociation, RRKM modeling, and molecular dynamics. The new low-energy fragmentation pathways resulting from oxidation of tyrosine and histidine were found to be entropically driven requiring significant conformational rearrangement in the formation of the transition states for each unimolecular reaction pathway. Oxidation of tyrosine, resulting in the addition of another hydroxyl group in the 2-position, was seen to induce acidic cleavage C-terminal to the modified residue. Although ozonolysis of histidine leads to a more complex picture, the energetics are determined mostly by the lowest energy dissociation mechanism resulting in the

$[MH+3O]^+$-45 fragment. This cleavage is driven by strong hydrogen bonding interactions within the modified histidine side chain as highlighted by the molecular dynamics results.

In addition to clarifying the affects of ozone exposure on peptides, these findings build upon the extended body of research involving the fundamentals of peptide fragmentation in the gas phase. The understanding of dissociation mechanisms for oxidized species is an essential next step. These results not only provide the basis for characterizing environmentally significant ozonolysis reactions but also provide valuable insight into how oxidized peptides fragment in general which can be used to more efficiently sequence modified proteins.

In Chapters 4-7 the focus shifted to understanding environmentally significant metal sulfide nucleation processes using ESI FT-ICR mass spectrometry. To begin with, there is a discussion on the unique observation of metal salt cluster growth in binary water-methanol solutions (Chapter 5). It was found that the relative concentrations of cadmium nitrate clusters shift to larger species following dilution of aqueous salt solutions with methanol. This behavior is thought to transpire due to a decrease in dielectric constant as the hydrogen bonding framework of water is disrupted by the addition of methanol. Placed in an environmental context, it is believed that metal salt clusters may be more appropriate starting points than completely dissociated ions in understanding metal sulfide reactions at hydrothermal vent sites under supercritical conditions.

Chapter 6 described our attempts to use molecular capping agents to interrupt particle formation in aqueous solutions. Solutions of cadmium nitrate and

the capping agent 2-mercaptopyridine following reaction with H_2S showed capped metal clusters with sulfate ligands added. Sulfate species are thought to be oxidized forms of sulfide ligands. The reactivity of cadmium nitrate clusters or, more specifically, the lack of observed reactivity for $[Cd(NO_3)_3]^-$ with H_2S in solution provided a valuable connection between similarities of solution based reactions and the gas phase ion-molecule reactions described in Chapter 7.

The gas phase ion-molecule reactions of metal salt clusters with hydrogen sulfide provided a unique approach for characterizing the initial steps of metal sulfide nucleation (Chapter 7). Ions produced from solutions of $Cd(NO_3)_2$, $Cd(CH_3COO)_2$, $CdCl_2$ and $ZnCl_2$ were analyzed. Anionic reactions were characterized as slow and constant with all steps having reaction efficiencies < 5%. An exception to this trend was $[Cd_4(CH_3COO)_9]^-$ which displayed very fast intermediate bisulfide substitutions following initial formation of $[Cd_4S(CH_3COO)_9]^-$. The cations on the other hand, generally react initially with much greater reaction efficiencies and slow down significantly as the reaction proceeds. Comparison of ligating species showed $NO_3^- > OH^- > Cl^-$ in terms of reaction efficiency and cadmium species were observed to react with faster rates than zinc.

As with all good research, the metal sulfide project has generated more new and interesting questions than answers. In the context of the overall project goals, ESI FT-ICR mass spectrometry has successfully characterized the realm of metal complexes and molecular clusters along the pathway through nanoparticulate to solid state material. Our collaborators, on the other hand, have been able to use UV/Vis spectroscopy to determine sizes of larger metal sulfide nanoparticles. Unfortunately, as depicted in Figure 8.1, the gap between these two domains was unable to be

bridged. Further work is needed to expand the capabilities of mass spectrometry to larger clusters and enlist new techniques to characterize smaller metal sulfide particles.

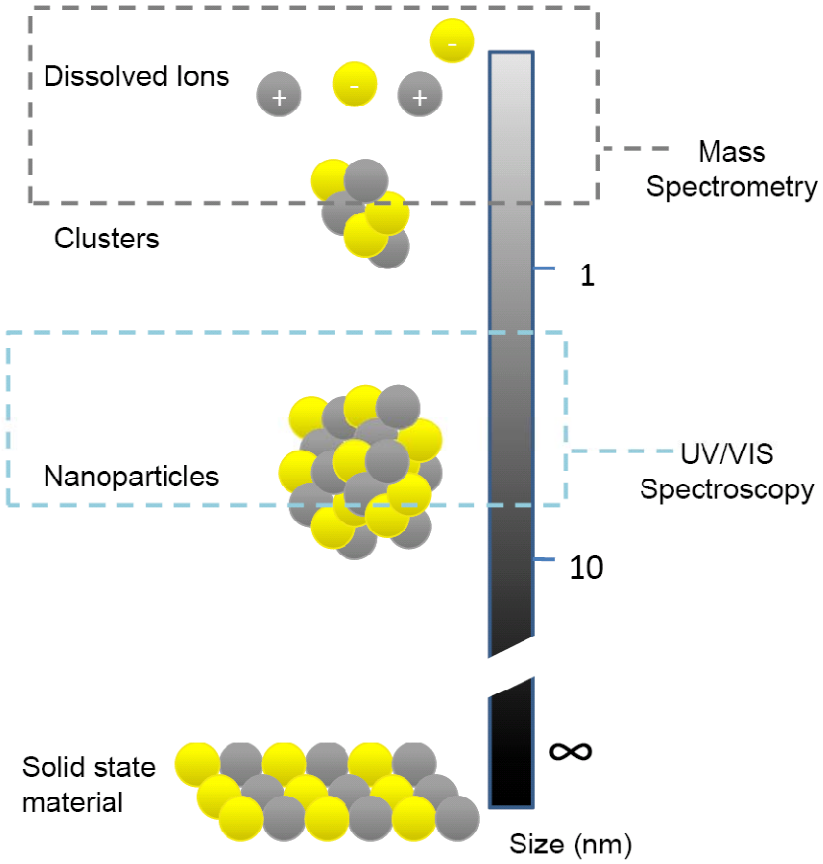

Figure 8.1. The study of metal sulfide precipitation using a collaborative multifaceted analytical approach. ESI mass spectrometry was found to be effective for characterizing metal sulfide complexes and clusters while UV/VIS spectroscopy was useful for determining size of nanoparticles.

The success of this work, however, is not strictly limited to understanding the mechanism of metal sulfide precipitation. A number of novel experiments have developed from the gas phase ion-molecule reactions of metal sulfides. In addition to the obvious shift to other metal systems such as iron and copper, a priority is to produce metal sulfide clusters in the source region of the FT-ICR mass spectrometer allowing isolation of product ions for structural analysis using various fragmentation techniques and IR spectroscopy. Producing metal sulfide clusters in the source region may also lead to a method for depositing mass selected clusters surfaces to generate novel semiconductor thin films. Additionally, interest in our work has sparked other research groups to take advantage of gas phase ion-molecule reactions to understand reactions of environmentally significant clusters and particles. Building from a positive relationship with the Johnston group at the University of Delaware, our work has been the starting point for their research on amine exchange reactions into ammonium bisulfate and ammonium nitrate clusters. This speaks to the true collaborative nature of science. It is not what has been done that motivates, but the possibility of what is to follow that truly inspires curiosity.

Appendix A

PERSONAL BIBLIOGRAPHY

A.1 Publications

Gas Phase Ion-Molecule Reactions of Metal Salt Clusters with Hydrogen Sulfide, Spraggins, Jeffrey; Papson, Kaitlin; Zeringo, Nick; Ridge, Douglas; *Manuscript in Preperation.*

Metal Salt Nucleation Observed using ESI FT-ICR MS, Spraggins, Jeffrey; Kim, Una; Ridge, Douglas; *Manuscript in Preperation.*

Hydrothermal Vents: Discovery of a New Ecosystem, Spraggins, Jeffrey; *Problem-Based Learning Clearinghouse: http://www.udel.edu/pblc* (2009)

Fragmentation Mechanisms of Oxidized Peptides Elucidated by SID, RRKM Modeling and Molecular Dynamics, Spraggins, Jeffrey; Lloyd, Julie; Johnston, Murray; Laskin, Julia; Ridge, Douglas; *J. Am. Soc. Mass Spec.* (2009), 20(9), 1579-1592.

Peptide Ozonolysis: Product Structures and Relative Reactivities for Oxidation of Tyrosine and Histidine Residues, Lloyd, Julie; Spraggins, Jeffrey; Johnston, Murray; Laskin, Julia; *J. Am. Soc. Mass Spec.* (2006), 17(9), 1289-1298.

Is it necessary to dry primary standards before analysis?, Spraggins, Jeffrey; Williams, Theodore; *J. Chem. Ed*. (2005), 82(2), 311-312.

A.2 Presentations

Poster Presentation: *peer reviewed* **June 2009**
57th ASMS conference on Mass Spectrometry. Philadelphia, PA. *Jeffrey Spraggins, Kaitlin Papson, Nick Zeringo, Una Kim, Katherine Mullaugh, Dr. George Luther and Dr. Douglas Ridge*: "Monitoring Gas Phase Ion-Molecule Reactions of Environmentally Significant Metal Clusters with Hydrogen Sulfide using FT-ICR MS."

Oral Presentation: *peer reviewed* **May 2009**
2009 NSF GK-12 Projects Annual Meeting. Washington D.C. *Pat Marsteller, Jordan Rose, George Watson, Jeffrey Spraggins, Neil Milan and Cris Hellerstein*: "Special Interest Session: Putting PBL in Your GK-12 Presentation."

Poster Presentation: *peer reviewed* **May 2009**
2009 NSF GK-12 Projects Annual Meeting. Washington D.C. *Jeffrey Spraggins*: "Understanding Hydrothermal Vents: Ions, Energy Transfer and Graduate Research."

Oral Presentation **October 2008**
30th East Coast Ion Chemistry Conference. Newark, DE. *Jeffrey M. Spraggins*: "Understanding Metal Cluster Formation through FT-ICR MS."

Poster Presentation: *peer reviewed* **June 2008**
56th ASMS conference on Mass Spectrometry. Denver, CO. *Jeffrey Spraggins, Kate Mullaugh, Clark Ridge, Dr. Murray Johnston, Dr. George Luther and Dr. Douglas Ridge*: "Monitoring Metal Sulfide Growth in the Gas Phase using FT-ICR MS."

Poster Presentation: *peer reviewed* **April 2008**
Lilly-East Conference on College and University Teaching. Newark, DE. *Jeffrey Spraggins*: "Introducing Science Students to Cutting Edge Research through PBL Activities."

Poster Presentation: *peer reviewed* **June 2007**
55th ASMS conference on Mass Spectrometry. Indianapolis, IN. *Jeffrey Spraggins, Kate Mullaugh, Dr. Julia Laskin, Dr. Murray Johnston, Dr. George Luther and Dr. Douglas Ridge*: "The Characterization of Environmentally Significant Oxidic and Sulfidic Metal Clusters."

Poster Presentation: *peer reviewed* **April 2007**
Lilly-East Conference on College and University Teaching. Newark, DE. *Jeffrey Spraggins*: "Learning by Teaching: Using Self-Explanation and Reciprocal Peer Teaching in the Laboratory."

Poster Presentation **January 2007**
Delaware EPSCoR Annual State Meeting. Newark, DE. *Jeffrey M. Spraggins II, Katherine Mullaugh, Dr. George W. Luther III, and Dr. Douglas P. Ridge*: "Metal Sulfide Clusters and Nanoparticles: Dynamic Nucleation and Growth in the Aquatic Environment."

Oral Presentation **September 2006**
28th East Coast Ion Chemistry Conference. Newark, DE. *Jeffrey M. Spraggins*: "Probing Gas Phase Fragmentation Reactions of Oxidized Peptides."

Poster Presentation: *peer reviewed* **June 2006**
54th ASMS conference on Mass Spectrometry. Seattle, WA. *Jeffrey M. Spraggins II, Dr. Julia Laskin, and Dr. Douglas P. Ridge*: "Using Parent Ion Conformations to Gain Insight into Fragmentation Mechanisms."

Oral Presentation **October 2005**
27th East Coast Ion Chemistry Conference. Newark, DE. *Jeffrey M. Spraggins*: "Ozonated Peptides: Fragmentation Energetics and Mechanisms."

Poster Presentation: *peer reviewed* **June 2005**
53rd ASMS conference on Mass Spectrometry. San Antonio, TX. *Jeffrey M. Spraggins II, Dr. Julia Laskin, Dr. Douglas P. Ridge and Dr. Murray Johnston*: "Ozonated Peptides: Insights into Structure and Fragmentation Energetics using FT-ICR MS."

Appendix B

HYDROTHERMAL VENTS: DISCOVERY OF A NEW ECOSYSTEM

B.1 Abstract

Described herein is a multifaceted Problem-based Learning activity in which students discover hydrothermal vents while being exposed to topics such as properties (physical and chemical), chemical bonding, oxidation states, and energy transfer in environmental systems. The activity is designed for students to work together in small groups (2-4 students) on a three stage project that helps students understand how to tackle complex problems. For advanced college students, the level of difficulty can be adjusted by only providing students with the 'Overview' section of the problem. The activity was designed for high school physical science classes made possible through funding from the University of Delaware GK-12 Fellowship program, a partnership with the New Castle County Vocational Technical School District (www.udel.edu/GK-12).

B.2 Problem Content

This activity is targeted towards high school physical science (9th grade), high school chemistry, and general college chemistry students. The problem is broken down into separate tasks to provide younger students with direction and is designed to be completed in two 50 minute class periods. See *Hydrothermal Vent Activity v3* at www.udel.edu/GK-12/spraggins.html for the project website.

B.2.1 Overview

Found in the deepest, darkest reaches of our planet hydrothermal vents (aka: 'black smokers') represent one of the more extreme environments on earth. Despite the difficulty in exploring these unique ecosystems, they continue to be the focus of much research which is proving to answer some of our greatest questions. Imagine that you and your partner are the first scientists to ever see a hydrothermal vent. As you plunge deep into the abyss near the Mid-Ocean Ridge system you see them... Chimneys reaching as high as a 15 story building with billowing smoke stacks shooting from their tops. Amazed by what you are seeing, you lean over to your fellow scientist and ask "How can there be smoke underwater? This is CRAZY!"

Your Task: Thinking like a Geochemist, describe the chemical makeup of the 'smoke' coming from these underwater chimneys. Use the provided links (see Student Resources: Websites) to work through Parts I-III. This should help you answer the question... What is the smoke?

B.2.2 Part I: The Basics

So, where to begin? Whenever faced with a tough problem, start with the basics. Hydrothermal Vents…What are they? Where do you find them? You have 10 min to work through this section....GO!

B.2.3 Part II: Properties

Now let's get down to business! You remember way back when we learned about Physical properties...Well, now it's time to dust off that piece of knowledge and use it. To scientifically describe hydrothermal vent 'smoke' we need to

understand the physical properties near hydrothermal vents. What is it like inside the vent? How do the physical properties change as you move away from the vent?

What about chemical properties? What atoms, ions, or molecules make up the 'smoke'? What reactions are taking place?

B.2.4 Part III: Energy

Well you made it! This is our last task for the day. Let's switch our focus a bit to how the 'smoke' is made. Think back to when we talked about energy transfer.

...Describe how energy is transferred in this system. To really understand how this underwater 'smoke' is made we need to understand how energy transfer and hydrothermal vents are related. Give it a shot....

B.3 Student Learning Objectives

- To understand matter classification: element vs. compound
- To differentiate atoms and ions.
- To determine oxidation numbers of elements using the periodic table
- Knowing oxidation numbers, be able to write balanced chemical reactions.
- To describe energy transfer in hydrothermal vent ecosystems (chemosynthesis).

B.4 Teacher Notes

This problem was originally designed for high school physical science classes (9th grade) which focus primarily on chemistry while lightly covering both physics and earth science. For this activity there were two instructors acting a roving

facilitators with a typical class size of roughly thirty students. Groups were comprised of 2-4 students with one computer for every two students. In addition to covering specific state testing standards (properties, chemical bonding, and oxidation numbers), we wanted to use this activity to highlight the connectivity between the course material and natural environments.

B.4.1 Teacher Notes: Overview

A good way kick off the activity and grab the students' attention is to show a short video clip of hydrothermal vents while the 'Overview' is read aloud. Discovery Channel has a number of specials covering vents. We observed that our high school students immediately go to Google and search 'what is smoke?' getting no search hits that are associated with hydrothermal vents. For this reason we adjusted the activity in later versions to only have students use the websites provided (See Student Recourses: Websites). For high school students, this is a great opportunity to talk to groups about how to effectively use the internet as a search tool. It can be useful to allow students to take some time to address the question before introducing Parts I-III which were written in later versions to help direct the students to a thorough answer and to ensure that we cover specific learning goals.

B.4.2 Teacher Notes: Part I

This section is pretty basic and students generally have little issue with answering these questions. For our high school students the major hurdle we faced was getting the students to expand their answers. They are in a multiple choice/short

answer mind set and PBL activities are a great way to help students develop more complete ideas.

B.4.3 Teacher Notes: Part II

Our students have prior experience with physical properties and this activity builds off their understanding. To properly describe the 'smoke' coming out of these vents a physical understanding of this extreme environment is essential. We want them to describe the area surrounding hydrothermal vents in terms of temperature gradients, pressure and lack of sunlight. Ultimately, our best student projects will highlight the connectivity between these physical factors and the chemical properties of this system. To ensure our students cover the appropriate learning goals, it is important to direct the students to describe the chemical reactions taking place inside the hydrothermal vents. In addition, understanding the difference between atoms and ions was an important concept that we wanted to cover with this activity; therefore, as we worked with the groups we introduced oxidation numbers which also led to discussion on how to balancing chemical reactions.

B.4.4 Teacher Notes: Part III

As a final aspect of the activity, we wanted to take the opportunity to have the students think about energy transfer in natural systems. Environments around hydrothermal vent communities provide a unique perspective on this subject due to the lack of sunlight and, therefore, lack of photosynthetic processes. Instead these ecosystems are powered by chemosynthesis which is ultimately driven by the nuclear decay reactions taking place within the core of our planet. It is a basic understanding

of the transfer of energy in the following natural sequence that we want our students to discover: exothermic nuclear decay reactions → heating water → specific chemical reactions → chemosynthetic bacteria → symbiotic relationship with vent-dwelling animals.

B.4.5 Teacher Notes: Thoughts on College Settings

Although this activity has been developed for high school students, many of the concepts covered are learning goals in college level courses such as general chemistry, biochemistry, and environmental chemistry. For students of this level it may be more appropriate to only provide the students with the 'Overview' section of the problem and use 'Parts I-III' as topic points as the facilitators work with individual groups. In addition, there is a vast body of literature in scientific journals (See Resources: Journals for examples) discussing hydrothermal vents for college level students to utilize.

B.5 Assessment Strategies

Two strategies have been used to assess student understanding depending on the amount of time we wanted to devote to this activity. The most straightforward assessment we have used is to have the students fill out an essay response form as they are working on the activity in class. At other times, we have had our students develop reports on their findings using a wiki software platform such as wikispaces.com. There is a bit of a learning curve for students with no wiki experience, but the advantage is that all group members can work on the activity outside of the classroom as long as an internet connection is available.

B.6 Student Resources

B.6.1 Websites

http://www.udel.edu/GK-12/Material/2008/CM/Spraggins/vent/hvoverview.html

- This entire activity can be found online as a part of the University of Delaware GK-12 Fellowship Program website under 'Materials' by Jeffrey Spraggins.

http://www.ocean.udel.edu/expeditions/

- The College of Marine and Earth Studies at the University of Delaware (Lewes, DE) has set up an amazing set of educational websites highlighting hydrothermal vents and the unique ecosystem found at these extreme environments. The sites can be used as the primary source of research for younger students and as a starting point for advanced students.

http://www.lostcity.washington.edu/index.html

- This is an additional resource covering hydrothermal vents set up by the University of Washington (Seattle, WA).

B.6.2 Journal Articles

Advanced students can use the following scientific journal articles as resources.

Martin, W., Baross, J., Kelley, D., & Russell, M. J. (2008). Hydrothermal vents and the origin of life. *Nature Reviews Microbiology, 6*(11), 805-814.

- This review article covers various types of hydrothermal vents and the chemical reactions taking which drive chemosynthesis in these extreme environments. It also discusses how these ecosystems relate to the early developmental stages of life on our planet.

Boetius, A. (2005). Ocean science: Lost city life. *Science (Washington, DC, United States), 307*(5714), 1420-1422.

- A review article that focuses on the submarine hydrothermal vent field know as the Lost City. This article describes the relationship between the unique chemistry taking place here and the organisms that call the Lost City home.

B.7 Instructor Resources

In addition to the sources listed under Section A.6: Student Resources, the following is a more comprehensive list of online references for instructors.

B.7.1 Websites

http://www.udel.edu/GK-12/Material/2008/CM/Spraggins/vent/hvoverview.html

http://www.ocean.udel.edu/expeditions/

http://www.lostcity.washington.edu/index.html

http://walrus.wr.usgs.gov/pubinfo/smokers.html

http://www.amnh.org/nationalcenter/expeditions/blacksmokers/

http://oceanexplorer.noaa.gov/explorations/02fire/welcome.html

http://www.wnet.org/savageseas/deep-side-smokers.html

http://www.panda.org/about_wwf/what_we_do/marine/news/stories/index.cfm?uNewsID=2593

http://www.sciencenews.org/articles/20010714/fob3.asp

http://www.accessexcellence.org/BF/bf03/somero/bf03a8.html

http://www.resa.net/nasa/ocean_hydrothermal.html

http://www.pmel.noaa.gov/vents/plumestudies.html

http://www.divediscover.whoi.edu/vents/index.html

Appendix C

OXIDIZED PEPTIDE PEAK LISTS FOR SURFACE INDUCED DISSOCIATION EXPERIMENTS

Provided below are the detailed peak lists for the 60 eV SID spectra of angiotensin II (AngII: DRVYIHPF) and the ozonolysis products AngII+O (DRVY*IHPF), AngII+3O (DRVYIH*PF) and AngII+4O (DRVY*IH*PF).

C.1. Detailed peak list for DRVYIHPF: 60 eV SID

Theoretical m/z	Peak Assignment	Experimental m/z	Abundance	Deviation
138.0667	H	138.06670	10.29352	0
211.1559	RV-28-17	211.15577	5.3219476	-0.00013
223.1559	IH-28	223.15571	5.801106	-0.00019
235.1195	HP	235.11971	18.9970665	0.00021
239.1508	RV-NH_3	239.15133	239.15133	0.00053
251.1508	IH	251.15053	251.15053	-0.00027
255.1093	b_2-NH_3	255.10934	255.10934	4E-05
256.1773	RV	256.17762	256.17762	0.00032
263.1396	y_2	263.13962	263.13962	2E-05
354.1777	b_3-NH_3	354.17823	15.9668512	0.00053
371.2043	b_3	371.20366	12.3357077	-0.00064
382.18794	y_3-18	382.18906	25.3343067	0.00112
396.20354	YIH-H_2O	396.20079	12.7393322	-0.00275
400.1985	y_3	400.20406	8.5834322	0.00556
402.2141	RVY-NH_3	402.21558	6.0762796	0.00148
414.2141	YIH	414.21472	28.638216	0.00062
419.2407	RVY	419.23903	9.824728	-0.00167
513.2825	y_4	513.28618	29.1089172	0.00368
513.2825	VYIH	513.28618	29.1089172	0.00368
532.3247	RVYI	532.32885	15.3489017	0.00415
534.2676	b_4	534.26905	13.229208	0.00145
619.3568	a_5	619.37763	11.1160393	0.02083
647.3517	b_5	647.36049	22.337162	0.00879
652.3571	RVYIH-NH_3	652.36528	21.1077824	0.00818

669.3837	RVYIH	669.38879	28.0422897	0.00509
676.3459	y_5	676.3544	21.2623196	0.0085
749.4099	RVYIHP-NH_3	749.3805	11.4085035	-0.0294
766.4364	RVYIHP	766.42836	13.9054604	-0.00804
767.40786	b_6-OH	767.40585	16.5666542	-0.00201
775.4143	y_6	775.42215	14.9000645	0.00785
784.4106	b_6	784.42914	38.652504	0.01854
896.47829	y_7-35	896.47915	12.6077023	0.00086
913.50484	y_7-H_2O	913.51786	12.921175	0.01302
914.4888	y_7-NH_3	914.48689	22.6723957	-0.00191
931.5154	y_7	931.51939	348.4616089	0.00399
1011.50519	MH^+ -35	1011.5155	33.7789688	0.01031
1012.4892	MH^+-2(NH_3)	1012.50537	18.000349	0.01617
1028.5318	MH^+-H_2O	1028.54153	121.8215561	0.00973
1046.5423	MH^+	1046.53786	249.5424805	-0.00444

C.2. Detailed peak list for DRVY*IHPF: 60 eV SID

Theoretical m/z	Peak Assignments	Experimental m/z	Abundance	Deviation
235.1195	HP	235.11942	5.3775167	-8E-05
239.1508	RV-NH_3	239.14996	4.5849276	-0.00084
251.1508	IH	251.15063	10.8221455	-0.00017
255.1093	b_2-NH_3	255.10937	9.8227024	7E-05
256.1773	RV	256.17691	6.8217607	-0.00039
263.1396	y_2	263.13815	13.8081198	-0.00145
263.1396	VY	263.13815	13.8081198	-0.00145
272.1359	b_2	272.13535	16.0829334	-0.00055
343.2094	a_3	343.20781	6.9622288	-0.00159
354.1777	b_3-NH_3	354.17696	5.1784577	-0.00074
364.19852	IHP+O	364.17737	9.9769268	-0.02115
371.2043	b_3	371.20386	10.5913181	-0.00044
418.20907	(RVY+O)-17	418.21188	4.058145	0.00281
430.20902	YIH+O	430.21322	3.7606411	0.0042
435.23562	RVY+O	435.23377	39.3845482	-0.00185
532.25196	b_4+O -H2O	532.24843	9.9473553	-0.00353
550.26252	b_4+O	550.25934	46.972702	-0.00318
800.40552	b_6+O	800.43889	8.8981953	0.03337
929.4885	(MH+O)-88-28-17	929.47887	9.2784557	-0.00963
947.51032	y_7+O	947.5034	54.2891579	-0.00692
1044.52666	$[MH+O]^+$-18	1044.51061	27.4118824	-0.01605
1062.53722	$[MH+O]^+$	1062.5391	56.9309959	0.00188

C.3. Detailed peak list for DRVYIH*PF: 60 eV SID

Theoretical m/z	Peak Assignment	Experimental m/z	Abundance	Deviation
239.1508	RV-NH_3	239.14987	4.4645228	-0.00093
255.1093	b_2-NH_3	255.10948	10.8239079	0.00018
256.1773	RV	256.17584	7.1648555	-0.00146
263.1396	y_2	263.13973	18.9752579	0.00013
263.1396	VY	263.13973	18.9752579	0.00013
272.1359	b_2	272.13594	18.9385376	4E-05
343.2094	a_3	343.21408	4.6760039	0.00468
354.1777	b_3-NH_3	354.17732	14.4782486	-0.00038
371.2043	b_3	371.20566	9.6021576	0.00136
532.3247	RVYI	532.32523	11.7448101	0.00053
629.3411	b_5-H_2O	629.34439	12.7828007	0.00329
630.3251	b_5-NH_3	630.3318	14.2256422	0.00670
647.3517	b_5	647.35378	80.7871628	0.00208
744.3721	wa_6	744.37036	37.7502327	-0.00174
762.3827	wa_6+H_2O	762.38493	47.6691933	0.00223
	?	891.469	14.2305212	
908.49943	(y_7 + 3O) -71	908.50128	42.1116486	0.00185
934.4787	(y_7 + 3O) -45	934.46479	10.2045393	-0.01391
979.50016	y_7 + 3O	979.50466	44.3430519	0.00450
1006.49979	$[MH+3O]^+$-88	1006.51035	33.2595901	0.01056
1023.526331	$[MH+3O]^+$-71	1023.53087	39.3978958	0.004539
1049.50560	$[MH+3O]^+$-45	1049.50654	116.0205917	0.00094
1076.51650	$[MH+3O]^+$-18	1076.53	30.0254688	0.01350
1094.52706	$[MH+3O]^+$	1094.53617	49.7111473	0.00911

C.4. Detailed peak list for DRVY*IH*PF: 60 eV SID

Theoretical m/z	Peak Assignment	Experimental m/z	Abundance	Deviation
255.1093	b_2-NH_3	255.10843	9.3342085	-0.00087
256.1773	RV	256.17652	6.8915644	-0.00078
263.1396	y_2	263.1387	9.3645544	-0.0009
263.1396	VY	263.1387	9.3645544	-0.0009
272.1359	b_2	272.1352	16.3724022	-0.0007
354.1777	b_3-NH_3	354.17662	8.5113182	-0.00108
371.2043	b_3	371.20258	12.8399677	-0.00172
435.23562	RVY + O	435.23596	10.9244194	0.00034
550.26252	b_4 + O	550.25675	20.9743118	-0.00577
	?	576.23599	12.4082508	
647.3517	b_5	647.35476	8.1913643	0.00306
663.34662	b_5 + O	663.349	23.1922569	0.00238
760.36702	wa_6 + O	760.35802	14.3755445	-0.009
	y_7 + 4O -71	924.47858	15.3116684	
995.49508	y_7 + 4O	995.48402	7.3689289	-0.01106
1021.47438	x_7 + 4O	1021.51488	7.946878	0.0405
	?	1039.51321	19.5150433	
1065.50052	$[MH+4O]^+$- 45	1065.481	43.3208733	-0.01952
1092.51142	$[MH+4O]^+$ - H_2O	1092.49134	7.7762146	-0.02008
1110.52198	$[MH+4O]^+$	1110.48132	12.9372873	-0.04066

Appendix D

POSITIVE MODE ESI FT-ICR MASS SPECTRUM OF METAL SALT SOLUTIONS

The attached spectrum is taken from a 0.3 mM solution of $Cd(NO_3)_2$ and glutathione (Glu: $C_{10}H_{17}N_3O_6S$) in a 1:1 water-methanol solution using positive mode ESI FT-ICR mass spectrometry. The results highlight the observed complexity associated with positive mode analysis for metal salt samples. All clusters labeled * are unidentifiable species.

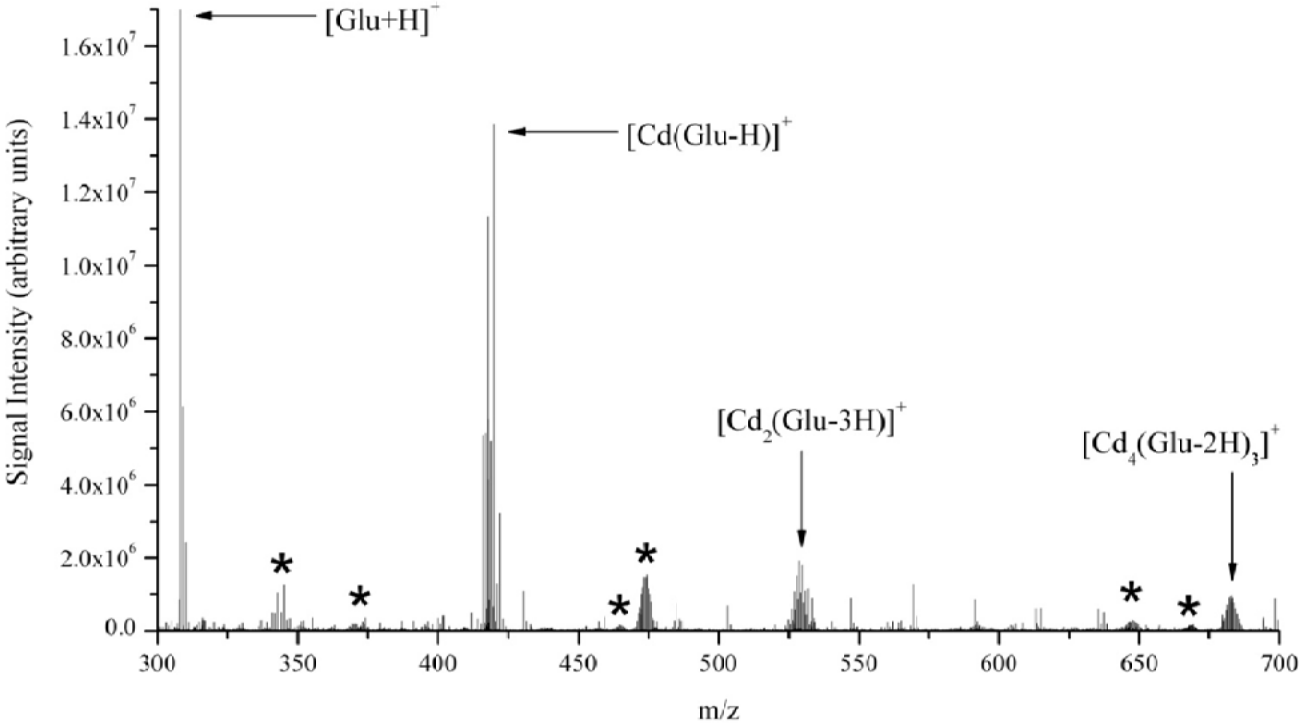
[Glu+H]⁻
[Cd(Glu-H)]⁺
[Cd2(Glu-3H)]⁺
[Cd4(Glu-2H)3]⁺
Signal Intensity (arbitrary units)
1.6x10⁷
1.4x10⁷
1.2x10⁷
1.0x10⁷
8.0x10⁶
6.0x10⁶
4.0x10⁶
2.0x10⁶
0.0
300
350
400
450
500
550
600
650
700
m/z

Appendix E

EXAMPLE MATHEMATICA OUTPUT FILES FOR SELECT METAL SULFIDE REACTIONS

The following are example Mathematica output files for the reactions between $[Cd(CH_3COO)_3]^-$ (Section D.1) and $[Cd_3(CH_3COO)_5]^+$ (Section D.2) with hydrogen sulfide. Nonlinear regression is used to fit the experimental kinetic data using appropriate integrated rate equations. A simplified sequential pseudo first-order model was used in all cases.

E.1. Reaction Between $[Cd(CH_3COO)_3]^-$ and H_2S ($4x10^{-9}$ Torr)

```
Clear[k1, k2, k3, k4]
Clear[k5, k6]
Needs[ "Statistics`NonlinearFit` " ]
General::obspkg :
  Statistics`NonlinearFit` is now obsolete. The legacy version being loaded
       may conflict with current Mathematica functionality.
       See the Compatibility Guide for updating information. >>
datCdAc290 = {{0.`, 1.`}, {2.`, 0.8835408204022254`},
    {4.`, 0.7437554836186391`}, {6.`, 0.6350539912387797`},
    {8.`, 0.4997314510735747`}, {10.`, 0.40904998365631096`},
    {12.`, 0.3386768126693693`}, {14.`, 0.2720625736522628`},
    {16.`, 0.22324027851978942`}, {18.`, 0.18810320476658338`},
    {20.`, 0.13374017413181777`}, {24.`, 0.09898212684870637`},
    {28.`, 0.06071725589735915`}, {32.`, 0.03667985596958875`},
    {36.`, 0.`}, {40.`, 0.`}, {45.`, 0.`}, {50.`, 0.`}, {55.`, 0.`}, {60.`, 0.`},
    {65.`, 0.`}, {70.`, 0.`}, {75.`, 0.`}, {80.`, 0.`}, {85.`, 0.`}, {90.`, 0.`}}
{{0., 1.}, {2., 0.883541}, {4., 0.743755}, {6., 0.635054}, {8., 0.499731},
  {10., 0.40905}, {12., 0.338677}, {14., 0.272063}, {16., 0.22324},
  {18., 0.188103}, {20., 0.13374}, {24., 0.0989821}, {28., 0.0607173},
  {32., 0.0366799}, {36., 0.}, {40., 0.}, {45., 0.}, {50., 0.}, {55., 0.},
  {60., 0.}, {65., 0.}, {70., 0.}, {75., 0.}, {80., 0.}, {85., 0.}, {90., 0.}}
```

```
datCdAc290plot = ListPlot[datCdAc290, PlotRange → All,
    Frame → True, FrameStyle → {Thickness[.008]},
    FrameLabel → {"Reaction Time (s)", "Relative Intensity"},
    FrameTicks → {Automatic, Automatic, None, None},
    TextStyle → {FontFamily → "Helvetica", FontSize → 18},
    PlotStyle → {PointSize[.01], Hue[0]}]
```

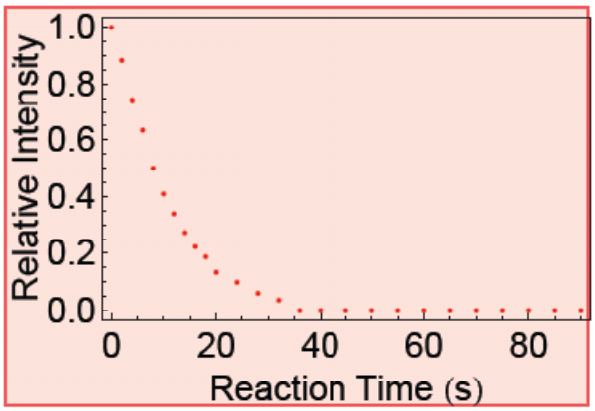


```
A1 = 1` E^-k1 t
```

$1.\, e^{-k1\, t}$

```
datCdAc290A1fit =
  NonlinearFit[datCdAc290, A1, {t}, {{k1, 1}}, ShowProgress -> True]
```

```
Iteration:1 ChiSquared:1.93107 Parameters:{0.661892}
Iteration:2 ChiSquared:1.33717 Parameters:{0.365634}
Iteration:3 ChiSquared:0.196379 Parameters:{0.135921}
Iteration:4 ChiSquared:0.078662 Parameters:{0.0721229}
Iteration:5 ChiSquared:0.012985 Parameters:{0.0885878}
Iteration:6 ChiSquared:0.0126032 Parameters:{0.0902289}
Iteration:7 ChiSquared:0.0126022 Parameters:{0.0901411}
Iteration:8 ChiSquared:0.0126022 Parameters:{0.0901469}
```

Iteration:9 ChiSquared:0.0126022 Parameters:{0.0901465}

Iteration:10 ChiSquared:0.0126022 Parameters:{0.0901465}

Iteration:11 ChiSquared:0.0126022 Parameters:{0.0901465}

$1.\ e^{-0.0901465\ t}$

```
datCdAc290A1fitplot = Plot[datCdAc290A1fit, {t, 0, 90},
    PlotRange → All, Frame → True, FrameStyle → {Thickness[.008]},
    FrameLabel → {"Reaction Time (s)", "Relative Intensity"},
    FrameTicks → {Automatic, Automatic, None, None},
    TextStyle → {FontFamily → "Helvetica", FontSize → 18},
    PlotStyle → {PointSize[.02], Hue[0]}]
```

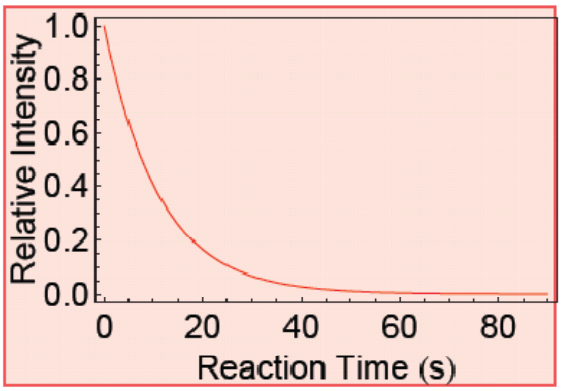


```
datCdAc290A1fit["BestFitParameters"]
NonlinearRegress[datCdAc290, A1, {t}, {k1}, ConfidenceLevel → 0.95]
```

$(1.\ e^{-0.0901465\ t})$[BestFitParameters]

{BestFitParameters → {k1 → 0.0901465}, ParameterCITable →

	Estimate	Asymptotic SE	CI
k1	0.0901465	0.00186705	{0.0863013, 0.0939918}

EstimatedVariance → 0.000504087, ANOVATable →

	DF	SumOfSq	MeanSq
Model	1	3.44822	3.44822
Error	25	0.0126022	0.000504087,
Uncorrected Total	26	3.46082	
Corrected Total	25	2.28746	

AsymptoticCorrelationMatrix → (1.),

FitCurvatureTable →

	Curvature
Max Intrinsic	0.0151842
Max Parameter–Effects	8.66973×10^{-20}
95. % Confidence Region	0.485546

Show[{datCdAc290plot, datCdAc290A1fitplot}]

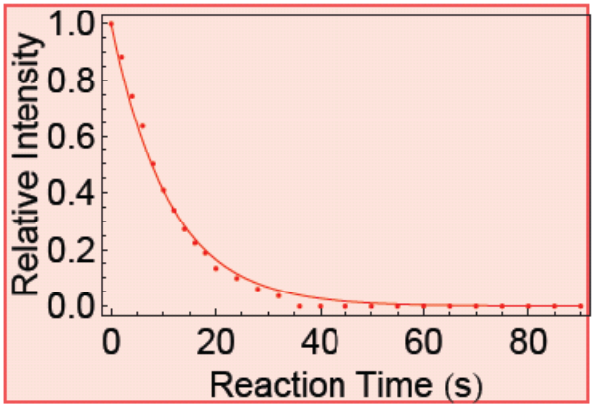

k1 = 0.09014654746046902`

0.0901465

datCdAc264 = {{0.`, 0.`}, {2.`, 0.11645917959777462`},
{4.`, 0.22529134508142987`}, {6.`, 0.28806150834611005`},
{8.`, 0.3402275025991049`}, {10.`, 0.35861011564851314`},
{12.`, 0.36984057297459877`}, {14.`, 0.35989799840952486`},
{16.`, 0.3342008739791945`}, {18.`, 0.3058530035507127`},

```
{20.`, 0.2999974996358978`}, {24.`, 0.2389048794287455`},
{28.`, 0.17959702887940587`}, {32.`, 0.1375315342794992`},
{36.`, 0.0984492620510328`}, {40.`, 0.08945514255463691`},
{45.`, 0.05484569115566023`}, {50.`, 0.`}, {55.`, 0.`}, {60.`, 0.`},
{65.`, 0.`}, {70.`, 0.`}, {75.`, 0.`}, {80.`, 0.`}, {85.`, 0.`}, {90.`, 0.`}}
```

```
{{0., 0.}, {2., 0.116459}, {4., 0.225291}, {6., 0.288062},
 {8., 0.340228}, {10., 0.35861}, {12., 0.369841}, {14., 0.359898},
 {16., 0.334201}, {18., 0.305853}, {20., 0.299997}, {24., 0.238905},
 {28., 0.179597}, {32., 0.137532}, {36., 0.0984493},
 {40., 0.0894551}, {45., 0.0548457}, {50., 0.}, {55., 0.}, {60., 0.},
 {65., 0.}, {70., 0.}, {75., 0.}, {80., 0.}, {85., 0.}, {90., 0.}}
```

```
datCdAc264plot = ListPlot[datCdAc264, PlotRange → All,
    Frame → True, FrameStyle → {Thickness[.008]},
    FrameLabel → {"Reaction Time (s)", "Relative Intensity"},
    FrameTicks → {Automatic, Automatic, None, None},
    TextStyle → {FontFamily → "Helvetica", FontSize → 18},
    PlotStyle → {PointSize[.01], Hue[0.6]}]
```

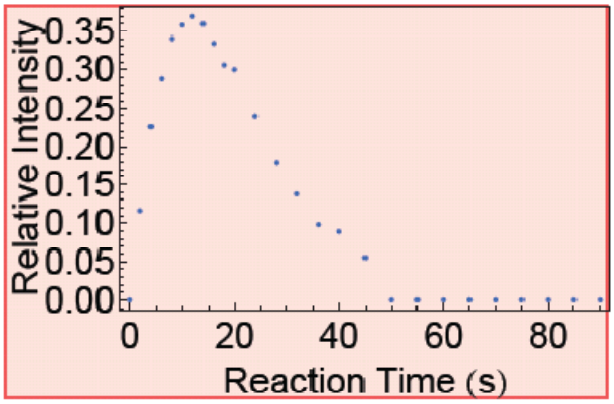

$$A2 = \frac{k1}{k2 - k1}\left(E^{-k1\,t} - E^{-k2\,t}\right)$$

$$\frac{0.0901465\left(e^{-0.0901465\,t}-e^{-k2\,t}\right)}{-0.0901465+k2}$$

```
datCdAc264fit =
  NonlinearFit[datCdAc264, A2, {t}, {{k2, 1}}, ShowProgress -> True]
```

```
Iteration:1 ChiSquared:0.640554 Parameters:{0.464209}
Iteration:2 ChiSquared:0.274562 Parameters:{0.214376}
Iteration:3 ChiSquared:0.0133307 Parameters:{0.0875253}
Iteration:4 ChiSquared:0.00709782 Parameters:{0.0961068}
Iteration:5 ChiSquared:0.00709265 Parameters:{0.0963899}
Iteration:6 ChiSquared:0.00709265 Parameters:{0.0963794}
Iteration:7 ChiSquared:0.00709265 Parameters:{0.0963798}
Iteration:8 ChiSquared:0.00709265 Parameters:{0.0963798}
```

$$14.4622\left(-e^{-0.0963798\,t}+e^{-0.0901465\,t}\right)$$

```
datCdAc264fitplot = Plot[datCdAc264fit, {t, 0, 90}, PlotRange → All,
    Frame → True, FrameStyle → {Thickness[.008]},
    FrameLabel → {"Reaction Time (s)", "Relative Intensity"},
    FrameTicks → {Automatic, Automatic, None, None},
    TextStyle → {FontFamily → "Helvetica", FontSize → 18},
    PlotStyle → {PointSize[.02], Hue[0.6]}]
```

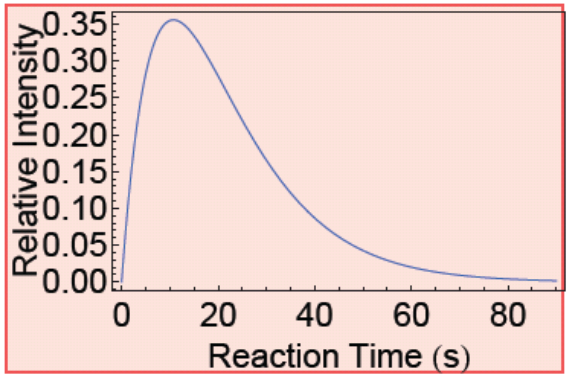

```
NonlinearRegress[datCdAc264, A2, {t}, {k2}, ConfidenceLevel → 0.95]
```

```
{BestFitParameters → {k2 → 0.0963798}, ParameterCITable →
```

	Estimate	Asymptotic SE	CI
k2	0.0963798	0.00206476	{0.0921273, 0.100632}

```
, EstimatedVariance → 0.000283706, ANOVATable →
```

	DF	SumOfSq	MeanSq
Model	1	1.07505	1.07505
Error	25	0.00709265	0.000283706,
Uncorrected Total	26	1.08215	
Corrected Total	25	0.527573	

```
AsymptoticCorrelationMatrix → ( 1. ),
```

```
FitCurvatureTable →
```

	Curvature
Max Intrinsic	0.0148575
Max Parameter–Effects	2.53009×10^{-19}
95. % Confidence Region	0.485546

```
}
k2 = 0.09637980464846753`
0.0963798
0.09637980464846753`

datCdAc238 = {{0.`, 0.`}, {2.`, 0.`},
    {4.`, 0.03095317129993098`}, {6.`, 0.07688450041511014`},
    {8.`, 0.13069761780982742`}, {10.`, 0.18362136306114274`},
    {12.`, 0.22599561139870383`}, {14.`, 0.2602023134881802`},
    {16.`, 0.306075472296518l`}, {18.`, 0.31745896802682155`},
    {20.`, 0.3360734363176365`}, {24.`, 0.3607686036770351`},
    {28.`, 0.34755102009296357`}, {32.`, 0.3172656366234489`},
    {36.`, 0.29893850529737553`}, {40.`, 0.2832704317608572`},
```

```
{45.`, 0.21324634523109712`}, {50.`, 0.18159784046663147`},
 {55.`, 0.1334933320632365`}, {60.`, 0.07570639164919249`},
 {65.`, 0.07152736164195277`}, {70.`, 0.0492575961955451`},
 {75.`, 0.031614468285393924`}, {80.`, 0.`}, {85.`, 0.`}, {90.`, 0.`}}
{{0., 0.}, {2., 0.}, {4., 0.0309532}, {6., 0.0768845}, {8., 0.130698},
 {10., 0.183621}, {12., 0.225996}, {14., 0.260202}, {16., 0.306075},
 {18., 0.317459}, {20., 0.336073}, {24., 0.360769}, {28., 0.347551},
 {32., 0.317266}, {36., 0.298939}, {40., 0.28327}, {45., 0.213246},
 {50., 0.181598}, {55., 0.133493}, {60., 0.0757064}, {65., 0.0715274},
 {70., 0.0492576}, {75., 0.0316145}, {80., 0.}, {85., 0.}, {90., 0.}}

datCdAc238plot = ListPlot[datCdAc238, PlotRange → All,
   Frame → True, FrameStyle → {Thickness[.008]},
   FrameLabel → {"Reaction Time (s)", "Relative Intensity"},
   FrameTicks → {Automatic, Automatic, None, None},
   TextStyle → {FontFamily → "Helvetica", FontSize → 18},
   PlotStyle → {PointSize[.01], Hue[0.3]}]
```

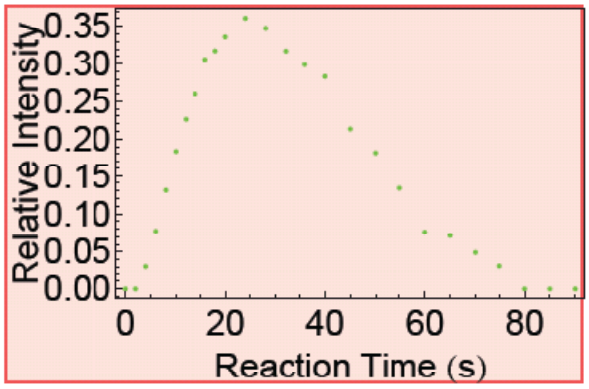

A3 =

$$k1\,k2\left(\frac{E^{-k1\,t}}{(k2-k1)\,(k3-k1)}+\frac{E^{-k2\,t}}{(k1-k2)\,(k3-k2)}+\frac{E^{-k3\,t}}{(k1-k3)\,(k2-k3)}\right)$$

$$0.00868831\left(\frac{e^{-k3\,t}}{(0.0901465-k3)\,(0.0963798-k3)}-\frac{160.43\,e^{-0.0963798\,t}}{-0.0963798+k3}+\frac{160.43\,e^{-0.0901465\,t}}{-0.0901465+k3}\right)$$

```
datCdAc238fit =
  NonlinearFit[datCdAc238, A3, {t}, {{k3, 1}}, ShowProgress -> True]
```

```
Iteration:1 ChiSquared:0.334042 Parameters:{0.161676}
Iteration:2 ChiSquared:0.122403 Parameters:{0.103691}
Iteration:3 ChiSquared:0.111642 Parameters:{0.045452}
Iteration:4 ChiSquared:0.0384483 Parameters:{0.0531749}
Iteration:5 ChiSquared:0.00887778 Parameters:{0.0637357}
Iteration:6 ChiSquared:0.00867066 Parameters:{0.0649011}
Iteration:7 ChiSquared:0.00867029 Parameters:{0.0648504}
Iteration:8 ChiSquared:0.00867029 Parameters:{0.0648533}
Iteration:9 ChiSquared:0.00867029 Parameters:{0.0648532}
Iteration:10 ChiSquared:0.00867029 Parameters:{0.0648532}
```

$$0.00868831\left(5088.71\,e^{-0.0963798\,t}-6342.76\,e^{-0.0901465\,t}+1254.05\,e^{-0.0648532\,t}\right)$$

```
datCdAc238fitplot = Plot[datCdAc238fit, {t, 0, 90}, PlotRange → All,
    Frame → True, FrameStyle → {Thickness[.008]},
    FrameLabel → {"Reaction Time (s)", "Relative Intensity"},
    FrameTicks → {Automatic, Automatic, None, None},
    TextStyle → {FontFamily → "Helvetica", FontSize → 18},
    PlotStyle → {PointSize[.02], Hue[0.3]}]
```

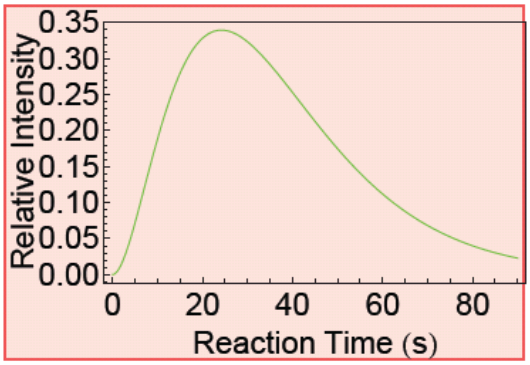

NonlinearRegress[datCdAc238, A3, {t}, {k3}, ConfidenceLevel → 0.95]

{BestFitParameters → {k3 → 0.0648532}, ParameterCITable →

	Estimate	Asymptotic SE	CI
k3	0.0648532	0.00150559	{0.0617524, 0.067954}

,

EstimatedVariance → 0.000346812, ANOVATable →

	DF	SumOfSq	MeanSq
Model	1	1.10694	1.10694
Error	25	0.00867029	0.000346812,
Uncorrected Total	26	1.11561	
Corrected Total	25	0.426706	

AsymptoticCorrelationMatrix → (1.),

FitCurvatureTable →

	Curvature
Max Intrinsic	0.0157373
Max Parameter–Effects	1.9691×10^{-15}
95. % Confidence Region	0.485546

}

k3 = 0.0648531899811508`

0.0648532

```
datCdAc212 = {{0.`, 0.`}, {2.`, 0.`}, {4.`, 0.`}, {6.`, 0.`},
    {8.`, 0.029343428517493088`}, {10.`, 0.04871853763403332`},
    {12.`, 0.06548700295732826`}, {14.`, 0.10783711445003227`},
    {16.`, 0.13648337520449785`}, {18.`, 0.1885848236558824`},
    {20.`, 0.23018888991464792`}, {24.`, 0.301344390045513`},
    {28.`, 0.4121346951302714`}, {32.`, 0.5085229731274632`},
    {36.`, 0.6026122326515916`}, {40.`, 0.6272744256845059`},
    {45.`, 0.7319079636132426`}, {50.`, 0.8184021595333686`},
    {55.`, 0.8665066679367635`}, {60.`, 0.9242936083508075`},
    {65.`, 0.9284726383580472`}, {70.`, 0.9507424038044548`},
    {75.`, 0.9683855317146061`}, {80.`, 1.`}, {85.`, 1.`}, {90.`, 1.`}}
```

```
{{0., 0.}, {2., 0.}, {4., 0.}, {6., 0.}, {8., 0.0293434},
  {10., 0.0487185}, {12., 0.065487}, {14., 0.107837}, {16., 0.136483},
  {18., 0.188585}, {20., 0.230189}, {24., 0.301344}, {28., 0.412135},
  {32., 0.508523}, {36., 0.602612}, {40., 0.627274}, {45., 0.731908},
  {50., 0.818402}, {55., 0.866507}, {60., 0.924294}, {65., 0.928473},
  {70., 0.950742}, {75., 0.968386}, {80., 1.}, {85., 1.}, {90., 1.}}
```

```
datCdAc212plot = ListPlot[datCdAc212, PlotRange → All,
    Frame → True, FrameStyle → {Thickness[.008]},
    FrameLabel → {"Reaction Time (s)", "Relative Intensity"},
    FrameTicks → {Automatic, Automatic, None, None},
    TextStyle → {FontFamily → "Helvetica", FontSize → 18},
    PlotStyle → {PointSize[.01], Hue[0.9]}]
```

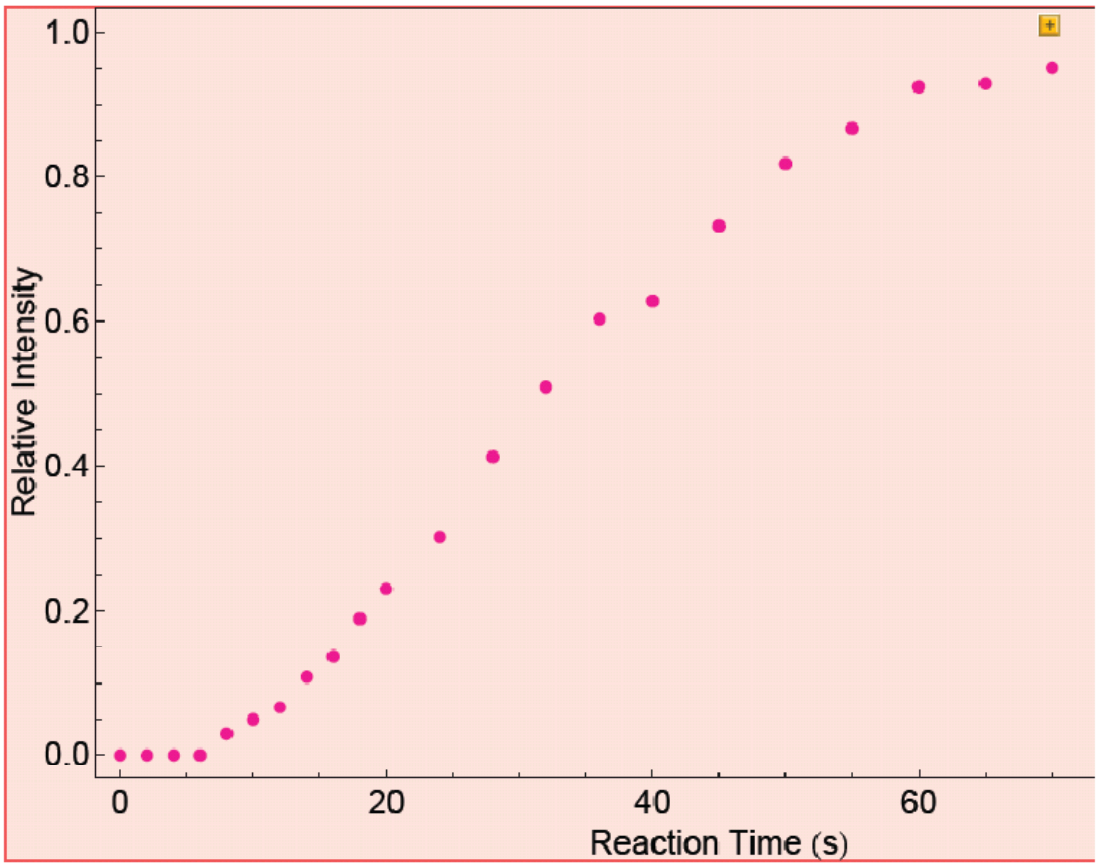

$$A4 = k1\,k2\,k3\left(\frac{E^{-k1\,t}}{(k2-k1)\,(k3-k1)\,(0-k1)} + \frac{E^{-k2\,t}}{(k1-k2)\,(k3-k2)\,(0-k2)} + \frac{E^{-k3\,t}}{(k1-k3)\,(k2-k3)\,(0-k3)} + \frac{E^{-0\,t}}{(k1-0)\,(k2-0)\,(k3-0)}\right)$$

0.000563464

$$\left(1774.74 - 52\,798.5\,e^{-0.0963798\,t} + 70\,360.6\,e^{-0.0901465\,t} - 19\,336.8\,e^{-0.0648532\,t}\right)$$

```
datCdAc212fitplot = Plot[A4, {t, 0, 90}, PlotRange → All,
    Frame → True, FrameStyle → {Thickness[.1]},
    FrameLabel → {"Reaction Time (s)", "Relative Intensity"},
    FrameTicks → {Automatic, Automatic, None, None},
    TextStyle → {FontFamily → "Helvetica", FontSize → 18},
    PlotStyle → {PointSize[.02], Hue[0.9]}]
```

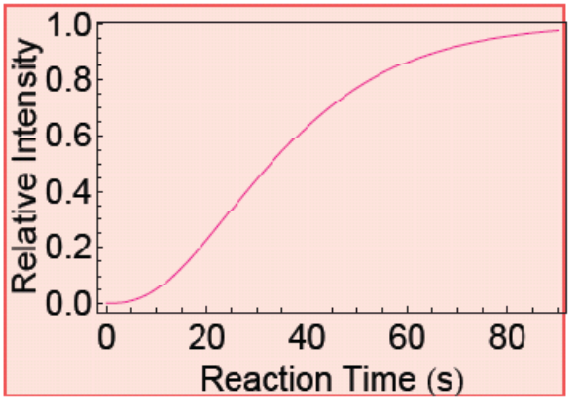


```
2008june18cdacnegcd1 =
  Show[{datCdAc290plot, datCdAc290A1fitplot, datCdAc264plot,
      datCdAc264fitplot, datCdAc238plot, datCdAc238fitplot,
      datCdAc212plot, datCdAc212fitplot}]
```

E.2. Reaction Between $[Cd_3(CH_3COO)_5]^+$ and H_2S ($4x10^{-9}$ Torr)

```
Clear[k1, k2, k3, k4]

Clear[k5, k6]

Needs["Statistics`NonlinearFit`"]

datCdAcS0 = {{0.`, 0.9147696163768304`}, {0.1`, 0.5419837643744964`},
    {0.2`, 0.3160714684719638`}, {0.3`, 0.1797813597671195`},
    {0.4`, 0.10188007184530377`}, {0.5`, 0.0562913303815725`},
    {0.6`, 0.03366613865652104`}, {0.7`, 0.017951227609547434`},
    {0.8`, 0.009834402035124807`}, {0.9`, 0.006294641203481293`},
    {1.`, 0.0031810491743640493`}, {1.2`, 0.`}, {1.4`, 0.`}, {1.6`, 0.`},
    {1.8`, 0.`}, {2.`, 0.`}, {2.5`, 0.`}, {3.`, 0.`}, {3.5`, 0.`}, {4.`, 0.`},
    {4.5`, 0.`}, {5.`, 0.`}, {6.`, 0.`}, {7.`, 0.`}, {8.`, 0.`}, {9.`, 0.`}, {10.`, 0.`}}
{{0., 0.91477}, {0.1, 0.541984}, {0.2, 0.316071}, {0.3, 0.179781},
  {0.4, 0.10188}, {0.5, 0.0562913}, {0.6, 0.0336661}, {0.7, 0.0179512},
  {0.8, 0.0098344}, {0.9, 0.00629464}, {1., 0.00318105}, {1.2, 0.},
  {1.4, 0.}, {1.6, 0.}, {1.8, 0.}, {2., 0.}, {2.5, 0.}, {3., 0.}, {3.5, 0.},
  {4., 0.}, {4.5, 0.}, {5., 0.}, {6., 0.}, {7., 0.}, {8., 0.}, {9., 0.}, {10., 0.}}
```

```
datCdAcS0plot = ListPlot[datCdAcS0, PlotRange → All,
    Frame → True, FrameStyle → {Thickness[.008]},
    FrameLabel → {"Reaction Time (s)", "Relative Intensity"},
    FrameTicks → {Automatic, Automatic, None, None},
    TextStyle → {FontFamily → "Helvetica", FontSize → 18},
    PlotStyle → {PointSize[.01], Hue[0]}]
```

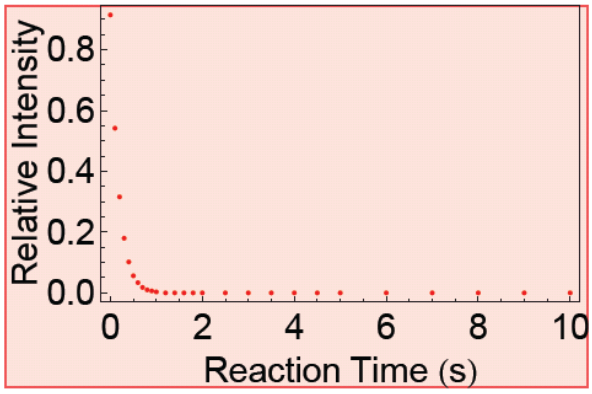


```
A1 = 0.9147696163768304` E^-k1 t
```

$0.91477\, e^{-k1\, t}$

```
datCdAcS0fit =
  NonlinearFit[datCdAcS0, A1, {t}, {{k1, 1}}, ShowProgress -> True]
```

```
Iteration:1 ChiSquared:0.497178 Parameters:{2.14362}
Iteration:2 ChiSquared:0.0678177 Parameters:{3.68135}
Iteration:3 ChiSquared:0.00294026 Parameters:{4.95233}
Iteration:4 ChiSquared:0.000170759 Parameters:{5.35763}
Iteration:5 ChiSquared:0.00016555 Parameters:{5.37742}
Iteration:6 ChiSquared:0.000165549 Parameters:{5.37714}
Iteration:7 ChiSquared:0.000165549 Parameters:{5.37715}
Iteration:8 ChiSquared:0.000165549 Parameters:{5.37715}
```

$0.91477\, e^{-5.37715\, t}$

```
datCdAcS0fitplot = Plot[datCdAcS0fit, {t, 0, 10}, PlotRange → All,
    Frame → True, FrameStyle → {Thickness[.008]},
    FrameLabel → {"Reaction Time (s)", "Relative Intensity"},
    FrameTicks → {Automatic, Automatic, None, None},
    TextStyle → {FontFamily → "Helvetica", FontSize → 18},
    PlotStyle → {PointSize[.02], Hue[0]}]
```

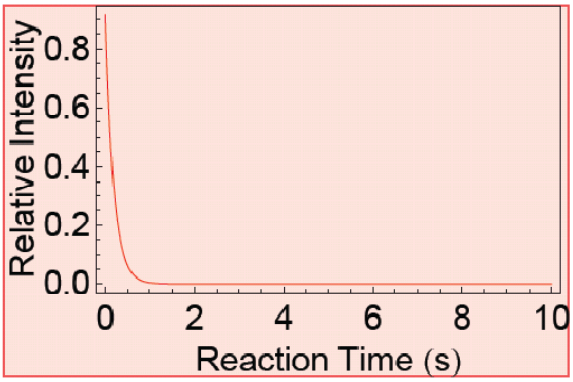


```
datCdAcS0fit["BestFitParameters"]
NonlinearRegress[datCdAcS0, A1, {t}, {k1}, ConfidenceLevel → 0.95]
(0.91477 e^(-5.37715 t))[BestFitParameters]
```

$$\{\text{BestFitParameters} \to \{k1 \to 5.37715\},$$

ParameterCITable →

	Estimate	Asymptotic SE	CI
k1	5.37715	0.021816	{5.33231, 5.42199}

$$\text{EstimatedVariance} \to 6.36728 \times 10^{-6},$$

ANOVATable →

	DF	SumOfSq	MeanSq
Model	1	1.27776	1.27776
Error	26	0.000165549	6.36728×10^{-6},
Uncorrected Total	27	1.27792	
Corrected Total	26	1.10163	

AsymptoticCorrelationMatrix → (1.),

FitCurvatureTable →

	Curvature
Max Intrinsic	0.00344951
Max Parameter–Effects	7.54769×10^{-21}
95. % Confidence Region	0.486493

Show[{datCdAcS0plot, datCdAcS0fitplot}]

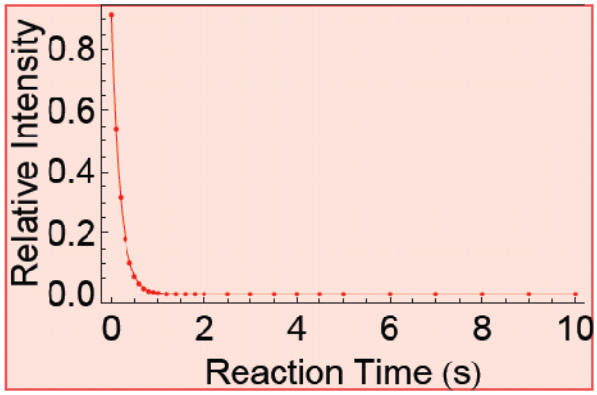

k1 = 5.3771490284840375`

5.37715

datCdAcS1 = {{0.`, 0.08523038362316948`},
{0.1`, 0.4406727830056816`}, {0.2`, 0.6327573086201217`},
{0.3`, 0.7326877783905352`}, {0.4`, 0.768658164239398`},
{0.5`, 0.7747643635752016`}, {0.6`, 0.7646925984554395`},
{0.7`, 0.7481923712461948`}, {0.8`, 0.7230334503780019`},
{0.9`, 0.6989322944505175`}, {1.`, 0.6746645978132538`},
{1.2`, 0.6223529518579245`}, {1.4`, 0.5795104250868189`},
{1.6`, 0.5316462229697912`}, {1.8`, 0.4925896052863775`},
{2.`, 0.4524315659060742`}, {2.5`, 0.36689847373346285`},
{3.`, 0.29975588902103933`}, {3.5`, 0.24114393354828176`},
{4.`, 0.1938145061910302`}, {4.5`, 0.1576741070970518`},

```
{5.`, 0.12717486305327869`}, {6.`, 0.08236115583741856`},
 {7.`, 0.05239495351696977`}, {8.`, 0.03339169556493384`},
 {9.`, 0.021753851397627384`}, {10.`, 0.01556801290768075`}}
```

```
{{0., 0.0852304}, {0.1, 0.440673}, {0.2, 0.632757},
 {0.3, 0.732688}, {0.4, 0.768658}, {0.5, 0.774764}, {0.6, 0.764693},
 {0.7, 0.748192}, {0.8, 0.723033}, {0.9, 0.698932}, {1., 0.674665},
 {1.2, 0.622353}, {1.4, 0.57951}, {1.6, 0.531646}, {1.8, 0.49259},
 {2., 0.452432}, {2.5, 0.366898}, {3., 0.299756}, {3.5, 0.241144},
 {4., 0.193815}, {4.5, 0.157674}, {5., 0.127175}, {6., 0.0823612},
 {7., 0.052395}, {8., 0.0333917}, {9., 0.0217539}, {10., 0.015568}}
```

```
datCdAcS1plot = ListPlot[datCdAcS1, PlotRange → All,
   Frame → True, FrameStyle → {Thickness[.008]},
   FrameLabel → {"Reaction Time (s)", "Relative Intensity"},
   FrameTicks → {Automatic, Automatic, None, None},
   TextStyle → {FontFamily → "Helvetica", FontSize → 18},
   PlotStyle → {PointSize[.01], Hue[0.6]}]
```

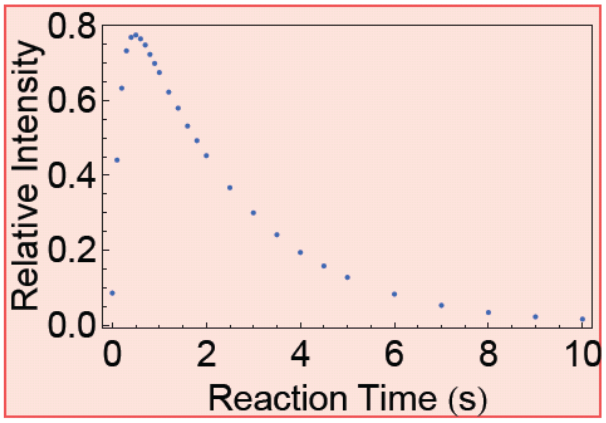

$$A2 = \frac{k1}{k2 - k1}\left(E^{-k1\,t} - E^{-k2\,t}\right)$$

$$\frac{5.37715\left(e^{-5.37715\,t} - e^{-k2\,t}\right)}{-5.37715 + k2}$$

```
datCdAcS1fit =
  NonlinearFit[datCdAcS1, A2, {t}, {{k2, 1}}, ShowProgress -> True]
```

```
Iteration:1 ChiSquared:0.643912 Parameters:{0.232531}
Iteration:2 ChiSquared:0.0563312 Parameters:{0.376937}
Iteration:3 ChiSquared:0.0137312 Parameters:{0.439854}
Iteration:4 ChiSquared:0.0132614 Parameters:{0.447611}
Iteration:5 ChiSquared:0.0132608 Parameters:{0.447892}
Iteration:6 ChiSquared:0.0132608 Parameters:{0.447899}
Iteration:7 ChiSquared:0.0132608 Parameters:{0.4479}
Iteration:8 ChiSquared:0.0132608 Parameters:{0.4479}
```

$$-1.09087\left(e^{-5.37715\,t}-e^{-0.4479\,t}\right)$$

```
datCdAcS1fitplot = Plot[datCdAcS1fit, {t, 0, 10}, PlotRange -> All,
    Frame -> True, FrameStyle -> {Thickness[.008]},
    FrameLabel -> {"Reaction Time (s)", "Relative Intensity"},
    FrameTicks -> {Automatic, Automatic, None, None},
    TextStyle -> {FontFamily -> "Helvetica", FontSize -> 18},
    PlotStyle -> {PointSize[.02], Hue[0.6]}]
```

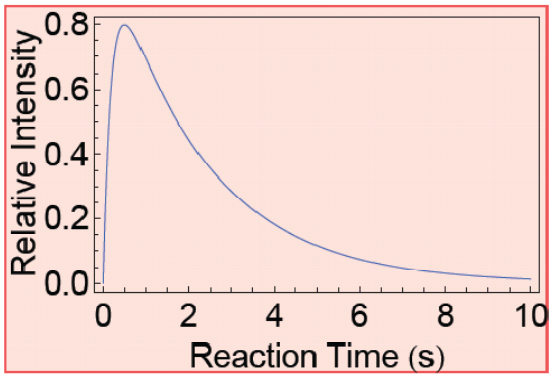


```
NonlinearRegress[datCdAcS1, A2, {t}, {k2}, ConfidenceLevel -> 0.95]
```

```
{BestFitParameters -> {k2 -> 0.4479},
```

ParameterCITable →

	Estimate	Asymptotic SE	CI
k2	0.4479	0.00834672	{0.430743, 0.465057}

,

EstimatedVariance → 0.000510031, ANOVATable →

	DF	SumOfSq	MeanSq
Model	1	6.75323	6.75323
Error	26	0.0132608	0.000510031,
Uncorrected Total	27	6.76649	
Corrected Total	26	2.02487	

AsymptoticCorrelationMatrix → (1.),

FitCurvatureTable →

	Curvature
Max Intrinsic	0.0133452
Max Parameter–Effects	6.26946×10^{-19}
95. % Confidence Region	0.486493

}

k2 = 0.4478996768012266`

0.4479

datCdAcS2 =

{{0.`, 0.`}, {0.1`, 0.0173434526198221`}, {0.2`, 0.05117122290791438`},
{0.3`, 0.08753086184234529`}, {0.4`, 0.12946176391529818`},
{0.5`, 0.16894430604322588`}, {0.6`, 0.20164126288803946`},
{0.7`, 0.23385640114425768`}, {0.8`, 0.2671321475868734`},
{0.9`, 0.2922144721753611`}, {1.`, 0.319290243567676`},
{1.2`, 0.36920680781572973`}, {1.4`, 0.4116285812490135`},
{1.6`, 0.45606068311754766`}, {1.8`, 0.49243983930124136`},
{2.`, 0.5282148595559073`}, {2.5`, 0.6059247311325666`},
{3.`, 0.6620674096257972`}, {3.5`, 0.7060773275800308`},
{4.`, 0.7394024559324748`}, {4.5`, 0.763389339481055`},
{5.`, 0.7770504953937`}, {6.`, 0.7951893524633459`},
{7.`, 0.7923044088941824`}, {8.`, 0.7822681560274815`},
{9.`, 0.7652731490244898`}, {10.`, 0.747918103655697`}}

```
{{0., 0.}, {0.1, 0.0173435}, {0.2, 0.0511712}, {0.3, 0.0875309}, {0.4, 0.129462},
 {0.5, 0.168944}, {0.6, 0.201641}, {0.7, 0.233856}, {0.8, 0.267132},
 {0.9, 0.292214}, {1., 0.31929}, {1.2, 0.369207}, {1.4, 0.411629},
 {1.6, 0.456061}, {1.8, 0.49244}, {2., 0.528215}, {2.5, 0.605925},
 {3., 0.662067}, {3.5, 0.706077}, {4., 0.739402}, {4.5, 0.763389}, {5., 0.77705},
 {6., 0.795189}, {7., 0.792304}, {8., 0.782268}, {9., 0.765273}, {10., 0.747918}}
```

```
datCdAcS2plot = ListPlot[datCdAcS2, PlotRange → All,
    Frame → True, FrameStyle → {Thickness[.008]},
    FrameLabel → {"Reaction Time (s)", "Relative Intensity"},
    FrameTicks → {Automatic, Automatic, None, None},
    TextStyle → {FontFamily → "Helvetica", FontSize → 18},
    PlotStyle → {PointSize[.01], Hue[0.3]}]
```

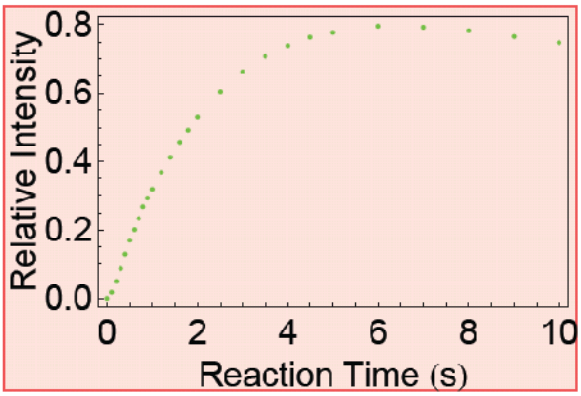

A3 =

$$k1\,k2\left(\frac{E^{-k1\,t}}{(k2-k1)\,(k3-k1)}+\frac{E^{-k2\,t}}{(k1-k2)\,(k3-k2)}+\frac{E^{-k3\,t}}{(k1-k3)\,(k2-k3)}\right)$$

2.40842

$$\left(\frac{e^{-k3\,t}}{(0.4479-k3)\,(5.37715-k3)}-\frac{0.202871\,e^{-5.37715\,t}}{-5.37715+k3}+\frac{0.202871\,e^{-0.4479\,t}}{-0.4479+k3}\right)$$

```
datCdAcS2fit =
  NonlinearFit[datCdAcS2, A3, {t}, {{k3, 1}}, ShowProgress -> True]
```

Iteration:1 ChiSquared:4.34217 Parameters:{0.693793}

Iteration:2 ChiSquared:2.76251 Parameters:{0.365685}

Iteration:3 ChiSquared:0.279054 Parameters:{0.0938453}

Iteration:4 ChiSquared:0.0209304 Parameters:{0.027589}

Iteration:5 ChiSquared:0.00799117 Parameters:{0.0373423}

Iteration:6 ChiSquared:0.00797798 Parameters:{0.037673}

Iteration:7 ChiSquared:0.00797798 Parameters:{0.0376741}

$$2.40842\left(0.0379945\, e^{-5.37715\, t} - 0.494534\, e^{-0.4479\, t} + 0.45654\, e^{-0.0376741\, t}\right)$$

```
datCdAcS2fitplot = Plot[datCdAcS2fit, {t, 0, 10}, PlotRange → All,
    Frame → True, FrameStyle → {Thickness[.008]},
    FrameLabel → {"Reaction Time (s)", "Relative Intensity"},
    FrameTicks → {Automatic, Automatic, None, None},
    TextStyle → {FontFamily → "Helvetica", FontSize → 18},
    PlotStyle → {PointSize[.02], Hue[0.3]}]
```

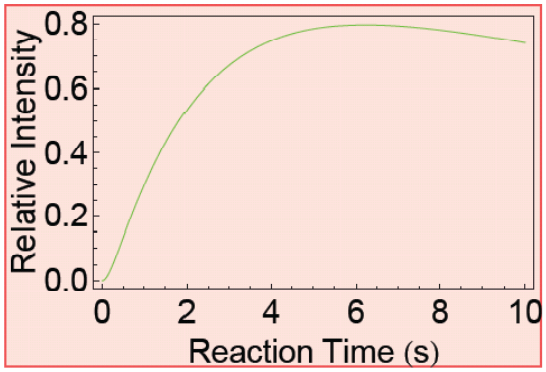


```
NonlinearRegress[datCdAcS2, A3, {t}, {k3}, ConfidenceLevel → 0.95]
```

{BestFitParameters → {k3 → 0.0376741}, ParameterCITable →

	Estimate	Asymptotic SE	CI
k3	0.0376741	0.0016002	{0.0343848, 0.0409633}

EstimatedVariance → 0.000306845, ANOVATable →

	DF	SumOfSq	MeanSq
Model	1	7.49155	7.49155
Error	26	0.00797798	0.000306845,
Uncorrected Total	27	7.49953	
Corrected Total	26	2.02032	

AsymptoticCorrelationMatrix → (1.),

FitCurvatureTable →

	Curvature
Max Intrinsic	0.00283646
Max Parameter–Effects	5.90456×10^{-19}
95. % Confidence Region	0.486493

k3 = 0.037674082758015856`

0.0376741

datCdAcS3 = {{0.`, 0.`}, {0.1`, 0.`}, {0.2`, 0.`}, {0.3`, 0.`},
{0.4`, 0.`}, {0.5`, 0.`}, {0.6`, 0.`}, {0.7`, 0.`}, {0.8`, 0.`},
{0.9`, 0.0025585921706400535`}, {1.`, 0.002864109444705958`},
{1.2`, 0.008440240326345652`}, {1.4`, 0.008860993664167587`},
{1.6`, 0.012293093912661097`}, {1.8`, 0.014970555412381155`},
{2.`, 0.019353574538018413`}, {2.5`, 0.027176795133970307`},
{3.`, 0.038176701353163464`}, {3.5`, 0.05277873887168762`},
{4.`, 0.066783037876495`}, {4.5`, 0.07893655342189303`},
{5.`, 0.09577464155302137`}, {6.`, 0.12244949169923572`},
{7.`, 0.15530063758884785`}, {8.`, 0.17814168334257163`},
{9.`, 0.20606387240340926`}, {10.`, 0.22835046934992292`}}

{{0., 0.}, {0.1, 0.}, {0.2, 0.}, {0.3, 0.}, {0.4, 0.}, {0.5, 0.},
{0.6, 0.}, {0.7, 0.}, {0.8, 0.}, {0.9, 0.00255859}, {1., 0.00286411},
{1.2, 0.00844024}, {1.4, 0.00886099}, {1.6, 0.0122931}, {1.8, 0.0149706},
{2., 0.0193536}, {2.5, 0.0271768}, {3., 0.0381767}, {3.5, 0.0527787},
{4., 0.066783}, {4.5, 0.0789366}, {5., 0.0957746}, {6., 0.122449},
{7., 0.155301}, {8., 0.178142}, {9., 0.206064}, {10., 0.22835}}

```
datCdAcS3plot = ListPlot[datCdAcS3, PlotRange → All,
    Frame → True, FrameStyle → {Thickness[.008]},
    FrameLabel → {"Reaction Time (s)", "Relative Intensity"},
    FrameTicks → {Automatic, Automatic, None, None},
    TextStyle → {FontFamily → "Helvetica", FontSize → 18},
    PlotStyle → {PointSize[.01], Hue[0.9]}]
```

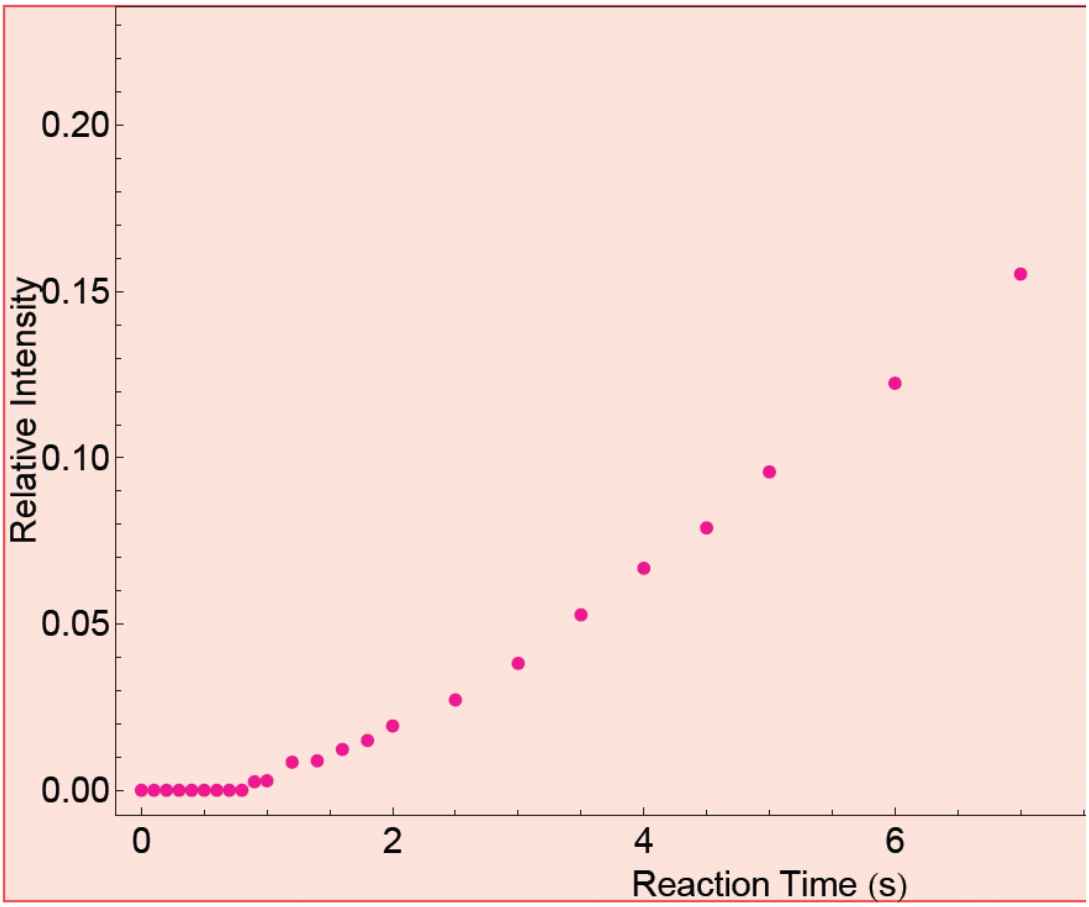

A4 =

$$k1\,k2\,k3\left(\frac{E^{-k1\,t}}{(k2-k1)\,(k3-k1)\,(k4-k1)}+\frac{E^{-k2\,t}}{(k1-k2)\,(k3-k2)\,(k4-k2)}+\frac{E^{-k3\,t}}{(k1-k3)\,(k2-k3)\,(k4-k3)}+\frac{E^{-k4\,t}}{(k1-k4)\,(k2-k4)\,(k3-k4)}\right)$$

$$0.0907351\left(\frac{e^{-k4\,t}}{(0.0376741-k4)\,(0.4479-k4)\,(5.37715-k4)}+\frac{0.0379945\,e^{-5.37715\,t}}{-5.37715+k4}-\frac{0.494534\,e^{-0.4479\,t}}{-0.4479+k4}+\frac{0.45654\,e^{-0.0376741\,t}}{-0.0376741+k4}\right)$$

datCdAcS3fit =

NonlinearFit[datCdAcS3, A4, {t}, {{k4, 1}}, ShowProgress -> True]

Iteration:1 ChiSquared:0.095142 Parameters:{0.567692}

Iteration:2 ChiSquared:0.0369066 Parameters:{0.221364}

Iteration:3 ChiSquared:0.00137344 Parameters:{−0.00484674}

Iteration:4 ChiSquared:0.000135903 Parameters:{0.0166075}

Iteration:5 ChiSquared:0.000132269 Parameters:{0.0179011}

Iteration:6 ChiSquared:0.000132269 Parameters:{0.0179077}

Iteration:7 ChiSquared:0.000132269 Parameters:{0.0179077}

$$0.0907351\left(-0.00708953\,e^{-5.37715\,t}+1.1501\,e^{-0.4479\,t}-23.0968\,e^{-0.0376741\,t}+21.9538\,e^{-0.0179077\,t}\right)$$

```
datCdAcS3fitplot = Plot[datCdAcS3fit, {t, 0, 10}, PlotRange → All,
    Frame → True, FrameStyle → {Thickness[.008]},
    FrameLabel → {"Reaction Time (s)", "Relative Intensity"},
    FrameTicks → {Automatic, Automatic, None, None},
    TextStyle → {FontFamily → "Helvetica", FontSize → 18},
    PlotStyle → {PointSize[.02], Hue[0.9]}]
```

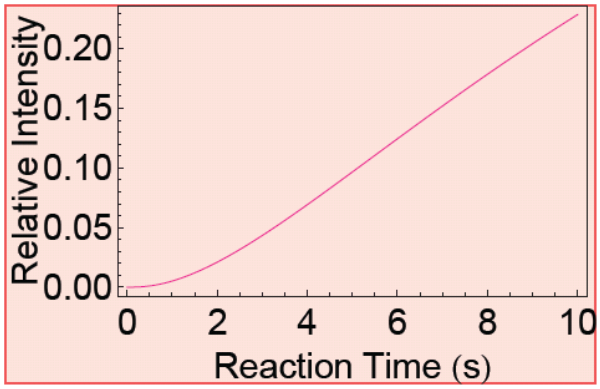

NonlinearRegress[datCdAcS3, A4, {t}, {k4}, ConfidenceLevel → 0.95]

{BestFitParameters → {k4 → 0.0179077}, ParameterCITable →

	Estimate	Asymptotic SE	CI
k4	0.0179077	0.00154192	{0.0147383, 0.0210772}

EstimatedVariance → 5.08728×10^{-6}, ANOVATable →

	DF	SumOfSq	MeanSq
Model	1	0.19108	0.19108
Error	26	0.000132269	5.08728×10^{-6},
Uncorrected Total	27	0.191213	
Corrected Total	26	0.12675	

AsymptoticCorrelationMatrix → (1.),

FitCurvatureTable →

	Curvature
Max Intrinsic	0.00130645
Max Parameter–Effects	1.39201×10^{-15}
95. % Confidence Region	0.486493

}

k4 = 0.017907715034809788`

0.0179077

```
datCdAcS4 = {{0.`, 0.`}, {0.1`, 0.`}, {0.2`, 0.`}, {0.3`, 0.`},
    {0.4`, 0.`}, {0.5`, 0.`}, {0.6`, 0.`}, {0.7`, 0.`}, {0.8`, 0.`},
    {0.9`, 0.`}, {1.`, 0.`}, {1.2`, 0.`}, {1.4`, 0.`}, {1.6`, 0.`}, {1.8`, 0.`},
    {2.`, 0.`}, {2.5`, 0.`}, {3.`, 0.`}, {3.5`, 0.`}, {4.`, 0.`}, {4.5`, 0.`},
    {5.`, 0.`}, {6.`, 0.`}, {7.`, 0.`}, {8.`, 0.0061984650650129 54`},
    {9.`, 0.006909127174473598`}, {10.`, 0.008163414086699412`}}
```

```
{{0., 0.}, {0.1, 0.}, {0.2, 0.}, {0.3, 0.}, {0.4, 0.}, {0.5, 0.}, {0.6, 0.}, {0.7, 0.},
  {0.8, 0.}, {0.9, 0.}, {1., 0.}, {1.2, 0.}, {1.4, 0.}, {1.6, 0.}, {1.8, 0.},
  {2., 0.}, {2.5, 0.}, {3., 0.}, {3.5, 0.}, {4., 0.}, {4.5, 0.}, {5., 0.}, {6., 0.},
  {7., 0.}, {8., 0.00619847}, {9., 0.00690913}, {10., 0.00816341}}
```

```
datCdAcS4plot = ListPlot[datCdAcS4, PlotRange → All,
    Frame → True, FrameStyle → {Thickness[.008]},
    FrameLabel → {"Reaction Time (s)", "Relative Intensity"},
    FrameTicks → {Automatic, Automatic, None, None},
    TextStyle → {FontFamily → "Helvetica", FontSize → 18},
    PlotStyle → {PointSize[.01], Hue[0.1]}]
```

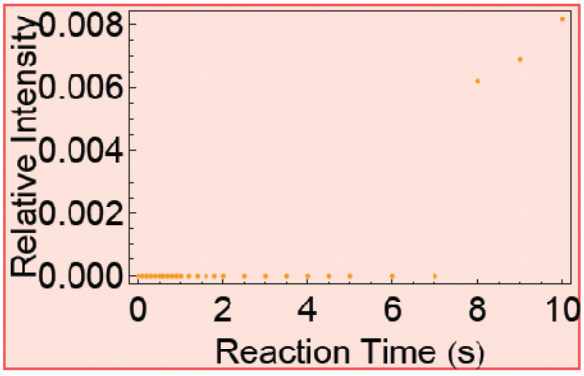

$$A5 = k1\,k2\,k3\,k4\left(\frac{E^{-k1\,t}}{(k2-k1)\,(k3-k1)\,(k4-k1)\,(0-k1)} + \frac{E^{-k2\,t}}{(k1-k2)\,(k3-k2)\,(k4-k2)\,(0-k2)} + \frac{E^{-k3\,t}}{(k1-k3)\,(k2-k3)\,(k4-k3)\,(0-k3)} + \frac{E^{-k4\,t}}{(k1-k4)\,(k2-k4)\,(k3-k4)\,(0-k4)} + \frac{E^{-0\,t}}{(k1-0)\,(k2-0)\,(k3-0)\,(k4-0)}\right)$$

$$0.00162486\,(615.438 + 0.00131845\,e^{-5.37715\,t} - 2.56777\,e^{-0.4479\,t} + 613.069\,e^{-0.0376741\,t} - 1225.94\,e^{-0.0179077\,t})$$

```
datCdAcS4fitplot = Plot[A5, {t, 0, 10}, PlotRange → All,
    Frame → True, FrameStyle → {Thickness[.1]},
    FrameLabel → {"Reaction Time (s)", "Relative Intensity"},
    FrameTicks → {Automatic, Automatic, None, None},
    TextStyle → {FontFamily → "Helvetica", FontSize → 18},
    PlotStyle → {PointSize[.02], Hue[0.1]}]
```